1-1-1990

Recent starbirth and starburst activity in nearby galaxies.

William H. Waller
University of Massachusetts Amherst

RECENT STARBIRTH AND STARBURST ACTIVITY IN NEARBY GALAXIES

A Dissertation Presented

by

WILLIAM HOWARD WALLER

Submitted to the Graduate School of the
University of Massachusetts in partial fulfillment
of the requirements for the degree of

DOCTOR OF PHILOSOPHY

February 1990

Department of Physics and Astronomy

RECENT STARBIRTH AND STARBURST ACTIVITY IN NEARBY GALAXIES

A Dissertation Presented

by

WILLIAM HOWARD WALLER

Approved as to style and content by:

Stephen E. Strom, Chairperson

Judith S. Young, Member

John Kwan, Member

Susan G. Kleinmann, Member

Nicholas Z. Scoville, Outside Member

Robert W. Mallary, Outside Member

Robert B. Hallock, Department Head
Department of Physics and Astronomy

Dedicated
to
Wonder

"*How is it that the sky feeds the stars?*"

- Lucretius

"*... regions of lucid matter taking form,*
Brushes of fire, hazy gleams,
Clusters and beds of worlds, and bee-like swarms
Of suns and starry streams ..."

- Tennyson

ACKNOWLEDGMENTS

First and foremost, I am beholden to Sandra E. Paille – my wedded mate. Besides crafting all of the tables for this dissertation, Sandy has given me much needed encouragement and emotional support. Her unflagging confidence has pulled me through many of the darker moments, and her cheerful companionship has made the work much less dreary. My parents, Patricia and Marvin Waller, have encouraged my astronomical leanings ever since I decided at the age of ten to switch from wanting to be a moving man to wanting to be an astronomer. They have waited a long time to see this become a reality. The rest of the Waller and Paille families have been rooting for me like diehard Celtics fans. Their patience has been phenomenal.

Throughout my graduate years at the University of Massachusetts, I have enjoyed the warm company of many friends and cohorts. Mark and Sheila Hemeon-Heyer, Rob Seaman and Julie Strom, Dave and Denise Taylor, Linda and Lowell Tacconi-Garman, Jeff and Jo Papa Kenney, Jim Morgan, Kevin Olson, Steve Lord, and my favorite lunchmate Sylvie Cabrit are just a few of the many good souls who transformed my tenure at UMass into a smorgasbord of pastoral picnics, dizzy dances, and cosmic conversations.

The good folks on my committee have given of themselves to ensure that my dissertation does not make a complete fool out of me. Their timely words of advice have made a real difference in stimulating, directing, and shaping my research. Steve Strom, my dissertation advisor, got me thinking about the types of stars that are created in ionizing clusters (*ie.* the Initial Mass Function [IMF]) and the use of the Hα equivalent width as a tracer of cluster IMFs. Much of the M101 chapter derives from lively conversations with Steve. Steve has also paid his dues as an advocate on my behalf. I can only hope that he is rewarded with another Celtics championship *soon.* Susan Kleinmann first suggested using the near-infrared emission from [SIII] to probe heavily obscured regions of ionized gas. The chapter on M82 makes full use of this dust-cutting technique. Sue also paved the way for me to observe at McGraw Hill Observatory, where much of the data in this thesis were obtained. Her spirited and gutsy philosophy of doing astronomy and just about everything else has left an indelible impression on me. John Kwan dispensed sober counseling with good humor, for which I am extremely grateful. His willingness to plow through clumsily derived theoretical arguments at a moments notice was often exploited. Nick Scoville has been an indefatigable source of insightful comments and rollicking good times. His long-standing concern for me has been a great help. Judy Young has inspired me with her love for galaxies and with her kind hospitality. Much of this dissertation has benefitted from Judy's astute comments. The astronomical get-togethers that she often organized—for lunch under some tree or for hand-cranked ice-cream at her home—comprise some of my finest memories of UMass. Outside member, Bob Mallary of the Fine Arts department is to be commended for being such a good sport. Our discussions on the visual aspects of astronomy from both scientific and artistic viewpoints were most refreshing. Graduate advisor, David Van Blerkom provided crucial council and encouragement in the final months. His efforts on my behalf are most deeply appreciated.

Many thanks are owed to the astronomers and support personnel at McGraw-Hill and Kitt Peak observatories. Besides giving me precious opportunities to observe with state-of-the-art instrumentation, they helped to make my observing runs both productive and enjoyable. Matt Johns, Gerry Luppino, and George Ricker at McGraw Hill, and Jeanette Barnes, Monique Chapman, George Jacoby, and Bill Schoening at Kitt Peak were especially generous with their time and efforts on my behalf. This sort of support for graduate student research was, in my case, crucial. I hope it will continue.

At the University of Washington, I have benefitted from fruitful conversations with Paul Hodge, Erica Bohm-Vitense, Carl Heinz Bohm, Myung Gyoon Lee, and Alex Raga. Beyond my host institutions, Alison Campbell, Darren DePoy, Marshall Joy, Rob Kennicutt, Richard Larson, and Donald Osterbrock have been generous with their expert knowledge and kind encouragement.

Lastly, I am grateful for having experienced Bart J. Bok and James M. Hendrix, wherever they are.

ABSTRACT

RECENT STARBIRTH AND STARBURST ACTIVITY IN NEARBY GALAXIES

FEBRUARY 1990

WILLIAM HOWARD WALLER, B.S., UNIVERSITY OF ARIZONA
M.S., WORCESTER POLYTECHNIC INSTITUTE
Ph.D., UNIVERSITY OF MASSACHUSETTS

Directed by: Professor Stephen E. Strom

The ionizing starbirth activity in M101. M82. and NGC 1569 has been investigated via CCD imagery at Hα. R. I. and [SIII] bands. The three galaxies are compared with one another and with M51. M83, and the Milky Way in terms of their starbirth intensities. starbirth efficiencies. and possible starbirth histories. The globally-averaged starbirth intensities that are inferred from the extinction-corrected Hα surface brightnesses vary by ~3 orders of magnitude. with M101 and the Milky Way defining the low end and with M82 defining the high-intensity regime. The annular-averaged starbirth intensities correlate strongly with the H_2 surface densities and with the total gas surface densities. where near-linear relationships are obtained. Unusually high starbirth efficiencies and eruptive gaseous morphologies are evident in M82. NGC 1569. and NGC 5461 — one of the supergiant HII region complexes in M101. Crude indices of the galaxies' starbirth histories indicate temporally declining starbirth intensities in M101 and the Milky Way but currently "bursting" starbirth intensities in M82 and NGC 1569.

In M101. annular-averaged photometry of the Hα emission yields a much flatter galactocentric profile of surface brightness than that of the red-continuum starlight. The corresponding e-folding scalelengths are 9 and 3.3 kpc. respectively, thus implying significant differences between the galactocentric distributions of current-epoch massive star formation and past-averaged star formation. Moreover, the giant HII regions in M101 show significant variations in Hα equivalent width as a function of both galactocentric radius and Hα luminosity. These variations can be attributed to changes in the upper stellar mass limits of the ionizing clusters — M(upper) increasing in the outer galaxy, where the brighter HII regions are more numerous. The galactocentric variation in Hα equivalent widths appears more closely related to the galaxy's radial profile of differential rotation than to its monotonic gradient in O/H abundances. The ionizing stellar populations in early-type, late-type, and starburst galaxies are discussed in terms of these results.

TABLE OF CONTENTS

LIST OF TABLES

LIST OF FIGURES

CHAPTER 1

INTRODUCTION

In the following chapters, I examine and compare various luminous tracers of recent star forming activity, as observed in 3 nearby galaxies. The primary tracers include the optical Hα emission from the galaxian HII regions (gas clouds ionized by underlying populations of hot OB-type stars), the red continuum emission from the young ionizing stellar populations, and the radio CO and HI emission from the star forming molecular and atomic gas clouds.

The observed galaxies, in order of decreasing mass, include a grand-design Sc spiral (M101), a "starburst" Irr II/Amorphous galaxy (M82), and a "posteruptive" Irr I galaxy (NGC 1569). These galaxies were chosen with an aim to better quantify the differences between the starbirth activity that characterizes most late-type galaxies and the more intense "starburst" behavior which is relatively rare today but may have been commonplace during earlier epochs of galaxian history. Key questions to be addressed are...

1. What is the typical relationship between the star formation rate and the available H_2 and HI gas content,

2. Does the "starburst" phenomenon represent an actual enhancement in the efficiency or "yield" of star formation per unit mass of available gas? and

3. Do massive stars form preferentially in certain environments (*i.e.* Which environmental factors, if any, affect the high-mass end of the initial mass function [IMF]?).

Scientific motivation for these questions is presented in a brief overview of galaxy birth and evolution (Chapter 2). Here, I emphasize the concept that galaxy evolution is driven by the transformation of gas into and out of stars. Therefore, the types of stars that are created (the IMF) and the vigor of the process (the starbirth efficiency) are crucial influences on the evolutionary histories of galaxies.

The starbirth *vs.* gas dependence is investigated in the chapter on M101 (Chapter 3) and pursued further in the Summation chapter (Chapter 6). Comparisons between the annular-averaged Hα, HI, and CO surface brightnesses in the disk of M101 indicate that the high-mass star formation intensity correlates with the 0.6 power of the H_2 surface density and with the 0.9 power of the total gas surface density. Combining the annular-averaged surface brightness data from M101, M83, M51, and the Milky Way again produces strong correlations between the starbirth intensity and the H_2 and total gas surface densities. Here, both relations are best fit by near-linear power laws. The supergiant HII region complex, NGC 5461, is shown to be truly exceptional, rivaling the "starburst" nucleus of M83 in both starbirth intensity and efficiency.

The question of the IMF is addressed the most in the chapter on M101 (Chapter 3), where the Hα luminosities and equivalent widths of 385 HII regions are used to trace changes in the high-mass IMF. An increase in the mean equivalent width is noted between the inner and outer galaxy. This galactocentric variation is attributed to the presence of higher-mass stars in the clusters that are located beyond 5 kpc of the nucleus. The form of the galactocentric variation resembles that of the differential rotation more than that of the O/H abundance gradient.

A correlation between the Hα equivalent widths and Hα luminosities is also evident, suggesting that the brighter HII regions contain the hotter, more massive stars. Such behavior bears upon the question of starbirth efficiencies as well as that of the IMF, because all computations of starbirth rates and efficiencies depend critically upon the IMF that is adopted. If intense "starburst" regions are, in fact, biased towards making the most massive stars, one may be significantly overestimating the starbirth efficiencies and underestimating the gas depletion times by adopting a "normal" IMF appropriate to the solar neighborhood.

Chapter 4 presents the classic starburst M82 as imaged in the light of Hα, near-infrared [SIII], red continuum, and near-infrared continuum emission. From these images, I have constructed a map of the [SIII]/Hα flux ratio which, in turn, has been interpreted in terms of the visual extinction. The resulting images and maps indicate pronounced obscuration along the major axis on opposite sides of the starburst nucleus. The circumnuclear obscuration is demonstrated to be coincident with sites of enhanced molecular hydrogen and CO emission. I attribute such a configuration of dust and gas to M82's "dusty chimney" that was caused by and is now collimating the central eruption. The resulting dereddened image of Hα emission indicates a more extended bar-like morphology of ionized gas — similar to the morphologies seen at 10 micron and radio continuum wavelengths. The surface density and efficiency of star formation in M82's nucleus, as derived from my extinction-corrected Hα fluxes and existing CO and HI data, are the highest seen in this study. Alterations of the IMF or the starbirth history would have to be especially severe in order to maintain gas depletion times longer than a Gyr.

Chapter 5 deals with the smallest and most metal-poor galaxy in the sample — NGC 1569. As in M82, the observed starburst activity in NGC 1569 is of global proportions, affecting the galaxy at-large. The strongest recent activity is concentrated at one end of the galaxy's "bar". The HII region complex there is equivalent in Hα luminosity to NGC 5461 — the supergiant HII region that dominates M101's much larger population of star forming regions. New-found evidence for Hα emitting "arcs" of ionized gas — well beyond the galaxy's main body — suggests that previous episodes of starburst activity have wracked NGC 1569. Such inconstant behavior could prolong the star-forming lifetime of NGC 1569 and of other starburst systems.

A comparison of the three galaxies is presented in Chapter 6. Galactocentric profiles of the surface densities and efficiencies of star formation are superposed with those of M51, M83, and the Milky Way and discussed. In this context, M82 appears as an intense but small "nuclear starburst," whose mean starbirth efficiency is 12 times higher than the mean efficiencies in M101 and the Milky Way. NGC 1569 appears as a "post-eruptive" dwarf irregular, whose nucleus is no longer bursting, but whose nuclear bar is still active with enough giant HII regions to produce an elevated starbirth efficiency. M101 most closely resembles the sprawling low-level activity evident in the Milky Way, that is, if the supergiant HII region complexes in the outer disk are ignored. Annular-averaged photometry on all 6 galaxies reveals strong starbirth correlations involving the H_2 surface density (where $\sigma(SFR) \propto \sigma(H_2)^{1.0\pm0.2}$) and the total gas surface density (where $\sigma(SFR) \propto \sigma(gas)^{1.1\pm0.2}$). By contrast, little correlation is evident between $\sigma(SFR)$ and $\sigma(HI)$.

The evidence for IMF variations in M101's ionizing clusters is briefly reviewed, and the case for possible dynamical effects on the IMF is re-iterated. The ionizing stellar populations in early-type, late-type, and starburst galaxies are discussed in terms of these results. Finally, global indices of the current-epoch *vs.* past-averaged starbirth activity in the 6 galaxies are compared. Bursting behavior is clearly evident in M82 and NGC 1569, while M101 and the Milky Way seem to be slowly declining in their stellar productivity. Inconsistencies among the various evolutionary indices are discussed in terms of possible anomolies in the birthrate histories and/or IMFs.

Appendix A is a tutorial on how one goes about computing star formation rates from indices of ionizing luminosity (such as the Hα luminosity). The sensitivity of this computation to the particular IMF that is adopted is demonstrated.

Appendix B is a tutorial on deriving emission-line fluxes and equivalent widths from narrow and broad-band images. A technique for separating the continuum emission from a broad-band image contaminated with spectral-line emission is introduced and demonstrated using the Orion nebula as an example.

Each chapter is formatted like a semi-autonomous paper. References, tables, and figures specific to each chapter appear at the end of that chapter. A comprehensive bibliography appears at the end of the dissertation.

CHAPTER 2

OVERVIEW

2.1 *Abstract*

In this chapter, I review galaxy evolution in terms of the star forming activity that drives the evolutionary process. I begin with galaxy birth by summarizing the case for a preferred epoch ~10 Gyr ago. The subsequent evolution of elliptical and spiral galaxies is then related to their respective star forming histories which are briefly described. The evidence for current-epoch star formation in spiral and irregular galaxies is presented, and questions regarding the stellar mass spectra (*i.e.* the initial mass functions (IMFs)) of the newborn populations are posed. Possible variations in the IMF, the astrophysical processes that could cause such modifications, and the evolutionary consequences of the "standard" and modified IMFs are discussed at length. To illustrate the possible antecedents and outcomes of the starbirth activity that is observed today in late-type galaxies, two simple evolutionary scenarios are considered — constant starbirth rate and constant starbirth efficiency. A rundown of other possibly relevant starbirth "laws" is also given. Finally, the starburst phenomenon is introduced and described in terms of observed tracers, possible causes, and probable consequences. Uncertainties and evolutionary implications regarding the IMFs in these intense regions are discussed.

2.2 *Galaxy Birth*

The present overview and all subsequent discussions assume that galaxy birth was a relatively coeval process occuring some 10 – 15 billion years ago. Although this assumption is far from iron-clad, it enjoys strong theoretical and observational support.

Theoretical support is provided by the physics of the standard Big Bang cosmology (*cf.* Narlikar 1983). Within the first billion years after the Big Bang — shortly after the decoupling of matter and radiation — the mean temperature and density of the decompressing universe would have been suitable for galaxy-size gravitational instabilities to grow. According to the classic Jeans criterion (Jeans

1928), gravitational instabilities grow, when the gravitational forces begin to exceed the opposing thermal pressures. This is satisfied for masses above the Jeans mass M_J, such that

$$M_{gal} > M_J \sim 10^{-11} \frac{T^{3/2}}{\rho^{1/2}} M_{\odot}. \qquad (2-1)$$

At the epoch of decoupling, $T \approx 4000K$ and $\rho \approx 10^{-21}$ $gm\ cm^{-3}$, which leads to $M_{gal} > 10^5 M_{\odot}$, thus placing a lower limit on the galaxy mass spectrum. Thereafter, the cooling temperature and decreasing density would have favored the formation of much smaller objects. Because the Local Group and, presumably, other groups of galaxies seem to be dominated by the larger objects (selection effects notwithstanding), the Jeans criterion implies an early epoch for their formation.

The actual moment of "turnaround" against universal expansion would have depended on the mass and size of the particular instability that was growing. Therefore, the actual epoch of galaxy "birth" could have been smeared out over a billion or so years following the era of decoupling (see Narlikar (1983) and Bowers and Deeming (1984) for further discussion). Subsequent evolution — including the accretion of neighboring protogalaxies, the general initiation of star formation, and the creation of bulge and disk components — would have depended on the mass, size, angular momentum, and environment of the accreting/collapsing protogalaxy. In some instances, it could have taken as long as 10^{10} years (Baron and White 1987), thus accounting for quiescent gas-rich laggards such as the recently discovered "protogalaxy" Malin-1 (Bothun *et al.* 1987).

Observational support for coeval galaxy birth is based primarily on the ages of stars. Extremely ancient stars are observed in both the Milky Way and the Magellanic Clouds. For example, the main-sequence turnoff ages of the oldest globular clusters in these galaxies are estimated to be at least 10 billion years old (*cf.* Mihalas and Binney 1981 and references therein; Hodge 1983; Hodge 1987a), thus indicating even greater ages for the host galaxies. The fact that three galaxies of such widely disparate masses could have such similar ages suggests that the emergence of galaxies *of all types* was a relatively simultaneous phenomenon. The composite spectra of elliptical galaxies and spiral bulges also show absorption lines characteristic of old red stars (Gunn *et al.* 1981; O'Connell 1986), again suggesting ancient birthdates for the host galaxies. *Direct* observational evidence for or against coeval galaxy birth at redshifts of $z = 3 - 5$ remains elusive and will probably require the advent of telescopes and instrumentation capable of detecting the actual birth pangs.[1] The recent discoveries of Lyman-alpha emitting "protogalaxies" at $z = 1 - 3$ (Djorgovski *et al.* 1987; McCarthy *et al.* 1987), rich fields of extremely faint blue galaxies at estimated redshifts of $z = 2 - 3$ (Tyson 1987), and the galaxian counterparts to quasar absorption-line systems at $z = 1 - 3$ (Schwarzschild 1987) suggest that such a capability may not be long in coming.

2.3 *Galaxy Evolution*

Galaxies evolve by cycling their primordial stores of gas into and out of stars. The vigor of this cycling process (the starbirth efficiency) and the variety of stars that are created (the initial mass function (IMF)) are the two critical parameters that set the pace of galaxy evolution. They do this by fixing the rate of chemical enrichment from exploding high-mass stars and by determining the mass lock-up rate in the form of low-mass stars and stellar remnants. The time-integrated efficacy of the transformation process can be crudely gauged in terms of the stellar mass fractions $M_*/(M_* + M_g)$ that are observed in galaxies at the current epoch. This fraction has been found to vary from galaxy to galaxy in a manner that approximately follows the Hubble sequence of morphological types. For example, the ellipticals are overwhelmingly stellar ($M_*/(M_* + M_g) > 0.99$), the spirals are about 80 – 90 percent stellar, and irregular galaxies are about 50 – 80 percent stellar.

Because ellipticals are dominated by stars whose colors indicate ~10 Gyr ages (Gunn *et al.* 1981; O'Connell 1986), these gas-poor systems can be regarded as having efficiently formed the bulk of their stars shortly after having coelesced as self-gravitating systems (see Figure 2–1). The higher central concentrations of mass and lower rotation rates of these galaxies would be consistent with rapid

[1] In a cosmology with $H_o = 50\ km\ s^{-1}\ Mpc^{-1}$ and $q_o = 0.5$, *i.e.* a flat universe, a redshift range of $z = 1 - 3 - 5$ corresponds to lookback times of $\tau = 8.4 - 11.4 - 12.2\ Gyr$ respectively.

evolution, especially if the stellar birthrate depends on some positive power of the gas density (Schmidt 1959; Larson 1987a). Additional considerations of the eccentric stellar orbits and remnant dust lanes found in ellipticals suggest to others that ellipticals resulted from mergers of spiral galaxies ~10 billion years ago, when the universe was more densely populated (Toomre 1977; Baron and White and references therein 1987). The enhanced gas cloud collision rates resulting from such mergers could have precipitated the higher star formation rates needed to consume the remaining gas in short order.

The spiral and irregular galaxies, having conserved 10 to 50 percent of their primordial gas, continue to be active sites of star formation. They therefore provide precious opportunities to observe star formation — and hence galaxy evolution — in progress (see Figure 2-1).

2.4 *Current Epoch Starbirth*

Irrefutable evidence for ongoing star formation has been found in a large number of spirals and irregulars. First, from mm-wave observations of the CO trace molecule, we now know that many late-type galaxies harbor large quantities of molecular gas (Young and Scoville 1982; Young *et al.* 1985). In our Galaxy, this gas is in the form of cold ($T \approx 10K$) dense ($n_{H_2} > 10^2\ cm^{-3}$) clouds (Scoville *et al.* 1987) which are supported against immediate collapse by dispersive velocity fields ($\Delta v \approx 3 - 10\ km\ s^{-1}$) and, perhaps, by magnetic pressure (Heyer *et al.* 1987). Nevertheless, collapse does occur, as evidenced in the Milky Way by the embedded, dust-enshrouded protostars that have been detected in great abundance at infrared wavelengths (Beichman 1987 and references therein). In HII regions, where the molecular material has been ionized by newborn OB-type stars, optical hydrogen-line and radio Brehmsstrahlung emission are readily observed. And, if the molecular material becomes sufficiently disrupted by the UV radiation and strong winds from the newborn hot stars, the stars become exposed and hence optically identifiable. In summary, the birth of stars leaves many traces, the most readily detected being the molecular gas clouds, the warmed dust, the ionized gas, and the naked newborn stars themselves.

2.5 *Newborn Stellar Populations and the Initial Mass Function*

Although we are confident that ongoing starbirth characterizes many late-type galaxies, our knowledge of the stellar birth processes in external galaxies is strongly limited by our ability to observe only the high-mass stars and their luminous consequences. Whether low-mass stars are forming along with the high-mass stars in proportions remotely resembling those seen in the solar neighborhood remains a nagging question of crucial importance. Unfortunately, the low-mass end of the IMF is virtually untraceable save for its bulk gravitational effects. The intermediate and high-mass portions, however, have observeable effects on the continua of the newborn clusters and — if the continua are sufficiently hot — on the emission-line spectra of the surrounding HII regions.

Variations in the high-mass IMF have been inferred from collective spectroscopic studies of giant HII regions in spiral, irregular, and HII galaxies (Viallefond 1985; Terlevich and Melnick 1985; Campbell *et al.* 1987; Campbell 1988). In these regions, the variation is observed to correlate with the metal abundance, in the sense that the highest mass stars tend to form in the most metal-poor systems. Such behavior has been attributed to several physical mechanisms, the most often cited being

- The accretion of gas onto a growing protostar and the dependence of the accretion process on the dust content (and by inference, the dust-to-gas ratio and thus the metallicity) of the infalling material: In dust-poor clouds, the opacity of the infalling material is greatly reduced, so that the radiation pressure exerted by the luminous protostar is also diminished. This leads to unimpeded accretion and thus a higher protostellar mass limit (Kahn 1974; Shields and Tinsley 1976); and
- The fragmentation of clouds into protostars and the dependence of the fragmenting masses on the cloud temperature (Jeans 1928; Spitzer 1978; Larson 1985; Silk 1986): In metal-poor clouds, radiative coolants such as CO and dust grains are relatively absent thus leading to higher cloud temperatures and higher values of the minimum fragmenting mass.

The observed correlation between IMF and metal abundance, however, can be re-interpreted in terms of an IMF-dynamics connection. For example, the most metal-poor galaxies tend to be the least massive (Pagel 1986; A. Campbell, private communication) and therefore characterized by the weakest tidal forcing and the lowest amounts of velocity dispersion and differential shear. The relative absence of dynamical disruption in these systems could therefore encourage the quiescent growth of large clouds (Larson 1987a; Larson 1988) and the preferential creation of massive stars inside the giant clouds — as is observed in the large clouds of the Milky Way (Larson 1982; Waller *et al.* 1987; Scoville *et al.* 1987). Similarly, the regions of low metal abundance and exceptionally high-mass star formation in large spiral galaxies tend to be well outside the tidally and kinematically stressed inner regions. These regions are associated with large gas complexes which are often part of spiral arms.

In M101, for example, the Hα equivalent widths (*i.e.* the line-to-continuum flux ratios) of individual HII regions are seen to vary with galactocentric radius (see Chapter 3). This finding can be interpreted as a radial variation in the upper stellar mass limit of the clusters underlying the HII regions. Therefore, the high-mass end of the IMF does seem to vary with position in the galaxy — an effect which seems more closely related to the galaxy's radial profile of differential rotation than to its O/H abundance gradient, contrary to previous suggestions (Shields and Tinsley 1976; Viallefond *et al.* 1982). A similar investigation of the HII regions in NGC 2403 has revealed steep O/H and N/H radial abundance gradients but no corresponding variations in the Hα or Hβ equivalent widths (Fierro *et al.* 1986). The observed invariance in these tracers of the high-mass IMF is again more consistent with the galaxy's radial profile of differential rotation than with its metallicity gradient.

Therefore, the observed variations in the high-mass IMF could be simply reflecting variations in the ability to assemble large clouds and cloud complexes. According to this picture, the giant spirals are able to make big stars by assembling giant clouds within the potential wells associated with their spiral density-wave crests. The largest clouds and most massive stellar offspring arise, where the tidal and kinematic stresses are lowest (preferentially in the slower-rotating later-type galaxies and away from their central bulges [Hodge 1987b]). The irregulars and HII galaxies achieve the same results by simply waiting for large instabilities to inexorably grow. The largest instabilities and highest-mass stars develop inside those gas-rich galaxies having the lowest velocity dispersions (and hence the lowest masses).

The observed variations in the high-mass end of the IMF, as discussed above, might also indicate that certain environments are conducive to forming high mass stars *at the expense* of low mass stars, as advocated by Larson (1987c) and others. If, in fact, the low-mass star formation is suppressed in some regions of high-mass star formation, then the usual extrapolations from high-mass observables to total star formation rates may be in serious error (see Appendix A). Furthermore, if the low mass end of the IMF is poorly represented, then most of the gas consumed by the star forming process will eventually be returned to the interstellar medium. Such enhanced cycling of the gas into and out of stars means that the gas depletion times are prolonged. Several studies of star formation rates in normal spirals have concluded that the IMF must be biased as outlined above. Otherwise, the predicted gas depletion timescales become disconcertingly short ($\tau_g \approx 10^9$ years) compared to the cosmological lifetimes of the galaxies (Jensen *et al.* 1981; Gusten and Mezger 1982; Larson 1986; Sandage 1986).

2.6 *Evolutionary Scenarios*

Still, the evidence for "biased" or "bimodal" IMFs is relatively weak (see Scalo 1986) and so it is worth considering the implications of stellar birth via a solar-neighborhood "Salpeter-type" IMF (see Appendix A). Two evolutionary scenarios can be most readily envisioned: Either a galaxy's starbirth activity proceeds at a *constant rate* equal to that extrapolated from the observed rate of massive starbirth, or starbirth proceeds at a *constant efficiency* equal to the extrapolated birthrate divided by the mass of available gas. In the first scenario, one obtains a straightforward gas depletion timescale by dividing the available gas mass M_g by the mass lockup rate MLR [For a Salpeter IMF, the MLR is 2/3 the total birthrate]. This leads to typical gas depletion times of a few 10^9 years (Kennicutt 1983; Thronson *et al.* 1987) or to appeals for abberant IMFs in order to extend the gas depletion times and so explain the relative rarity of gas-poor ("anemic") spirals that is evident outside of crowded galaxy clusters (van den Bergh 1976).

In the second scenario, the constant efficiency insures that the gas supply never runs out — it just decays exponentially with an e-folding time equal to the gas depletion time of the constant SFR scenario. In similar fashion, the star formation rate declines at an exponential rate set by the efficiency. This simple scenario enables one to extrapolate backwards in time from current values of a galaxy's starbirth rate and efficiency and so determine the stellar birthrate shortly after the galaxy's formation (*cf.* Talbot 1980). For the Milky Way, the current birthrate of 3 $M_\odot/yr$ (Gusten and Mezger 1982) would imply a primeval starbirth rate of ~100 $M_\odot$/yr. Evidence for such intense activity has been found in several high-redshift galaxies, whose Lyα and OII luminosities are consistent with birthrates exceeding 100 $M_\odot/yr$ (McCarthy *et al.* 1987). Comparisons of current-epoch starbirth rates (calculated from Hα luminosities) with past-averaged rates (calculated from blue luminosities and from the ratio of dynamical mass to cosmological age: $\langle SFR \rangle = M_{dyn}/\tau_{gal}$) also lead to the conclusion that "normal" spiral galaxies began their lives vigorously forming stars and have since become less productive (Gallagher *et al.* 1984; see also Figure 2–1). Some irregular galaxies, however, appear to be *increasing* in stellar productivity as time goes on. Such behavior is clearly inconsistent with the constant-efficiency scenario, unless some sort of gas infall process is also invoked.

2.7 "*Laws*" *of Star Formation*

Whether constant rates or efficiencies best describe the current-epoch star formation evident in late-type galaxies has yet to be worked out. Indeed, a multitude of "essential laws" governing star formation have been proposed to explain the data at hand. This may not represent a failure on our part, however. The star formation rates within individual molecular clouds, molecular cloud complexes, spiral arm fragments, galaxian nuclei, and interacting galaxies may depend on complex blends of many different influences. Because the dominant factors have yet to be isolated with much satisfaction, it is important to consider all the possibilities. The following dependencies, being the most simplistic, are the most often invoked.

• The starbirth rate is *constant* with respect to available gas content and evolutionary time. This implies an *increasing efficiency* (defined as SFR/M_g) with time and a gas depletion time proportional to the reciprocal of the efficiency. Kennicutt (1983) found that nearly constant starbirth rates plus a Salpeter-type IMF could best reproduce the global UBV colors and Hα equivalent widths obtained from a sample of 170 nearby late-type galaxies. The resulting gas depletion times ranged between 10^9 and 10^{10} years with a median timescale of 4 Gyr — significantly lower than the galaxies' cosmological lifetimes.

• The starbirth rate depends *linearly* on the available gas mass, surface density, or volume density. For example,

$$\sigma(SFR) = K\ \sigma(gas), \qquad (2-2)$$

where $\sigma(gas)$ is the surface density of gas, $\sigma(SFR)$ is the surface density of star formation, and K is the starbirth efficiency. This implies a *constant efficiency* of star formation, an exponentially depleting gas content, and an exponentially declining starbirth rate with respect to time. Such behavior has been inferred from FIR and CO measurements of giant molecular clouds in the Milky Way (Rengarajan 1984); radial profiles of blue starlight and CO luminosity in spiral galaxies (Young and Scoville 1982 and references therein); radial profiles of Hα, CO, and HI fluxes in Sc spirals (DeGoia-Eastwood *et al.* 1984; Lord 1987; Waller *et al.* 1988); and global measurements of FIR and CO fluxes in late-type galaxies (Young *et al.* 1985; Rengarajan and Verma 1986).

• The starbirth rate depends *quadratically* on the available gas content, *e.g.*

$$\sigma(SFR) \propto \sigma(gas)^2. \qquad (2-3)$$

This implies an efficiency that decreases as $1/\tau$ and a starbirth rate that decreases as $1/\tau^2$. Such non-linear behavior can result, for instance, if cloud-cloud collisions lead to cloud growth and enhanced birthrates. The cloud-cloud collisions, in turn, can arise from the orbit crowding in spiral density waves or from the tidal mixing induced by galaxy-galaxy interactions. First proposed by Schmidt (1959), the quadratic dependence continues to be championed as the exclusive outcome of a variety of cloud-growth scenarios (Larson 1988). Evidence for quadratic or higher-exponent dependencies has been inferred from comparisons of the ionized and molecular components in the Milky Way (Waller 1984; Scoville, Sanders, and Clemens 1986), in the spiral arms of M51 (Lord 1987; Vogel *et al.* 1988), in the supergiant star forming regions of M101 (see Chapter 3), and in samples of interacting galaxies (Young *et al.* 1986a; Sanders *et al.* 1987).

• The starbirth rate depends both on the available gas content and on its "pressurization" by the underlying stellar gravitational potential. *e.g.*

$$\sigma(SFR) \propto \sigma(gas)\,\sigma(*). \qquad (2-4)$$

[If a galaxy's surface density of gas follows that of its stars, the dependence reduces to the quadratic "Schmidt" law.] According to such behavior, large star forming regions could create especially high pressurizations thereby amplifying the original birth activity in a feedback-type fashion. Using this "auto-catalytic" law, Dopita (1985) successfully modeled the HI and UV fluxes of late-type galaxies measured by Donas and Deharveng (1984). In a CO, HI, and Hα study of M51 and M83, however, Lord (1987) was unable to match the radial profiles of starbirth rate with Dopita's model. A similar mismatch is also seen in M101, where $\sigma(SFR)$ depends more closely upon $\sigma(gas)$ than upon the product $\sigma(gas)\,\sigma(*)$ — the exception being near the supergiant HII regions (see Chapter 3).

• The starbirth rate depends on the degree of compression in encounters of disk gas with spiral density waves, *e.g.*

$$\sigma(SFR) \propto \sigma(gas)[(\Omega(gas) - \Omega_p)R], \qquad (2-5)$$

or with other non-axisymmetric gravitational potentials. This scenario may again relate to the quadratic law, in that the dynamical effects may lead to enhanced cloud growth and thus star formation rates that vary as some non-linear power of the local gas surface density.

Again, the evidence for all these dependencies concerns only the high-mass star forming component. Therefore, the nonlinear effects that have been claimed may actually reflect variations in the IMF rather than true enhancements in the overall star forming efficiency.

2.8 *Starburst Behavior*

As outlined in Section 2.6, the early evolution of many large galaxies may have been characterized by intense "starburst" activity. Fortunately, galaxies on the fringes of the observable universe are not the only arenas where starburst activity can be found and studied.

The starburst phenomenon — where the conversion of gas into stars proceeds at unusually prodigious rates — has been observed on scales ranging from a few parsecs (*e.g.* the Orion nebula) to several kpc (*e.g.* M82, NGC 253, NGC 3690).[2] Hallmarks of such activity include high infrared luminosities, strong radio continuum emission, dazzling hydrogen recombination-line intensities, and warm CO antenna temperatures (see the excellent discussion by Soifer *et al.* (1987)). These various tracers of massive star formation have been used to infer unusually high starbirth efficiencies (Rieke *et al.* 1980; Young *et al.* 1986b; Lo *et al.* 1986; Waller *et al.* 1988; and the present thesis) which would imply gas depletion times of only $10^7 - 10^8$ years (if an IMF appropriate to the solar neighborhood is adopted). For those galaxies that are completely involved with such starburst activity, the pace of evolution is hastened drastically, challenging one to explain the historic origins of their present tumult and to predict the imminent futures of their gaseous reserves.

In Figure 2–2, starburst activity appears in the form of high infrared luminosities and high L_{IR}/L_{CO} luminosity ratios. The luminosity ratios (and by inference, the starbirth efficiencies) of the well-known starburst systems M82 and NGC 253 are elevated above those of "normal" spirals by a factor of $\sim$5. Even higher luminosity ratios are evident in the "ultraluminous infrared galaxies" exemplified by Arp 220 and Mrk 231. However, physical processes other than efficient starbirth may be contributing to the high L_{IR}/L_{CO} ratios seen in these disturbed systems. Sanders *et al.* (1988) suggest that active galactic nuclei (AGNs) are contributing to the ultraluminous FIR emission, and that such

---

[2] Such regions include the giant extragalactic HII regions (GEHRs) and the "Violent Star-Forming Regions" (VSFRs) coined by Terlevich and Melnick (1981).

exotic activity — and perhaps the Seyfert and quasar phenomena as well — are the evolutionary byproducts of previous nuclear starbursts (see also Norman 1987).

Evidence for galaxy-galaxy interactions triggering starburst activity continues to accrue (Condon 1982; Keel *et al.* 1985; Bushouse 1986; Young *et al.* 1986a; Kennicutt *et al.* 1987). Correlations between starburst activity and the presence of a central bar are also being found (Hawarden *et al.* 1986; Devereux 1987). These connections give strong credence to the concept of tidal influences driving the aggregation of massive and dense clouds, in which starbursts can occur (Larson 1987a).

Intense episodes of star formation may entail more than just large accumulations of gas, however. Timing may also play a crucial role. Theoretical considerations of the relative timescales for cloud growth, starbirth ignition, and resulting cloud destruction have shown that an intriguing variety of starbirth behavior can ensue (Scalo and Struck-Marcell 1986). When the cloud destruction time is much shorter than the cloud formation time, the system is rapidly damped, "self-regulated," and hence extremely stable. However, as the cloud destruction time begins to exceed the formation time, the system exhibits limit cycles and eventually a transition to chaotic behavior — in both cases accompanied by bursts of star formation. If, for example, the cloud destruction time is set equal to the typical lifetime of ionizing stars ($\tau \approx 3\ Myr$), then bursting conditions would require cloud growth times of only $\sim 10^6$ yrs. To assemble a bursting system such as M82 in such a short time would require high gas inflow rates at radial velocities exceeding 50 km/s (Larson 1987a). Numerical N-body simulations of galaxies have demonstrated that central bars and tidal interactions between galaxies can induce sufficient redistributions of angular momentum for such radial inflows to occur (Larson 1987a and references therein).

Once initiated, the starburst exerts tremendous changes upon its environment. The high radiative and mechanical luminosities of the massive stars and — later — of the resulting supernovae can produce large-scale outflows of ionized gas (see Chapters 4 and 5) and wholesale reorganization of whatever gas that isn't blown away. A possible scenario for the evolution of a starburst and its host galaxy has been outlined by Rieke *et al.* (1988). By comparing near-infrared tracers of the photo-ionized H^+ gas, the shocked H_2 gas, and the recently evolved stars in a selection of 5 galaxies, they were able to sequence the galaxies in terms of time following the initial burst. The sequence is characterized by a rapid emergence of high-mass stars in the galaxy's nucleus (NGC 5253 and NGC 253), followed by shocking of the circumnuclear gas and windy outflows (M82), and ending with an evolved stellar population in the nucleus and ongoing "repercussions" in the disk (NGC 4736 and M31).

If not expelling or disrupting the host galaxy's gas (Larson 1987a; see also Chapter 5), starburst eruptions might autocatalyse further starburst activity. This can be modeled in terms of the excess pressurization (Dopita 1985) and compression (Rieke *et al.* 1988; Sofue *et al.* 1986; see also Chapter 4) that starbursts create. Another possible "secondary" effect of starburst energetics is a modification of the IMF governing all subsequent star formation. If, for example, fragmentation and gravitational instability play dominant roles in determining the ultimate masses of stars, then the higher temperatures in starburst regions may prevent fragmentation below a few solar masses (Larson 1987c) thereby skewing the starbirth process toward higher masses.

Rieke *et al.* (1980) came to such a conclusion for NGC 253 and M82, based on infrared spectroscopy and photometry of the ionized and stellar components along with dynamical constraints on the total mass. Comparison of these observations with models of evolving stellar populations led to an IMF lacking in stars below 3 $M_{\odot}$ and above 30 $M_{\odot}$. However, their analysis suffered from significant ambiguities in correcting the 2 micron continuum for extinction by dust and in interpreting the resulting fluxes in terms of main-sequence, giant, and supergiant populations. Different corrections of the 2-micron fluxes and/or different mixes of dwarfs, giants, and supergiants could have yielded a much wider range of masses.

Similar modeling of the optical, infrared and radio emission from NGC 3690 (Gehrz, Sramek, and Weedman 1983) also yielded an IMF that was confined to a mass range of $6 - 25\ M_{\odot}$. Here, the interpretations of the non-thermal radio emission in terms of a supernova rate and, by inference, a massive star formation rate are highly ambiguous. Unfortunately, there are too many free parameters and too few unambiguous spectral discriminators of the highest and lowest-mass regimes to do much better with spatially integrated data (see, for example, the modeling of UV spectra by Sekiguchi and Anderson (1987)).

In the one major starburst system whose stars can be resolved (30 Doradus in the LMC), stellar masses ranging from the detection limit of $\sim$4 $M_\odot$ up to $\sim$150 $M_\odot$ have been identified (Melnick 1985). Moreover, the distribution of masses appears to follow a Salpeter-type power law, thus suggesting a "normal" IMF except for the extended upper mass limit. Indirect evidence for "top-heavy" IMFs correlating with starbirth intensity has been found in the giant HII regions of M101 (see Chapter 3). If this behavior can be applied to the nuclear starbursts (Kennicutt 1984; see also Chapter 6), then extremely massive stars may, in fact, be driving much of the violent activity seen in starburst nuclei.

The evolutionary aftermath of such "top-heavy" starbursts would be a plethora of dark solar-mass remnants. Larson (1987c) has suggested that these starburst "ashes" could account for the "missing mass" that is evident today in spiral galaxies. Indeed, rampant starburst activity during the early universe could have manufactured much of the dark matter that dominates the dynamics of the present epoch! To test this provocative scenario, much better spectra of extremely faint high-redshift galaxies will need to be obtained and analysed in terms of starburst *vs.* other activity. The 8-meter and larger-class telescopes that are currently under development will play important roles in this regard.

In the following chapters, three nearby galaxies are studied in terms of their relative starbirth activity. Because the observed tracers of star formation are mostly sensitive to the high-mass activity, they can only address the relative degrees of *starburst* activity in the host galaxies, *i.e.* the relative rates and efficiencies of *massive* star formation. Nevertheless, overall rates and efficiencies have been extrapolated from tracers of the high-mass activity according to a Salpeter-type IMF. This was done more to facilitate comparisons with similar studies (especially that of Kennicutt [1983]), then to claim a common brand of starbirth for the entire sample. All starbirth efficiencies and gas depletion times that have been computed from the observations are presented with this caveat in mind.

References

Baron, E. and White, S. D. M. 1987, *Ap. J.*, **322**, 585.

Beichman, C. A. 1987, *Ann. Rev. Astr. Ap.*, **25**, 521.

Bothun, G. D., Impey, C. D., Malin, D. F., and Mould, J. R. 1987, *A. J.*, **94**, 23.

Bowers, R. L. and Deeming, T. 1984, in *Astrophysics II [Interstellar Matter and Galaxies]* (Boston: Jones and Bartlett) p. 576.

Bushouse, H. A. 1986, *A. J.*, **91**, 255.

Campbell, A., Terlevich, R., and Melnick, J. 1987, *M. N. R. A. S.*, **223**, 811.

Campbell, A. 1988, *Ap. J.*, Dec. 15, in press.

Condon, J. J., Condon, M. A., Gisler, G., Puschell, J. J. 1982, *Ap. J.*, **252**, 102.

DeGioia-Eastwood, K., Grasdalen, G. L., Strom, S. E., and Strom, K. M. 1984, *Ap. J.*, **278**, 564.

Devereux, N. 1987, *Ap. J.*, **323**, 91.

Djorgovski, S., Strauss, M. A., Perley, R. A., Spinrad, H., and McCarthy, P. 1987, *A. J.*, **93**, 1318.

Donas, J. and Deharveng, J. M. 1984, *Astr. Ap.*, **140**, 325.

Dopita, M. A. 1985, *Ap. J. (Letters)*, **295**, L5.

Fierro, J., Torres-Peimbert, S., and Peimbert, M. 1986, *Pub. A. S. P.*, **98**, 1032.

Gallagher, J. S., Hunter, D. A., and Tutukov, A. V. 1984, *Ap. J.*, **284**, 544.

Gehrz, R. D., Sramek, R. A., and Weedman, D. W. 1983, *Ap. J.*, **267**, 551.

Gunn, E., Struper, L. L., and Tinsley, B. M. 1981, *Ap. J.*, **249**, 48.

Gusten, R. and Mezger, P. G. 1982, in *Vistas in Astronomy*, **26**, 159.

Hawarden, T. G., Mountain, C. M., Lessett, S. K., and Poxley, P. J. 1986, *M. N. R. A. S.*, **221**, 41P.

Heyer, M. H., Vrba, F. J., Snell, R. L., Schloerb, F. P., Strom, S. E., Goldsmith, P. F., and Strom, K. M. 1987, *Ap. J.*, **321**, 855.

Hodge, P. W. 1983, *Ap. J.*, **264**, 470.

Hodge, P. W. 1987a, *Pub. A. S. P.*, **99**, 724.

Hodge, P. W. 1987b, *Pub. A. S. P.*, **99**, 915.

Jeans, Sir J. H. 1928, *Astronomy and Cosmogony* (Cambridge: Cambridge University Press).

Jensen, E. B., Talbot, R. J., and Dufour, R. J. 1981, *Ap. J.*, **243**, 716.

Kahn, F. D. 1974, *Astr. Ap.*, **37**, 149.

Keel, W. C., Kennicutt, R. C., Hummel, E., and van der Hulst, J. M. 1985, *A. J.*, **90**, 708.

Kennicutt, R. C. 1983, *Ap. J.*, **272**, 54.

Kennicutt, R. C. 1984, *Ap. J.*, **287**, 116.

Kennicutt, R. C., Keel, W. C., van der Hulst, J. M., Hummel, E., and Roettiger, K. A. 1987, *A. J.*, **93**, 1011.

Larson, R. B. 1982, *M. N. R. A. S.*, **200**, 159.

——. 1985, *M. N. R. A. S.*, **214**, 379.

——. 1986, *M. N. R. A. S.*, **218**, 409.

——. 1987a, in *Starbursts and Galaxy Evolution*, ed. J. Montmerle and J. T. T. Van (Yvette, France: Editions Frontieres).

——. 1987b, in *Globular Cluster Systems in Galaxies*, IAU Symp. No. 126, ed. A. G. D. Philip and J. E. Grindlay (Dordrecht: D. Reidel), p. 311.

——. 1987c, *American Scientist*, **75**, 376.

——. 1988, in *Galactic and Extragalactic Star Formation*, ed. R. E. Pudritz and M. Fich (Dordrecht: D. Reidel), p. 459.

Lo, K. Y., Cheung, K. W., Masson, C. R., Phillips, T. G., Scott, S. L., and Woody, D. P. 1987, *Ap. J.*, **312**, 574.

Lord, S. D. 1987, Ph. D. Thesis, University of Massachusetts.

McCarthy, P., Spinrad, H., Djorgovski, S., Strauss, M., van Breugel, W., and Liebert, J. 1987, *Ap. J.(Letters)*, **319**, L39.

Melnick, J. 1986, *Astr. Ap.*, **153**, 235.

Mihalas, D. and Binney, J. 1981, *Galactic Astronomy* (San Francisco: W. H. Freeman and Co.).

Narlikar, J. V. 1983, *Cosmology* (Boston: Jones and Bartlett) p. 168.

Norman, C. A. 1987 in *Star Formation in Galaxies* (NASA Conf. Publ. 2466) ed. C. J. Lonsdale Persson (Wash., D. C.: U. S. Govt. Print. Off.), p. 395.

O'Connell, R. W. 1986, *Pub. A. S. P.*, **98**, 163.

Pagel, B. E. J. 1986, *Highlights of Astronomy* General Assembly of the IAU, **7**, 551.

Rengarajan, T. N. 1984, *Ap. J.*, **287**, 671.

Rengarajan, T. N. and Verma, R. P. 1986, *Astr. Ap.*, **165**, 300.

Rieke, H., Lebofsky, M. J., Thompson, R. I., Low, F. J., and Tokunaga, A. T. 1980, *Ap.J.*, **238**, 24.

Rieke, G. H., Lebofsky, M. J., and Walker, C. E. 1988, *Ap. J.*, **325**, 679.

Sandage, A. 1986, *Astr. Ap.*, **161**, 89.

Sanders, D. B., Young, J. S., Scoville, N. Z., Soifer, B. T., and Danielson, G. E. 1987, *Ap. J. (Letters)*, **312**, L5.

Sanders, D. B., Soifer, B. T., Elias, J. H., Madore, B. F., Matthews, K., Neugebauer, G., and Scoville, N. Z. 1988, *Ap. J.*, **325**, 74.

Scalo, J. M. 1986, *Fundam. Cosmic Phys.*, **11**, 1.

Scalo, J. M. and Struck-Marcell, C. 1986, *Ap. J.*, **301**, 77.

Schmidt, M. 1959, *Ap. J.* , **129**, 243.

Schwarzschild, B. 1987, *Physics Today*, **40**, No. 11 (November), 17.

Scoville, N. Z., Yun, M. J., Clemens, D. P., Sanders, D. B., and Waller, W. H. 1987, *Ap. J. Suppl.*, **63**, 821.

Scoville, N. Z., and Clemens, D. P. 1986, *Ap. J. (Letters)*, **310**, L77.

Sekiguchi, K. and Anderson, K. S. 1987, *A. J.*, **94**, 644.

Shields, G. A. and Tinsley, B. M. 1976, *Ap. J.*, **203**, 66.

Silk, J. 1986, in *Luminous Stars and Associations in Galaxies*, IAU Symp. 116, ed. C. W. H. DeLoore, A. J. Willis, and P. Laskarides (Dordrecht: D. Reidel), p. 301.

Sofue, Y., Handa, T., Hayashi, M., and Nakai, N. 1987, in *Star Formation in Galaxies* (NASA Conf. Publ. 2466), ed. C. Persson (Wash., D. C.: NASA), 179.

Soifer, B. T., Houck, J. R., and Neugebauer, G. 1987, *Ann. Rev. Astr. Ap.*, **25**, 187.

Spitzer, L. 1978, *Physical Processes in the Interstellar Medium* (New York: John Wiley and Sons), p. 228.

Talbot, R. J. 1980, *Ap. J.*, **235**, 821.

Terlevich, R. and Melnick, J. 1981, *M. N. R. A. S.*, **195**, 839.

Terlevich, R. and Melnick, J. 1985, *M. N. R. A. S.*, **213**, 841.

Thronson, H. A., Walker, C. K., and Maloney, P. 1987, *Ap. J.*, **321**, 855.

Toomre, A. 1977, in *Evolution of the Galaxies and Stellar Populations*, ed. B. M. Tinsley and R. B. Larson (Yale: University Obs.), p. 401.

Tyson, A. 1987, in *Nearly Normal Galaxies from the Planck Time to the Present*, ed. S. M. Faber (Springer).

van den Bergh, S. 1976, *Ap. J.*, **206**, 883.

Viallefond, F., Goss, W.M., and Allen, R. J. 1982, *Astr. Ap.*, **115**, 373.

Viallefond, F. 1985, in *Star Forming Dwarf Galaxies*, ed. D. Kunth, T. X. Thuan, and J. Tran Thanh Van (Yvette, France: Editions Frontieres).

Vogel, S. N., Kulkarni, S. R., and Scoville, N. Z. 1988, *Nature*, **334**, 402.

Waller, W. H. 1984, M.S. Thesis, University of Massachusetts.

Waller, W. H., Clemens, D. P., Sanders, D. B., and Scoville, N. Z. 1987, *Ap. J.*, **314**, 397.

Waller, W. H., Kleinmann, S. G., and Ricker, G. R. 1988, *A. J.*, **95**, 1057.

Young, J. S. and Scoville, N. Z. 1982, *Ap. J.*, **258**, 467.

Young, J. S., Scoville, N. Z., and Brady, E. 1985, *Ap. J.*, **288**, 487.

Young, J. S., Kenney, J. D., Tacconi, L., Claussen, M. J., Huang, Y. L., Tacconi-Garman, L., Xie, S., and Schloerb, F. P. 1986a, *Ap. J.*, **311**, L17.

Young, J. S., Schloerb, F. P., Kenney, J., and Lord, S. D. 1986b, *Ap. J.*, **304**, 443.

Figures

Figure 2–1

Star forming histories.

a. Time averaged star formation rates based on three different indices of activity. The Hα luminosities of HII regions sample the short-lived OB star population and hence the most recent star formation ($\tau < 10^8$ yrs). The blue luminosities are produced mostly by stars that last less than 6 Gyr. Finally, the dynamical mass of a galaxy approximates the mass of stars that have formed over the galaxy's lifetime ($\tau < 15$ Gyr). Note the rapidly declining $\langle SFR \rangle$s of the Sb galaxy NGC 2841 that is obtained from these three time samples. By contrast, the lower-mass irregular galaxies appear to have increased in starbirth activity. Adapted from Gallagher *et al.* (1984).

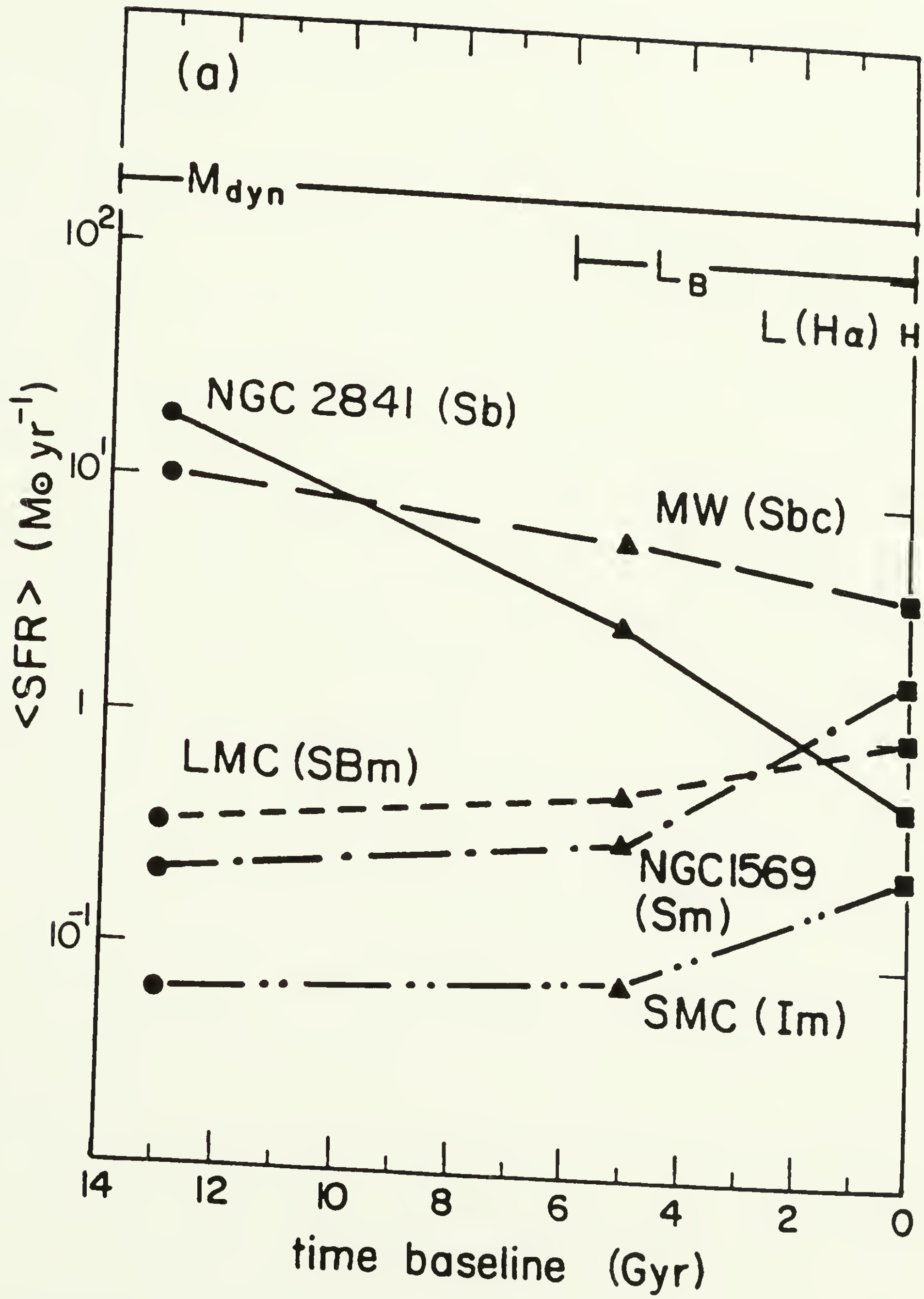
(a)
Mdyn
LB
L(Hα)
NGC 2841 (Sb)
MW (Sbc)
LMC (SBm)
NGC1569 (Sm)
SMC (Im)
10²
10¹
1
10⁻¹
<SFR> (M⊙ yr⁻¹)
14
12
10
8
6
4
2
0
time baseline (Gyr)

Figure 2-1 (cont.)

b. Schematic star forming histories as a function of morphological type. Taken from Sandage (1986). who bases the scheme on the trends found by Gallagher *et al.* (1984) and on observed variations of surface brightness. color. and bulge-to-disk ratio with Hubble type.

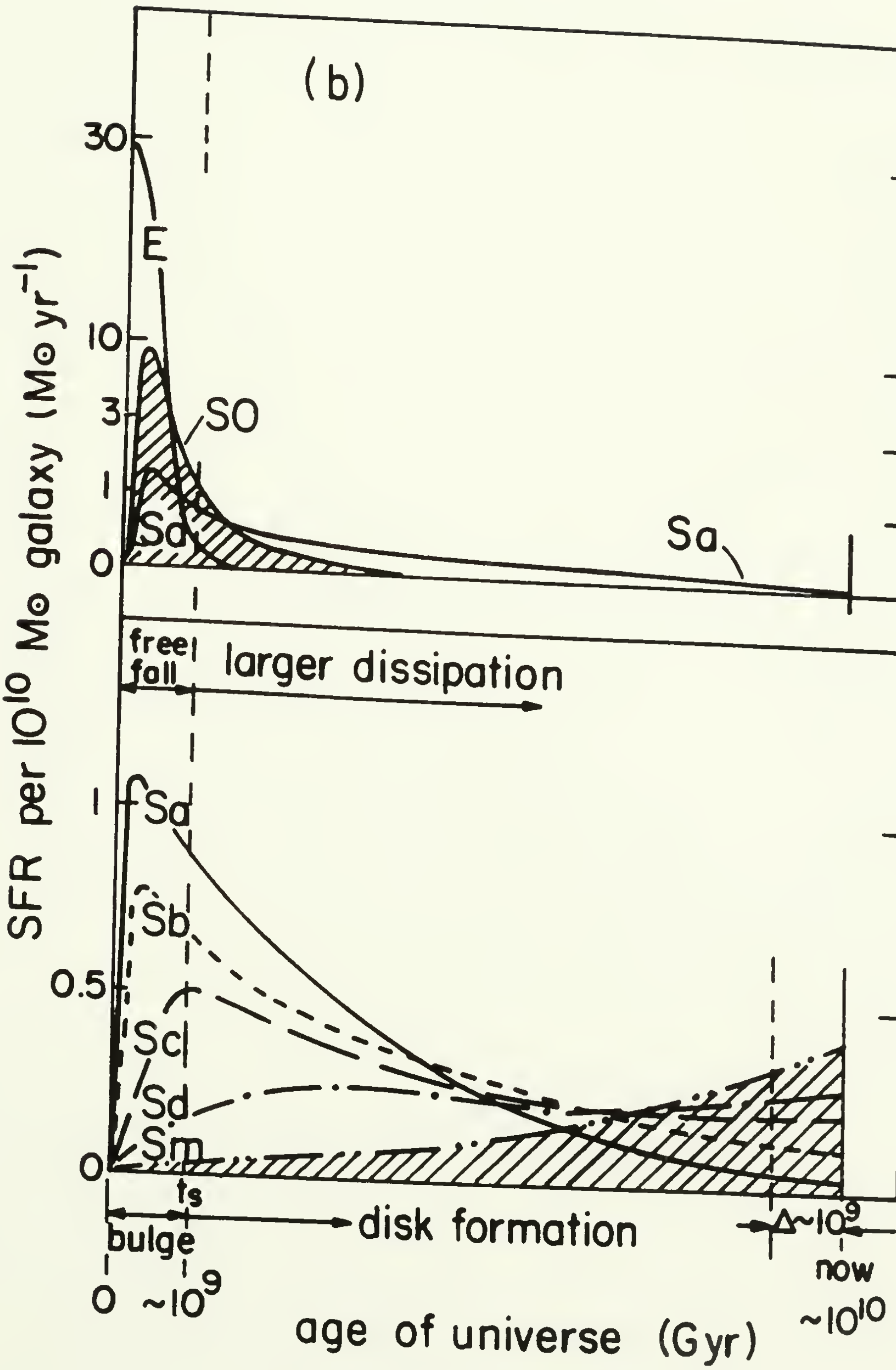
(b)
30
10
3
1
0
E
SO
Sa
Sa
SFR per 10^{10} M☉ galaxy (M☉ yr^{-1})
free fall
larger dissipation
1
0.5
0
Sa
Sb
Sc
Sd
Sm
ts
bulge
disk formation
Δ~10^9
now
0
~10^9
~10^{10}
age of universe (Gyr)

Figure 2–2

Luminosities and molecular masses of galaxies.

The ratio of total far-infrared luminosity and total H_2 mass in molecular clouds *vs.* L_{FIR} for "normal" and bright IRAS galaxies. The straight solid lines represent an $L_{FIR}/M(H_2)$ value of 4 $L_\odot/M_\odot$, typical of the mean value found for molecular gas-rich spirals, and an $L_{FIR}/M(H_2)$ value of 20 $L_\odot/M_\odot$, characteristic of the nearby starburst galaxies M82 and NGC 253. The large circles represent "ultraluminous infrared galaxies" which may be powered by both starburst and AGN-type activity. Taken from Sanders *et al.* (1988).

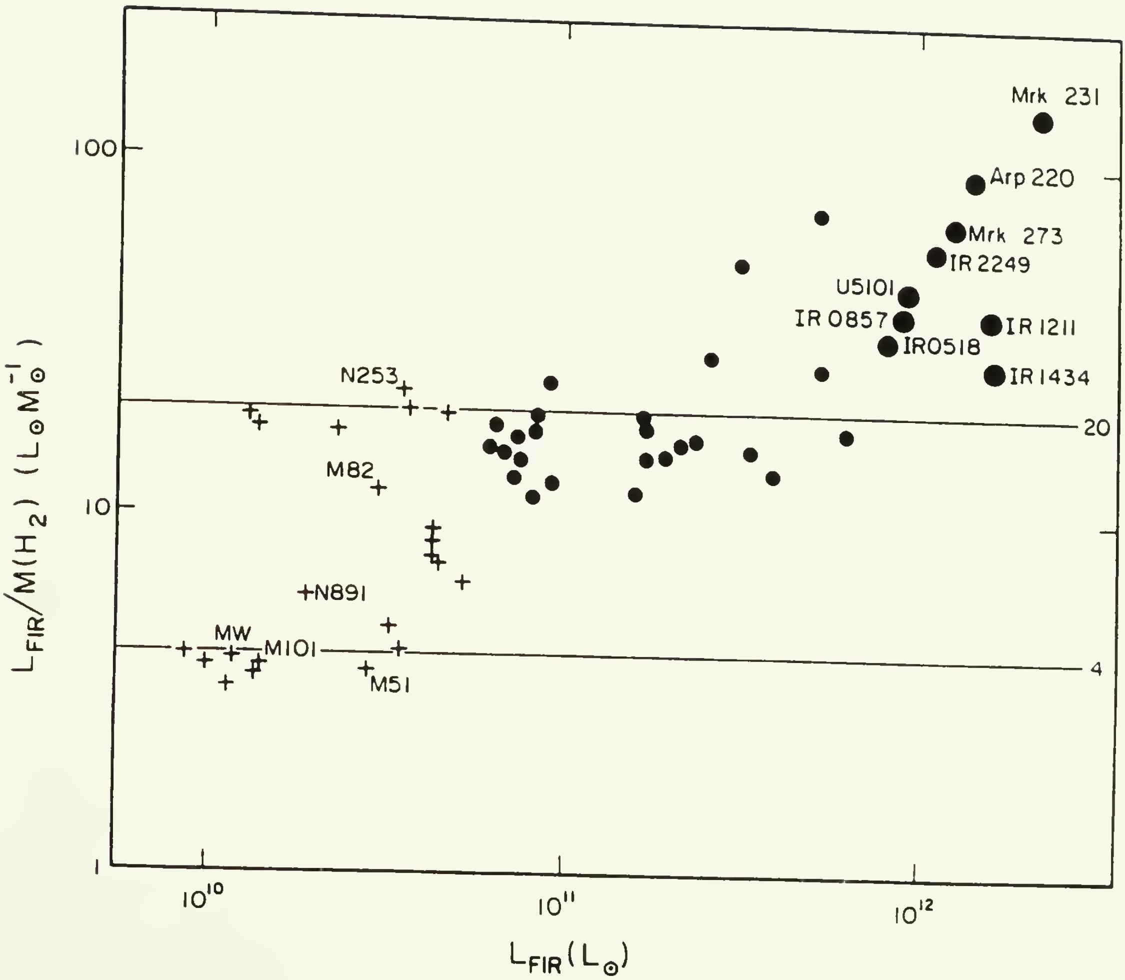
Mrk 231
Arp 220
Mrk 273
IR 2249
U5101
IR 0857
IR 1211
IR0518
IR 1434
N253
M82
N891
MW
M101
M51
100
10
1
20
4
10^{10}
10^{11}
10^{12}
$L_{FIR}(L_\odot)$
$L_{FIR}/M(H_2)$ $(L_\odot M_\odot^{-1})$

CHAPTER 3

M101

3.1 *Abstract*

CCD images of M101 at Hα, R, and I-bands have been obtained and analyzed with the aim of delineating the current-epoch massive star formation in the disk. From annular-averaged photometry of the Hα and R-band imagery, galactocentric emission profiles are derived. The profile of Hα emission is much flatter (with an e-folding scalelength of 9 kpc) than that of the red-continuum starlight (with an e-folding scalelength of 3.3 kpc), thus implying significant differences between the galactocentric distributions of current-epoch massive star formation and past-averaged star formation. The annular-averaged Hα surface brightness measurements are converted into starbirth intensities (using a Salpeter-type IMF) and compared with corresponding measures of the H_2 and HI surface densities. These comparisons reveal strong star formation correlations involving the H_2 surface density (where $\sigma(SFR) \propto \sigma(H_2)^{0.6}$) as well as the total gas surface density (where $\sigma(SFR) \propto \sigma(gas)^{0.9}$). The supergiant HII region complex, NGC 5461, has a starbirth intensity that is 16 times higher than the mean in the disk and a starbirth efficiency that is 10 times higher than the mean.

From synthetic-aperture photometry of the CCD images, the positions, sizes, Hα fluxes, and Hα equivalent widths of 385 HII regions are reported. The resulting Hα luminosity functions for the inner and outer galaxy reveal proportionately fewer high-luminosity HII regions within 5 kpc of the nucleus compared to the outer arms. The Hα equivalent widths (line-to-continuum ratios) of the inner galaxy HII regions are also lower, on average, by a factor of 1.5 compared to those of the outer galaxy. Selection, obscuration, and evolution effects seem unable to account for this behavior. The lower equivalent widths are more likely due to a significant decrease in the initial upper mass limits of the ionizing clusters. A simple model yields $EW(H\alpha) \propto M_u^{1.1\pm0.3}$ and thus a corresponding decrease in M_u by a factor of 1.3 to 1.7. The galactocentric variation in the Hα equivalent widths appears more closely related to the galaxy's

radial profile of differential rotation than to its monotonic gradient in O/H abundances.

A well-defined relationship is evident between the Hα equivalent width and the Hα luminosity, such that $L(H\alpha) \propto EW(H\alpha)^{1.8}$, for $L(H\alpha) < 10^{38.6}$ erg s^{-1}. The sense is for the brighter HII regions to contain the hotter, more massive stars. This "temperature-luminosity" relation is modeled in terms of a stellar mass spectrum with a constant "slope" of $\alpha = 2.9 \pm 0.3$ but with a variable upper mass limit.

3.2 *Introduction*

As the closest face-on Sc I galaxy visible from the northern hemisphere, M101 (NGC 5457) exemplifies the archetypal "giant spiral." Its prominent spiral arms and supergiant OB/HII associations have motivated several studies concerned with the orchestration of spiral structure and concurrent star formation on scales exceeding several kpc (*cf.* Sandage 1961; Schweizer 1976; Jenson *et al.* 1976; Viallefond *et al.* 1982; Elmegreen and Elmegreen 1984; Hill *et al.* 1984). These studies reveal an asymmetric spiral pattern that can be traced all the way into the nucleus (Sandage 1961); arm amplitudes at blue and ultraviolet wavelengths that are 40% - 200% higher than the underlying disk and -0.59 mag bluer at (U - B) (Schweizer 1976; Hill *et al.* 1984); broader lower amplitude arms at red and infrared wavelengths that have been attributed to density waves in the underlying stellar disk (Schweizer 1976; Elmegreen and Elmegreen 1984; also see counterargument in Hill *et al.* [1984]); and elongated OB/HII/HI associations that may represent transient ($\tau < 10^8$ yr) responses to the dynamical sweeping of gas in the presence of density waves and shearing flows (Viallefond *et al.* 1982).

Although the relationship between spiral structure and massive star formation in M101 has been intensively studied, the more general relationships between the recent massive star formation, the past-averaged record of star formation, and the available gas content have yet to be adequately addressed. Recent global and resolved studies of other late-type galaxies indicate significant correlations between various tracers of the massive star formation rate and tracers of the HI and H_2 gas (Lord 1987; Kennicutt 1989; Young *et al.* 1989). Evidence for an "autocatalytic" dependence between the current-epoch star formation rate and previous star forming activity has also been seen on global scales (Dopita 1985; also see Chapter 2).

In the first part of this Chapter (Sections 3.5 and 3.6) the galactocentric distribution of recent star formation is examined with the above relations in mind. *The primary goal of this annular-averaged study is to compare the current-epoch star forming activity with the past-averaged record of star formation and with the available gas content.* The current-epoch star formation is traced by calibrating and measuring the distribution of Hα surface brightness from CCD images of the inner disk and outer (eastern) arms. The Hα emission is a direct tracer of the ionizing photons that are being produced by young hot stars ($\tau < 10$ Myr). It therefore provides an observable index of the current-epoch high-mass star formation rate that is more directly quantifiable than the blue surface brightness or the HII region number density used in previous studies (Schweizer 1976; Kennicutt *et al.* 1989). The past-averaged record of star formation is traced by measuring the red-continuum emission in the disk. At R-band the light from the disk is dominated by late-type giants (70%) with ages exceeding 1 Gyr (Renzini and Buzzoni 1986). The available gas content is traced via the 21 cm HI spectral line emission mapped by Allen and Goss (1979) and via the 2.6 mm ^{12}CO spectral line emission mapped by Solomon *et al.* (1983).

Galactocentric distributions of the *annular-averaged* Hα intensities, red-continuum intensities, and Hα equivalent widths are compared in terms of e-folding scalelengths (Section 3.5). These reveal significant differences between the current-epoch and past-averaged distributions of star formation. The Hα intensities are then converted into equivalent star formation intensities, using Kennicutt's (1983) initial mass function (IMF) to characterize the newborn stellar populations, and compared with similarly derived starbirth intensities in M83, M51, and the Milky Way (Section 3.6.1). The efficiency of star formation is determined by comparing Gaussian-smoothed annular averages of the starbirth intensity with similarly resolved annular averages of the H_2 and HI surface densities (Section 3.6.2). These comparisons reveal a near-constant starbirth efficiency with radius, if both the molecular and atomic components are considered.

Finally, correlations between the inferred starbirth intensities and gas surface densities in M101 and in the other 3 galaxies are presented and compared with the findings of Kennicutt (1989) and Young *et al.* (1989) (Section 3.6.3).

Besides providing a well-resolved testing ground for theories of spiral structure and "laws" of star formation, M101 offers a well-stocked laboratory for the investigation of young stellar populations. This is because M101 contains hundreds of readily detectable HII regions spanning more than 3 decades in Hα luminosity — from HII regions as bright as the Orion nebula to HII region complexes more brilliant than the Large Magellanic Cloud! To date, only $\sim$10 of the most luminous star forming regions have been studied in terms of their nebular properties and underlying stellar populations. These have revealed a $\sim$1 dex radial gradient in the O/H abundance ratio and possible indications (from Hβ equivalent widths) for hotter stellar populations ionizing the metal-poor HII regions in the outer galaxy.

In the remainder of this Chapter (Section 3.7), an enlarged sample of 385 HII regions is examined in terms of their Hα luminosities and Hα equivalent widths. The primary aim here is *to test previous claims for a galactocentric variation in the effective temperatures of the ionizing stellar populations, and if evident, to see whether the variation is anticorrelated with the observed gradient in O/H abundances, as previously proposed.* Much of the analysis is based on the utility of the Hα equivalent width as a tracer of effective temperature. Being a line-to-continuum ratio, the Hα equivalent width of an isolated HII region traces the relative balance between the ionizing and non-ionizing flux from the underlying stellar population. It is therefore a crude but effective probe of the ionizing cluster's effective temperature and, by inference, of the cluster's high-mass IMF.

A brief discussion of previous studies concerned with giant HII regions in M101 and other late-type galaxies is first presented (Section 3.7.1). The sample of 385 HII regions is then described (Section 3.7.2), and problems associated with the HII region photometry are discussed (Sections 3.7.3 and 3.7.4). These include the treatment of the diffuse Hα emission, the effects of blending in crowded regions, and the isolation of the young cluster continuum from the light of the ambient disk. The resulting fluxes from the individual HII regions are tabulated and plotted in the form of luminosity functions and galactocentric distributions (Section 3.7.5). An apparent difference in slope between the inner and outer galaxy Hα luminosity functions is noted, and statistical tests are made which validate the difference.

The Hα equivalent widths of the 102 ionizing clusters with high signal-to-noise continuum fluxes are presented as a function of galactocentric radius, Hα luminosity, and red-continuum luminosity (Sections 3.7.6 - 3.7.10). Possible selection, obscuration, and aging effects on the Hα equivalent widths are extensively addressed (Sections 3.7.7 and 3.7.8), but found to inadequately account for the observed galactocentric variation in EW(Hα). To minimize the effects of obscuration, the sample of 102 HII regions is reduced to those 41 clusters which show minimally reddened ($\lambda6563 - \lambda8380$) colors. The resulting galactocentric distribution of Hα equivalent widths (including spectroscopic measurements of HII regions beyond the imaged fields) is compared with galactocentric profiles of the O/H abundance ratio, the differential rotation $d\Omega/dR$, the shear rate A, and the tidal stress T (Section 3.7.9). The poor relationship between O/H and EW(Hα) is contrasted with an apparent anti-correlation between the various dynamical quantities and EW(Hα). The latter relations are discussed in terms of a possible dynamical constraint on the high-mass IMF.

"Temperature-Luminosity" diagrams, where the Hα equivalent width is plotted against the Hα luminosity, are used to better characterize the ionizing stellar populations (Section 3.7.10). A robust correlation between the two plotted quantities (for luminosities below $10^{38.6}$ erg s^{-1}) is noted and modeled in terms of an IMF with a constant slope of $\alpha \approx 2.9 \pm 0.3$ but with an upper mass limit that varies by $\sim$3. Further relations between the upper mass limit and the ionizing cluster's total mass and lower mass limit are also modeled and discussed (Section 3.7.11).

Results from the annular-averaged starbirth study and the HII/stellar population study are summarized at the end of the Chapter (Section 3.8).

3.3 *Adopted Properties*

Table 3-1 lists the properties of M101 that have been adopted. The position angle of the major axis and inclination are based on the kinematic symmetries and aspect ratio of the HI emission (Bosma, Goss, and Allen 1981). I have calculated the galactocentric radii of the HII regions using the adopted elements. Because M101 is nearly face-on, the difference between galactocentric radii in the plane of the sky and in the plane of the galaxy never exceeds 5 percent. The dispersion of position angles and inclinations in the literature is sufficiently small to produce negligible uncertainties ($< 5\%$) in the computed galactocentric radii.

More problematic is the distance determination. As a crucial rung in the cosmological distance ladder, M101 has been the subject of many distance determinations. Unfortunately, the dispersion of results is approximately at the 50 percent level! At the high end are Sandage and Tammann (1974) who used the HII regions in the neighboring irregular galaxy NGC 5477 to derive a distance of 7.3 Mpc. This has been supported by HI observations of M101 and NGC 5477 (Allen *et al.* 1978) which show a physical connection between M101 and its calibrator. At the low end is de Vaucouleurs (1979) who used the velocity width *vs.* diameter relation for the HII regions in M101 to derive a distance of 4.2 Mpc. More recently, two Cepheids have been identified whose sparsely sampled periods and R-band magnitudes indicate a "preliminary" distance range of 7.5 Mpc down to 5.7 Mpc, depending on the obscuration of the Cepheids and the adopted distance to the LMC (Cook *et al.* 1986). I have decided to adopt the even closer value of Humphreys and Aaronson (1987) who compared optical and IR photometry of the brightest red supergiants in M101 with theoretical calibrations of these standard candles ($M_V \approx -8$) thus obtaining a distance of 4.8 Mpc. The effect of using this distance is to reduce the size of the galaxy and the luminosities of the brightest stars and HII regions to less anomolous levels than would otherwise exist (*cf.* Humphreys and Aaronson 1987). For the sake of consistency, I have also chosen "conservatively" low distances for the other galaxies in this dissertation.

Figure 3–1 depicts the kinematic properties of M101's disk that can be derived from the HI data of Bosma *et al.* (1981) — assuming a distance of 4.8 Mpc. These are shown as galactocentric profiles of the rotational velocity V_{rot}, the angular velocity Ω, the difference between the angular and epicyclic frequencies $\Omega - \kappa/2$, the spiral-arm crossing velocity V_{rel}, the differential rotation $d\Omega/dR$, the coefficient of rotational shear, *i.e.* Oort's constant A, and the coefficient of tidal acceleration T.

Of particular interest is the strong enhancement in the amplitude of the differential rotation ($d\Omega/dR$) at galactocentric radii between 1 and 4 kpc. This enhancement could be an artifact of the HI observations (resolution ≈ 0.5 kpc), whereby the beam smoothing produces underestimated rotation velocities near the nucleus and hence erroneous values of the differential rotation. However, a similarly strong enhancement in $|d\Omega/dR|$ can be derived from the rotation curve of Comte *et al.* (1979), where high-resolution Fabry-Perot observations at Hα, [SII], and [NII] were used to determine the rotation velocities of 302 HII regions (see their Figure 6). The observed enhancement in differential rotation leads to similar enhancements in the shearing flow and tidal acceleration at the small galactocentric radii. Such dynamical variations have been previously noted by Stark and Blitz (1978) and Blitz and Glassgold (1982) (in the context of the Milky Way, the LMC, and M101).

Figure 3–2 depicts the spectroscopic properties (culled from the literature) of the brightest HII regions as a function of galactocentric radius. These include the [OIII]/Hβ, [OIII]/[OII], ([OIII]+[OII])/Hβ, and [NII]/Hα line ratios; the inferred O/H abundance ratio; and the Hβ equivalent width. References to these properties will be made throughout the Chapter.

3.4 *Observations and Reductions*

A summary of the CCD imagery obtained for this study is provided in Table 3-2. The Hα, R, and I-band images were obtained at the Cassegrain focus of the McGraw-Hill Observatory 1.3 m telescope on Kitt Peak during clear, moonlit sky conditions.[1] The imaging device was the "MASCOT" CCD camera developed at MIT (Meyer and Ricker 1980), a dual-chip system which enables a variety of simultaneous observing modes. I did not take advantage of this versatility and

---

[1] The McGraw-Hill Observatory is operated by Dartmouth College, Massachusetts Institute of Technology, and the University of Michigan, with partial support from the National Science Foundation, the Alfred P. Sloan Foundation, and McGraw-Hill, Inc.

simply imaged on one of the chips — a TI 4849 virtual phase CCD (Luppino *et al.* 1987) which had replaced the poorer quality chip used in the observations of NGC 253 (see Waller *et al.* [1988]). Although the full chip size is 584 × 390 pixels, only 476 × 390 worth was saved after recording and trimming. Of this amount, approximately 15 percent was vignetted by the beam splitter in the MASCOT camera. The vignetting is evident in the southwest corner of the resulting images (see Figures 3–3 and 3–4). With the $f/13.5$ secondary in place, the resolution per pixel is 0.81", and the unvignetted field of view is approximately 5'×5'. The point source response function within the unvignetted field is estimated to have a FWHM of $\approx 2''$, as measured from radial profiles of foreground stars in the galaxy images.

Imaging at Hα was conducted using an interference filter (#1276, λ6563) kindly loaned by Kitt Peak National Observatory. The galaxy's systemic redshift of 5 Å causes the $\Delta\lambda = 36$ Å filter to pass Hα(λ_o6563) with 0.74 transmissivity, [NII](λ_o6584) with 0.15 transmissivity, and [NII](λ_o6548) with 0.68 transmissivity. The net contamination in the Hα images due to [NII] emission is expected to be 10 ± 5 percent depending on position in the galaxy: Within 170" (4 kpc) of the nucleus, where $f([NII])/f(H\alpha) \approx 0.5$, the [NII] contamination is about 15%; and beyond 340" (8 kpc) from the nucleus, where $f([NII]/f(H\alpha) \approx 0.15$, the contamination is about 5% (see Figure 3–2). Imaging of the red and far-red continua was conducted using the resident "R-band" and "I-band" filters at McGraw-Hill Observatory. Their wavelengths of peak transmissivity and FWHM bandpasses are similar to those of the Mould system R and I filters commonly used at Kitt Peak.

Images centered on the galaxy's nucleus and displaced 4.3' to the east of the nucleus were obtained through all filters (see Figures 3–3 and 3–4). Shortly thereafter, images of the subdwarf flux standard stars BD+17°4708 and BD+26°2606 (Oke and Gunn 1983) were obtained. Domeflat images were taken at the beginning of each night.

Initial processing of the CCD imagery was accomplished using the Mountain Photometry Code package at Kitt Peak headquarters. Bias averaging and subtraction as well as flatfield division were performed automatically using the standard algorithm. Because of the relatively short exposure times that were involved, darkframe subtraction was found to be unnecessary. Further processing, including image arithmetic, HII region identification, and synthetic aperture photometry, was conducted at the Universities of Massachusetts and Washington using *initially* the image interface and photometry package written by Robert Seaman for the Five College Astronomy Image Analysis Laboratory (FCAIAL) and, later, the Image Reduction and Analysis Facility (IRAF) software created at Kitt Peak National Observatory along with the Astronomical Image Processing System (AIPS) software created at the National Radio Astronomy Observatory (NRAO).

All measured fluxes were corrected for atmospheric extinction, using the airmass at the time of observation and Beer's Law:

$$R_\circ = R\ 10^{0.4K_\lambda sec\ z}, \qquad (3-1)$$

where $R_\circ$ denotes the corrected count rate per pixel (in $ADU s^{-1}$), z is the zenith distance, $K(\lambda 6563) = 0.1$, and $K(\lambda 8380) = 0.06$ as estimated from CCD observations of Landolt standards taken at Kitt Peak during 1986 (Bushouse, private communication). Synthetic aperture photometry on the images of the sdF-type standard stars BD+17°4708 and BD+26°2606 yielded the following conversions between flux and count rate (after bias subtraction, flatfield division, and atmospheric extinction correction):

$$f_\lambda(R\ band)(erg\ cm^{-2}\ s^{-1}\ \text{Å}^{-1}) = (4.1 \pm 0.2) \times 10^{-17}\ R_\circ(R\ band)(ADU\ s^{-1}), \qquad (3-2)$$

where the flux density calibration is for a central wavelength of 6563 Å,

$$f_\lambda(I\ band)(erg\ cm^{-2}\ s^{-1}\ \text{Å}^{-1}) = (3.1 \pm 0.1) \times 10^{-17}\ R_\circ(I\ band)(ADU\ s^{-1}), \qquad (3-3)$$

where the flux density calibration is for a central wavelength of 8380 Å, and

$$f_\lambda(H\alpha\ band)(erg\ cm^{-2}\ s^{-1}\ \text{Å}^{-1}) = (1.0 \pm 0.04) \times 10^{-17}\ R_\circ(H\alpha\ band)(ADU\ s^{-1}), \qquad (3-4)$$

so that

$$f(H\alpha\ band)(erg\ cm^{-2}\ s^{-1}) = (3.6 \pm 0.1) \times 10^{-14}\ R_{\circ}(H\alpha\ band)(ADU\ s^{-1}), \tag{3-5}$$

for an Hα filter bandwidth of 36 Å (FWHM).

Sky values were estimated from synthetic aperture photometry of the displaced R and Hα images, where the interarm regions have especially low surface brightness and thus are most strongly affected by the sky brightness. By comparing the measured surface brightness in these regions with the corresponding photometry of Schweizer (1976) (whose larger field of view permitted more direct sky determinations and subtractions), satisfactory fits to the sky background levels in the dispaced images were determined. The sky background levels in the centered images were determined and eliminated by taking advantage of the 10" overlap between the centered and displaced images and by equalizing the surface brightness levels within this common region. The dispersion in the subtracted sky background across each image is believed to be the primary source of noise in the derived Hα and continuum fluxes. This is estimated to be $\delta I_{\lambda}(R\ band) \approx 1.4 \times 10^{-18}\ erg\ cm^{-2}\ s^{-1}\ arcsec^{-2}$ $Å^{-1}$, $\delta I_{\lambda}(I\ band) \approx 1.1 \times 10^{-18}\ erg\ cm^{-2}\ s^{-1}\ arcsec^{-2}\ Å^{-1}$, and $\delta I(H\alpha\ band) \approx 7.6 \times 10^{-17}\ erg\ cm^{-2}\ s^{-1}\ arcsec^{-2}$, respectively, based on photometry of the low-surface-brightness regions in the displaced images. These dispersions represent 2.6, 2.0, and 2.5 percent of the respective sky backgrounds that were subtracted.

To obtain Hα images that are free from contamination by the stellar and nebular continua, it was necessary to subtract a shifted and scaled version of the calibrated R-band image from the original calibrated Hα-band image. The shifting in x and y was determined by comparing the centroid positions of 7 foreground stars in the 2 respective fields of view and was implemented via a linear interpolation scheme in the IRAF data reduction package. Determination of the scaling factor S was based on photometry of the standard stars and on the condition that

$$f(H\alpha) = f(H\alpha\ band) - S f_{\lambda}(R\ band) = 0 \tag{3-6}$$

for continuum sources (see also Appendix B). According to the previous calibrations (eqs. 3-2 to 3-5), the scaling factor is simply the Hα filter bandwidth (FWHM). To obtain red-continuum images that are free from contamination by the $H\alpha$ emission line within the R bandpass, subtraction of scaled Hα-band images from the calibrated R-band images was performed, where the scaling was determined from the relative bandwidths of the Hα and R-band filters according to

$$f_\lambda(\lambda 6563) \approx f_\lambda(R\ band) - f_\lambda(H\alpha\ band) bw(H\alpha\ band)/bw(R\ band) \qquad (3-7)$$

(see Appendix B for further discussion). All subsequent Hα and λ6563 red-continuum fluxes refer to the decontaminated values.

As a consistency check on the decontaminated Hα and red-continuum imagery, I have compared the Hα equivalent widths (*i.e.* line-to-continuum ratios) that were obtained from synthetic aperture photometry of the *processed* imagery against those derived from photometry of the original Hα-band and R-band images (see Figure 3–5). The derivation of EW(Hα) from the "raw" Hα-band and R-band images is based on considerations similar to those presented in Appendix B. It assumes that the flux through the R-band filter can be approximated by

$$f(R\ band) \approx f_\lambda[EW(H\alpha) + bw(R\ band)], \qquad (3-8)$$

where bw(R band) corresponds to the FWHM bandwidth of the R filter. Similarly, the flux through the Hα-band filter can be approximated by

$$f(H\alpha\ band) \approx f_\lambda[EW(H\alpha) + bw(H\alpha\ band)]. \qquad (3-9)$$

These approximations are valid only if the continuum flux density f_λ is relatively constant across the respective bandwidths. The flux ratio is then

$$\frac{f(H\alpha\ band)}{f(R\ band)} = \frac{[EW(H\alpha) + bw(H\alpha\ band)]}{[EW(H\alpha) + bw(R\ band)]}, \qquad (3-10)$$

which leads to the following solution for EW(Hα)...

$$EW(H\alpha) = \frac{[bw(H\alpha\ band) - bw(R\ band) f(H\alpha\ band)/f(R\ band)]}{[f(H\alpha\ band)/f(R\ band) - 1]}. \qquad (3-11)$$

Figure 3–5 shows that the equivalent widths, EW_R, thus derived from photometry of the "raw" Hα-band and R-band images, closely match the equivalent widths, EW_P, obtained from photometry of the "processed" Hα and red-continuum images. The "raw" and "processed" quantities agree to within 5 percent. More specifically,

$$\langle EW_P(H\alpha)/EW_R(H\alpha)\rangle = 1.016 \pm 0.046. \qquad (3-12)$$

with a standard error in the mean of 0.002. A least-squares linear regression on the two quantities gives

$$EW_P(H\alpha) = (-0.78 \pm 0.85) + (1.020 \pm 0.005)EW_R(H\alpha). \qquad (3-13)$$

Such close correspondence indicates that the "processed" and "raw" fluxes are mutually consistent with one another, and that nothing unexpected has resulted from the image manipulations.

Further checks on the Hα and red-continuum imagery were made by examining the few bright HII regions, whose line and continuum fluxes have been measured spectroscopically (Searle 1971; Torres-Peimbert *et al.* 1989). By tailoring synthetic apertures to match the $12.4'' \times 3.8''$ slit of Torres-Peimbert *et al.* (1989) and the 14" diameter circular entrance aperture of Searle (1971), photometric comparisons could be made for 5 HII regions. The spectroscopic and imaged fluxes agreed, on average, to within 10 percent. More specifically,

$$\langle f(H\alpha)_{spect}/f(H\alpha)_{image}\rangle \;=\; 1.00 \pm 0.25 \qquad (3-14)$$

with a standard error in the mean of ± 0.09, and

$$\langle f_\lambda(6563)_{spect}/f_\lambda(6563)_{image}\rangle \;=\; 1.03 \pm 0.34 \qquad (3-15)$$

with a standard error of ± 0.13. The relatively high dispersions about the mean are noteworthy and may indicate the actual uncertainties in the flux measurements as determined from photometry of the processed Hα-band and R-band imagery. However, the spectroscopic determinations are uncertain by 20 - 30 percent as well, thus contributing to the high dispersion that is evident in the comparison.

Propagation of systematic errors due to potential errors in the atmospheric extinction correction ($\pm$ 5%); uncertainties in the sky subtraction ($\pm$ 7%); variations in the [NII] contamination ($\pm$ 5%); uncertainties in the standard-star calibration conversions ($\pm$ 5%); differences between M101 and the standard stars in the slopes of the continua across the R and I bandpasses ($\pm$ 6%); and faulty isolation of the Hα and continuum emission ($\pm$ 15%) gives an rms systemic uncertainty of $\pm$ 20%. Propagation of random errors due to noise in the subtracted sky backgrounds gives uncertainties for a typical HII region of ($\pm$ 4%) at Hα and ($\pm$ 2%) in the continuum. The total estimated uncertainties are then approximately 20 to 25 percent for the line and continuum fluxes.

The photometric uncertainties become more severe, of course, in regions of low surface brightness. In the outer galaxy — where the lowest levels of continuum emission are $\sim 10^{-18}$ erg s^{-1} cm^{-2} s^{-1} arcsec^{-2} Å^{-1} — the sky-subtraction uncertainty becomes especially important, resulting in a net uncertainty in the continuum intensities of $\pm$50%. This affects the annular-averaged galactocentric distribution of continuum intensities, such that the e-folding scalelength becomes uncertain by $\pm$20% (see next Section).

In the following Sections, a mean photometric uncertainty of $\pm$25% is assumed. Additional uncertainties, (*e.g.* standard deviations about mean values, standard errors in the mean values, errors in HII region fluxes due to blending, uncertainties in the cluster continuum fluxes due to uncertain background subtractions, etc.) are noted, tabulated, and plotted where they apply.

3.5 *Surface Brightness Distributions*

3.5.1 *Emission Morphology*

Figures 3-3 and 3-4 show the resulting Hα and red continuum emission from the two imaged fields. A casual inspection of the Hα images will reveal that the inner disk of M101 is riddled with numerous "small" HII regions, whereas the outer arms are dominated by huge HII complexes. One can also see that in the emission-line images, the contrast between the HII regions and the rest of the disk is well-pronounced. By comparison, the underlying young star clusters in the continuum images are much less noticeable. This relatively poor showing of the young *stellar* component will be discussed in the section on HII region flux measurements (Section 3.7.3).

Contour diagrams of the Hα and red-continuum emission from the combined fields are presented in Figure 3–6. These were created by trimming off the vignetted portions from the original images, combining the fields according to their respective offsets ($\Delta X = 260''$, $\Delta Y = -24''$), taking the logarithm of the calibrated surface brightnesses, spatially smoothing the logarithmic values with a 8 pix × 8 pix ($6.5'' \times 6.5''$) boxcar window, and contouring the smoothed logarithmic values. These diagrams reveal a ragged 2-armed spiral component in the inner disk that is traced by both the line and continuum emission. The continuum spiral arms, however, are smoother, broader, and of lower contrast compared to the Hα arms.

3.5.2 *A Possible Starburst Outflow?*

Figure 3–7 shows the supergiant HII regions NGC 5461 and NGC 5462 at higher magnification. Each of these complexes is of similar size and Hα luminosity as the Large Magellanic Cloud! Closer inspection reveals that the morphologies of the two giant complexes differ.

NGC 5462 consists of 2 strongly emitting HII regions — the brightest having an Hα luminosity equivalent to 70 Orion Nebulae ($L(H\alpha) = 9.4 \times 10^{38}$ $erg\ s^{-1}$ before dereddening) — along with many other less luminous regions. The entire complex has a luminosity of 9.8×10^{39} $erg\ s^{-1}$ before dereddening. Close inspection of the Hα image reveals a total of 34 HII peaks in the NGC 5462 chain. This figure is very similar to the 32-peak tally counted by Hodge and Kennicutt (1988) from inspection of an image-tube plate.

NGC 5461 is dominated by a single unresolved HII region with an Hα luminosity equivalent to 710 Orion Nebulae ($L(H\alpha) = 9.6 \times 10^{39}$ $erg\ s^{-1}$ before dereddening). The total complex has a luminosity of 1.8×10^{40} $erg\ s^{-1}$ before dereddening, rivaling that of the starburst irregular galaxy NGC 1569 (see Chapter 5). Figure 3–7(b) shows 3 plume-like features of diffuse ionized gas diverging from the brilliant core toward the South, Southeast, and Southwest. Detailed examination of corresponding continuum images (*cf.* Sandage 1989 and the present images) indicates that only the southern plume has any sort of stellar counterpart. The other plumes are clearly diffuse with no underlying hot stars. Seen in projection, the plumes extend for roughly 28" (650 pc). An HI map with a resolution of 30" (700 pc) reveals a pronounced bulging on the southeast ("plume") side of NGC 5461 (Viallefond *et al.* 1981). Higher resolution mapping of the HI emission (using the VLA) as well as sensitive radial-velocity mapping of the diffuse Hα emission (using Fabry-Perot interferometry or dense-pack multifiber spectroscopy) would greatly aid in the correct interpretation of this possible outflow candidate. Kinematic evidence for energetic outflow activity has been found in other "starburst" systems including M82 (see Chapter 4) and NGC 1569 (see Chapter 5).

3.5.3 *Annular-Averaged Photometry*

To obtain galactocentric profiles of the Hα and red-continuum emission, annular-averaged photometry was conducted on the combined images. The annuli were elliptical with the position angle of their major axes equal to that of the galaxy, and with $b/a = \cos i$. The width of each annulus corresponded to 30" in the plane of the galaxy. In the case of the Hα emission, the annular-averaged photometry was conducted on both the unsmoothed image and on one that had been convolved with a 60" (FWHM) Gaussian "beam." The latter smoothing was done to facilitate comparisons with CO observations of similar resolution (see Section 3.6.2). The resulting annular-averaged Hα surface brightnesses, their standard deviations, and standard errors are tabulated in Table 3-3.

Figure 3–8(a) shows the galactocentric surface brightness profiles of the Hα and red continuum emission. Here, the unsmoothed Hα emission is plotted. One can immediately see that the dispersions in the Hα emission are much greater than the dispersions in the red-continuum emission. This reflects the discrete, high-contrast, nature of the Hα emission. The standard errors in the annular-averaged values are very small, however, barely rivaling the sizes of the plotted points for both the Hα and red-continuum distributions. Also evident in Figure 3–8(a) are enhancements in the Hα surface brightness at the annuli which contain the supergiant HII region complexes NGC 5461 and NGC 5462. These enhancements could be overestimated due to the azimuthal undersampling of the annuli at these galactocentric radii.

Perhaps most important, Figure 3–8(a) shows that the galactocentric distribution of Hα emission is flatter than that of the red continuum. A least-squares regression that is weighted by the standard deviations gives for the *smoothed* Hα intensities

$$log\langle I(H\alpha)\rangle = (-15.50 \pm 0.03) - (1.12 \pm 0.14) \times 10^{-3} R, \qquad (3-16)$$

where I(Hα) is in $erg\ cm^{-2}\ s^{-1}\ arcsec^{-2}$, R is in arcsec, the quoted uncertainties are statistical, and the correlation coefficient, r_c, is -0.93 yielding a correlation significance level which exceeds 0.999. The corresponding $1/e$ scalelength of the Hα distribution is $388'' \pm 49''$ (9.0 ± 1.1 kpc!). By contrast, the red-continuum is best fit by

$$log\langle I_\lambda(6563A)\rangle = (-16.69 \pm 0.06) - (3.10 \pm 0.44) \times 10^{-3} R, \qquad (3-17)$$

where $r_c = -0.98$. The corresponding e-folding scalelength here is $140'' \pm 19.9''$ (3.3 ± 0.5 kpc) which compares favorably with Schweizer's value of 151", based on photometry of an O-band ($\lambda_o 6440$) photographic plate (1976). Taking the mode instead of the mean within each annulus gives an even steeper radial profile in the red continuum with an e-folding scalelength of $126'' \pm 16''$ (2.9 ± 0.4 kpc). This again compares favorably with Schweizer, who obtains for the disk alone (*i.e.* having eliminated the spiral arm component) a scalelength of 117". A much better correspondence between the Hα emission and the starlight can be achieved by considering only the spiral arm components of the B-band continuum. (see Figure 7(a) in Schweizer (1976) which indicates an e-folding scalelength of about 312"). This is not surprising: since Hα emission is a primary tracer of spiral structure, it is to be expected that its galactocentric distribution would resemble that of the blue starlight from the spiral arms.

The different galactocentric profiles of surface brightness can be further investigated by examining the galactocentric distribution of Hα equivalent widths. Being a line-to-continuum ratio, the annular-averaged Hα equivalent width traces the relative proportions of current-epoch massive star formation to past-averaged star formation in the disk. Figure 3–8(b) shows the Hα equivalent width increasing with galactocentric radius. A least-squares regression weighted by the standard deviations gives

$$logEW(H\alpha) = (1.11 \pm 0.24) + (1.84 \pm 0.89) \times 10^{-3} R, \qquad (3-18)$$

where $r_c = 0.93$ with a correlation significance level exceeding 0.995. The corresponding e-folding scalelength for the radially *increasing* EWs is $236'' \pm 114''$ (5.5 ± 2.7 kpc). Such behavior indicates that the current-epoch massive star formation becomes increasing more important in the outer galaxy compared to the past-averaged star formation. This is not a universal situation among disk galaxies. For example, both M31 and the Milky Way have their massive star formation concentrated in a ring about their centers (*cf.* Walterbos and Kennicutt (1987); Gusten and Mezger 1982).

3.6 *Star Formation Rates and Efficiencies*

3.6.1 *Starbirth Rates*

To convert the Hα intensities into starbirth intensities (*e.g.* star formation rates per unit area in the plane of the galaxy), it is necessary to adopt some sort of initial mass function (IMF) that will connect the ionizing photon luminosity to the overall star formation rate. In Appendix A, a variety of IMFs are considered and the resulting conversions tabulated. In the present section, however, a single "universal" IMF will be assumed, so that comparisons can be made between the derived starbirth parameters in M101 and similarly derived starbirth parameters in other galaxies (Kennicutt 1983; Lord 1987; Waller *et al.* 1988). The IMF "of choice" is the "extended Miller-Scalo IMF" formulated by Kennicutt (1983), where

$$N(M)\, dM \propto M^{-1.4} dM \qquad (0.1 < M < 1.0\ M_\odot) \qquad (3-19)$$

$$N(M)\, dM \propto M^{-2.5} dM \qquad (1.0 < M < 100\ M_\odot). \qquad (3-20)$$

This IMF leads to the following conversion between star formation rate and ionizing photon luminosity.

$$SFR(M_\odot\ yr^{-1}) = 1.2 \times 10^{-53}\ N_i\ (photons\ s^{-1}). \qquad (3-21)$$

with the ionizing luminosity depending on the Hα luminosity according to

$$N_i\ (photons\ s^{-1})\ =\ 7.4 \times 10^{11}\ L(H\alpha)\ (erg\ s^{-1}), \qquad (3-22)$$

if case B recombination at an electron temperature of $10^4\ K$ is assumed (Osterbrock 1974). Compared to the regular Miller-Scalo IMF (Miller and Scalo 1979), this formulation yields conservatively low starbirth rates and efficiencies (see Appendix A). Possible spatial variations in the IMF will be deferred to later sections of this Chapter.

Figure 3–9 shows the galactocentric profile of starbirth intensities in the plane of the disk, based on annular-averaged photometry of the Gaussian-smoothed Hα image (see Table 3-3). In the absence of any spatially resolved measurements of the visual extinction, a correction factor of 1.61 (corresponding to a global extinction of $A_v\ =\ 0.72$ mag) has been applied. This value is based on spectroscopic measurements of the $f(H\alpha)/f(H\beta)$ flux ratio in several bright HII regions (Smith 1975; Rayo *et al.* 1982; McCall *et al.* 1985). Because no galactocentric variations in A_v are evident from these data (see Section 3.7.5), a global extinction seems justifiable. Higher extinctions ($A_v\ \approx\ 2$) have been found in the brightest HII regions from measurements of the $S(6\ cm)/f(H\alpha)$ flux ratio (Israel and Kennicutt 1980). Therefore, the extinction correction applied to Figure 3–9 could be too low by a factor of ~2. No correction has been made for the absorption of UV photons by dust within the HII regions. This absorption reduces the amount of ionized gas and so affects the radio continuum and hydrogen line emission equally. Another factor of ~2 could be hiding because of this "internal" effect (Gusten and Mezger 1982; see also Section 3.7.7).

Galactocentric profiles of the starbirth intensities in M83, M51, and the Milky Way are also plotted. The M83 and M51 intensities are based on the extinction-corrected Hα intensities tabulated by Lord (1987), where the same $\sigma(SFR)/I_o(H\alpha)$ conversion has been used. The Milky Way starbirth rates are based on radio continuum measurements of the Galactic plane (Gusten and Mezger 1982), where the same SFR/N_i conversion has been used.

Two main conclusions can be inferred from the galactocentric profiles. The first is that the distribution of starbirth activity in M101 is spread over a large area in the disk. This sprawling activity is as pronounced in M101 as in the Milky Way. If a higher distance is adopted, the sprawl would become that much greater. The second conclusion is that the starbirth intensities in M101 are significantly less than those in M83 and M51 but are similar to those in the Milky Way. Being area-averaged quantities, the starbirth intensities are not dependent on distance (although their galactocentric extents are), and so the differences and similarities in amplitude between the 4 galactocentric profiles are worth further consideration. From these profiles, the starbirth intensities in M101 are about 1/7 those in M83, 1/3 those in M51, and between 1/3 and 3 times those in the Milky Way. The integrated starbirth rate within $R = 10$ kpc is estimated to be 3.4 $M_{\odot}\ yr^{-1}$, or about the same as the corresponding rate in the Milky Way.

3.6.2 *Starbirth Efficiencies*

To compare the starbirth activity with the corresponding amounts of available gas, I have plotted the galactocentric profiles of atomic and molecular hydrogen surface densities (see Figure 3-10(a)). The atomic profile is based on a $24'' \times 45''$ resolution mapping of the 21 cm HI spectral line emission (Allen and Goss 1979). The molecular hydrogen profile is based on a 60" resolution mapping of the 2.6 mm ^{12}CO spectral line emission (Solomon *et al.* 1983). A constant $\sigma(H_2)/I(CO)$ conversion was applied to the CO data corresponding to

$$N_{H_2}/I(CO) = 2.8 \times 10^{20}\ (cos\ i)\ cm^{-2}/K[T_R^*]\ km\ s^{-1}, \qquad (3-23)$$

or equivalently

$$\sigma(H_2)/I(CO) = 6.42\ (cos\ i)\ M_{\odot}\ pc^{-2}/K[T_R^*]\ km\ s^{-1}, \qquad (3-24)$$

as determined by Bloeman *et al.* (1986) from gamma-ray studies of the molecular and atomic hydrogen gas in the Milky Way. If this "constant" conversion is, instead, inversely proportional to the C/H and O/H abundance ratios (Maloney and Black 1988; Cohen *et al.* 1988), then the strong O/H abundance gradient in M101 could end up flattening the plotted profile of molecular gas.

The star forming "efficiency" is here defined as the ratio of the starbirth rate per solar mass of available gas, *i.e.*

$$SFE = SFR/M_{gas} = \sigma(SFR)/\sigma(gas) \qquad (3-25)$$

and is expressed in units of Gyr^{-1}. In computing the starbirth efficiencies, care was taken to compare identically resolved annular measures of the starbirth intensity and gas surface density. Figure 3-10(b) shows the galactocentric profiles of starbirth efficiency relevant to the H_2 alone, the HI alone, and the total gas content. For the sake of comparison, starbirth efficiency profiles for M83, M51, and the Milky Way are also plotted (see Figure 3-11). The efficiencies for M83 and M51 are based on the annular-averaged $H\alpha$ and CO intensities obtained by Lord (1987), where identical $\sigma(SFR)/I(H\alpha)$ and $\sigma(H_2)/I(CO)$ conversions have been used. The efficiencies for the Milky Way are based on the radio-continuum measurements of Gusten and Mezger (1982), where the same SFR/N_i conversion has been used, and on the CO measurements of Sanders, Solomon, and Scoville (1984), where the same $\sigma(H_2)/I(CO)$ conversion has been used.

Consideration of the molecular gas alone leads to starbirth efficiencies in M101 that increase from 0.65 Gyr^{-1} near the nucleus to 1.92 Gyr^{-1} in the outer disk. Similar behavior is seen in M51 (where the mean efficiency is 2 times lower) but not in M83 or in the Milky Way, where the efficiencies show radially *decreasing* behavior. The Milky Way seems most discrepant, with ~2 higher efficiencies within 5 kpc of the nucleus, but with ~2 *lower* efficiencies between 6 and 10 kpc.

The flattest galactocentric profile results from considering *both* the molecular and atomic gas components as contributors to the starbirth process. The starbirth efficiency in the disk of M101 then varies between 0.47 and 0.67 Gyr^{-1}, with the highest value coinciding with the annuli containing the supergiant HII region complexes NGC 5461 and NGC 5462. The relatively constant efficiencies found in M101 are roughly 1.7 times higher than the radially falling and rising efficiencies in M51 and 1.3 times lower than the radially rising and falling efficiencies in M83. Compared to the Milky Way, the starbirth efficiencies in M101 are 2.8 times lower within 5 kpc of the nucleus and nearly equal between 6 and 10 kpc.

The radially invariant starbirth efficiencies that are found in M101 are based on the assumption of an invariant IMF and $N(H_2)/I(CO)$ ratio across the disk of M101. If, instead, the high mass IMF is suppressed inside of $R = 5$ kpc (as the results in Section 3.7 seem to indicate), then the *computed* starbirth intensities could be too low. For example, a decrease in the upper mass limit, M_u, from 100 $M_\odot$ to 60 $M_\odot$ in the inner disk would correspond to an increase in the *actual* SFR/L(Hα) conversion by a factor of 1.5 for a Kennicutt-type IMF (see Appendix A for further discussion). This effect would increase the starbirth efficiencies in the inner galaxy compared to what would otherwise be computed. An abundance-sensitive $\sigma(H_2)/I(CO)$ conversion would further amplify these modifications. Because the inner galaxy is more metal-rich and hence has a higher CO/H_2 ratio, the actual surface densities of molecular hydrogen could be lower than what the standard conversion would otherwise yield. The lower H_2 surface densities would then increase the actual starbirth efficiencies even more. Beyond $R \approx 7$ kpc, the opposite effect could be occurring. Overall, the $\sim$0.6 dex radial gradient in O/H abundances within R = 10 kpc could be producing variations in the $\sigma(H_2)/I(CO)$ conversion of similar amplitude (*cf.* Maloney and Black 1988; Cohen *et al.* 1988). Therefore, the relatively constant and low efficiencies evident in Figure 3–11 could be distorted misrepresentations of a more steeply declining efficiency that varies by $\sim$0.8 dex.

If the near-constant efficiencies are accepted at face value, however, and if a Salpeter-type IMF (such as Kennicutt's formulation) is adopted, then the e-folding gas depletion timescale is $\tau(HI + H_2 + He) \approx 1.6/SFE \approx 2.7\ Gyr$ (see Appendix A and Section 2.6 of the Overview). Any modifications of the $\sigma(SFR)/I(H\alpha)$ ratio (*e.g.* adopting higher extinctions or more "bottom-heavy" IMFs such as the standard Miller-Scalo formulation) would most likely *decrease* the depletion timescale even further. Similarly "imminent" depletion timescales have been determined for the Milky Way (Gusten and Mezger 1982; Knapp 1987) and for other late-type spirals (Kennicutt 1983). Whether these galaxies are actually about to "hit the wall" in terms of their star forming activity remains highly uncertain (see Chapter 2).

3.6.3 *A Near-Linear Schmidt Law*

To investigate the relationship between gas content and star formation rates, the annular-averaged starbirth "intensities" have been plotted as a function of H_2, HI, and H_2 + HI + He surface densities (see Figure 3–12). Corresponding quantities for M51, M83, and the Milky Way are also plotted. Casual inspection will reveal strong correlations between $\sigma(SFR)$ and $\sigma(H_2)$ as well as between $\sigma(SFR)$ and $\sigma(HI + H_2 + He)$. By contrast, an *anticorrelation* is evident between $\sigma(SFR)$ and $\sigma(HI)$ in M101. No other galaxy in the sample shows such behavior. In general, the star formation intensities and HI surface densities are very poorly correlated.

Least-squares regressions on the M101 data give

$$log\ \sigma(SFR) = (1.58 \pm 0.06) - (0.90 \pm 0.10) log\ \sigma(HI), \quad (3-26)$$

with $r_c = -.97$ yielding a correlation significance level of 0.999,

$$log\ \sigma(SFR) = (0.49 \pm 0.16) + (0.55 \pm 0.08) log\ \sigma(H_2), \quad (3-27)$$

with $r_c = 0.96$ yielding a correlation significance level of 0.999, and

$$log\ \sigma(SFR) = (-0.10 \pm 0.17) + (0.87 \pm 0.14) log\ \sigma(gas), \quad (3-28)$$

with $r_c = 0.96$. The intercepts, slopes, and standard deviations of these least-squares fits are all based on having run the regressions in both directions.

Inclusion of the M51 and M83 data destroys the SFR-HI correlation while making both the SFR-H_2 and SFR-gas relations near-linear in form. Least-squares regressions give

$$log\ \sigma(SFR) = (0.03 \pm 0.05) + (0.88 \pm 0.03) log\ \sigma(H_2), \quad (3-29)$$

with $r_c = 0.98$ yielding a correlation significance level exceeding 0.999, and

$$log\ \sigma(SFR) = (-0.10 \pm 0.17) + (0.87 \pm 0.14) log\ \sigma(gas), \quad (3-30)$$

with $r_c = 0.99$. Inclusion of the Milky Way data gives similarly near-linear relations.

These results agree with the conclusions of Young and Scoville (1982) and Young *et al.* (1989) which are based on total far-infrared *luminosities* and gas *masses*. Such studies have been criticized as being subject to scaling artifacts (such that bigger galaxies have more of everything) and to distance errors. To eliminate these effects, Kennicutt (1989) has considered the mean Hα *intensities* and gas *surface densities* within the optical diameters (D_{25}) of 63 galaxies. He finds a correlation between $\sigma(SFR)$ and $\sigma(HI)$ as well as between $\sigma(SFR)$ and $\sigma(gas)$ with power-law exponents of 1.4 ± 0.2 for both dependences, but, surprisingly, no correlation between $\sigma(SFR)$ and $\sigma(H_2)$. The annular-averaged results presented here are therefore inconsistent with Kennicutt's globally-based results. Kennicutt also compared annular-averaged measures of starbirth intensity and gas surface density for the inner parts of 15 nearby galaxies. Here, most of the starbirth intensities were determined from annular-averaged *number densities* of HII regions instead of extinction-corrected Hα surface brightnesses. Nevertheless, they are probably reasonable approximations (within a factor of 2-5) to the actual Hα surface brightnesses. He again obtains a correlation between $\sigma(SFR)$ and $\sigma(gas)$ with a power-law exponent 1.3 ± 0.3. Although Kennicutt does not report the H_2 dependence, it is probably similar to that of the total gas content in these denser, H_2-dominated regions. Therefore, the annular-averaged results of Kennicutt agree with those reported here except in the value of the power-law exponent — his being 0.4 higher than the 0.9 ± 0.1 value that I find. Other possible star formation dependences are reviewed in Chapter 2.

3.6.4 *NGC 5461's High Starbirth Efficiency*

In Section 3.5, the Hα emission from the supergiant HII region complex was described. Comparable in size and Hα luminosity to the starburst irregular galaxy NGC 1569, this region also shows morphological evidence for an energetic outflow of diffuse, ionized gas. To estimate the starbirth efficiency in this region, the Hα emission from a 60" diameter circular region centered on the emission centroid was measured and compared with CO and HI observations of similar resolution (Blitz *et al.* 1981). The 60" (FWHM) Gaussian-smoothed Hα image was used for this comparison. The resulting mean Hα surface brightness is 3.3×10^{-15} $erg\ cm^{-2}\ s^{-1}\ arcsec^{-2}$, which after dereddening for $A_v \approx 1$ mag (Smith 1975), converts into a starbirth intensity of 208 $M_\odot\ Gyr^{-1}\ pc^{-2}$. The corresponding surface densities of gas are 8.1 $M_\odot\ pc^{-2}$ in H_2, 14.4 $M_\odot\ pc^{-2}$ in HI, and 6.3 $M_\odot\ pc^{-2}$ in HII gas (assuming a mean ion density of 25 cm^{-3}

[Kennicutt 1984]). Multiplying the summed surface density by 1.33 to account for the presence of Helium gives a total gas surface density of 38.3 $M_\odot\ pc^{-2}$. The starbirth efficiency of this exceptional region is then 5.4 Gyr^{-1}, or roughly 10 times the mean efficiency in the disk of M101 and more than 2 times higher than the highest annular-averaged efficiency sampled in the 4 galaxies.

Figure 3–12(c) shows this region rivaling the starburst nucleus of M83 in starbirth intensity, but exceeding it in starbirth efficiency. A power-law fit through this one point would have $\sigma(SFR) = \sigma(gas)^{1.5}$ compared to the $\sigma(SFR) \approx \sigma(gas)^{0.9}$ dependence that is found from the annular-averaged photometry. Similar "nonlinear" behavior has been seen in the spiral arms of M51 and M83 (Lord 1987; Vogel *et al.* 1988; see also Chapter 2).

3.7 *Individual HII Regions and their Ionizing Stellar Populations*

3.7.1 *Previous Studies of Individual HII Regions*

As noted in the Introduction, M101 contains a wealth of readily detectable HII regions, of which only the ~10 most luminous have been studied in terms of their underlying stellar populations. Topping the range of luminosities are the kpc-size "superassociations" of star clusters and HII regions that dominate the outer spiral arms. These have been noted since Herschel first began examining Messier's nebular objects with his 19" reflector (Hoskins 1963; Burnham 1978). Designated NGC numbers of their own, they are (in order of increasing galactocentric distance) NGC 5461, NGC 5462, NGC 5455, NGC 5447, and NGC 5471. Both NGC 5461 and NGC 5471 are optically bright enough to rival "starburst" regions such as 30 Doradus in the LMC and the nucleus of M83 (Kennicutt 1984; also see Chapter 6). How these colossal star forming regions formed so far away from the galaxy's central gravitational field remains an intriguing property of M101's disk (*cf.* Elmegreen 1979; Viallefond *et al.* 1982).

Spectroscopic observations of the outer superassociations and the brightest HII regions of the inner galaxy have revealed a pronounced radial gradient in the "excitation" of the HII regions (Searle 1971; Smith 1975). The sense of this gradient is that the spectral-line intensity of [OIII]($\lambda\lambda$4959, 5007) relative to that of Hβ(λ4861) increases with radius by 2 orders of magnitude (see Figure 3–2).

This effect was attributed to changes in the O/H abundance ratio. Subsequent observations by McCall *et al.* (1985) have confirmed that the excitation gradient is at least partly an abundance effect, such that the abundance-sensitive line ratio of [OII](λ3727) + [OIII] relative to Hβ also exhibits a clear radial gradient of about one dex. Using the [OII]+[OIII]/Hβ line ratio plus empirical abundance calibrations based on high S/N optical spectroscopy of a few bright HII regions (Shields and Searle 1978; Torres-Peimbert *et al.* 1989), several investigators have obtained strong O/H abundance gradients in M101 (Rayo *et al.* 1982; McCall *et al.* 1985; Evans 1986; Torres-Peimbert *et al.* 1989), thus confirming the earlier interpretations (Searle 1971; Smith 1975). The sense of the gradient is that the O/H abundance *decreases* with galactocentric radius, spanning about 1.3 dex across the measured disk (see Figure 3–2).

However, the abundance gradient does not completely explain the observed "excitation" gradient whose range is considerably higher. Observed gradients in the [OIII]/[OII] line ratio and the Hβ line-to-continuum ratio (*i.e.* the Hβ equivalent width) could be indicating that the ionizing radiation field of the underlying star clusters is changing along with the abundance. Shields and Tinsley (1976), noting that Searle's Hβ equivalent widths increase with radius, interpreted this behavior in terms of an increase in the upper mass limit of the ionizing clusters. Citing Kahn's (1974) theory of dust-inhibited protostellar accretion, they proposed that the upper mass limit is highest in regions of low metal abundance, because the relative absence of dust grains reduces the opacity of the infalling material, thus encouraging unimpeded accretion and higher-mass protostars. Abundance-sensitive IMFs have since become commonplace in discussions of extragalactic HII regions and HII galaxies (Viallefond *et al.* 1982; Viallefond 1985; Terlevich and Melnick 1985; Campbell *et al.* 1987; Campbell 1988; Vilchez and Pagel 1988). However, in M101, the correlation between abundance and IMF variations is still based on only ~10 points (see Figure 3–2), and so merits a more detailed re-evaluation.

3.7.2 *The HII Region Sample*

Identification of HII regions from the Hα images was conducted interactively using a video display and cursor-controlled readout. Different contrast and intensity levels were displayed, beginning at the high end and working to lower intensity levels. In this way, resolution of complexes into individual HII regions could be optimized. Radial profiles of Hα surface brightness were then plotted for each HII region (see Figure 3–13), from which emission centroids, blended and unblended radii, and background levels were determined. A total of 389 HII regions were identified in this manner. Because identifications were made "by eye," they do not comprise a complete magnitude-limited sample. However, the resulting Hα luminosity function indicates, that completeness probably sets in at luminosity levels corresponding to ~3 Orion nebulae (*i.e.* $L(H\alpha) \geq 10^{37.5}$ $erg\ s^{-1}$; see Section 3.7.4). This completeness limit is similar to those obtained for M81, M33, and the Milky Way (*cf.* Smith and Kennicutt 1989) but about 1 dex higher than the limits obtained in the LMC and SMC (*cf.* Kennicutt and Hodge 1986).

Figures 3–14, 3–15, and 3–16 show the resulting identifications plotted in the plane of the sky, and Table 3-4 gives the listing of HII region positions.

3.7.3 *HII Region Flux Measurements*

To measure the fluxes of the HII regions and their underlying stellar clusters, synthetic apertures were tailored to each HII region according to its centroid position and size. In the absence of blending (see next section for further discussion), the tailored radius is background limited and thus is approximately equivalent to an isophotal radius, where the limiting Hα surface brightness is $I_{lim}(H\alpha) = (6.4 \pm 5.5) \times 10^{-17}$ $erg\ cm^{-2}\ s^{-1}$. For the "typical" HII region, this background contributes about 25 percent to the total flux; for bright HII regions such as S3 and S4, the background contributes about 5 percent. The high dispersion about the background mean is caused by the spatial variations in the diffuse ionized component across the galaxy. Since the level of the diffuse component increases near HII region complexes, the ionization of the gas must be at least partially related to the hot stars in the HII regions. Therefore, I have decided to include the "diffuse" background component as part of the total measured Hα flux from each HII region.

Aperture-tailored photometry was conducted on both the Hα and red-continuum images. To obtain fluxes of the young stellar clusters *without contamination from the older disk starlight*, background continuum levels were determined and subtracted from each cluster flux. This was done via three different techniques...

• By measuring the mode of the surface brightness in concentric annulli — each annulus being 10 pixels (8 arcsec) wide and separated from the next by 5 pixels (4 arcsec). The resulting axisymmetric profile of surface brightness was then used for the background subtraction. Though crude (it isolates the arm enhancements as well as the cluster light), this method is at least reproducible.

• By "smoothing" the red-continuum image with a median filter whose $16'' \times 16''$ dimension is approximately twice the size of a typical HII region, and then subtracting this smoothed image from the original image. This technique produced residual images with prominent cluster contrast and with the background levels flat and centered at zero intensity. It also enhanced the visibility of the dust lanes responsible for obscuring many of the clusters. Such revealing and easily reproducible results have made the median filtration approach my "technique of choice" for isolating all but the largest clusters.

• By plotting the radial distribution of continuum surface brightness for each and every HII region (see Figure 3–13), by setting the continuum background level from inspection of each radial plot, and by subtracting this level from the total cluster flux. Any creeping subjective bias in the determination of the background level was nullified by alternately plotting inner and outer-galaxy HII regions. The advantage of this technique is that it is individualized, thereby handling the biggest HII regions better than the median filtration technique does. Its big disadvantage is that it involves some subjectivity in setting the background level and is therefore not reproducible.

Of the 389 HII regions originally studied, 385 were sufficiently unvignetted to have their fluxes measured. Of them, only 102 had red-continuum flux densities that were more than 5-sigma above the dispersion in the ambient continuum.

Inspection of the residual continuum image revealed that discrete dust lanes and clouds are responsible for obscuring many of the other continuum sources.

3.7.4 *The Effects of Blending*

Of the 385 measured HII regions, 23 percent are blended at some level with neighboring HII regions. Such blending involves the common overlapping of HII region "haloes" which can extend significantly beyond the brighter and more discrete "cores." In the present imagery, the HII regions and their underlying clusters do not share a characteristic size or structure. Therefore, I could not fit a single "point spread function" to the discrete cores of the crowded HII regions and so deduce the total integrated fluxes. Instead, I have chosen to tailor the photometric apertures to the *unblended* diameters of the crowded HII regions, thereby minimizing the contaminating effects of blending but introducing errors in the form of underestimated total fluxes.

Table 3-4 lists the total (background-limited) and unblended radii that I measure from radial plots of the Hα emission from each HII region. Figure 3–17 shows the frequency distribution of HII region sizes for both the "total" and "unblended" cases. The "total" size distribution can be fit by an exponential with a scalelength of about 2.5 arcsec, corresponding to 60 pc at a distance of 4.8 Mpc or about 93 $(H_o/50)^{-1}$ pc (for $v_o = 372$ km s^{-1}). This latter value is consistent with the scalelengths obtained in a sample of Sc galaxies, where the radii were similarly background-limited, and where the distances were based on the galaxies' recession velocities and $H_o = 50$ km s^{-1} Mpc^{-1} (Hodge 1987).

Figure 3–17 also shows a relative underabundance of large HII regions in the "unblended" distribution. This is due to the greater truncations suffered by the larger HII regions in order to avoid blending. The mean truncation for the entire sample of 385 HII regions is $\langle r_{unb}/r_{tot}\rangle = 0.9 \pm 0.2$, whereas the mean truncation for the large HII regions ($r_{tot} > 5''$) is $\langle r_{unb}/r_{tot}\rangle = 0.8 \pm 0.2$. The greatest truncation exists for the large HII regions in the outer galaxy ($R > 5kpc$), where $\langle r_{unb}/r_{tot}\rangle = 0.7 \pm 0.3$ compared to 0.8 ± 0.2 for the large inner-galaxy HII regions. No galactocentric variation in truncation is evident for the small HII regions.

These truncations yield underestimated Hα fluxes and Hα equivalent widths, the magnitude of which can be estimated from the following "curve-of-growth" analysis.

Figure 3–13 presents radial distributions of the Hα and red-continuum intensities for 4 isolated HII regions. These particular HII regions were chosen, because they span the range of intensities — and hence signal-to-noise ratios — that exist among the 385 HII regions. Figure 3–18 presents the corresponding "curves of growth" for the Hα flux, background-subtracted red-continuum flux density, and Hα equivalent width. These curves indicate that a mean truncation of $r/r_o = 0.9$ yields Hα fluxes and Hα equivalent widths that are underestimated by approximately 5 - 15 percent. The higher truncations suffered by the larger and brighter HII regions of the outer galaxy produce 10 - 20 percent underestimations in the Hα fluxes and cluster equivalent widths. Therefore the following photometric results should be accurate to within 30 percent (including the photometric uncertainties described in Section 3.4) and mutually consistent to within 15 percent.

3.7.5 *Hα and Red-Continuum Luminosities*

The photometric properties of all 385 HII regions are listed in Table 3-5, where the Hα flux, total Hα equivalent width, cluster Hα equivalent width, and corresponding signal-to-noise ratios are tabulated. Figure 3–19 shows the frequency distribution of Hα luminosities for the inner and outer HII regions of M101. The binned counts are also listed in Table 3-6. The highest bin in the outer regions is represented by the core of the NGC 5461 complex. Unresolved at 1"-2" resolution, this supergiant HII region is as bright at Hα as ~700 Orion nebulae *before* correcting for extinction. Even if one ignores this exceptional region, one can still discern differences between the outer and inner luminosity functions. In particular, the slope at high luminosities appears to be flatter for the outer-galaxy HII regions. This difference is shown more clearly in Figure 3–20, where the cumulative luminosity functions are compared.

To test the apparent differences in the inner and outer luminosity functions, a chi-square test was performed on the binned counts beyond $L(H\alpha) = 10^{37.25}$ erg s^{-1}. After the outer-galaxy distribution was normalized to that of the inner galaxy (according to the ratio of total counts beyond L(Hα) = $10^{37.25}$ erg s^{-1}), the chi-square test gave a reduced chi-square of $\chi_\nu = 2.9$ for 9 degrees of freedom and hence a probability of 0.003 that the two distributions could be generated from the same parent distribution. Chi-square testing of the cumulative luminosity functions gave less than a 0.001 probability for the 2 distributions being drawn from the same parent distribution. Therefore, the inner and outer luminosity functions *are* significantly different at high luminosity. Least-squares fits to the high-luminosity distributions, where each point is weighted according to its statistical uncertainty, give a change in slope of 0.4 ± 0.1. The sense is to favor a greater proportion of high-luminosity HII regions in the outer regions. This is intuitively obvious upon visual examination of the 2 observed fields: the big HII region *complexes* are all located beyond 5 kpc from the nucleus. However, the luminosity functions plotted here are not based on photometry of the complexes as a whole but on photometry of their resolved subcomponent HII regions. That the luminosity functions continue to differ in shape indicates *a modest but real disparity in the types of individual HII regions being formed.*

The differential and cumulative luminosity functions for the *combined* fields are shown in Figure 3–21. The high-luminosity HII regions (L(Hα) $\geq 10^{37.5}$ erg s^{-1}) from the combined fields are distributed according to a power law of $N(L) \propto L^{-2.1\pm0.1}$ (after correction for the logarithmic binning). This is similar to the power laws determined in NGC 628 (Kennicutt and Hodge 1980), M83 (Rumstay and Kaufman 1983), and the Magellanic Clouds (Kennicutt and Hodge 1980), but is significantly flatter than the power law determined in the earlier-type galaxy M81 (Kaufman *et al.* 1987), where a slope of -3.0 was obtained.

Figure 3–22 shows the galactocentric distribution of Hα and red continuum luminosities (without any extinction correction) for the 102 HII regions with detectable red continua ($S/N \geq 5.0$). The Hα luminosities of this smaller sample are higher, on average, beyond 5 kpc of the nucleus — the ratio of the outer and inner-galaxy mean luminosities yielding

$$\frac{\langle L_{H\alpha}(R > 5kpc)\rangle}{\langle L_{H\alpha}(R < 5kpc)\rangle} = 3.25 \pm 1.87, \qquad (3-31)$$

where the uncertainty in the ratio is based on a propagation of the standard errors in the respective averages. The red-continuum luminosities show less of a systematic variation with galactocentric radius, giving

$$\frac{\langle L_\lambda(R > 5kpc)\rangle}{\langle L_\lambda(R < 5kpc)\rangle} = 1.78 \pm 1.24. \qquad (3-32)$$

Because the red continuum flux of ionizing clusters mostly traces main sequence stars of type B-F, the radial invariance of the continuum fluxes could be indicating a similar invariance in the intermediate-mass stellar populations. Such behavior suggests that the main sequences of the ionizing clusters are populated with similar amounts of intermediate-mass stars but have upper-mass limits that are sensitive to position in the galaxy. This will be pursued further in the next section.

3.7.6 *Hα Equivalent Widths*

The relationship between the Hα and red-continuum luminosities is shown in Figure 3–23. As anticipated, the two luminosities are correlated, though the form of the correlation is more complicated than can be fit by a simple linear or power law. This correlation can be further explored by investigating the line-to-continuum ratio (*i.e.* the Hα equivalent width) and the potential influences upon it. The equivalent width is an especially useful quantity, because it provides a crude index of the ionizing cluster's effective temperature and hence of the cluster's main-sequence population at the high mass end.

Figure 3–24 shows the galactocentric distribution of Hα equivalent widths that results, when the total red-continuum flux density is used, *i.e.* without prior subtraction of the ambient disk light. Gradients in such distributions have been cited as evidence for IMF variations (Kennicutt, Keel, and Blaha 1989). Although a strong gradient is evident here, it probably has very little to do with variations in the ionizing stellar populations. Instead, it demonstrates the strong radial increase in the ratio of current-epoch massive star formation to past-averaged star formation that is present in disk galaxies. This was previously — and more convincingly — demonstrated in Figure 3–8(b), where annular-averaged Hα and red-continuum fluxes were used for the equivalent width calculations.

Figure 3–25 shows the galactocentric distributions of Hα equivalent widths that result after applying the 3 different techniques for isolating the cluster continuum emission. Although there are some differences between the 3 distributions, they are all much flatter than that obtained without having first isolated the cluster light in some manner. Instead of a 2 dex dynamic range between 10 and 1000 Angstroms, the variations in EW(Hα) are now confined mostly to a 1 dex range between 100 and 1000 Angstroms. Though higher on average, these values are still lower than the range of 2000 to 4000 Angstroms that ZAMS cluster models predict in the absence of dust (A. Campbell, private communication). As developed in the next section, the presence of UV absorbing dust could be responsible for producing the lower EWs.

The best isolation of the cluster emission was obtained from the median filtration and individual plotting techniques. The resulting 2 galactocentric distributions both show proportionately higher equivalent widths beyond the inner 5 kpc. From the median filtration method, I find that inside of R = 5 kpc, the mean equivalent width is 640 Å with a standard deviation of 299 Å and standard error of 34 Å; outside of R = 5 kpc, the mean equivalent width is higher at 941 Å with a standard deviation of 366 Å and a standard error of 73 Å. In other words, the radial variation in equivalent widths is roughly of similar magnitude as the propagated standard deviations and about 3.4 times the propagated standard errors; *i.e.*

$$\frac{EW(R > 5\ kpc)}{EW(R < 5\ kpc)} = 1.47 \pm 0.14, \qquad (3-32)$$

where the standard errors have been used to calculate the uncertainty.

3.7.7 *Selection and Obscuration Effects*

In the previous section, I presented evidence for a decrease in the mean Hα equivalent width for those HII regions within 5 kpc of the nucleus. Several effects — aside from changes in the ionizing stellar populations — could be responsible for reducing the Hα equivalent widths in the inner galaxy. Selection effects, in particular, could be biasing the data as observed. Because the plotted samples have been selected according to the signal-to-noise ratio of the red cluster emission, it is possible that higher luminosity clusters were selected in the brighter inner galaxy, where the cluster *vs.* disk contrast would be lower. Figure 3–22 shows that this is not the case, however. The galactocentric distribution of red luminosities is, instead, relatively flat (see previous section). Therefore, the primary selection criterion does not appear to influence the Hα equivalent widths and their galactocentric distribution.

Varying amounts of nebular dust could also be responsible for altering the Hα equivalent widths as observed. To investigate this possibility, one can consider two extreme idealizations. In the first, the stars, gas, and entrained dust are all uniformly distributed. The Hα flux from the ionized gas and the red continuum flux from the stars should then be subject to the same degrees of extinction. Therefore, the line-to-continuum ratio (*i.e.* the Hα equivalent width) should remain unaffected. In the present situation, however, the red-continuum fluxes are based on images taken through an R-band filter, whose transmissivity peaks 523 Å shortward of the Hα filter's peak. Therefore, the *measured* red-continuum fluxes could be subject to more obscuration than the Hα fluxes. For $1/\lambda$-type extinction, the extinction coefficients are related by

$$k(\lambda 6563)/k(\lambda 6040) \approx 0.92, \qquad (3-34)$$

and the equivalent widths are altered according to

$$\frac{EW(H\alpha)}{EW_{\circ}(H\alpha)} \approx 10^{0.31 A_v}. \qquad (3-35)$$

For $A_v \leq 3$, this amounts to ≤ 19 percent changes in the EWs. If the dust-to-gas ratio in M101 follows the galactocentric profile of O/H (Viallefond *et al.* 1982), one might expect the inner galaxy to be dustier, and therefore the equivalent widths to be enhanced. *The opposite effect is observed, however!*

In the second idealization, the stars are clustered at the backside of the nebula (as in the "champagne" model of HII regions [Tenorio-Tagle 1982]). In this more "segregated" scenario, the starlight is attenuated by the foreground nebular dust according to

$$\frac{f(\lambda 6563)}{f_o(\lambda 6563)} = e^{-\tau}, \qquad (3-36)$$

where the optical depth τ of dust at 6563 Å is proportional to the column density N_{HII} of foreground gas and to the dust-to-gas ratio χ_g. By contrast, the Hα emission from the nebula of ionized hydrogen and entrained dust is attenuated according to

$$\frac{f(H\alpha)}{f_o(H\alpha)} = \frac{(1-e^{-\tau})}{\tau}. \qquad (3-37)$$

The ratio of these two formulations gives the dependence of the Hα equivalent width on the optical depth, *i.e.*

$$\frac{EW(H\alpha)}{EW_o(H\alpha)} = \frac{(1-e^{-\tau})}{\tau e^{-\tau}}. \qquad (3-38)$$

This dependence has been plotted in Figure 3–26, which shows a non-linear *enhancement* in the EW(Hα) as τ increases. If the inner galaxy is dustier than the outer galaxy, one would expect τ to be much higher in the inner galaxy, and therefore the equivalent widths to be enhanced. *The opposite effect is once again observed!*

An alternate possibility is that the entrained dust is absorbing a significant fraction of the ionizing photons ($\lambda < 912$ Å), thereby reducing the ionization rate and hence the Hα luminosity. This could also explain the fact that the highest observed Hα equivalent widths are about 1500 Å, whereas theoretical models of the line and continuum emission from dust-free HII regions predict values of 2000 Å to 4000 Å (A. Campbell, private communication). By reducing the volume of the "Stromgren spheres," dustier nebulae in the inner galaxy could be reducing the equivalent widths as observed. Following the treatment of Spitzer (1978), a mean gas density of $n_H \approx 25\ cm^{-3}$ (Kennicutt 1984) and a standard gas-to-dust ratio of 200 will yield a reduction in the Stromgren sphere radius by about 0.80 ± 0.05 and thus a reduction in the total amount of ionized hydrogen by $(0.80 \pm 0.05)^3 \approx 0.5 \pm 0.1$. The H$\alpha$ luminosity and equivalent width would be reduced by approximately the same factor. Using this to correct the observed EWs would yield values in the range predicted by the theoretical models. Here, an enhancement in the dust-to-gas ratio in the inner galaxy would lead to lower EWs, as is observed.

To explore the possible effects of dust on the line and continuum fluxes, I have plotted the galactocentric distributions of the nebular extinction (culled from the literature) and the cluster color (λ6563 - λ8380) (see Figure 3–27). Here, I am assuming that the cluster color is dominated by the reddening effects of dust rather than by the young stellar population, itself. Spectrophotometric models of ZAMS and evolved ionizing clusters indicate that this sort of assumption is valid for those clusters redder than $(\lambda6563 - \lambda8380) = 0.5$ (Jacoby *et al.* 1984; Terlevich and Melnick 1985). For example, the reddest cluster in Terlevich and Melnick's models has an age of 3 Myr, an IMF slope of $\alpha = 3.0$, $M_l = 0.1\ M_\odot$, and $M_u = 40\ M_\odot$. These parameters give a $V - K$ color of 0.6 which corresponds to a $(\lambda6563 - \lambda8380)$ color of 0.35 (Johnson 1966), as would be produced by a single G5V star. Jacoby *et al.* (1984) have used their stellar spectra library to synthesize the spectrum of a 10 Myr-old cluster with a Miller-Scalo IMF and $M_u = 50\ M_\odot$. The resulting spectral energy distribution, when extrapolated past 7500 Å, gives $(\lambda6563 - \lambda8380) = 0.38$, or the equivalent of a G8V star. Colors redder than 0.5 would correspond to even older clusters which no longer contain any ZAMS stars capable of ionizing a detectable HII region. Therefore, the significantly redder colors in the ionizing clusters that are considered here are most likely due to reddening by dust.

Neither the color nor the nebular extinction in Figure 3–27 show any systematic galactocentric behavior, though the large scatter and poor sampling could be masking something. If the dust/gas ratio follows the O/H ratio, then the nebular extinction should increase toward the inner galaxy — where the dust/gas ratio should be enhanced — and the color should redden accordingly. Neither of these effects are apparent from the plots, however, thus indicating that the O/H ratio, the nebular extinction, and the reddening are by-and-large uncorrelated.

I have also plotted the color against the Hα equivalent width (see Figure 3–28). The lack of any correlation between these two variables further indicates that the equivalent widths are not very sensitive to the degree of reddening. Lastly, I have used the colors to sort the data into "reddened" and "unreddened" bins. Ignoring all regions with colors redder than $(\lambda6563 - \lambda8380) = 0.5$, I have replotted the galactocentric distribution of Hα equivalent widths. Figure 3–29 shows that the "unreddened" sample of 41 clusters continues to show depressed equivalent widths in the inner galaxy: Within 5 kpc $\langle EW(H\alpha)\rangle = 650$ Å $\pm$ 51

Å (std. error), whereas beyond 5 kpc $\langle EW(H\alpha)\rangle = 1021 \pm 90$ Å. Therefore, the observed radial variation in EW(Hα) appears to be an effect that exists with or without large amounts of reddening.

Finally, the depressed Hα equivalent widths inside of R = 5 kpc could be tracing enhancements in the absorption of UV photons by the atmospheres of the hot stars themselves. If line-blanketing effects at wavelengths shortward of 912 Å are greater in the atmospheres of metal-rich stars than in their metal-poor counterparts, then the Hα equivalent widths will naturally be lower in the metal-rich regions. LTE and non-LTE computations by Terlevich and Melnick (1985) have shown that the total ionizing luminosity of any star more massive than 10 $M_\odot$ is independent ($\pm 10\%$) of its metallicity; at lower masses, the metal-rich stars ($Z/Z_\odot = 1$) show ~2 times lower ionizing luminosities than their metal-poor equivalents ($Z/Z_\odot = 0.02$). Since the HII regions considered here are ionized primarily by the higher-mass stars ($M \geq 30\ M_\odot$), the 50% change in mean Hα equivalent widths cannot be attributed to stellar atmospheres of varying metallicity.

To summarize, several selection and obscuration effects on the Hα equivalent widths have been considered. Only one of these can account for the depressed EWs within 5 kpc of the nucleus. The absorption of ionizing photons by dust could conceivably be greater in the inner galaxy, where the dust-to-gas ratio is expected to be higher. The resulting shrinkage of the "Stromgren spheres" would then yield lower Hα luminosities and equivalent widths. However, the observed lack of any radial variation in nebular extinction or cluster reddening, plus the lack of any correlation between the cluster reddening and the Hα equivalent width indicate that the observed variations in EW(Hα) are not produced by dust.

3.7.8 *IMF vs. Aging Effects on the Hα Equivalent Widths*

In the previous section, possible selection and obscuration effects on the Hα equivalent widths were considered. None seemed able to account for the observed decrease in EW(Hα) within 5 kpc of the nucleus. In this section, I develop a simple relation between the Hα equivalent width and the upper mass limit of the ionizing stellar population. According to this relation, the radial variation in

EW(Hα) indicates that significant differences in the upper mass limit exist across the galaxy. IMF *vs.* aging effects on the upper mass limit are then discussed.

The most simplifying assumption is to let the ionizing clusters consist solely of zero-age main-sequence stars. The effects of evolution are restricted to truncating the upper mass limit of the main sequence. This simplification neglects the contribution of supergiant and WR stars which, though short-lived relative to the hydrogen-burning stars of equivalent mass (Maeder and Meynet 1988), can contribute 15 - 25 pe· ·nt to the bolometric luminosity of the cluster (Renzini and Buzzoni 1986). This simplification is therefore most relevant to those clusters with the highest equivalent widths for their luminosity and galactocentric radius (*i.e.* the least evolved clusters). Using the ZAMS assumption, one can model the emerging Hα luminosity from an ionizing cluster as an IMF-weighted summation of the ionizing luminosities from the individual ZAMS stars —

$$L_{H\alpha}(cl) \propto N_* \langle N_i(M) \rangle \propto N_* \int_{M_l}^{M_u} M^{-\alpha} N_i(M)\, dM. \qquad (3-39)$$

where N_* is the number of stars in the cluster, N_i is the ionizing luminosity in photons/sec. M_l and M_u are the lower and upper stellar mass limits, and α is the power of the initial mass spectrum ($\alpha = 2.35$ for a Salpeter IMF). For stars more massive than 30 $M_\odot$, the mass-ionizing luminosity relationship goes as $N_i(M) \approx 3.8 \times 10^{42}\ M^{3.9}$ (see Appendix A), thus leading to

$$L_{H\alpha}(cl) \propto {M_u}^{4.9-\alpha} - {M_l}^{4.9-\alpha}. \qquad (3-40)$$

The red-continuum luminosity from the cluster involves a similar IMF-weighted summation, where

$$L_R(cl) = N_* \langle L_R(M) \rangle \propto N_* \int_{M_l}^{M_u} M^{-\alpha} L_R(M)\, dM. \qquad (3-41)$$

Using stellar masses and absolute visual magnitudes corresponding to the standard main sequence (Allen 1973) plus their corresponding $V-R$ colors (Johnson 1966), one can readily derive a mass-red luminosity relationship of $L_R(M) \approx 1.7 \times 10^{30}\ M^{2.3}$ (where $M \geq 1\ M_\odot$). The integrated red-continuum luminosity from the cluster is then of the form

$$L_R(cl) \propto M_u^{3.3-\alpha} - M_l^{3.3-\alpha}. \qquad (3-42)$$

For IMFs with $\alpha < 3.3$ and $M_l \ll M_u$, the integrated luminosities can be approximated by

$$L_{H\alpha}(cl) \propto M_u^{4.9-\alpha}, \qquad (3-43)$$

and

$$L_B(cl) \propto M_u^{3.3-\alpha}, \qquad (3-44)$$

so that

$$EW_*(H\alpha) \propto M_u^{1.6}, \qquad (3-45)$$

independent of the IMF slope. According to this relation, the observed decrease by 1.5 in the mean equivalent width of the inner-galaxy HII regions would imply a decrease by 1.3 in the mean upper mass limit.

It can be shown that the inclusion of nebular continuum emission along with UV-absorbing nebular dust will change the above relationship according to

$$EW(H\alpha)^{-1} = \beta EW_*(H\alpha)^{-1} + EW_{neb}(H\alpha)^{-1}, \qquad (3-46)$$

where β is the fraction of ionizing photons that is not absorbed by the dust, and where EW_{neb} is the line-to-continuum ratio that refers to the nebular continuum. For electron temperatures near 10^4 K, $EW_{neb}(H\alpha) \approx 5500$ Å(see Appendix B). And for mean gas densities of 10^{-3} cm^{-3} and gas-to-dust ratios of 200, $\beta \approx 0.5$ (see Section 3.7.7). The resulting relationship between the Hα equivalent width and the upper stellar mass limit can be approximated by

$$EW(H\alpha) \propto M_u^{1.1\pm0.3}. \qquad (3-47)$$

The observed decrease in mean equivalent width should therefore correspond to a decrease by 1.3 to 1.7 in the mean upper mass limit. A more thorough treatment of the population and dust-dependent Hα equivalent widths is plotted in Figure 3-30. Here, the $EW_*(H\alpha)$ curve is based on the results of A. Campbell (private communication) which were derived from the population synthesis program described in Terlevich and Melnick (1985). Similar dependences between $EW(H\alpha)$ and M_u are obtained from this more sophisticated treatment.

The inferred changes in the upper stellar mass limit can arise from changes in the cluster IMF or from evolution of the highest mass stars off the main sequence. The former possibility will be discussed more extensively in the Discussion section. The effects of cluster age are considered here. Main sequence turn-off ages for 120 $M_\odot$, 60 $M_\odot$, 25 $M_\odot$ and 15 $M_\odot$ stars are estimated to be 1.5, 2.5, 5.0, and 9.0 Myr respectively (Maeder and Meynet 1988). Therefore, a few million years of evolution can significantly truncate a cluster's upper main sequence. This can be quantified using Maeder and Meynet's power-law formulation for the turn-off age,

$$log\ \tau = -0.86\ log\ M/M_\odot + 8.06, \qquad (3-48)$$

which gives

$$M_u = (1.15 \times 10^8/\tau)^{1.16}. \qquad (3-49)$$

The time-evolution of the equivalent width is then

$$EW(H\alpha)/EW_o(H\alpha) = M_{u_o}^{-1.0} \left(\frac{1.15 \times 10^8}{\tau}\right)^{1.16}. \qquad (3-50)$$

For $M_{u_o} = 100\ M_\odot$, the EW will decline to 0.7 of its initial value in 3 Myr and to 0.4 of its initial value in 5 Myr. From this simple analysis, one can see that variations in cluster age can significantly modify the Hα equivalent widths.

There are two basic reasons for thinking that the radial variation in Hα equivalent widths *is not* an evolutionary effect. First, a significant number of the HII regions in the observed sample are probably un-evolved. Given a minimum turnoff age of 1.5 Myr (corresponding to a 120 $M_\odot$ star) and a maximum turnoff age of ionizing significance of 5 Myr (corresponding to a 25 $M_\odot$ star), the minimum fraction of un-evolved clusters would be 0.3. For the "unreddened" sample of 41 clusters, this minimum fraction represents 9 HII regions within 5 kpc of the nucleus and 4 HII regions between 5 and 10 kpc from the nucleus — which is barely enough to trace the upper envelope of the galactocentric distribution. The downturn in the upper-envelope EWs at low galactocentric radii is therefore worth noting (see Figure 3–29).

The second reason against an age-based radial variation in Hα equivalent widths is the difficulty in devising a scheme for coherently sequencing the cluster ages as a function of galactocentric radius. If cluster age was the dominant factor, then the inner galaxy would have to contain a greater proportion of older clusters. Such a small yet global difference in cluster ages ($\Delta\tau \sim 3\ Myr$) is difficult to create in the disk of a galaxy such as M101, because the relevant timescales for star formation (*e.g.* density-wave propagation time, molecular-cloud lifetime, etc.) are all much longer ($\tau \sim 100$ Myr). Indeed, incrementing the mean age of the inner-galaxy clusters by a few Myr would be as ad hoc as requiring the rainstorms in the Pacific Northwest to begin 2 hours earlier than those over the Great Lakes!

These two reasons — the significant presence of un-evolved clusters and the ad hoc quality of radially sequencing the cluster ages — argue against an age-based decrease in the inner-galaxy equivalent widths and for a decrease that follows reductions in the *initial* upper mass limit.

3.7.9 *Galactocentric Comparisons*

As discussed in the Introduction, several investigators have found a strong O/H abundance gradient in the disk of M101. Moreover, the radial gradient has been linked to similar variations in the Hβ equivalent width and other spectral indices of the high-mass IMF (*e.g.* [OIII]/Hβ and [OIII]/[OII] line ratios). To further investigate and test these relations, I have expanded my galactocentric distribution of Hα equivalent widths to include spectroscopic measurements of HII regions beyond 10 kpc of the nucleus (see Figure 3–31). This "composite" distribution covers a greater range of galactocentric distances and hence can be better compared with the wide-ranging distributions of the O/H abundance (see Figure 3–2) and of the various kinematic and dynamical properties (*e.g.* shear rate and tidal stress) that have been plotted (see Figure 3–1). It should be noted that the spectroscopic measurements of EW(Hα) involve entrance apertures of differing sizes and shapes. The work of Searle (1971) used an aperture most similar to that of the present study and thus should be the best matched. Also, Searle made some effort to estimate and subtract background continuum levels from the measured cluster flux densities, as has been done in the present study. *The resulting galactocentric distribution of equivalent widths is notable for its relative flatness between 5 and 20 kpc from the nucleus and for its decline at smaller* *galactocentric radii.* This sort of behavior is qualitatively very different from that shown by the O/H abundances. Instead of a relatively flat galactocentric distribution, the O/H abundances decrease *monotonically* by ~1 dex from 2 to 17 kpc. Therefore, the case for an abundance-sensitive IMF, as traced by the Hα equivalent width, is simply not seen.

Other galactocentric distributions come closer to resembling that of the Hα equivalent widths. In particular, the profiles of the differential rotation $d\Omega/dR$, the shear rate A, and the tidal stress T are all relatively flat and weak beyond 5 kpc of the nucleus but become increasing stronger at smaller galactocentric radii (see Figure 3–1. The sense of the resemblance is to have fewer high-temperature clusters forming in regions, where the shear rate and tidal stress are strong. This relationship, *if significant*, can be understood, if high-mass star formation depends on the formation and sustenance of massive gas clouds (Larson 1982; Waller *et al.* 1987; Scoville *et al.* 1987). Because shear flows and tidal stresses can hinder the formation of massive clouds (Toomre 1966; Stark and Blitz 1978; Blitz and Glassgold 1982; Elmegreen 1979; Larson 1987; and Binney and Tremaine 1987), they can reduce the numbers of high-mass stars that would otherwise be created inside the large clouds. The present data leaves open the possibility of an IMF that is sensitive to the dynamics in the disk. However, more stringent tests will have to be conducted, before such a sensitivity can be verified.

3.7.10 *A Possible Starbirth Intensity - IMF Connection?*

Another way to explore the high-mass IMFs of the ionizing clusters is to construct "temperature-luminosity" diagrams, where the Hα equivalent width is used as an index of the cluster's "effective temperature." Figure 3–32 shows such diagrams for the sample of 102 HII regions with detectable red continua. The $EW - L(H\alpha)$ diagram, in particular, shows a strong correlation over 1 dex in L(Hα). Elimination of all "reddened" clusters from the sample has a neglible effect on this correlation (see Figure 3–33), thus demonstrating that dust is not responsible for the trend. For Hα luminosities below $10^{38.6}$ $erg\ s^{-1}$, the correlation can be approximated by the following power law

$$logL(H\alpha) = (33.10 \pm 1.44) + (1.80 \pm 0.05)\, logEW(H\alpha), \qquad (3-51)$$

where the correlation coefficient of 0.79 yields for the 86 points a correlation significance level which exceeds 0.999. By contrast, the red continuum luminosity is weakly correlated with EW(Hα). These "temperature-luminosity" diagrams can be understood in terms of an intensity-dependent IMF, such that the brighter HII regions contain the hotter, more massive stars (Larson 1987). According to this interpretation, the correlation seen in the EW(Hα)-L(Hα) plane corresponds to a sequence of ever higher stellar masses and ionizing luminosities being added to the upper main sequence. An alternative viewpoint is that the sequence traces the *removal* of high-mass stars from the main sequence as each cluster evolves. Above an Hα luminosity of $10^{38.6}$ $erg\ s^{-1}$, the correlation appears to break down, as if maximum cluster temperatures have been reached. The well-correlated points below this cutoff provide a constraint on the high-mass IMF which can be modeled in the following way. Recalling from Section 3.7.6 that $L_{H\alpha}(cl) \propto M_u^{4.9-\alpha}$, and $EW(H\alpha) \propto M_u^{1.1\pm0.3}$, we can formulate

$$L_{H\alpha}(cl) \propto EW(H\alpha)^{(4.9-\alpha)/(1.1\pm0.3)}. \qquad (3-52)$$

The observed correlation between L(Hα) and EW(Hα) implies an IMF with $\alpha \approx 2.9 \pm 0.3$, thus resembling the high-mass regime of the standard Miller-Scalo IMF (Miller and Scalo 1979). Similar results are obtained from examinations of the observed L_λ(6563 Å)-L(Hα) and the weaker L_λ(6563 Å)-EW(Hα) correlations. According to Eq. 3-51, the observed one-dex range in Hα luminosities corresponds to a factor of 3.6 variation in the upper mass limit. This variation includes possible evolutionary effects, however, and should not be confused with the factor of 1.3 to 1.7 variation in the *initial* upper mass limit inferred from the radial variation in the mean EWs.

3.7.11 *Discussion*

Although the effects of extinction and age cannot be completely discounted, changes in the *initial* upper mass limit of the ionizing clusters seem to best explain the observed galactocentric variation in Hα equivalent widths. Assuming that this is so, one can imagine the upper-mass limit of the IMF being inherently lower, on average, within 5 kpc of the nucleus, or the maximum *realizeable* mass being constrained to be lower. This latter possibility can occur by decreasing the cluster mass and/or decreasing the lower mass limit.

Reddish (1978) has shown that, due to low number statistics at the top end of the IMF, the highest stellar mass in a cluster can be proportional to the cluster mass. His treatment allows the *theoretical* upper mass limit to be made infinite and then asks what the *realizeable* mass limit is, if a Salpeter IMF is operating. Generalizing his treatment to other IMF slopes and allowing for a finite theoretical limit yields

$$M_{max} = \left(M_u^{1-\alpha} - \left(\frac{1-\alpha}{2-\alpha}\right) \frac{(M_u^{2-\alpha} - M_l^{2-\alpha})}{M_{cl}} \right)^{1/(1-\alpha)} . \qquad (3-51)$$

where M_{max} is the realizeable stellar mass limit (the probability of having a *single* star of this mass or greater being equal to unity), M_u is the theoretical upper mass limit that can be achieved before radiation pressure and pulsational instabilities become overwhelming, M_l is the lower mass limit, M_{cl} is the total mass of the cluster, and α is the IMF slope. Different combinations of these parameters are listed in Table 3-7, where the theoretical upper limit for a quasi-stable star is set at 200 $M_\odot$ (Humphreys and Aaronson 1987). For example, by setting $\alpha = 2.5$ and letting $M_l = 0.1$, a 10^3 $M_\odot$ cluster would have $M_{max} = 22$ $M_\odot$, while a 10^6 $M_\odot$ cluster would have $M_{max} = 197$ $M_\odot$. Steeper IMF slopes would result in even lower realizeable masses. Such a dependence of the upper main sequence on cluster mass would imply that even the largest star forming regions (*e.g.* 30 Doradus and NGC 5461) could be constrained by small number statistics to forming stars below a certain mass threshold. A comparison of the resolved stellar populations in 30 Doradus and the Orion nebula would seem to support this scenario: the 30 Doradus cluster has a total mass of $\sim 10^5$ $M_\odot$ (Kennicutt and Chu 1988) with an upper mass limit exceeding 120 $M_\odot$ (Melnick 1985), whereas the Orion cluster has a total mass of $\sim 10^{(3-4)}$ $M_\odot$ with an upper mass limit of 40 $M_\odot$ (*cf.* Larson 1982).

Keeping the cluster mass constant and decreasing the lower mass limit can produce a similar lowering of the realizeable upper mass limit, thereby reducing the observed Hα equivalent width. The lowest mass stars need not be on the main sequence either. Because they are undetectable in both the PMS and MS stages, they have no direct effect on the observed Hα equivalent widths. Rather, their importance is in the mass which they take away from the upper main sequence. Based on these exercises, it seems possible to explain the observed Hα luminosities and equivalent widths in terms of ionizing clusters with similar slopes to their initial mass spectra but with upper mass limits that are dependent on the clusters' finite masses and/or lower mass limits.

3.8 *Conclusions*

A photometric analysis of the Hα and red-continuum emission from M101 has led to the following key results:

• Within 10 kpc of the nucleus, the annular-averaged Hα emission shows a flat galactocentric profile, its e-folding scalelength of 9 kpc exceeding that of the red-continuum starlight by a factor of 2.7. This comparison indicates a significant difference between the galactocentric distributions of current-epoch massive star formation and past-averaged star formation in M101.

• The starbirth intensity in the disk, as inferred from annular averages of the Hα surface brightness, is strongly correlated with both the H_2 and total gas surface densities, yet is anticorrelated with the HI surface density. Least-squares fits give $\sigma(SFR) \propto \sigma(H_2)^{0.6}$, $\sigma(SFR) \propto \sigma(gas)^{0.9}$, and $\sigma(SFR) \propto \sigma(HI)^{-0.9}$

• The supergiant HII region complex, NGC 5461, has a starbirth intensity that is 16 times the mean intensity in the disk and a starbirth efficiency that is 10 times the mean efficiency in the disk, thus suggesting that some non-linear dependence is at work (*e.g.* $\sigma(SFR) \propto \sigma(gas)^{1.5}$) or that the IMF is biased towards the production of massive stars. The Hα image shows 3 plume-like features of diffuse ionized gas diverging from the dominant HII region towards the South, Southeast, and East.

• From synthetic-aperture photometry of 385 HII regions, I obtain a frequency distribution of Hα luminosities that can be approximated by $N(L)dL \propto L^{-2.1\pm0.1}$ at the high-luminosity end ($L \geq 10^{37.5}$ $erg\ s^{-1}$). This luminosity function is similar to the power laws found for other Sc and later-type galaxies, but is significantly flatter than the power laws found in earlier-type galaxies (see Kaufman *et al.* 1987; Hodge 1987).

• There are proportionately fewer high-luminosity HII regions within 5 kpc of the nucleus compared to the outer disk. This shows up as a difference of 0.4 ± 0.1 in the "slopes" of the inner and outer-galaxy luminosity functions. The observed difference, though small, parallels the more striking fact that the supergiant HII region *complexes* are all located beyond the inner 5 kpc.

• The Hα equivalent widths of the ionizing clusters are significantly lower, on average, in the inner galaxy compared to those beyond 5 kpc of the nucleus: $\langle EW(R < 5\ kpc)\rangle = 641 \pm 34$ Å, whereas $\langle EW(R > 5\ kpc)\rangle = 941 \pm 73$ Å. Selection, obscuration, and evolution effects seem unable to account for this behavior. Variations in the initial upper stellar mass limit of the ionizing clusters can alter the Hα equivalent widths as observed. A simple model of the Hα and red-continuum emission from an ionizing stellar population gives EW(Hα) $\propto M_u^{1.1\pm0.3}$ and hence predicts a radial variation in the mean M_u by a factor of 1.3 to 1.7.

• Measurable changes in EW(Hα) seem restricted to the inner 5 kpc, whereas the O/H abundance ratio decreases linearly by ~1 dex from 2 to 17 kpc. The dissimilarity in form between these two galactocentric distributions weakens previous arguments for abundance-sensitive IMFs. Closer similarities in form can be found between the galactocentric distribution of the equivalent widths and the galactocentric profiles of the differential rotation, shear rate, and tidal acceleration in the disk. The sense is to have lower equivalent widths, where the shear flow and tidal stress are higher.

• "Temperature-Luminosity" diagrams reveal a well-defined relationship between the Hα equivalent width (which traces the cluster's effective temperature) and the Hα luminosity. The sense is for the brighter HII regions to contain the hotter, more massive stars. This relationship can be modeled in terms of a stellar mass spectrum with a constant "slope" of $\alpha = 2.9 \pm 0.3$ but with a variable upper mass limit which is dependent on the cluster mass and/or lower mass limit.

The present conclusions are based on imagery of only two $5' \times 5'$ fields in M101, one of them centered on the nucleus, the other shifted 4.3' to the East. Consequently, the database of HII regions beyond 5 kpc radii is not as complete as that of the inner-galaxy HII regions. The intriguing differences between the inner and outer-galaxy luminosity functions and Hα equivalent widths must await further measurements, before they can be safely regarded as being representative of the entire disk.

References

Allen, C. W. 1973, *Astrophysical Quantities*, (London, The Athlone Press).

Allen, R. J., van der Hulst, J. M., Goss, W. M., and Huchtmeier, W. 1978, *Astr. Ap.*, **64**, 359.

Allen, R. J. and Goss, W. M. 1979, *Astr. Ap. Suppl.*, **36**, 135.

Binney, J. and Tremaine, S. 1987, *Galactic Dynamics* (New Jersey: Princeton University Press). p. 393.

Blitz, L., Israel, F. P., Neugebauer, G., Gatley, I., Lee, T. J., and Beattie, D. H. 1981, *Ap. J.*, **249**, 76.

Blitz, L. and Glassgold, A. E. 1982, *Ap. J.*, **252**, 481.

Bloeman, J. B. G. M., Strong, A. W., Blitz, L., Cohen, R. S., Dame, T., Grabelsky, D. A., Hermen, W., Lebrun, F., Mayer-Hasselwander, H. A., and Thaddeus, P. 1986, *Astr. Ap.*, **154**, 25.

Bosma, A., Goss, W. M., and Allen, R. J. 1981, *Astr. Ap.*, **93**, 106.

Burnham, R. 1978, *Burnham's Celestial Handbook*, **Vol. 3**, (New York: Dover). p. 2002.

Campbell, A., Terlevich, R., and Melnick, J. 1987, *M. N. R. A. S.*, **223**, 811.

Campbell, A. 1988, *Ap. J.*, **335**, 644.

Cohen, R. S., Dame, T. M., Garay, G., Montani, J., Rubio, M., and Thaddeus, P. 1988, *Ap. J. (Letters)*, **331**, L95.

Cook, K., Aaronson, M., and Illingworth, G. 1986, *Ap. J. (Letters)*, **301**, L45.

Comte, G., Monnet, G., and Rosado, M. 1979, *Astr. Ap.*, **72**, 73.

Davidson, K., Humphreys, R. M., and Blaha, C. 1985, *A. J.*, **90**, 192.

Dopita, M. A. 1985, *Ap. J. (Letters)*, **295**, L5.

de Vaucouleurs, G., de Vaucouleurs, A., and Corwin, H. 1976, *Second Reference Catalogue of Bright Galaxies*, (Austin: The University of Texas).

de Vaucouleurs, G. 1979, Astr. Ap., **79**, 274.

Elmegreen, B. G. 1979, *Ap. J.*, **231**, 372.

Elmegreen, D. M. and Elmegreen, B. G. 1984, *Ap. J. Suppl.*, **54**, 127.

Evans, I. N. 1986, *Ap. J.*, **309**, 544.

Gusten, R. and Mezger, P. G. 1982, *Vistas in Astronomy*, **26**, 159.

Hill, J. K., Bohlin, R. C., and Stecher, T. P. 1984, *Ap. J.*, **277**, 542.

Hodge, P. W. 1969, *Ap. J. Suppl.*, **18**, 73.

Hodge, P. 1987, *Pub. A. S. P.*, **99**, 915.

Hodge, P. W. and Kennicutt, R. C. 1988, unpublished.

Hoskins, M. A. 1963, *William Herschel and the Construction of the Heavens*, (London: Oldbourne Book Co.), p. 73.

Humphreys, R. M. and Aaronson, M. 1987, *Ap. J. (Letters)*, **318**, L69.

Israel, F. and Kennicutt, R. C. 1980, *Ap. Letters*, **21**, 1.

Jacoby, G. H., Hunter, D. A., and Christian, C. A. 1984, *Ap. J. Suppl.*, **56**, 257.

Jensen, E. B., Strom, K. M., and Strom, S. E. 1976, *Ap. J.*, **209**, 748.

Johnson, H. L., 1966, *Ann. Rev. Astr. Ap.*, **4**, 193.

Kahn, F. D. 1974, *Astr. Ap.*, **37**, 149.

Kaufman, M., Bash, F. N., Kennicutt, R. C., and Hodge, P. W. 1987, *Ap. J.*, **319**, 61.

Kennicutt, R. C. and Hodge, P. W. 1980, *Ap. J.*, **241**, 573.

Kennicutt, R. 1983, *Ap. J.*, **272**, 54.

Kennicutt, R. C. 1984, *Ap. J.*, **287**, 116.

Kennicutt, R. C. and Chu, Y. 1988, *A. J.*, **95**, 720.

Kennicutt, R. C., Keel, W. C., and Blaha, C. A. 1989, *A. J.*, **97**, 1022.

Kennicutt, R. C. 1989, *Ap. J.*, in press.

Knapp, G. R. 1987, *Pub. A. S. P.*, **99**, 1134.

Larson, R. B. 1982, *M. N. R. A. S.*, **200**, 159.

Larson, R. 1987, in *Starbursts and Galaxy Evolution*. ed. J. Montmerle and J. T. T. Van (Yvette, France: Editions Frontieres).

Lord S. 1987, Ph.D. Thesis, University of Massachusetts.

Luppino, G. A., Ceglio, N. M., Doty, J. P., Ricker, G. R., and Vallerga, J. V. 1987, *Opt. Eng.*, **26**, 1048.

Maeder, A. and Meynet, G. 1988. *Astr. Ap. Suppl.*, **76**, 411.

Maloney, P. and Black, J. H. 1988, *Ap. J.*, **325**, 389.

McCall, M. L., Rybski, P. M., and Shields, G. A. 1985, *Ap. J. Suppl.*, **57**, 1.

Meyer, S. S. and Ricker, G. R. 1980, *Applications of Digital Imaging to Astronomy*. SPIE Proceedings No. 264 (Bellingham, WA: SPIE), p. 38.

Miller, G. E. and Scalo, J. M. 1979, *Ap. J. Suppl.*, **41**, 513.

Oke, J. B. and Gunn, J. E. 1983, *Ap. J.*, **266**, 713.

Osterbrock, D. E. 1974. *Astrophysics of Gaseous Nebulae* (San Francisco: Freeman).

Rayo, J. F., Peimbert, M., and Torres-Peimbert, S. 1982, *Ap. J.*, **255**, 1.

Reddish, V. C. 1978. *Stellar Formation* (New York: Pergamon), p. 63.

Renzini, A. and Buzzoni, A. 1986, in *Spectral Evolution of Galaxies*. ed. C. Chiosi and A. Renzini (Dordrecht: D. Reidel), p. 283.

Rumstay, K. S. and Kaufman, M. 1983, *Ap. J.*, **274**, 611.

Sandage, A. 1961, *The Hubble Atlas of Galaxies* (Wash., D. C.: Carnegie Inst. of Wash.).

Sandage, A. and Tammann, G. 1974, *Ap. J.*, **172**, 593.

Sandage, A. R. and Tammann, G. A. 1981, *A Revised Shapley-Ames Catalog of Bright Galaxies* (Washington, D. C.: Carnegie Institution).

Sandage, A. and Bedke, J. 1988, *Atlas of Galaxies*, (Wash., D. C.: NASA).

Sanders, D. B., Solomon, P. M., and Scoville, N. Z. 1984, *Ap. J.*, **276**, 182.

Schweizer, F. 1976, *Ap. J. Suppl.*, **31**, 313.

Scoville, N. Z., Yun, M. S., Clemens, D. P., Sanders, D. B., and Waller, W. H. 1987, *Ap. J. Suppl.*, **63**, 821.

Searle, L. 1971, *Ap. J.*, **168**, 327.

Shields, G. A. and Tinsley, B. M. 1976, *Ap. J.*, **203**, 66.

Shields, G. A. and Searle, L. 1978, *Ap. J.*, **222**, 821.

Smith, H. E. 1975, *Ap. J.*, **199**, 591.

Smith, T. R. and Kennicutt, R. C. 1989, *Pub. A. S. P.*, **101**, 649.

Solomon, P. M., Barrett, J., Sanders, D. B., and de Zafra, R. 1983, *Ap. J. (Letters)*, **266**, L103.

Stark, A. A. and Blitz, L. 1978, *Ap. J. (Letters)*, **225**, L15.

Tenorio-Tagle, G. 1982, in *Regions of Recent Star Formation* (Dordrecht: D. Reidel), p. 1.

Terlevich, R. and Melnick, J. 1985, *M. N. R. A. S.*, **213**, 841.

Toomre, A. and Toomre, J. 1966, *Ap. J.*, **146**, 810.

Torres-Peimbert, S., Peimbert, M., and Fierro, J. 1989, *Ap. J.*, in press.

Van Buren, D. 1985, *Ap. J.*, **294**, 567.

Viallefond, F., Goss, W. M., and Allen, R. J. 1982, *Astr. Ap.*, **115**, 373.

Viallefond, F. 1985, in *Star Forming Dwarf Galaxies*, ed. D. Kunth, T. X. Thuan, and J. T. T. T. Van (Yvette, France: Editions Frontieres).

Vilchez, J. M. and Pagel, B. E. J. 1988, *M. N. R. A. S.*, **231**, 257.

Vogel, S. N., Kulkarni, S. R., and Scoville, N. Z. 1988, *Nature*, **334**, 402.

Waller, W. H., Clemens, D. P., Sanders, D. B., and Scoville, N. Z. 1987, *Ap. J.*, **314**, 397.

Waller, W. H., Kleinmann, S. G., and Ricker, G. R. 1988, *A. J.*, **95**, 1057.

Walterbos, R. A. M. and Kennicutt, R. C. 1987, *Astr. Ap. Suppl.*, **69**, 311.

Young, J. S., Xie, S., Kenney, J. D. P., and Rice, W. L. 1989, *Ap. J. Suppl.*, in press.

Table 3–1

Adopted Properties of M101

Type[a]	Sc(s) I
R.A. (1950)[a]	$14^h\ 01^m\ 28^s$
Declination (1950)[a]	54° 35' 36"
Radial velocity (heliocentric)[b]	242 km s^{-1}
Position angle of major axis[b]	39°
Inclination[b]	18°
Distance[c]	4.8 Mpc
Holmberg radius[d]	14' (20 kpc)

[a] Sandage and Tammann 1981

[b] Bosma *et al.* 1981

[c] Humphreys and Aaronson 1987

[d] de Vaucouleurs *et al.* 1976

Table 3–2

Observing Log

Telescope	MHO 1.3 m @$f/13.5$
Pixel size	0.81"
Field of view	5' x 6'

6/19/86

Filter	"I"	"I"
λ_0	8380Å	"
FWHM	2050Å	"
T_0	88%	"
Integration time	373s	303s
Region	central	4.3' E

6/20/86

Filter	Hα	Hα	Hα	"R"	"R"
λ_0	6563Å	"	"	6040Å	"
FWHM	36Å	"	"	1504Å	"
T_0	75%	"	"	77%	"
Integration time	2403s	2403s	503s	281s	329s
Region	central	4.3' E	4.3' E	central	4.3' E

Table 3–3

Annular-Averaged Hα Surface Brightness

R" (1)	$\langle I(H\alpha)\rangle$ (2)	$\delta I(H\alpha)$ (3)	$\delta\langle I(H\alpha)\rangle$ (4)	$\langle I_{sm}(H\alpha)\rangle$ (5)	$\delta I_{sm}(H\alpha)$ (6)	$\delta\langle I(H\alpha)\rangle$ (7)	Notes (8)
0-30	4.66	5.81	0.18	3.29	0.22	0.01	
30-60	2.30	1.64	0.03	2.50	0.36	0.01	
60-90	1.98	2.14	0.03	1.95	0.36	0.01	
90-120	1.62	2.91	0.03	1.68	0.46	0.01	
120-150	1.54	2.54	0.03	1.46	0.72	0.01	
150-180	1.71	5.35	0.06	1.18	0.91	0.01	
180-210	2.15	3.21	0.05	1.06	0.84	0.01	a
210-240	1.74	1.38	0.02	1.23	0.67	0.01	
240-270	1.45	1.79	0.03	2.03	1.22	0.02	
270-300	4.61	13.19	0.21	2.36	1.73	0.03	
300-330	0.82	0.71	0.01	1.49	1.10	0.02	b
330-360	0.84	1.53	0.02	1.18	0.74	0.01	
360-390	2.56	3.96	0.06	1.41	0.86	0.01	
390-420	1.27	1.13	0.02	1.23	0.57	0.01	c
420-450	1.33	0.31	0.01	1.07	0.14	0.00	

Explanation of Columns for Table 3-3

(1) Range of galactocentric radii as measured in the plane of the galaxy (in arcseconds).

(2) Annular-averaged surface brightness (in 10^{-16} erg cm^{-2} s^{-1} arcsec^{-2}).

(3) Dispersion (standard deviation) in the Hα surface brightness (in 10^{-16} erg cm^{-2} s^{-1} arcsec^{-2}).

(4) Uncertainty (standard error) in the mean Hα surface brightness, based on $\delta\langle I(H\alpha)\rangle = \delta I(H\alpha)/\sqrt{N_{pix}}$ (in 10^{-16} erg cm^{-2} s^{-1} arcsec^{-2}).

(5) Same as (2), except that the Hα image has been convolved with a 60" (FWHM) Gaussian "beam."

(6) Same as (3), except for the Gaussian smoothing.

(7) Same as (4), except for the Gaussian smoothing.

(8)

(a) Largest fully sampled annulus.

(b) Annulus includes NGC 5461.

(c) Annulus includes NGC 5462.

Table 3–4

Positions and Sizes of HII Regions

No. (1)	ΔX (2)	ΔY (3)	R(gal) (4)	r(unb) (5)	r(tot) (6)	Id (7)
1	1.40	2.78	187.10	7.13	7.13	
2	1.19	2.72	178.58	6.40	6.40	
3	1.55	2.99	202.39	5.75	5.75	
4	1.29	3.00	196.69	6.07	6.07	
5	1.35	2.96	195.94	3.16	3.16	
6	2.07	2.83	210.32	4.05	7.86	
7	2.06	2.82	209.55	4.62	4.62	
8	1.19	2.72	178.58	6.16	6.16	
9	1.06	3.01	192.35	9.40	9.40	
10	0.71	2.84	177.41	4.62	4.62	
11	0.58	2.76	170.92	3.32	3.32	
12	0.21	2.82	172.48	4.45	4.45	
13	-0.06	2.75	168.53	6.89	6.89	
14	-0.32	2.69	166.89	4.05	9.64/2.27	
15	-0.41	2.81	175.26	4.05	4.05	
16	-0.51	2.76	173.43	3.81	3.81	
17	-0.78	2.69	173.85	5.67	5.67	
18	-0.95	2.69	177.39	2.75	2.75	
19	-0.79	1.95	130.87	4.21	4.21	
20	-0.22	1.99	123.13	4.45	4.45	
21	-0.19	2.27	140.06	3.16	9.80	
22	0.14	1.92	117.42	7.61	7.61	
23	0.55	1.91	120.00	4.94	4.94	
24	0.60	2.16	135.84	4.94	4.94	
25	1.16	1.95	136.02	4.45	4.45	
26	1.44	2.15	155.38	5.02	5.02	
27	1.68	1.95	154.38	3.32	3.32	
28	1.86	1.69	151.10	3.56	3.56	
29	1.76	1.45	137.39	4.94	4.94	
30	1.05	1.41	105.59	3.73	3.73	
31	0.93	1.42	102.14	3.48	3.48	
32	-0.62	1.30	90.16	3.81	3.81	
33	-0.32	1.30	83.03	5.02	5.02	
34	0.02	1.25	76.64	3.48	3.48	
35	0.77	1.27	88.95	4.37	4.37	

(cont., next page)

Table 3-4 (cont.)

No. (1)	ΔX (2)	ΔY (3)	R(gal) (4)	r(unb) (5)	r(tot) (6)	Id (7)
36	0.93	1.29	95.65	3.64	3.64	
37	1.74	1.21	127.67	2.11	4.29	
38	1.54	1.22	118.10	2.67	2.67	
39	1.90	1.08	131.86	2.03	2.03	
40	1.54	0.95	109.44	5.51	5.51	
41	1.26	0.96	95.26	5.02	5.02	
42	1.00	0.95	82.67	5.18	5.18	
43	0.86	0.90	75.09	2.59	2.59	
44	0.48	0.87	59.79	7.37	7.37	
45	0.33	1.00	63.58	7.21	7.21	
46	0.01	1.01	61.67	4.78	4.78	
47	-0.10	1.10	68.00	5.18	5.18	
48	-0.15	0.90	56.21	5.18	5.18	
49	-0.48	1.14	77.14	4.05	4.05	
50	-0.57	1.07	75.74	3.32	3.32	
51	-0.68	0.91	71.36	3.64	3.64	
52	-0.89	0.99	84.04	4.13	4.13	
53	-0.93	0.76	75.59	5.67	5.67	S1. H105
54	-0.81	0.68	66.93	5.10	5.10	
55	-0.51	0.74	56.68	5.83	5.83	
56	0.86	0.72	67.09	4.45	4.45	
57	0.98	0.71	72.59	3.73	3.73	
58	1.29	0.69	88.47	4.70	4.70	
59	1.46	0.72	98.67	5.26	5.26	
60	1.66	0.64	108.15	5.59	5.59	
61	1.82	0.73	118.84	4.70	4.70	
62	1.90	0.63	121.60	4.94	4.94	
63	2.02	0.73	131.04	4.62	4.62	
64	2.10	0.53	132.28	3.08	5.43	
65	1.65	0.32	102.88	6.48	6.48	
66	0.72	0.20	45.83	5.18	5.18	
67	-0.06	0.13	8.96	2.51	2.51	
68	-0.33	0.01	20.71	9.64	9.64/2.35	

(cont.. next page)

Table 3-4 (cont.)

No. (1)	ΔX (2)	ΔY (3)	R(gal) (4)	r(unb) (5)	r(tot) (6)	Id (7)
69	-0.81	-0.05	50.26	5.02	5.02	
70	-0.98	0.15	61.46	4.62	5.67	
71	-1.02	0.30	66.76	5.10	5.10	
72	-1.09	0.00	67.32	6.97	6.97	
73	-0.81	-0.05	50.26	4.86	4.86	
74	0.00	-0.06	3.61	7.94	13.69	near nucleus
75	0.17	-0.07	11.67	3.97	7.29	
76	2.00	0.01	123.65	6.32	6.32	
77	1.69	-0.09	105.23	4.54	4.54	
78	1.44	-0.12	89.71	4.45	4.45	
79	1.15	-0.10	71.51	5.35	5.35	
80	0.68	-0.28	46.47	3.08	3.08	
81	0.60	-0.25	40.94	4.05	4.05	
82	0.55	-0.38	42.04	4.54	4.54	
83	0.41	-0.07	25.96	3.40	3.40	
84	-0.83	-0.22	52.59	4.94	4.94	
85	-1.08	-0.39	69.69	4.54	4.54	
86	-1.06	-0.51	71.48	4.94	4.94	
87	-1.03	-0.64	73.43	3.81	3.81	
88	-0.49	-0.63	47.97	3.73	3.73	
89	-0.44	-0.77	53.11	4.05	4.05	
90	0.19	-0.81	51.44	3.64	3.64	
91	0.35	-0.53	40.00	5.26	5.26	
92	0.75	-0.43	54.22	4.62	4.62	
93	0.82	-0.59	63.64	3.89	3.89	
94	0.75	-0.64	62.00	3.24	4.62	
95	0.69	-0.76	64.70	3.64	3.64	
96	1.08	-0.71	81.40	4.05	4.05	
97	1.31	-0.58	90.39	4.37	4.37	
98	1.26	-0.45	83.65	3.48	3.48	
99	1.16	-0.39	76.79	4.37	4.37	
100	1.09	-0.30	70.49	3.81	3.81	
101	1.03	-0.22	65.99	3.56	3.56	
102	0.91	-0.18	57.72	4.29	4.29	

(cont., next page)

Table 3-4 (cont.)

No. (1)	ΔX (2)	ΔY (3)	R(gal) (4)	r(unb) (5)	r(tot) (6)	Id (7)
103	1.37	-0.30	87.36	4.05	6.72	
104	1.59	-0.35	102.02	4.70	7.70	
105	1.99	-0.20	124.50	3.81	6.24	
106	1.76	-0.64	117.36	5.10	5.10	
107	1.68	-0.88	119.33	3.16	3.16	
108	1.51	-0.98	113.44	4.62	4.62	
109	0.94	-0.85	79.86	4.94	4.94	
110	0.49	-0.86	62.27	6.24	6.24	
111	0.37	-0.92	62.06	4.54	4.54	
112	-0.02	-0.90	54.97	5.02	7.05	
113	-0.42	-1.05	68.06	4.45	4.45	
114	-0.86	-0.84	72.19	5.18	5.18	
115	-0.28	-1.50	92.71	4.05	5.67	
116	-0.08	-1.21	73.90	4.05	4.05	
117	0.17	-1.13	70.52	4.70	4.70	
118	0.20	-1.25	77.97	4.62	5.67	
119	0.54	-1.59	104.26	4.86	4.86	
120	0.78	-1.29	94.33	4.29	4.29	
121	0.92	-1.12	91.40	4.94	4.94	
122	1.23	-1.28	111.91	3.56	5.10	
123	1.31	-1.59	129.93	3.64	3.64	
124	1.32	-1.46	124.08	4.45	4.45	
125	1.23	-1.28	111.91	3.24	5.10	
126	1.36	-1.26	117.03	5.18	5.18	
127	1.63	-1.54	141.44	4.70	5.43	
128	1.72	-1.12	129.11	4.05	4.05	
129	1.81	-1.22	137.81	4.86	6.56	
130	1.87	-0.94	132.12	3.81	3.81	
131	1.93	-1.06	138.62	2.92	7.05	
132	2.00	-1.12	144.10	2.11	7.53	
133	1.99	-1.05	141.79	2.11	2.11	
134	2.08	-1.10	148.07	3.97	7.13	
135	1.90	-1.89	168.87	2.51	4.29	
136	1.95	-1.87	170.01	2.19	2.19	

(cont., next page)

Table 3-4 (cont.)

No. (1)	ΔX (2)	ΔY (3)	R(gal) (4)	r(unb) (5)	r(tot) (6)	Id (7)
137	1.41	-1.91	149.37	3.81	3.81	
138	0.85	-1.83	126.32	5.10	5.10	
139	0.67	-1.96	129.19	4.21	4.21	
140	0.67	-1.97	129.79	4.21	4.21	
141	0.48	-1.93	123.18	3.48	6.24	
142	0.37	-1.94	122.03	3.16	11.66/2.51	
143	0.19	-1.82	112.37	3.32	3.32	
144	0.08	-1.96	120.47	5.67	5.67	
145	-0.05	-1.99	121.66	4.45	5.99	
146	-0.50	-1.81	113.68	4.54	4.54	
147	-0.75	-2.02	130.21	5.75	5.75	
148	-0.79	-1.89	123.21	4.05	4.05	
149	-1.19	-1.65	122.10	4.86	4.86	
150	-0.78	-1.65	110.20	5.26	5.26	
151	-1.05	-1.73	121.73	7.29	12.47/2.59	S2, H108
152	-0.62	-2.34	146.79	4.29	4.29	
153	-0.70	-2.55	159.89	6.64	6.64	
154	-0.13	-2.67	163.39	6.07	8.51	
155	0.06	-2.62	160.75	3.56	3.56	
156	0.28	-2.73	168.88	4.78	4.78	
157	0.41	-2.84	177.28	5.83	5.83	
158	0.49	-2.97	185.86	4.37	4.37	
159	0.05	-3.17	194.30	2.92	4.05	
160	0.72	-2.94	187.67	3.24	3.24	
161	0.83	-2.29	151.57	3.64	5.35	
162	0.95	-2.27	153.69	3.00	3.00	
163	1.33	-2.24	163.54	3.97	3.97	
164	1.44	-2.16	163.43	2.51	2.51	
165	1.54	-2.25	171.22	3.73	3.73	
166	1.59	-2.47	184.40	4.62	4.62	
167	1.81	-2.28	183.40	2.92	2.92	
168	-1.30	-2.21	154.04	5.67	5.67	
169	-0.96	-2.00	133.58	4.29	4.29	
170	-1.99	-1.61	154.00	3.73	3.73	

(cont., next page)

Table 3-4 (cont.)

No. (1)	ΔX (2)	ΔY (3)	R(gal) (4)	r(unb) (5)	r(tot) (6)	Id (7)
171	-1.91	-1.52	146.99	3.81	3.81	
172	-1.99	-1.30	143.41	4.86	4.86	
173	-1.53	-1.42	125.39	2.51	4.86	
174	-1.47	-1.37	120.49	4.21	4.21	
175	-1.45	-1.22	113.87	4.45	4.21	
176	-1.36	-1.13	106.26	3.97	4.45	
177	-1.37	-1.11	105.90	2.19	3.97	
178	-1.26	-1.05	98.99	4.29	1.86	
179	-1.36	-0.90	98.15	5.18	4.29	H111
180	-1.42	-0.99	103.95	3.32	5.18	
181	-1.54	-1.08	113.62	3.81	3.32/1.09	
182	-1.68	-1.16	122.89	5.18	3.81	
183	-1.99	-0.97	134.27	4.70	5.18	
184	-1.52	-0.89	106.73	3.08	4.70	
185	-1.52	-0.75	102.58	3.81	3.08	
186	-1.42	-0.74	96.98	4.05	3.81	
187	-1.56	-0.58	101.04	3.73	4.05	
188	-1.50	-0.62	98.85	2.11	3.73	
189	-1.44	-0.63	95.61	3.40	2.11	
190	-1.29	-0.67	87.81	3.81	3.40	
191	-1.17	-0.57	78.70	3.56	3.81	
192	-1.29	-0.53	84.75	4.29	3.56	
193	-1.30	-0.40	82.99	3.97	4.29	
194	-1.23	-0.24	76.63	3.89	3.97	
195	-1.76	-0.26	109.04	3.64	3.89	
196	-1.76	0.00	108.73	3.56	3.64	
197	-1.91	0.12	118.85	2.92	5.83	
198	-1.80	0.15	112.20	5.99	2.92	
199	-1.53	0.09	95.19	3.32	5.99	
200	-1.33	-0.12	82.22	4.54	6.07	
201	-1.19	0.16	74.81	2.92	4.54	
202	-1.74	0.40	111.34	5.59	2.92	
203	-1.62	0.46	105.67	2.92	7.53	
204	-1.25	0.45	83.23	4.62	2.92	

(cont.. next page)

Table 3-4 (cont.)

No. (1)	ΔX (2)	ΔY (3)	R(gal) (4)	r(unb) (5)	r(tot) (6)	Id (7)
205	-1.89	0.56	123.49	3.81	3.81	
206	-0.51	1.00	70.13	2.43	2.43	
207	-1.82	1.09	133.56	2.51	2.51	
208	-2.58	1.50	187.79	7.70	7.70/2.84	S5, H124, H125 (vignetted)
209	-2.55	1.36	182.15	2.27		
210	-1.55	1.62	141.19	4.45	4.70	
211	-2.06	1.80	172.76	3.48	4.45	
212	-2.26	1.80	182.56	5.18	3.48	
213	-2.23	2.05	190.74	5.75	5.18	
214	-1.81	2.07	173.17	3.16	5.75	
215	-1.55	2.02	160.47	3.81	3.16	
216	-1.40	1.96	151.62	3.24	3.81	
217	-1.33	1.93	147.51	3.32	4.05	
218	-1.15	1.92	140.41	3.81	3.32	
219	-1.05	1.78	129.45	2.92	3.81	
220	-0.98	2.22	151.51	3.40	2.92	
221	-1.49	2.29	171.42	5.43	3.40	
222	-1.61	2.17	169.59	4.21	5.43	
223	-2.48	2.54	223.90	4.78	4.21	
224	-2.39	2.63	223.74	3.48	4.78	
225	-2.31	2.66	222.06	3.48	3.48	
226	-2.15	2.56	210.39	3.48	4.78	
227	-2.00	2.57	205.03	6.24	3.48	
228	-1.99	2.75	213.20	3.73	7.53/1.86	
229	-1.61	2.61	192.35	2.27	3.73	
230	-1.64	2.69	197.96	3.08	4.21	
231	-1.57	2.89	206.24	3.73	6.32	
232	-1.33	3.01	205.59	4.78	3.73	
233	-1.27	2.89	197.15	3.32	4.78	
234	-1.17	2.94	197.53	3.81	6.40	
235	-1.12	2.72	183.70	3.97	4.62	
236	-0.95	2.69	177.39	3.81	3.97	
237	-1.01	2.72	180.96	2.59	3.81	
238	4.09	3.36	318.49	4.13	3.81	
					4.13	

(cont.. next page)

Table 3-4 (cont.)

No. (1)	ΔX (2)	ΔY (3)	R(gal) (4)	r(unb) (5)	r(tot) (6)	Id (7)
239	3.70	3.41	302.18	3.56	3.56	
240	3.07	3.26	268.94	4.21	4.21	
241	2.45	3.35	249.01	4.21	4.21	
242	2.25	3.38	243.81	6.16	6.16/1.94	
243	2.29	3.21	236.83	5.02	5.02	
244	2.45	3.05	234.73	3.24	4.05	
245	2.40	2.97	229.14	3.73	3.73	
246	2.08	2.83	210.46	8.10	8.10	
247	2.00	3.12	222.17	7.70	7.70/2.51	
248	2.97	2.91	249.71	3.00	3.00	
249	2.68	2.34	213.58	3.48	3.48	
250	2.58	2.34	209.19	3.97	3.97	
251	2.17	2.59	202.97	3.40	3.40	
252	2.09	2.13	179.29	3.81	3.81	
253	2.07	2.22	182.45	3.24	3.24	
254	2.70	2.22	210.04	3.24	4.54	
255	2.70	2.21	209.80	3.24	3.24	
256	1.75	2.31	174.09	5.26	5.26	
257	1.85	1.69	150.86	4.13	4.13	
258	1.77	1.46	137.73	4.29	4.29	
259	2.78	1.97	205.01	4.86	4.86	
260	2.95	1.89	210.96	3.32	3.32	
261	2.48	1.82	185.07	3.73	3.73	
262	2.42	1.59	174.79	4.62	4.62	
263	2.26	1.46	162.26	4.13	4.13	
264	2.32	1.34	161.70	2.92	5.75	
265	3.46	1.46	227.81	3.40	3.40	
266	3.41	1.28	221.67	3.56	3.56	
267	3.15	1.63	214.86	3.89	8.75/1.86	
268	2.85	1.60	197.30	4.29	9.15/2.03	
269	2.65	1.78	192.50	3.97	9.40	
270	2.39	1.82	180.76	2.75	5.02	

(cont., next page)

Table 3-4 (cont.)

No. (1)	ΔX (2)	ΔY (3)	R(gal) (4)	r(unb) (5)	r(tot) (6)	Id (7)
271	2.37	1.90	182.57	3.64	7.86	
272	3.04	1.17	198.27	3.32	8.75	
273	3.05	1.04	196.27	4.13	4.13	
274	2.93	0.93	187.51	5.10	5.10	
275	2.74	1.05	178.12	3.48	3.48	
276	2.59	0.87	166.09	5.43	5.43	
277	2.23	1.02	148.72	4.70	6.07	
278	1.89	1.08	131.65	3.24	3.24	
279	1.85	0.87	124.22	3.16	3.16	
280	1.81	0.72	118.19	3.64	3.64	
281	1.90	0.63	121.82	3.81	3.81	
282	2.03	0.74	131.48	4.94	4.94	
283	2.09	0.53	131.62	5.83	5.83	
284	2.12	0.50	133.26	5.02	5.02	
285	2.21	0.78	143.01	7.21	8.51/2.35	
286	2.53	0.42	157.46	2.51	4.05	
287	2.66	0.49	165.76	9.48	9.48/2.35	S3, H40
288	2.84	0.58	177.40	4.05	4.05	
289	3.24	0.53	201.31	4.45	4.45	
290	3.12	0.46	193.84	3.48	3.48	
291	3.15	0.35	194.79	4.45	4.45	
292	3.26	0.27	201.88	4.94	4.94	
293	2.29	0.41	142.71	6.56	6.56	
294	2.12	0.50	133.26	4.78	4.78	
295	2.08	0.54	131.46	5.91	5.91	
296	3.14	-0.03	194.33	5.10	5.10	
297	2.28	0.20	140.83	4.13	4.94	
298	1.99	0.01	123.40	5.10	6.89	
299	1.98	-0.19	123.92	4.37	4.37	
300	2.15	-0.23	134.45	3.73	3.73	
301	2.26	-0.30	141.75	11.50	11.50	
302	2.38	-0.17	148.10	4.13	4.13	
303	2.92	-0.66	187.01	11.91	11.91/2.43	S4
304	2.59	-0.99	174.03	6.48	6.48	

(cont.. next page)

Table 3-4 (cont.)

No. (1)	ΔX (2)	ΔY (3)	R(gal) (4)	r(unb) (5)	r(tot) (6)	Id (7)
305	2.68	-0.92	177.56	3.81	3.81	
306	2.34	-0.99	159.80	5.26	5.26/2.35	
307	2.17	-1.00	150.50	4.45	8.02	
308	2.41	-1.09	166.68	3.32	3.32	
309	2.78	-1.85	210.31	3.64	3.64	
310	2.93	-1.80	216.80	4.29	4.29	
311	3.08	-1.96	230.39	3.32	3.32	
312	3.43	-1.53	236.25	6.89	6.89	
313	3.57	-1.00	232.46	2.11	2.11	
314	3.89	-1.04	251.80	4.70	4.70	
315	4.76	-0.36	296.64	3.56	3.56	
316	4.72	-0.66	296.65	3.48	3.48	
317	4.82	-1.01	307.77	4.29	4.29	
318	4.67	-0.93	297.44	6.07	6.07	
319	4.65	-0.99	296.71	2.75	6.24	
320	4.61	-1.12	296.70	4.86	7.05	
321	4.41	-1.41	290.35	6.80	6.80	
322	4.29	-1.41	283.06	4.29	4.29	
323	4.19	-1.79	286.46	9.23	9.23/2.35	NGC 5461 (core), S7
324	4.09	-1.85	282.18	2.84	11.18	
325	3.98	-1.95	278.65	4.37	9.23/2.43	
326	3.95	-1.87	274.76	1.86	6.32	
327	4.14	-2.17	294.66	5.91	5.91	
328	3.88	-2.09	277.29	4.37	6.24	
329	3.76	-2.08	270.48	4.21	7.78/2.03	
330	4.01	-2.34	292.59	4.78	4.78	
331	4.04	-2.49	299.26	3.89	3.89	
332	3.88	-2.76	300.00	5.35	5.35	
333	3.56	-2.57	277.14	3.73	3.73	
334	3.38	-2.23	255.23	3.00	3.00	
335	3.17	-2.35	248.76	6.89	6.89/1.10	
336	3.13	-2.29	244.42	1.62	5.02	
337	4.87	-2.76	352.49	3.73	3.73	
338	5.74	-1.98	380.69	3.40	3.40	

(cont., next page)

Table 3-4 (cont.)

No. (1)	ΔX (2)	ΔY (3)	R(gal) (4)	r(unb) (5)	r(tot) (6)	Id (7)
339	5.20	-1.20	333.31	4.94	4.94	
340	5.12	-0.75	322.18	3.32	3.32	
341	4.97	-0.80	313.67	3.48	3.48	
342	5.83	3.27	403.90	3.56	3.56	
343	5.86	3.10	401.38	2.59	2.59	
344	5.89	2.49	387.87	4.13	4.13	
345	4.90	1.53	312.89	4.62	4.62	
346	4.95	1.30	312.90	3.40	3.40	
347	6.44	3.03	431.39	4.70	4.70	
348	6.51	2.97	433.70	3.40	3.40	
349	6.30	2.60	414.18	6.32	6.32	
350	6.50	2.48	422.92	3.16	3.16	
351	6.29	2.04	403.02	4.37	11.26/2.19	
352	6.20	2.07	398.13	2.51	5.02	
353	6.07	2.05	390.22	2.27	4.21	
354	6.13	1.95	391.84	2.84	4.45	
355	5.97	2.01	383.83	4.54	4.54	
356	6.05	1.77	384.38	3.00	4.45	
357	6.14	1.71	388.90	2.51	3.56	
358	6.24	1.45	391.89	6.89	6.89	
359	6.02	1.40	377.90	4.21	4.21	
360	5.83	1.39	366.60	3.00	5.43	
361	5.55	1.22	347.68	3.40	4.78	
362	5.55	1.35	349.36	2.67	12.80/2.19	
363	5.62	1.38	353.64	1.94	5.02/2.61	
364	5.71	1.44	359.85	2.92	9.64/1.10	
365	5.71	1.51	360.73	2.27	5.67	
366	5.64	1.56	357.40	2.59	5.35	
367	5.72	1.61	362.98	4.70	11.99/2.27	NGC 5462 (brightest)
368	5.83	1.70	370.50	4.37	10.69/2.43	
369	5.47	1.02	341.33	5.83	7.45	
370	5.58	0.85	347.00	3.16	5.02	
371	5.65	0.87	351.07	2.35	5.51	

(cont., next page)

Table 3-4 (cont.)

No. (1)	ΔX (2)	ΔY (3)	R(gal) (4)	r(unb) (5)	r(tot) (6)	Id (7)
372	5.65	0.95	351.63	3.64	3.64	
373	5.77	1.02	359.46	5.59	5.59	
374	5.73	1.10	357.82	2.75	5.26	
375	6.05	1.10	376.93	4.54	4.54	
376	6.17	1.38	387.15	4.37	6.16	
377	6.24	1.45	391.89	4.13	6.89	
378	5.84	0.85	362.74	3.73	3.73	
379	5.81	0.72	360.38	4.62	4.62	
380	5.71	0.73	354.07	4.13	4.13	
381	5.71	0.61	353.67	6.16	6.16/1.54	
382	5.42	0.65	335.58	4.94	4.94	
383	5.51	0.52	340.88	4.54	4.54	
384	5.52	0.41	341.54	4.45	4.45	
385	5.34	0.46	330.17	4.78	4.78	
386	5.89	2.49	387.87	4.13	4.13	
387	6.30	2.60	414.18	7.21	7.21	
388	6.50	2.48	423.00	3.56	3.56	
389	6.44	3.03	431.39	8.42	8.42	

Explanation of Columns for Table 3-4

(1) The HII region number as mapped in Figures 3-7 and 3-8.

(2) Offset in Right Ascension from the nucleus, measured in arcminutes in the detector plane (not on the celestial sphere).

(3) Offset in Declination from the nucleus, measured in arcminutes in the detector plane.

(4) Galactocentric radius in the plane of the galaxy (in arcseconds).

(5) Unblended radius of HII region (in arcseconds).

(6) Total radius of HII region (in arcseconds). For 27 of the brightest HII regions, the HWHM radius is also given.

(7) Cross-referenced identification of HII region, for which spectroscopic information exists (see Evans 1986 and references therein).
"S" refers to Searle (1971); "H" refers to Hodge (1969).

Table 3–5

Photometric Properties of HII Regions

No. (1)	R (2)	log f(Hα) (3)	δlog f(Hα) (4)	EW_{tot} (5)	S/N (6)	EW_{cl} (7)	S/N (8)
1	187.1	-13.092	0.004	94.6	57.8	1291.2	4.9
2	178.6	-13.601	0.011	37.2	33.5	1096.5	2.0
3†	202.4	...	...	...	...	...	...
4†	196.7	...	...	...	...	...	...
5	195.9	-13.989	0.011	86.3	20.8	553.4	3.8
6	210.3	-13.346	0.004	132.4	39.2	679.2	8.3
7	209.6	-13.347	0.004	120.5	42.3	507.0	11.0
8	178.6	-13.601	0.011	37.2	33.5	1096.5	2.0
9†	192.4	...	...	...	...	...	...
10	177.4	-13.630	0.008	63.4	34.7	695.0	4.2
11	170.9	-13.828	0.010	55.6	29.6	552.1	4.2
12	172.5	-13.938	0.017	36.1	21.8	1778.3	0.8
13	168.5	-13.261	0.006	55.5	54.8	1066.6	4.0
14	166.9	-13.096	0.002	155.2	60.7	883.1	11.3
15	175.3	-13.515	0.006	65.2	44.6	677.6	5.6
16	173.4	-13.549	0.005	83.4	44.1	496.6	8.8
17	173.9	-13.201	0.004	63.4	66.8	631.0	8.9
18	177.4	-14.005	0.012	53.0	26.9	275.4	7.3
19	130.9	-13.753	0.011	49.8	29.6	...	...
20	123.1	-13.846	0.014	36.1	26.9	851.1	2.1
21	140.1	-14.180	0.017	44.3	19.4	441.6	3.1
22	117.4	-13.468	0.010	24.0	39.1	666.8	3.5
23	120.0	-13.637	0.010	36.9	36.1	993.1	2.4
24	135.8	-13.708	0.012	34.5	31.3	924.7	2.2
25	136.0	-13.946	0.017	26.2	23.0	1074.0	1.3
26	155.4	-13.806	0.015	25.7	26.7	734.5	2.2
27	154.4	-13.993	0.015	38.1	23.6	5807.6	0.3
28	151.1	-14.130	0.021	28.7	18.5	2691.5	0.4
29	137.4	-13.670	0.011	30.1	35.3	418.8	5.3
30	105.6	-14.067	0.018	30.0	21.2	1288.2	1.0
31	102.1	-14.036	0.017	31.0	22.6	...	...
32	90.2	-14.050	0.017	30.8	21.9	...	...
33	83.0	-13.530	0.008	37.7	45.9	2606.2	1.2
34	76.6	-14.043	0.017	23.9	23.4	...	...
35	88.9	-13.922	0.016	21.5	25.1	1267.7	1.2

(cont., next page)

Table 3-5 (cont.)

No. (1)	R (2)	log f(Hα) (3)	δlog f(Hα) (4)	EW_{tot} (5)	S/N (6)	EW_{cl} (7)	S/N (8)
36	95.6	-14.224	0.026	19.8	15.8	...	...
37	127.7	-14.665	0.036	28.5	10.6	...	...
38	118.1	-14.278	0.022	34.8	16.8	29376.5	0.0
39	131.9	-14.572	0.029	27.9	13.2	212.3	3.7
40	109.4	-13.703	0.012	31.3	32.5	...	...
41	95.3	-13.785	0.014	25.2	28.1	2766.9	0.6
42	82.7	-13.575	0.009	35.4	42.2	1321.3	2.1
43	75.1	-14.149	0.016	32.3	23.0	384.6	3.8
44	59.8	-13.348	0.008	20.4	52.8	6950.3	0.4
45	63.6	-13.516	0.010	18.1	40.9	4677.4	0.5
46	61.7	-13.865	0.014	19.6	28.9	...	...
47	68.0	-13.704	0.012	22.3	34.5	...	...
48	56.2	-13.861	0.017	13.8	25.1	549.5	2.6
49	77.1	-13.786	0.012	30.7	32.2	6516.3	0.3
50	75.7	-13.920	0.013	33.1	29.1	...	...
51	71.4	-13.804	0.010	42.0	35.3	...	...
52	84.0	-13.644	0.009	36.3	42.7	353.2	7.9
53	75.6	-13.321	0.006	41.6	61.5	881.1	4.8
54	66.9	-13.388	0.006	50.0	57.2	...	...
55	56.7	-13.433	0.007	28.1	53.0	1153.5	2.9
56	67.1	-13.918	0.016	22.6	25.1	...	...
57	72.6	-13.994	0.015	29.1	25.3	1798.9	0.9
58	88.5	-13.854	0.014	27.8	28.1	2243.9	0.8
59	98.7	-13.730	0.012	24.7	32.0	288.4	6.6
60	108.1	-13.276	0.004	71.3	61.2	1145.5	4.8
61	118.8	-13.758	0.011	34.1	33.4	...	...
62	121.6	-13.520	0.008	39.9	46.1	3758.4	0.8
63	131.0	-13.384	0.005	77.3	54.2	8810.5	0.6
64	132.3	-13.560	0.004	123.0	42.5	818.5	7.0
65	102.9	-13.410	0.008	28.1	49.0	8491.8	0.4
66	45.8	-13.569	0.009	21.1	47.4	699.8	4.0
67	9.0	-13.685	0.006	27.2	69.6	317.0	13.4
68	20.7	-12.796	0.003	26.2	148.4	1465.5	6.2
69	50.3	-13.466	0.007	25.9	58.2	322.1	10.9
70	61.5	-13.404	0.005	59.8	60.3	...	...

(cont., next page)

Table 3-5 (cont.)

No. (1)	R (2)	log f(Hα) (3)	δ log f(Hα) (4)	EW_{tot} (5)	S/N (6)	EW_{cl} (7)	S/N (8)
71	66.8	-13.364	0.005	42.6	64.5	1261.8	3.6
72	67.3	-13.221	0.005	34.4	72.1	...	...
73	50.3	-13.466	0.007	25.9	58.2	322.1	10.9
74	3.6	-12.469	0.001	28.1	379.6	81.5	239.6
75	11.7	-13.229	0.003	51.4	122.0	1247.4	7.4
76	123.6	-13.108	0.003	86.9	67.6	1559.6	4.5
77	105.2	-13.830	0.013	29.4	29.4	635.3	2.9
78	89.7	-13.857	0.014	23.6	28.8	375.0	4.6
79	71.5	-13.471	0.007	36.1	53.3	2786.1	1.3
80	46.5	-13.784	0.007	58.5	42.5	1177.6	2.9
81	40.9	-13.318	0.004	52.7	78.4	765.6	7.8
82	42.0	-13.460	0.006	43.3	61.5	1432.2	3.0
83	26.0	-13.862	0.011	20.7	36.3	...	...
84	52.6	-13.620	0.010	21.0	42.2	555.9	4.5
85	69.7	-13.837	0.013	22.6	30.3	442.6	4.1
86	71.5	-13.788	0.014	18.7	29.0	4613.2	0.4
87	73.4	-14.157	0.022	18.2	18.6	2079.7	0.5
88	48.0	-13.944	0.014	22.0	29.8	290.4	6.0
89	53.1	-13.860	0.014	20.6	29.1	...	...
90	51.4	-14.006	0.016	23.2	25.6	...	...
91	40.0	-13.707	0.012	18.2	35.1	8394.6	0.2
92	54.2	-13.765	0.011	26.7	34.8	...	...
93	63.6	-13.888	0.012	28.1	32.5	447.7	4.5
94	62.0	-13.774	0.009	36.9	39.5	412.1	6.3
95	64.7	-13.776	0.009	41.3	37.9	...	...
96	81.4	-13.459	0.006	52.6	56.7	613.8	7.0
97	90.4	-13.375	0.005	74.3	56.8	1349.0	3.9
98	83.7	-13.676	0.007	54.8	42.3	2722.7	1.2
99	76.8	-13.476	0.006	53.9	53.9	...	...
100	70.5	-13.644	0.007	50.8	47.2	903.7	3.9
101	66.0	-13.763	0.009	37.2	40.4	472.1	5.7
102	57.7	-13.745	0.011	26.6	36.5	2290.9	1.0
103	87.4	-13.509	0.006	55.6	49.2	...	...
104	102.0	-13.533	0.007	58.6	45.3	2660.7	1.4
105	124.5	-13.698	0.008	65.0	36.7	517.6	6.0

(cont.. next page)

Table 3-5 (cont.)

No. (1)	R (2)	log f(Hα) (3)	δ log f(Hα) (4)	EW$_{tot}$ (5)	S/N (6)	EW$_{cl}$ (7)	S/N (8)
106	117.4	-13.852	0.016	26.1	23.9	...	...
107	119.3	-14.210	0.019	37.4	19.2	645.7	2.0
108	113.4	-13.921	0.016	31.0	23.5	...	...
109	79.9	-13.680	0.011	24.6	35.9	762.1	2.9
110	62.3	-13.249	0.005	42.9	71.8	1150.8	4.4
111	62.1	-13.632	0.008	35.4	44.2	1954.3	1.5
112	55.0	-13.261	0.004	53.8	74.0	990.8	5.8
113	68.1	-14.124	0.026	14.5	16.4	...	...
114	72.2	-13.847	0.016	18.2	25.4	...	...
115	92.7	-13.614	0.008	60.9	36.8	...	...
116	73.9	-13.974	0.018	22.7	22.1	...	...
117	70.5	-13.707	0.010	33.3	37.9	496.6	4.9
118	78.0	-13.680	0.009	46.0	36.2	...	...
119	104.3	-14.129	0.031	14.9	13.5	...	...
120	94.3	-13.860	0.014	30.5	27.2	333.4	5.1
121	91.4	-13.746	0.013	29.0	29.9	2600.2	0.7
122	111.9	-14.178	0.023	29.1	16.6	693.4	1.5
123	129.9	-14.098	0.019	36.2	18.8	418.8	2.9
124	124.1	-13.929	0.016	37.6	21.9	14825.2	0.1
125	111.9	-14.178	0.023	29.1	16.6	693.4	1.5
126	117.0	-14.068	0.027	17.9	15.3	...	...
127	141.4	-14.104	0.025	22.5	16.4	1757.9	0.6
128	129.1	-13.564	0.007	54.3	43.9	1150.8	3.0
129	137.8	-13.159	0.003	101.4	62.6	2558.6	2.8
130	132.1	-13.768	0.009	51.5	35.2	899.5	3.0
131	138.6	-13.463	0.003	145.9	46.0	1023.3	7.0
132	144.1	-13.843	0.005	113.0	35.0	402.7	10.8
133	141.8	-13.859	0.006	108.4	34.9	389.0	10.8
134	148.1	-13.185	0.002	152.8	62.9	703.1	14.5
135	168.9	-14.323	0.024	42.9	14.1	1828.1	0.5
136	170.0	-14.656	0.036	47.0	9.3	...	...
137	149.4	-13.911	0.013	40.8	27.9	253.5	7.4
138	126.3	-13.263	0.004	89.1	54.3	597.0	9.5
139	129.2	-13.647	0.009	53.2	36.6	1119.4	2.5
140	129.8	-13.555	0.007	63.4	41.3	1064.1	3.3

(cont.. next page)

Table 3-5 (cont.)

No. (1)	R (2)	log f(Hα) (3)	δ log f(Hα) (4)	EW_{tot} (5)	S/N (6)	EW_{cl} (7)	S/N (8)
141	123.2	-13.438	0.004	105.4	47.9	626.6	9.1
142	122.0	-13.305	0.002	219.3	45.7	751.6	13.7
143	112.4	-13.805	0.010	58.9	30.3	753.4	3.2
144	120.5	-13.417	0.007	49.2	46.1	15488.2	0.2
145	121.7	-13.777	0.012	36.6	31.4	399.0	5.2
146	113.7	-13.901	0.015	25.7	25.6	436.5	3.6
147	130.2	-13.665	0.012	22.4	32.3	673.0	2.9
148	123.2	-13.826	0.013	27.9	30.0	2421.0	0.8
149	122.1	-13.248	0.004	70.3	65.8	1678.8	3.5
150	110.2	-13.500	0.007	39.4	48.5	489.8	6.7
151	121.7	-12.531	0.001	138.7	137.2	845.3	24.2
152	146.8	-13.621	0.008	55.2	38.2	743.0	4.0
153	159.9	-13.416	0.008	40.5	43.8	553.4	5.4
154	163.4	-13.340	0.006	59.8	50.0	714.5	5.7
155	160.8	-14.127	0.021	34.0	17.9	...	...
156	168.9	-13.713	0.010	52.5	31.6	3069.0	0.8
157	177.3	-13.168	0.004	94.0	55.6	948.4	6.4
158	185.9	-13.536	0.007	90.6	34.2	1104.1	3.3
159	194.3	-14.018	0.012	66.7	23.1	629.5	3.2
160	187.7	-14.049	0.017	43.4	19.8	373.3	3.7
161	151.6	-14.399	0.039	15.7	10.8	1538.2	0.4
162	153.7	-14.723	0.061	13.7	6.9	...	...
163	163.5	-15.284	0.296	2.4	1.5	...	...
164	163.4	-14.843	0.081	10.6	5.3	363.1	0.8
165	171.2	-14.261	0.028	26.1	14.0	1188.5	0.7
166	184.4	-13.961	0.018	41.7	19.7	...	...
167	183.4	-15.249	0.205	6.0	2.1	...	...
168	154.0	-13.890	0.021	19.6	19.5	8609.9	0.1
169	133.6	-13.978	0.018	23.1	21.8	...	...
170	154.0	-13.812	0.010	56.8	30.4	1757.9	1.4
171	147.0	-13.909	0.012	45.6	26.8	494.3	3.9
172	143.4	-13.821	0.015	30.3	24.9	...	...
173	125.4	-13.929	0.010	65.2	28.7	...	...
174	120.5	-13.344	0.004	73.3	61.5	5199.9	1.1
175	113.9	-13.375	0.005	62.4	63.1	...	...

(cont., next page)

Table 3-5 (cont.)

No. (1)	R (2)	log f(Hα) (3)	δ log f(Hα) (4)	EW_{tot} (5)	S/N (6)	EW_{cl} (7)	S/N (8)
176	106.3	-13.548	0.005	62.1	53.2	873.0	5.1
177	105.9	-13.994	0.008	63.4	36.9	236.6	12.8
178	99.0	-13.701	0.010	34.6	38.0	...	...
179	98.2	-13.260	0.004	53.1	74.7	511.7	11.2
180	103.9	-13.701	0.008	35.0	47.4	223.9	13.5
181	113.6	-13.794	0.010	37.3	37.6	520.0	4.8
182	122.9	-13.470	0.007	47.6	48.3	1276.4	2.8
183	134.3	-13.645	0.009	65.8	32.9	1981.5	1.4
184	106.7	-14.179	0.017	31.9	21.6	2254.2	0.6
185	102.6	-13.800	0.010	41.3	35.8	1918.7	1.3
186	97.0	-13.610	0.008	37.6	45.7	1224.6	2.5
187	101.0	-13.827	0.010	38.8	34.4	909.9	2.6
188	98.8	-14.326	0.017	44.9	20.3	826.0	1.7
189	95.6	-13.869	0.011	31.3	33.2	865.0	2.4
190	87.8	-13.873	0.012	35.4	31.8	...	...
191	78.7	-14.084	0.019	20.8	21.7	1081.4	1.2
192	84.7	-13.709	0.010	30.8	38.4	...	...
193	83.0	-13.999	0.015	25.5	25.7	...	...
194	76.6	-14.148	0.022	18.2	19.0	...	...
195	109.0	-14.054	0.017	38.5	20.4	...	...
196	108.7	-13.777	0.009	65.9	30.3	78886.0	0.0
197	118.8	-14.216	0.019	35.3	19.3	196.8	6.2
198	112.2	-13.440	0.007	39.1	47.8	505.8	6.4
199	95.2	-13.963	0.014	34.8	26.0	1037.5	1.6
200	82.2	-13.955	0.017	17.2	23.8	909.9	1.5
201	74.8	-13.962	0.011	38.5	33.7	613.8	3.7
202	111.3	-13.500	0.007	50.0	44.2	550.8	6.0
203	105.7	-14.246	0.020	33.7	18.2	334.2	3.5
204	83.2	-12.964	0.002	164.8	78.0	816.6	16.6
205	123.5	-14.267	0.028	25.8	13.8	...	...
206	70.1	-14.308	0.023	38.3	15.2	325.8	3.1
207	133.6	-14.107	0.015	56.0	20.7	341.2	4.7
208†	187.8	-12.506	0.001	151.4	134.6	557.2	38.8
209	182.2	-13.963	0.007	139.6	22.2	1174.9	2.8
210	141.2	-13.694	0.010	57.5	31.6	1909.9	1.3

(cont.. next page)

Table 3-5 (cont.)

No. (1)	R (2)	log f(Hα) (3)	δ log f(Hα) (4)	EW_{tot} (5)	S/N (6)	EW_{cl} (7)	S/N (8)
211	172.8	-13.968	0.014	41.4	24.3	...	...
212	182.6	-13.708	0.012	34.7	31.2	3311.3	0.6
213	190.7	-13.545	0.009	35.6	38.6	544.5	4.7
214	173.2	-14.274	0.022	31.0	17.4	297.2	3.7
215	160.5	-14.006	0.016	36.6	23.2	537.0	2.9
216	151.6	-13.931	0.013	46.5	25.3	1047.1	1.7
217	147.5	-13.725	0.008	69.2	33.2	563.6	5.2
218	140.4	-13.869	0.011	60.9	25.7	...	...
219	129.4	-14.869	0.086	10.4	5.0	368.1	0.8
220	151.5	-14.368	0.036	18.9	11.4	...	...
221	171.4	-13.460	0.007	49.3	48.7	440.6	8.2
222	169.6	-13.940	0.017	26.5	23.3	749.9	1.9
223	223.9	-13.400	0.005	168.3	28.1	...	...
224	223.7	-13.991	0.015	43.7	22.6	239.3	6.5
225	222.1	-13.879	0.012	62.2	24.8	861.0	2.4
226	210.4	-13.761	0.009	69.3	30.5	571.5	4.7
227	205.0	-12.816	0.002	175.4	74.2	885.1	15.4
228	213.2	-14.261	0.028	25.5	14.0	897.4	0.9
229	192.4	-14.513	0.026	53.9	12.2	...	...
230	198.0	-13.962	0.011	73.1	24.8	501.2	4.5
231	206.2	-14.427	0.041	17.0	10.1	...	...
232†	205.6	...	...	...	...	...	...
233	197.1	-13.384	0.004	136.1	43.9	820.4	7.9
234	197.5	-13.606	0.006	84.3	38.4	552.1	7.0
235	183.7	-14.054	0.017	38.3	20.5	...	...
236	177.4	-13.835	0.011	47.0	31.4	334.2	6.8
237	180.9	-14.093	0.014	51.9	22.1	644.2	2.6
238	318.5	-13.510	0.006	301.3	12.6	1081.4	3.6
239	302.2	-13.857	0.011	266.7	8.0	1061.7	2.0
240	268.9	-13.781	0.012	127.9	14.8	765.6	2.7
241	249.0	-13.749	0.011	62.5	26.6	450.8	4.9
242	243.8	-13.047	0.003	122.7	59.5	1327.4	6.0
243	236.8	-13.560	0.008	65.9	33.4	3258.4	0.9
244	234.7	-13.768	0.009	94.6	24.3	478.6	5.5
245	229.1	-13.787	0.009	104.0	21.7	5370.3	0.5

(cont., next page)

Table 3-5 (cont.)

No. (1)	R (2)	log f(Hα) (3)	δ log f(Hα) (4)	EW_{tot} (5)	S/N (6)	EW_{cl} (7)	S/N (8)
246	210.5	-12.913	0.003	94.4	69.9	931.1	8.2
247	222.2	-12.621	0.001	182.0	87.5	1028.0	16.2
248	249.7	-14.003	0.012	129.7	14.7	701.5	2.9
249	213.6	-13.875	0.012	54.5	26.8	185.8	10.8
250	209.2	-13.833	0.010	76.7	24.3	606.7	3.8
251	203.0	-14.090	0.019	51.2	16.8	...	...
252	179.3	-14.066	0.018	46.1	18.6	1219.0	1.1
253	182.5	-14.293	0.030	29.0	12.7	1412.5	0.6
254	210.0	-13.940	0.013	64.9	21.0	12647.4	0.1
255	209.8	-13.916	0.013	61.2	23.0	875.0	2.2
256	174.1	-13.873	0.017	32.7	21.7	...	...
257	150.9	-13.941	0.017	29.0	22.8	2404.4	0.6
258	137.7	-13.619	0.008	47.9	41.0	461.3	6.5
259	205.0	-13.475	0.007	78.5	36.4	1078.9	3.2
260	211.0	-13.813	0.010	106.9	20.0	2824.9	0.9
261	185.1	-13.730	0.008	95.3	26.4	3706.8	0.8
262	174.8	-13.833	0.013	48.2	24.9	...	...
263	162.3	-13.885	0.015	36.4	24.5	...	...
264	161.7	-14.141	0.016	47.8	20.6	1148.2	1.3
265	227.8	-14.123	0.020	97.1	10.5	719.4	1.6
266	221.7	-14.137	0.021	91.2	10.7	2904.0	0.4
267	214.9	-13.114	0.002	396.3	30.1	990.8	12.1
268	197.3	-12.968	0.002	246.6	53.2	883.1	15.2
269	192.5	-13.180	0.002	192.3	51.6	493.2	20.8
270	180.8	-13.654	0.005	153.8	28.3	613.8	7.5
271	182.6	-13.363	0.004	162.9	39.4	591.6	11.4
272	198.3	-13.541	0.005	161.4	26.4	778.0	5.8
273	196.3	-13.792	0.012	72.8	22.0	1049.5	1.9
274	187.5	-13.770	0.014	49.4	23.8	877.0	2.0
275	178.1	-13.983	0.015	55.3	20.8	...	...
276	166.1	-13.460	0.007	67.6	41.4	1790.6	2.0
277	148.7	-13.366	0.004	105.4	45.1	...	...
278	131.6	-14.125	0.021	22.9	19.5	847.2	1.4
279	124.2	-14.240	0.020	32.7	18.6	...	...
280	118.2	-13.830	0.010	43.1	32.9	1023.3	2.3

(cont.. next page)

Table 3-5 (cont.)

No. (1)	R (2)	log f(Hα) (3)	δ log f(Hα) (4)	EW_{tot} (5)	S/N (6)	EW_{cl} (7)	S/N (8)
281	121.8	-13.723	0.008	53.0	38.6	1233.1	2.4
282	131.5	-13.245	0.004	73.8	64.3	13740.4	0.4
283	131.6	-13.069	0.003	75.7	81.2	1166.8	6.5
284	133.3	-13.160	0.003	82.2	72.8	905.7	8.0
285	143.0	-12.658	0.001	137.4	116.3	704.7	24.4
286	157.5	-13.602	0.005	173.0	28.7	2317.4	2.2
287	165.8	-12.083	0.001	345.1	134.6	1180.3	39.8
288	177.4	-13.765	0.011	73.3	23.3	...	...
289	201.3	-13.882	0.015	90.2	15.5	2760.6	0.6
290	193.8	-13.997	0.015	86.1	15.4	875.0	1.8
291	194.8	-13.589	0.007	115.1	25.2	550.8	5.8
292	201.9	-13.181	0.004	151.0	42.8	374.1	18.2
293	142.7	-12.912	0.003	100.2	83.8	863.0	11.1
294	133.3	-13.268	0.004	89.9	63.7	849.2	7.9
295	131.5	-13.069	0.003	75.7	81.2	1166.8	6.5
296	194.3	-13.748	0.013	86.9	18.1	2152.8	0.9
297	140.8	-13.687	0.009	54.2	33.1	...	...
298	123.4	-13.107	0.003	116.1	63.4	1330.5	6.1
299	123.9	-13.544	0.007	60.8	43.3	547.0	6.5
300	134.5	-13.647	0.007	80.5	36.1	...	...
301	141.8	-12.610	0.002	68.9	124.1	758.6	14.4
302	148.1	-13.623	0.008	54.6	38.2	1318.3	2.3
303	187.0	-12.351	0.001	209.9	91.8	1233.1	16.1
304	174.0	-13.199	0.005	93.1	45.7	1044.7	4.7
305	177.6	-13.848	0.011	86.9	21.5	2404.4	0.9
306	159.8	-13.622	0.010	52.5	32.6	9749.9	0.3
307	150.5	-13.025	0.002	161.8	68.9	926.8	12.7
308	166.7	-14.114	0.020	48.0	16.4	19952.6	0.1
309	210.3	-14.182	0.023	46.2	14.2	...	...
310	216.8	-13.868	0.014	69.3	19.1	1078.9	1.6
311	230.4	-14.089	0.019	66.1	14.8	714.5	1.8
312	236.3	-13.587	0.012	72.8	22.2	5662.4	0.4
313	232.5	-14.835	0.054	107.9	3.7	...	...
314	251.8	-13.912	0.016	134.6	10.5	765.6	2.0
315	296.6	-14.233	0.026	218.3	4.1	...	...

(cont., next page)

Table 3-5 (cont.)

No. (1)	R (2)	log f(Hα) (3)	δ log f(Hα) (4)	EW_{tot} (5)	S/N (6)	EW_{cl} (7)	S/N (8)
316	296.6	-14.158	0.022	192.3	5.4	2118.4	0.5
317	307.8	-13.876	0.015	132.4	11.6	1318.3	1.3
318	297.4	-13.253	0.005	258.8	18.9	1432.2	3.5
319	296.7	-13.775	0.007	330.4	10.5	1213.4	2.9
320	296.7	-13.136	0.003	386.4	19.6	2060.6	3.7
321	290.4	-12.868	0.002	279.9	37.2	1386.8	7.7
322	283.1	-13.380	0.005	289.1	17.7	5781.0	0.9
323	286.5	-11.460	0.000	701.5	280.7	847.5	100.8
324	282.2	-12.952	0.001	405.5	56.9	1402.8	16.6
325	278.7	-12.467	0.001	497.7	85.1	1066.6	39.9
326	274.8	-13.739	0.004	309.7	17.8	1345.9	4.2
327	294.7	-13.246	0.005	156.3	30.6	1342.8	3.8
328	277.3	-13.034	0.002	324.3	35.1	1584.9	7.3
329	270.5	-12.772	0.001	435.5	48.1	955.0	22.1
330	292.6	-13.877	0.015	87.7	16.0	1534.6	1.1
331	299.3	-14.080	0.019	72.8	14.2	327.3	3.9
332	300.0	-13.839	0.016	816.6	1.8	...	...
333	277.1	-14.281	0.029	100.0	7.2	...	...
334	255.2	-14.302	0.023	82.4	10.5	3243.4	0.3
335	248.8	-12.617	0.001	338.8	55.2	1129.8	16.7
336	244.4	-13.989	0.008	188.8	16.0	527.2	5.9
337	352.5	-14.168	0.023	606.7	1.7	7128.5	0.1
338	380.7	-14.030	0.017	...	...	...	...
339	333.3	-13.927	0.020	91.8	11.5	478.6	2.6
340	322.2	-13.841	0.011	152.1	13.9	296.5	7.5
341	313.7	-13.971	0.014	162.6	9.7	1081.4	1.5
342	403.9	-13.856	0.011	420.7	5.1	3564.5	0.6
343	401.4	-14.302	0.023	266.1	3.8	765.6	1.4
344	387.9	-14.085	0.023	139.6	6.8	394.5	2.6
345	312.9	-13.884	0.015	378.4	4.3	4187.9	0.4
346	312.9	-14.090	0.019	234.4	5.3	659.2	1.9
347	431.4	-13.503	0.006	258.2	14.9	751.6	5.2
348	433.7	-13.988	0.015	161.8	9.4	950.6	1.7
349	414.2	-13.321	0.006	334.2	12.6	1717.9	2.5
350	422.9	-14.330	0.025	369.8	2.6	3890.5	0.3

(cont., next page)

Table 3-5 (cont.)

No. (1)	R (2)	log f(Hα) (3)	δ log f(Hα) (4)	EW_{tot} (5)	S/N (6)	EW_{cl} (7)	S/N (8)
351	403.0	-12.995	0.002	638.3	19.7	1614.4	7.8
352	398.1	-13.503	0.004	357.3	18.1	841.4	7.8
353	390.2	-14.308	0.016	258.2	5.7	1158.8	1.3
354	391.8	-13.834	0.008	263.6	11.3	979.5	3.1
355	383.8	-13.899	0.015	217.8	7.0	...	...
356	384.4	-13.803	0.007	263.6	12.2	787.0	4.2
357	388.9	-14.038	0.013	260.6	7.2	2666.9	0.7
358	391.9	-13.169	0.005	384.6	13.7	1663.4	3.2
359	377.9	-13.413	0.005	296.5	16.0	1496.2	3.2
360	366.6	-13.605	0.005	337.3	15.1	2890.7	1.8
361	347.7	-13.343	0.003	179.5	37.8	613.8	11.5
362	349.4	-13.023	0.001	477.5	41.1	984.0	20.1
363	353.6	-13.436	0.002	580.8	19.3	6137.6	1.8
364	359.9	-13.079	0.001	380.2	45.2	875.0	19.9
365	360.7	-13.456	0.002	354.0	30.0	963.8	11.1
366	357.4	-13.378	0.003	528.4	16.4	4830.6	1.8
367	363.0	-12.470	0.001	578.1	72.9	1241.7	34.0
368	370.5	-12.455	0.001	582.1	74.9	961.6	45.5
369	341.3	-13.234	0.005	191.9	26.1	1013.9	5.1
370	347.0	-13.814	0.008	243.8	12.8	1172.2	2.7
371	351.1	-14.172	0.012	203.7	9.8	762.1	2.7
372	351.6	-13.743	0.009	141.9	18.6	4149.5	0.7
373	359.5	-13.310	0.005	155.9	30.9	855.1	6.0
374	357.8	-13.904	0.009	167.1	14.8	...	...
375	376.9	-13.704	0.010	227.0	10.6	1025.7	2.4
376	387.2	-13.528	0.007	246.6	14.7	538.3	6.8
377	391.9	-13.445	0.005	463.4	9.6	1584.9	2.8
378	362.7	-13.861	0.011	285.8	7.4	...	...
379	360.4	-13.485	0.006	363.1	11.1	15452.5	0.3
380	354.1	-13.633	0.008	232.8	12.2	...	...
381	353.7	-13.173	0.004	289.1	20.4	1261.8	4.8
382	335.6	-13.699	0.012	170.2	11.7	1896.7	1.1
383	340.9	-13.829	0.013	372.4	4.9	...	...
384	341.5	-13.949	0.017	192.3	7.0	1853.5	0.8
385	330.2	-14.019	0.020	170.6	6.7	4797.3	0.2

(cont.. next page)

Table 3-5 (cont.)

No. (1)	R (2)	log f(Hα) (3)	δ log f(Hα) (4)	EW_{tot} (5)	S/N (6)	EW_{cl} (7)	S/N (8)
386	387.9	-14.101	0.024	135.2	6.8	417.8	2.3
387	414.2	-13.282	0.006	289.7	13.9	1595.9	2.6
388	423.0	-14.158	0.022	267.9	4.0	1690.4	0.6
389	431.4	-13.179	0.006	187.1	21.3	1161.4	3.6

Explanation of Columns for Table 3-5

(1) The HII region number as mapped in Figures 3-7 and 3-8.

(2) Galactocentric radius in the plane of the galaxy (in arcminutes).

(3) Logarithm of Hα flux ($erg\ cm^{-2}\ s^{-1}$).

(4) Uncertainty in log f(Hα), based on noise in the subtracted sky brightness.

(5) Hα equivalent width (in Å), where the ambient disk light is included as part of the red continuum.

(6) Signal-to-noise ratio pertaining to EW_{tot}, based on combined uncertainties in the Hα and red-continuum emission.

(7) Hα equivalent width (in Å) of the ionizing cluster, where the ambient disk light has been subtracted.

(8) Signal-to-noise ratio pertaining to EW_{cl}, based on combined uncertainties in the Hα emission of the HII region and the red-continuum emission of the isolated cluster.

† Vignetted in image(s).

Table 3–6
Hα Luminosity Distributions

log L(Hα) (1)	N (R < 5 kpc) (2)	N (5 kpc < R < 10 kpc) (3)
36.00 - 36.25	2	0
36.25 - 36.50	0	0
36.50 - 36.75	3	1
36.75 - 37.00	4	0
37.00 - 37.25	17	6
37.25 - 37.50	55	20
37.50 - 37.75	87	27
37.75 - 38.00	60	11
38.00 - 38.25	35	12
38.25 - 38.50	16	10
38.50 - 38.75	4	2
38.75 - 39.00	5	5
39.00 - 39.25	1	0
39.25 - 39.50	1	0
39.50 - 39.75	0	0
> 39.75	0	1

Explanation of Columns for Table 3-6

(1) Range of Hα luminosities, where the assumed distance to M101 is 4.8 Mpc. No correction for extinction has been made. A mean extinction of $A_v = 1$ would shift the bins by 0.29 in log L(Hα). The extinction uncertainty is of similar magnitude.

(2) Number of HII regions that are located within a galactocentric radius of 5 kpc. The total number of such HII regions is 290.

(3) Number of HII regions that are located between R = 5 kpc and R = 10 kpc. The total number obtained from the observed fields is 95. However, this under-represents the total number between R = 5 kpc and R = 10 kpc by a factor of roughly 6 (based on the fraction of the annulus that was actually imaged).

Table 3–7

Maximum Likely Stellar Masses in Finite Clusters

(where the theoretical upper mass limit is 200 $M_\odot$)

	$\alpha = 2.0$			$\alpha = 2.5$			$\alpha = 3.0$		
M_l	0.1	1.0	3.0	0.1	1.0	3.0	0.1	1.0	3.0
M_{cl}									
10^3	79	97	109	22	47	66	7	20	38
10^4	174	181	184	85	136	158	22	67	105
10^5	197	198	198	172	191	195	67	149	178
10^6	200	200	200	197	200	200	149	192	197

Figures

Figure 3–1

Kinematic properties of M101's disk. All quantities are based on the HI rotation curve of Bosma *et al.* (1981), which was derived from the synthesis mapping of Allen and Goss (1979). The corresponding spatial resolution is 45″ (1.05 kpc at 4.8 Mpc distance).

a. The HI rotation curve of Bosma *et al.* (1981). The last 3 points (not plotted by Bosma *et al.*) were taken from their kinematic map. The increasing uncertainties at larger galactocentric radii are caused by the increasing asymmetry in the distribution and kinematics of the HI at these radii.

b. The angular velocity Ω and the difference between the angular velocity and the epicyclic frequency κ divided by the number of spiral arms. According to the density wave theory of spiral structure, the regime of spiral structure is confined by these two profiles. For example, a spiral wave with a pattern speed of $\Omega_p = 20\ km\ s^{-1}\ kpc^{-1}$ would be able to operate between inner Lindblad resonance at $R \approx 2$ kpc and corotation at $R \approx 10$ kpc. The spiral structure in M101, however, is observed to go all the way into the nucleus (Sandage 1961), thus complicating the simple picture outlined by the density wave theory.

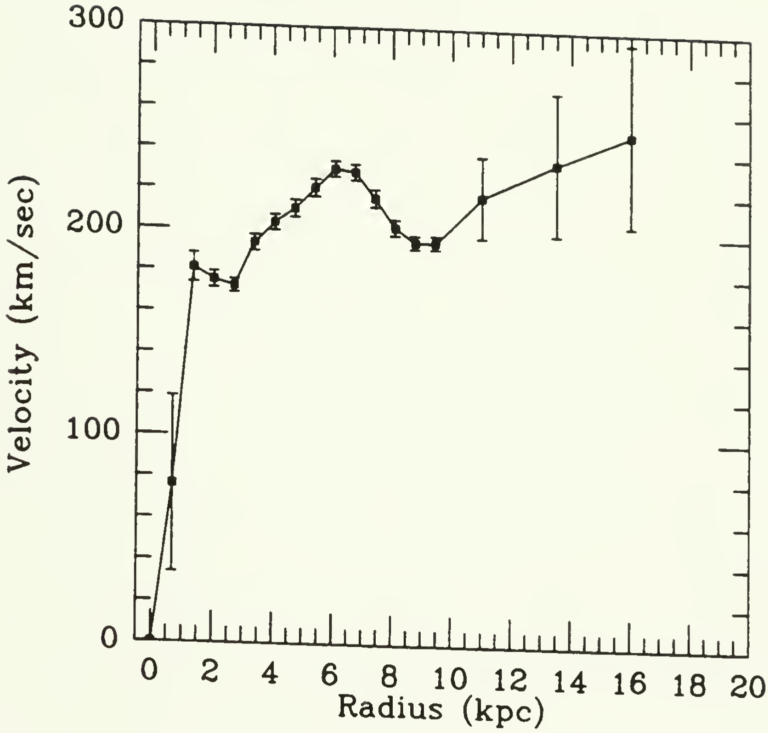

300
200
100
0
Velocity (km/sec)
0 2 4 6 8 10 12 14 16 18 20
Radius (kpc)

a ▲ b ▼

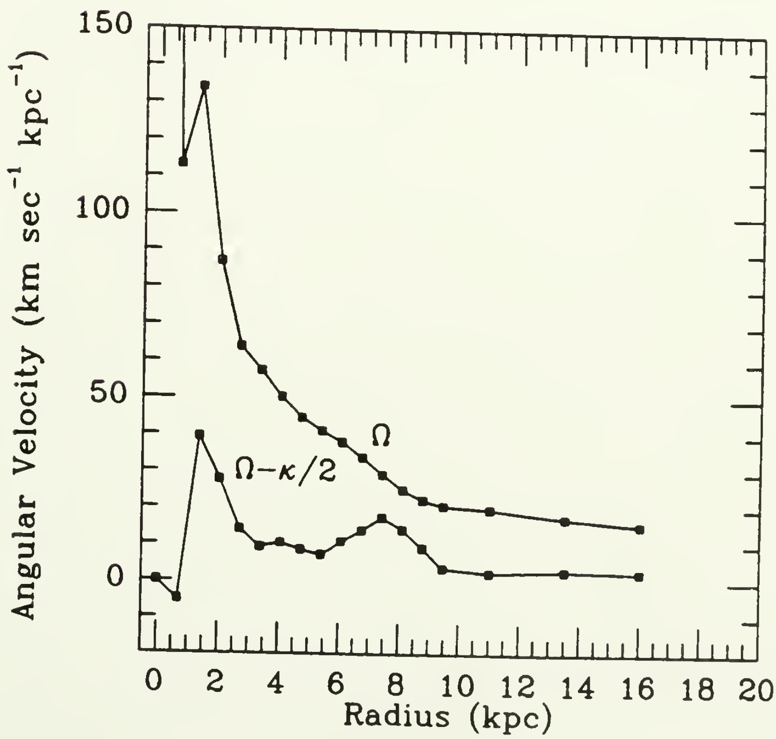

150
100
50
0
Angular Velocity (km sec^{-1} kpc^{-1})
Ω
Ω−κ/2
0 2 4 6 8 10 12 14 16 18 20
Radius (kpc)

Figure 3-1 (cont.)

c. The relative velocity between the gas in the disk and the spiral wave for 3 different values of the pattern speed. If star formation depends on gas-wave interactions. (*i.e.* $\sigma(SFR) \propto \sigma(gas)R(\Omega - \Omega_p)$), then it should show a strong decline beyond 6 kpc radii. See, however, Figure 3-9.

d. The differential rotation, $d\Omega/dR$, in the disk. Solid-body rotation corresponds to $d\Omega/dR = 0$.

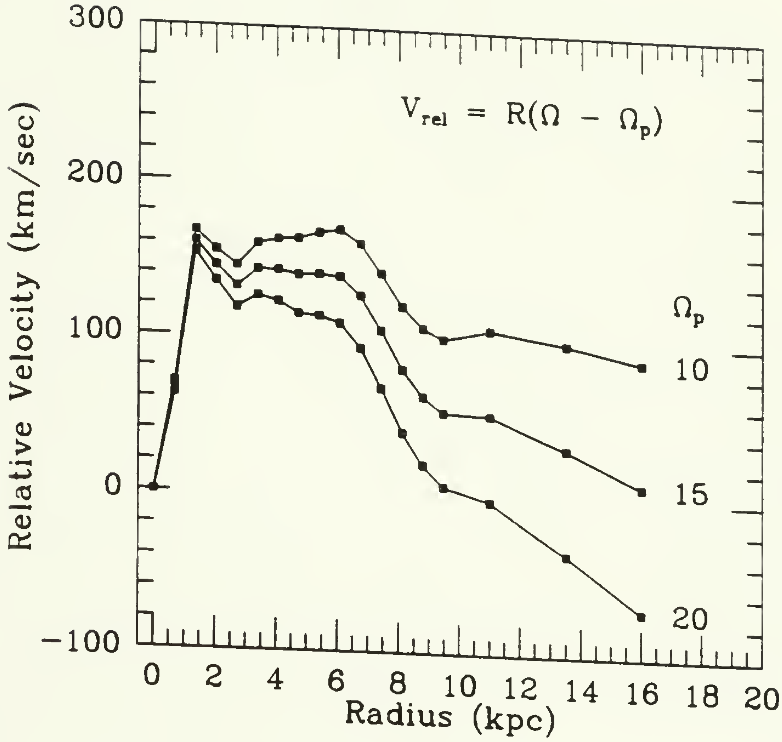
300
200
100
0
−100
Relative Velocity (km/sec)
$V_{rel} = R(\Omega - \Omega_p)$
Ω_p
10
15
20
0
2
4
6
8
10
12
14
16
18
20
Radius (kpc)

c ▲ d ▼

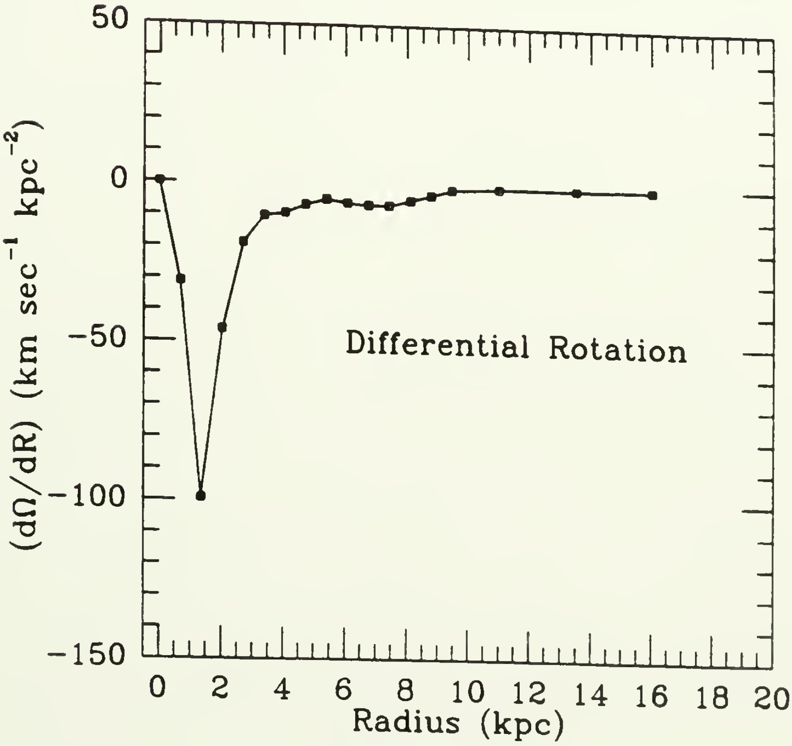
50
0
−50
−100
−150
$(d\Omega/dR)$ (km sec^{-1} kpc^{-2})
Differential Rotation
0
2
4
6
8
10
12
14
16
18
20
Radius (kpc)

Figure 3-1 (cont.)

e. The coefficient of rotational shear, otherwise known as Oort's constant A, in units of km s^{-1} kpc^{-1}, where the shear flow is $\Delta V = -2A\Delta R$.

f. The coefficient of tidal acceleration, in units of km s^{-2} kpc^{-2}, where the acceleration is in the radial direction. From the formulation of Stark and Blitz (1978) (see also Blitz and Glassgold [1982]).

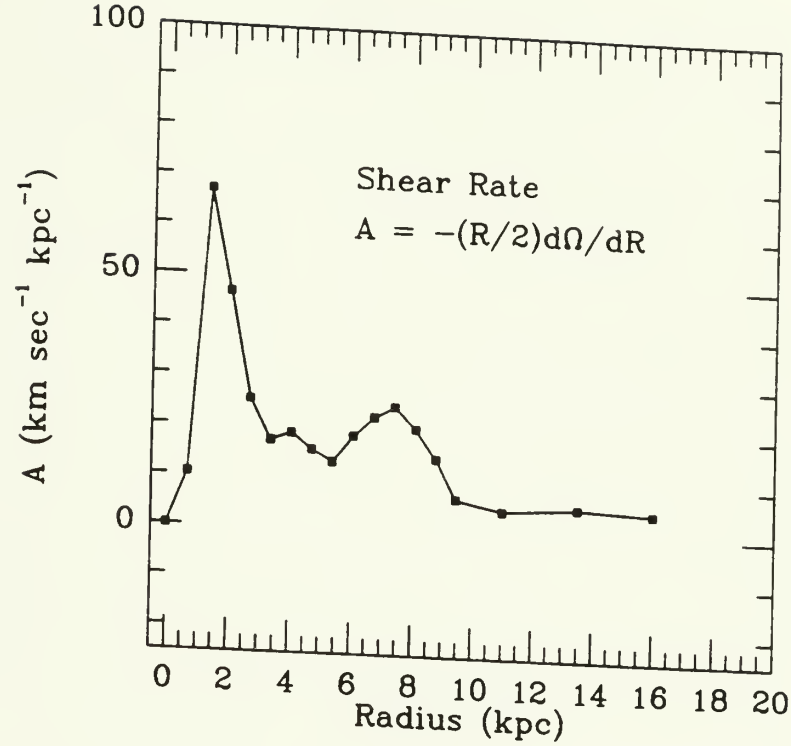
100
50
0
A (km sec^{-1} kpc^{-1})
Shear Rate
A = −(R/2)dΩ/dR
0 2 4 6 8 10 12 14 16 18 20
Radius (kpc)

e ▲ f ▼

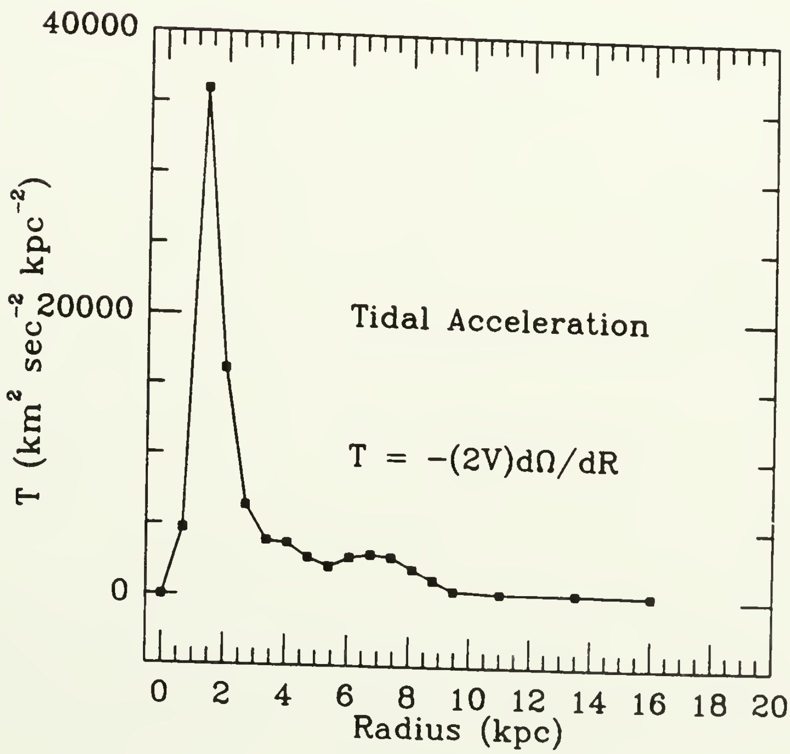
40000
20000
0
T (km^2 sec^{-2} kpc^{-2})
Tidal Acceleration
T = −(2V)dΩ/dR
0 2 4 6 8 10 12 14 16 18 20
Radius (kpc)

Figure 3–2

Spectroscopic properties of bright HII regions in M101. The spectroscopic line ratios and equivalent widths have been culled from Searle (1971), Smith (1975), Shields and Searle (1978), Rayo *et al.* (1982), McCall *et al.* (1985), and Davidson *et al.* (1985). Galactocentric radii have been computed using $d(M101) = 4.8$ Mpc. The ratios deal with relative fluxes or relative abundances (rather than the logarithm of these quantities) and are plotted on a logarithmic scale.

a. The ratio of the [OIII]($\lambda\lambda$4959, 5007) flux relative to the Hβ(λ4861) flux. This is also known as the "excitation" of the HII region. It is sensitive to both changes in the O/H abundance ratio and in the hardness of the UV radiation field from the exciting stars.

b. The ratio of the [OIII] flux relative to the OII(λ3727) flux. It is sensitive to the hardness of the stellar UV radiation field, the geometry of the HII region, and the degree of reddening.

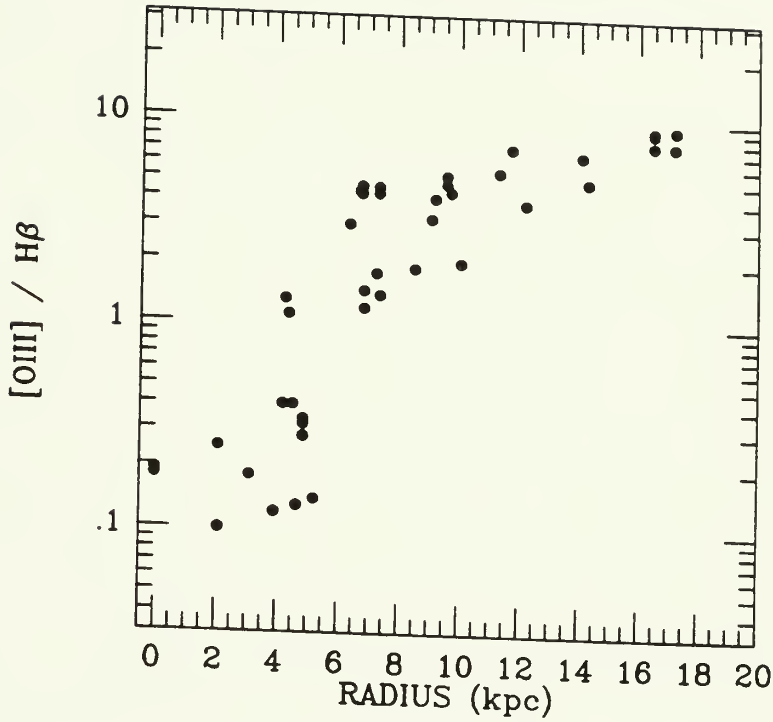
10
1
.1
[OIII] / Hβ
0
2
4
6
8
10
12
14
16
18
20
RADIUS (kpc)

a ▲ **b ▼**

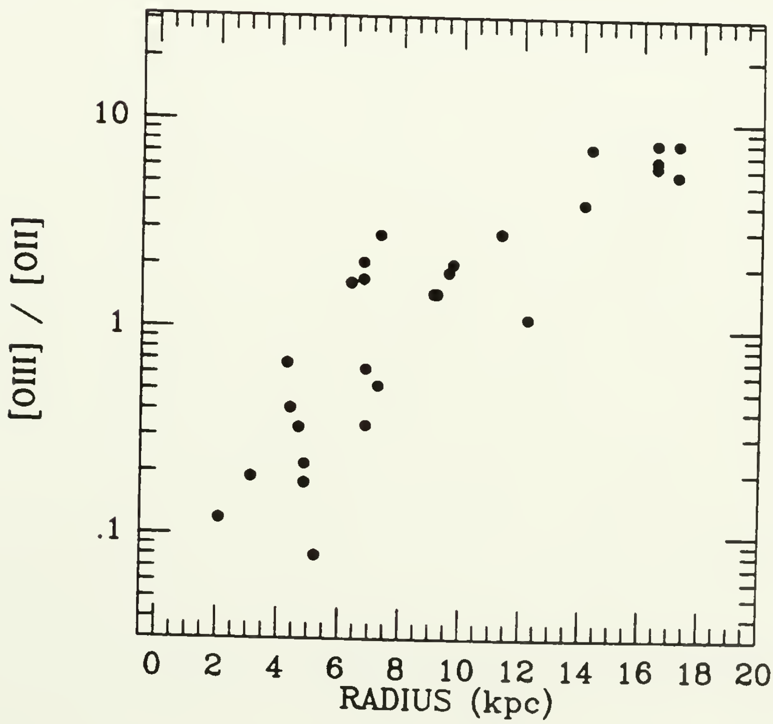
10
1
.1
[OIII] / [OII]
0
2
4
6
8
10
12
14
16
18
20
RADIUS (kpc)

Figure 3-2 (cont.)

c. The ratio of the [OII] + [OIII] fluxes relative to the Hβ flux. This ratio is highly sensitive to the O/H abundance ratio except at the metal-rich end, where the calibration is less certain.

d. The O/H abundance ratio as determined from the semi-empirical calibration of the [OII] + [OIII] / Hβ ratio by McCall *et al.* (1985). The straight line is the fit obtained by Evans (1986) using a similar database but a slightly different calibration. The connected triangles represent especially bright HII regions, whose faint [OIII]λ4363 auroral emission has been measured spectroscopically, thus enabling a more precise computation of the O/H abundance (Torres-Peimbert *et al.* 1989). In all three representations, the O/H abundance ratio exhibits a smooth (*i.e.* monotonic) decrease with galactocentic radius. Solar abundance is indicated by the ⊙ symbol.

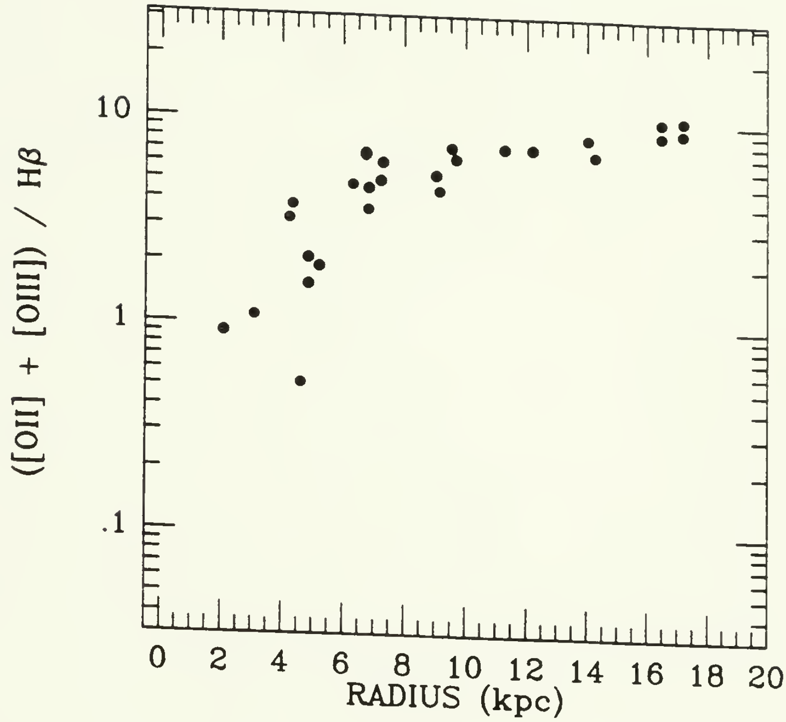
([OII] + [OIII]) / Hβ
10
1
.1
0 2 4 6 8 10 12 14 16 18 20
RADIUS (kpc)

c ▲ **d ▼**

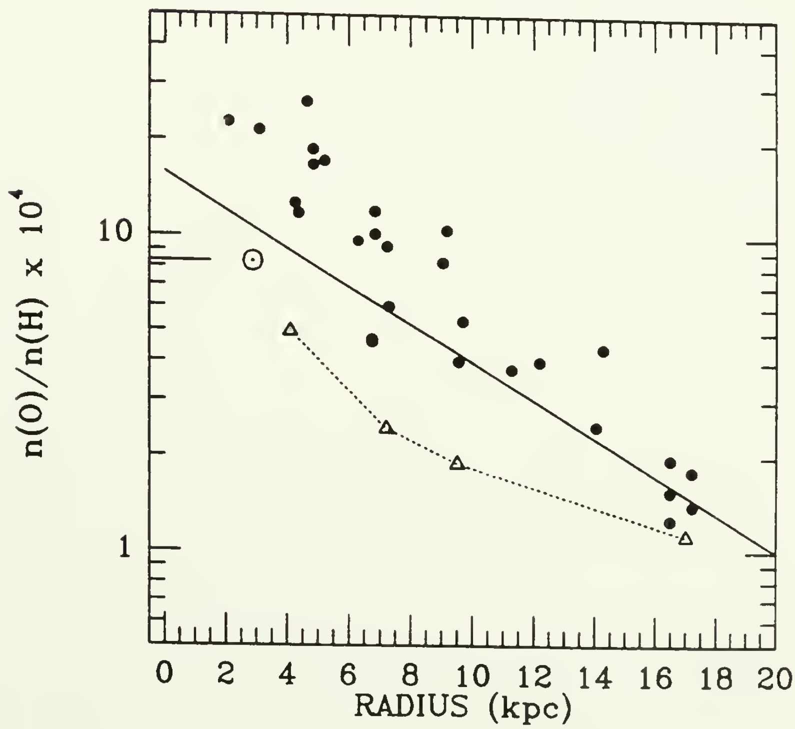
n(O)/n(H) x 10^4
10
1
0 2 4 6 8 10 12 14 16 18 20
RADIUS (kpc)

Figure 3-2 (cont.)

e. The ratio of the [NII] ($\lambda\lambda$6548, 6584) flux relative to the Hα(λ6563) flux.

f. The Hβ line-to-continuum ratio or "equivalent width" of the ionizing clusters. The squares denote the original 6 HII regions observed by Searle (1971) and interpreted by Shields and Tinsley (1976). Some attempt has been made to subtract off the ambient starlight of the disk from the measured continua, so that the equivalent widths better trace the radiation fields of the ionizing clusters. The circles are from McCall *et al.* (1985), and the triangles are from Rayo *et al.* (1982), where the equivalent widths include the starlight of the ambient disk.

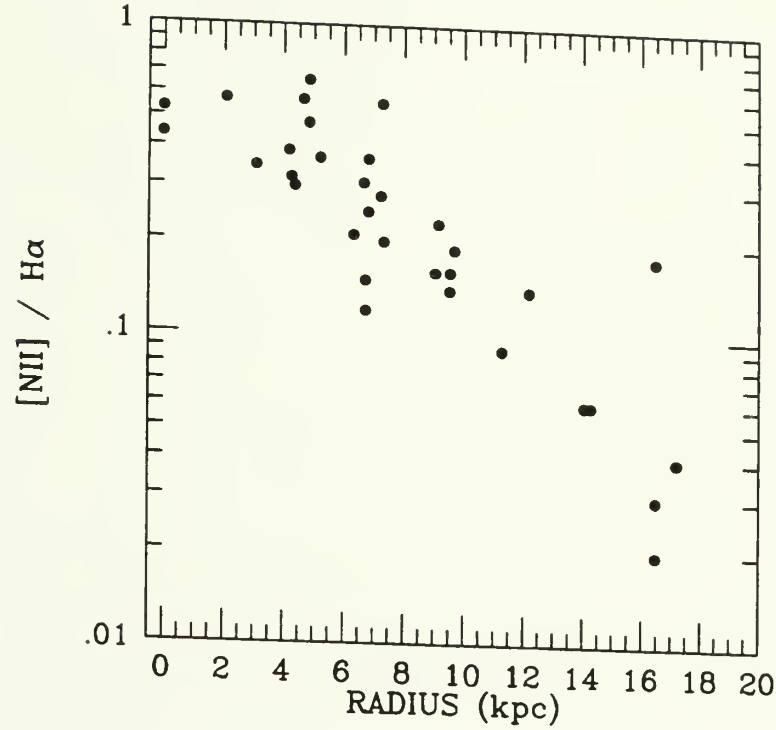
1
.1
.01
[NII] / Hα
0 2 4 6 8 10 12 14 16 18 20
RADIUS (kpc)

e▲ **f▼**

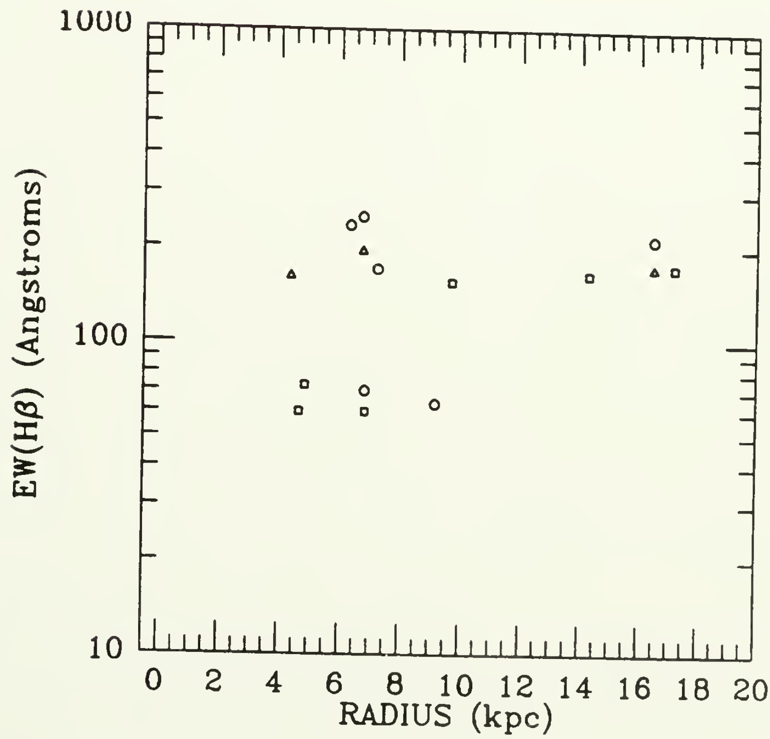
1000
100
10
EW(Hβ) (Angstroms)
0 2 4 6 8 10 12 14 16 18 20
RADIUS (kpc)

Figure 3–3

Red continuum and Hα imagery (inner galaxy).

Images of the red continuum and Hα emission from the inner disk of M101. North is up and East is to the left. The total field of view is about $5' \times 6'$. However, vignetting at the margins of the field reduces the relevant field to about $5' \times 5'$.

a. Red continuum emission, based on an R-band image whose Hα emission within the bandpass has been removed (see Appendix B).

b. Hα emission, based on a 36 Å bandwidth Hα image whose continuum emission within the bandpass has been removed (see Appendix B).

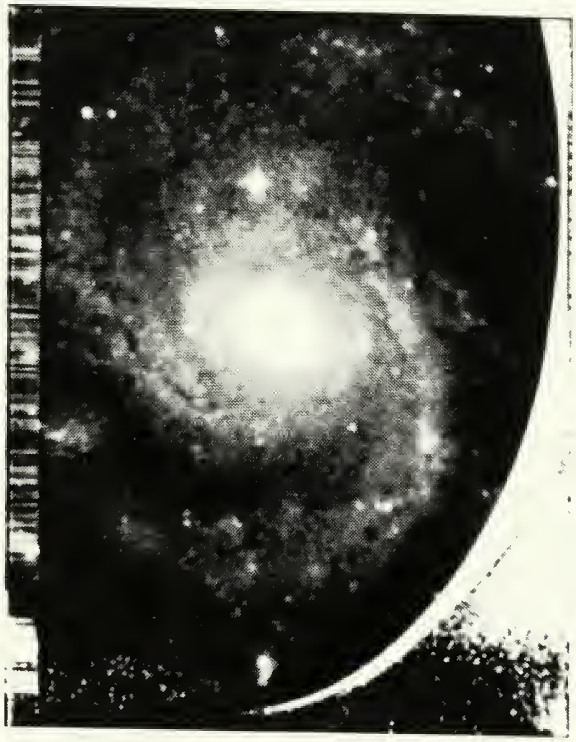

a ▲ b ▼

Figure 3–4

Red continuum and Hα imagery (eastern arms).

Images of the red continuum and Hα emission from the eastern spiral arms of M101. These images are displaced eastward about 4.3′ with respect to those of the inner galaxy. The same angular dimensions as in the inner galaxy images. Most prominent are the "superassociations" NGC 5462 to the North and NGC 5461 to the South.

a. Red continuum emission, based on an R-band image whose $H\alpha$ emission within the bandpass has been removed (see Appendix B).

b. Hα emission, based on a 36 Å bandwidth Hα image whose continuum emission within the bandpass has been removed (see Appendix B).

a ▲ b ▼

Figure 3–5

Comparison of raw and processed photometry.

Comparison of equivalent width EW_R, based on photometry of *raw* R band and Hα band images, with EW_P, based on photometry of *processed* red-continuum and Hα emission-line images. The straight line denotes $EW_P = EW_R$. Derivations from this line are less than 5 percent.

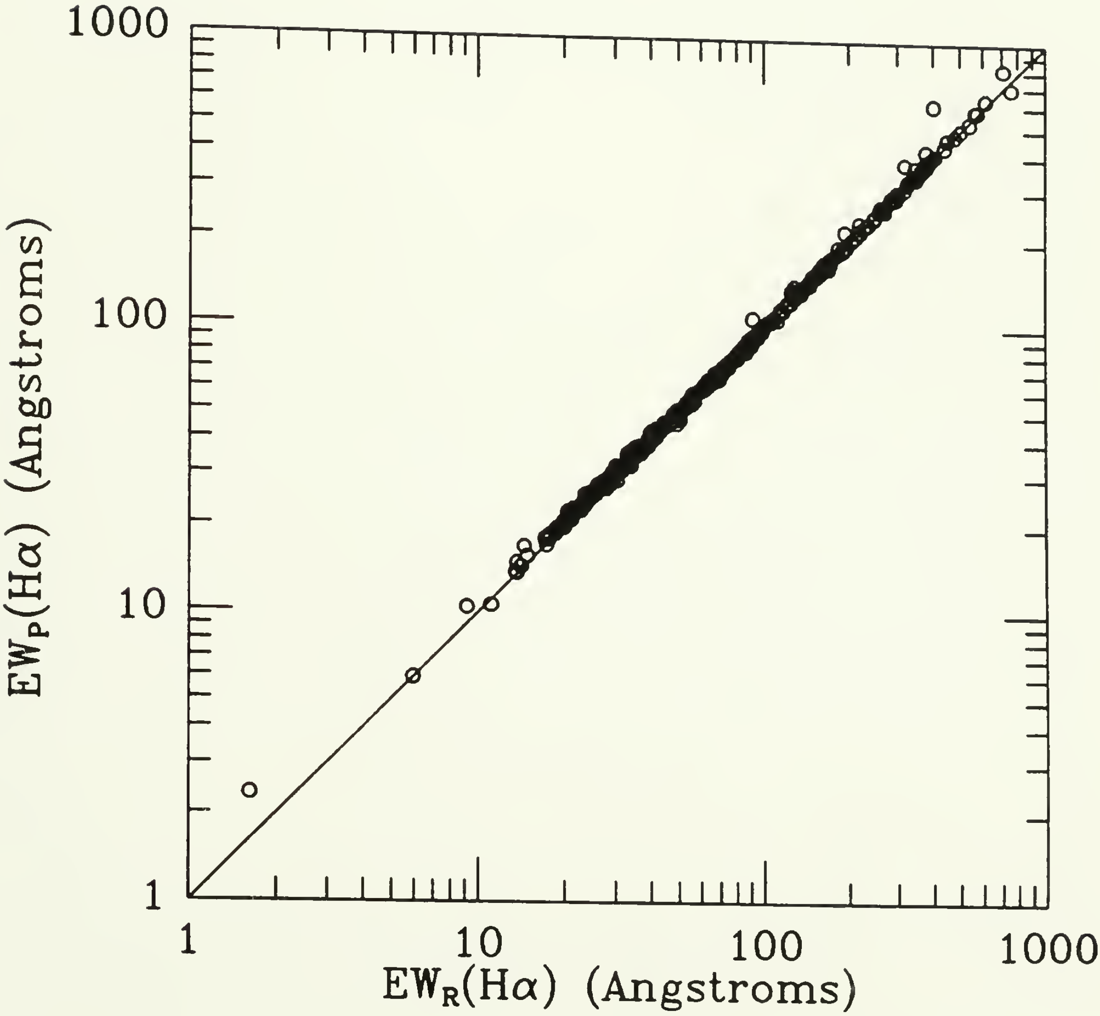
1000
100
10
1
1
10
100
1000
$EW_P(H\alpha)$ (Angstroms)
$EW_R(H\alpha)$ (Angstroms)

Figure 3-6

Contour diagrams of the red continuum and Hα emission from M101. The imaged fields have been combined with the vignetted regions removed. The combined field has been demagnified by 1/2, such that 10 "pixels" represents 16" in the plane of the sky. The total field of view is 10.3' × 3.1'. A 4 × 4 pix boxcar smoothing function has been applied in the contouring.

a. Red continuum emission. The surface brightness is contoured logarithmically with contour intervals of 0.1 dex beginning at 10^{-18} $erg\ cm^{-2}\ s^{-1}\ arcsec^{-2}$ Å^{-1} and peaking in the nucleus at $10^{-16.1}$ $erg\ cm^{-2}\ s^{-1}\ arcsec^{-2}\ \text{Å}^{-1}$.

b. Hα emission. The surface brightness is contoured logarithmically with contour intervals of 0.25 dex beginning at 10^{-16} $erg\ cm^{-2}\ s^{-1}\ arcsec^{-2}$.

M101 Red Continuum (log scale)

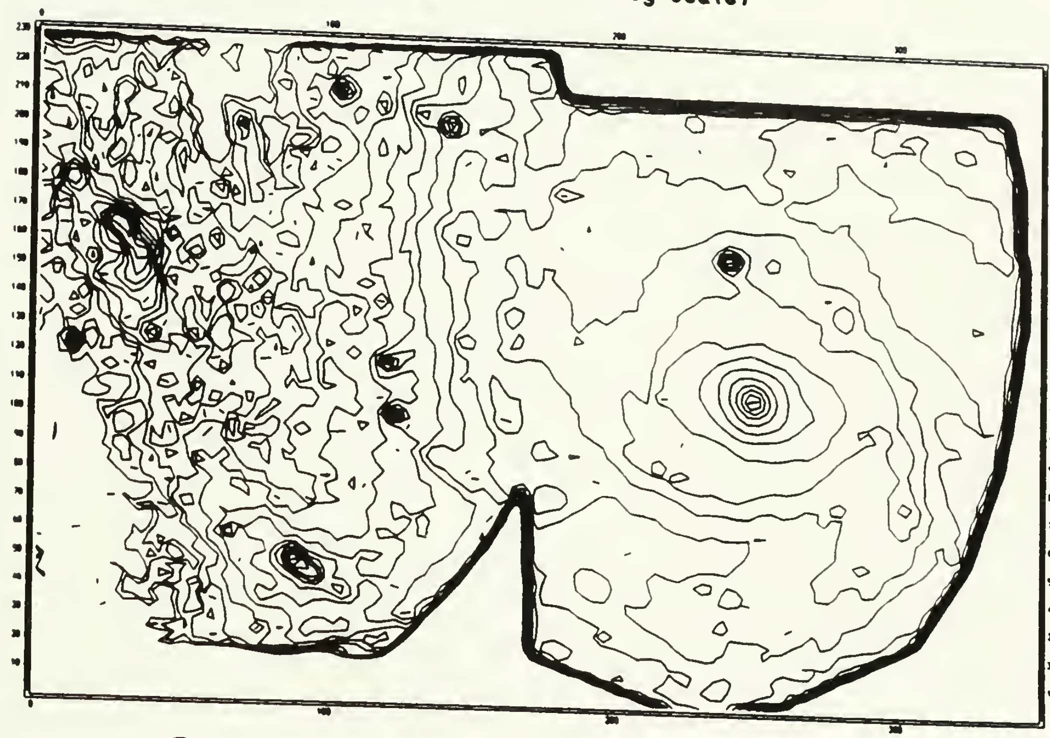

a ▲

b ▼

M101 H-alpha (log scale)

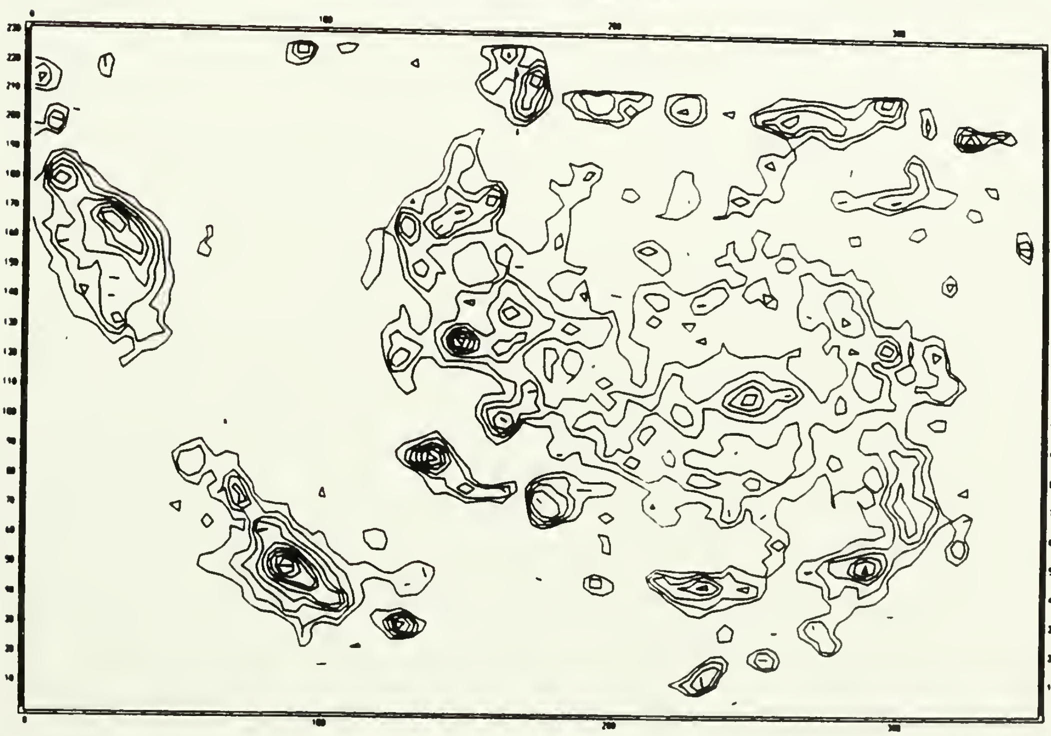

Figure 3–7

Contour diagrams of Hα emission from the "supergiant HII region complexes" NGC 5462 and NGC 5461. The field of view is $1.43' \times 1.43'$ (2 kpc $\times$ 2 kpc) for both diagrams. The surface brightness is contoured in logarithmic intervals of 0.25 starting at 1.0×10^{-16} $erg\ s^{-1}\ cm^{-2}\ arcsec^{-2}$.

a. The NGC 5462 complex shows two especially bright HII regions plus an extended region containing several other weaker HII regions.

b. The NGC 5461 complex is dominated by a single brilliant HII region. This region is 10 times more luminous than any other HII region measured in this study. Low surface-brightness plumes of ionized gas are evident, diverging from the brilliant core toward the South, Southeast, and East.

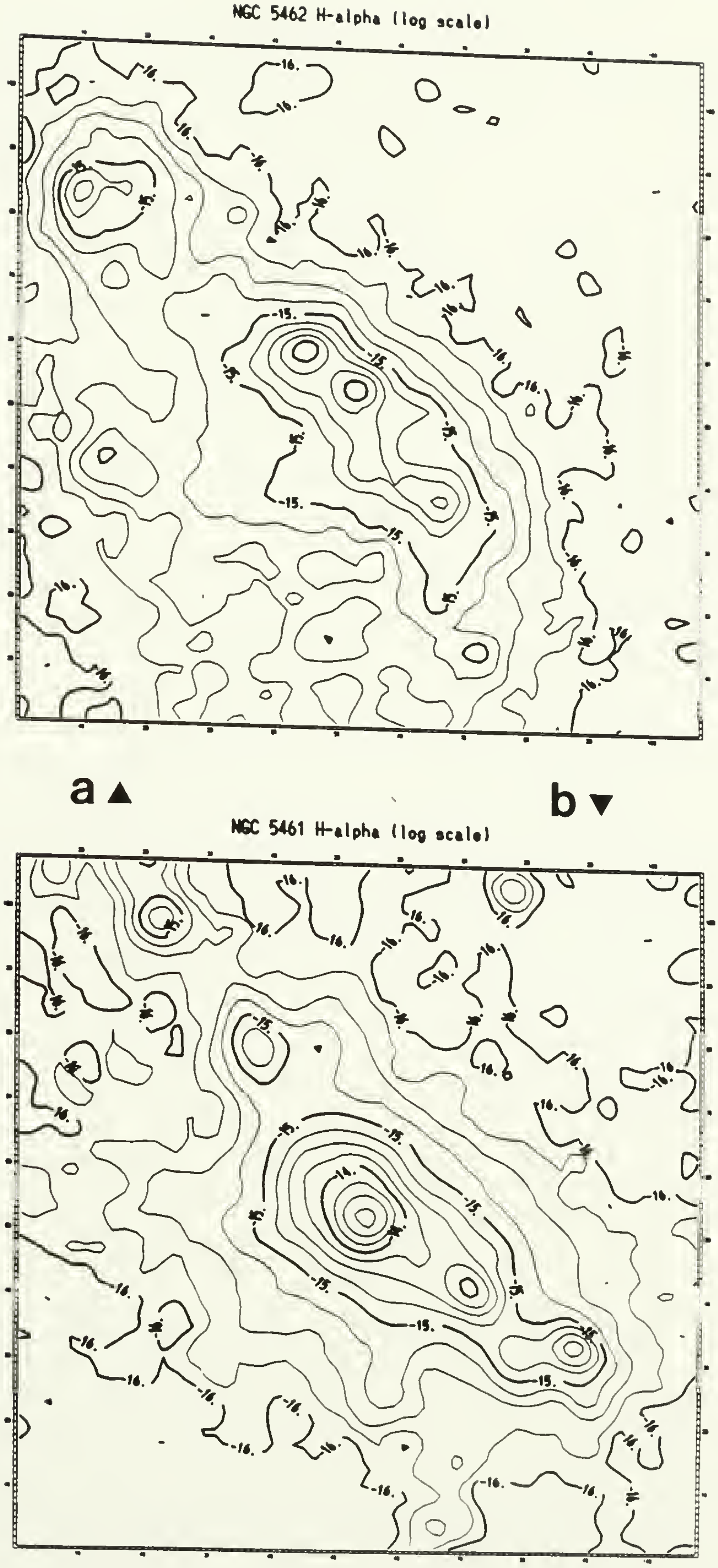
NGC 5462 H-alpha (log scale)
a ▲
b ▼
NGC 5461 H-alpha (log scale)

Figure 3–8

Annular-averaged galactocentric profiles of the Hα intensity, red-continuum intensity, and Hα equivalent width. Each point represents a 30" annular bin in the plane of the galaxy. The error bars represent standard deviations about the annular-averaged values. The standard errors in the mean values are also plotted but are no larger than the plotted points.

a. Galactocentric profiles of the Hα intensity (in $erg\ cm^{-2}\ s^{-1}\ arcsec^{-2}$) and the red-continuum intensity (in $erg\ cm^{-2}\ s^{-1}\ arcsec^{-2}\ \text{Å}^{-1}$).

b. Galactocentric profile of the Hα equivalent width. The error bars are based on a propagation of the standard deviations in the Hα and red-continuum intensities.

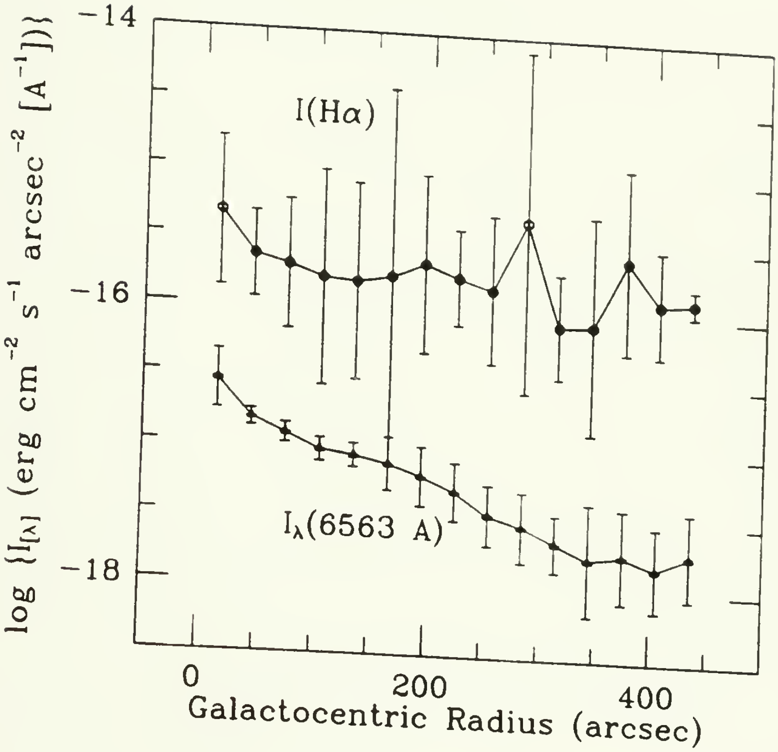

I(Hα)
Iλ(6563 A)
log {I[λ] (erg cm^-2 s^-1 arcsec^-2 [A^-1])}
−14
−16
−18
0
200
400
Galactocentric Radius (arcsec)

a ▲ **b ▼**

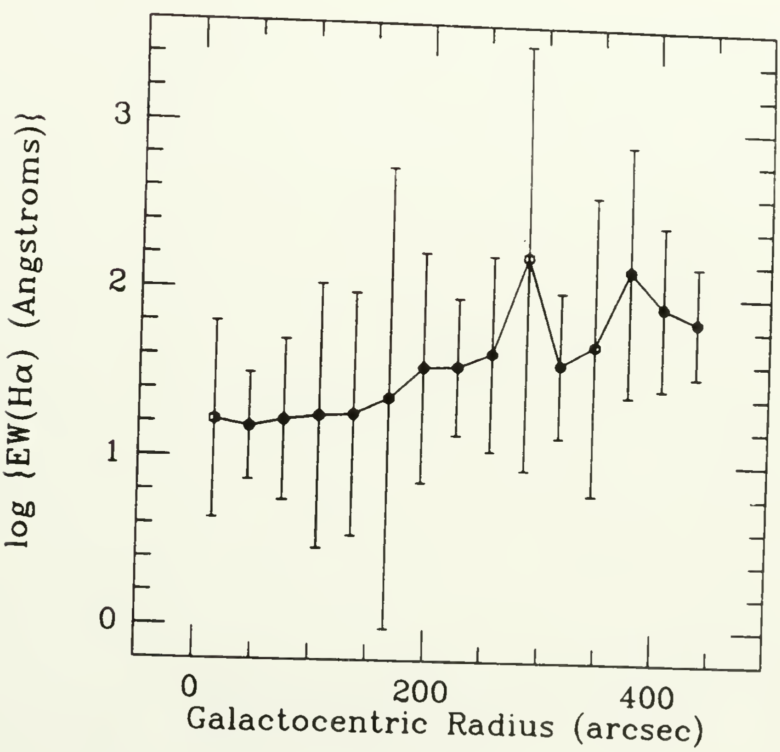

log {EW(Hα) (Angstroms)}
0
1
2
3
0
200
400
Galactocentric Radius (arcsec)

Figure 3–9

Galactocentric distribution of starbirth intensities. The star formation intensities are plotted as surface densities in the plane of the galaxy, $\sigma(SFR)$. A visual extinction of 0.72 mag has been assumed in the computation of $\sigma(SFR)$ from the observed surface brightness $I(H\alpha)$. The secondary peak in the profile is coincident with the annuli containing the supergiant HII regions NGC 5461 and NGC 5462. Because only 1/6 of the total annulus at this radius has been observed and measured, the measured effect of the supergiant HII regions could be disproportionately high. For comparison, galactocentric profiles of the starbirth intensities in M83, M51, and the Milky Way are also shown. The data for M83 and M51 are from Lord (1987), and the data for the Milky Way are from Gusten and Mezger (1982). All values of $\sigma(SFR)$ are based on the $\sigma(SFR)/N_i$ conversion of Kennicutt (1983).

a. Starbirth intensities as a function of galactocentric distance in kpc. The adopted distances to M101, M83, M51, and the center of the Milky Way are 4.8 Mpc, 3.7 Mpc, 7 Mpc, and 10 kpc respectively.

b. Starbirth intensities as a function of galactocentric distance normalized to the "optical radius," R_{25}, of each galaxy. The adopted optical radii of M101, M83, M51, and the Milky Way are 845", 486", 314", and 11.9 kpc respectively.

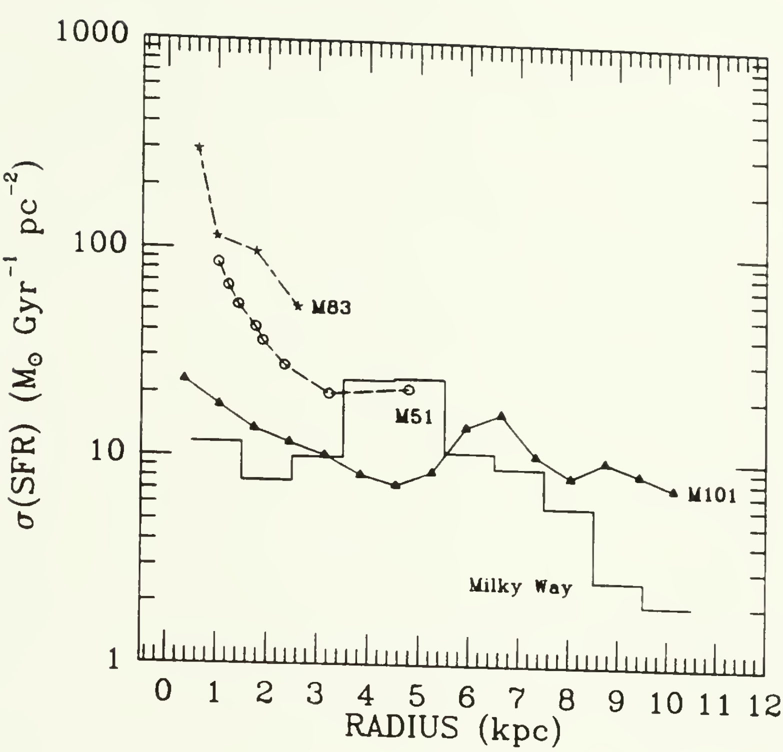
1000
100
10
1
σ(SFR) (M⊙ Gyr⁻¹ pc⁻²)
M83
M51
M101
Milky Way
0 1 2 3 4 5 6 7 8 9 10 11 12
RADIUS (kpc)

a ▲ b ▼

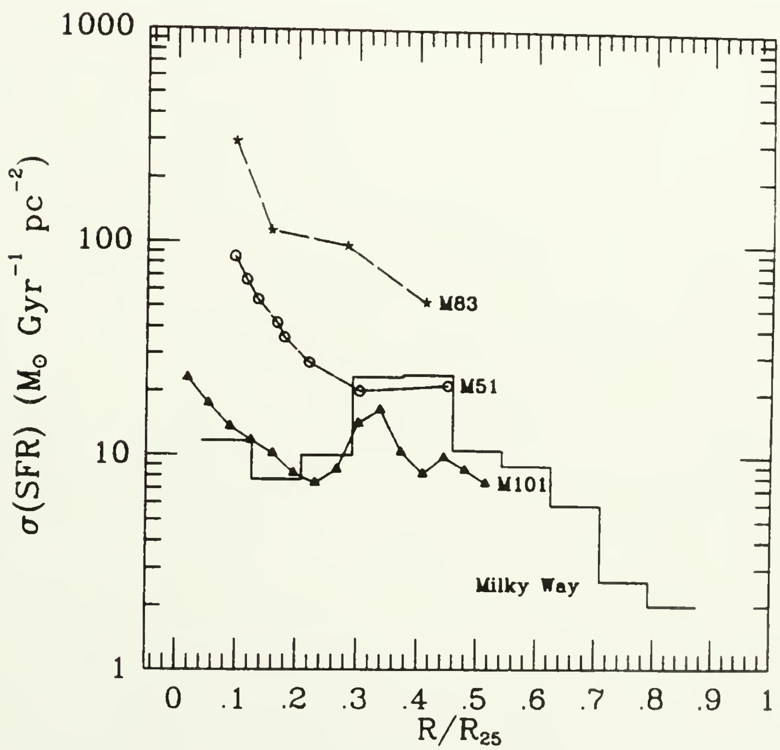
1000
100
10
1
σ(SFR) (M⊙ Gyr⁻¹ pc⁻²)
M83
M51
M101
Milky Way
0 .1 .2 .3 .4 .5 .6 .7 .8 .9 1
R/R25

Figure 3–10

Galactocentric profiles of the gas and corresponding starbirth efficiency in M101.

a. Galactocentric profiles of the H_2, HI, and $H_2 + HI + He$ surface densities. The H_2 and HI data are from Solomon *et al.* (1983). A constant conversion between I(CO) and $\sigma(H_2)$ has been applied, thus ignoring possible variations in the conversion caused by the 0.6 dex variation in metallicity across the measured disk. The He component assumes an He abundance of $Y = 0.25$ throughout.

b. Galactocentric profiles of the starbirth efficiency with respect to the H_2, HI, and total gas surface densities. Considerations of the IMF and extinction-dependent conversion between I(Hα) and σ(SFR), as well as the uncertain conversion between I(CO) and $\sigma(H_2)$ indicate that the plotted SFEs are absolutely certain to within a factor of about 3 (or ± 0.5 dex as plotted here) and self-consistent to within a factor of about 2 (or ± 0.3 dex as plotted here).

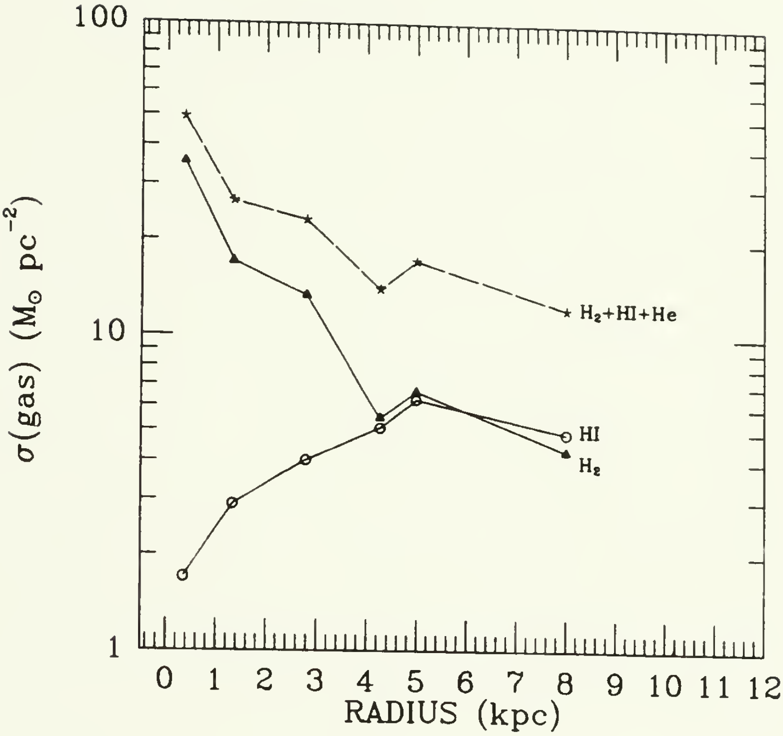
100
10
1
σ(gas) (M⊙ pc⁻²)
H_2+HI+He
HI
H_2
0 1 2 3 4 5 6 7 8 9 10 11 12
RADIUS (kpc)

a ▲ **b ▼**

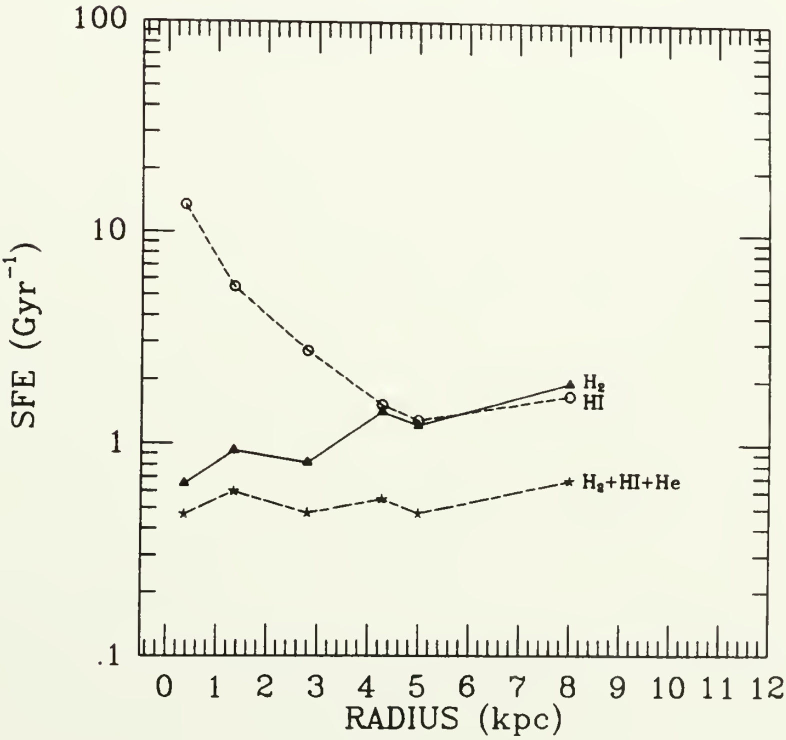
100
10
1
.1
SFE (Gyr⁻¹)
H_2
HI
H_2+HI+He
0 1 2 3 4 5 6 7 8 9 10 11 12
RADIUS (kpc)

Figure 3–11

Galactocentric distributions of the starbirth efficiency in M101 and other disk galaxies. The annular-averaged H_2 and HI data for M83 and M51, from which the starbirth efficiencies are derived, are from Lord (1987); the H_2 and HI data for the Milky Way are from Sanders *et al.* (1984). Considerations of the IMF and extinction-dependent conversion between I(Hα) and σ(SFR), as well as the uncertain conversion between I(CO) and $\sigma(H_2)$ indicate that the plotted SFEs are absolutely certain to within a factor of about 3 (or ± 0.5 dex as plotted here) and self-consistent to within a factor of about 2 (or ± 0.3 dex as plotted here).

a. Galactocentric profiles of the starbirth efficiency with respect to the H_2 surface density alone.

b. Galactocentric profiles of the starbirth efficiency with respect to the total gas surface density.

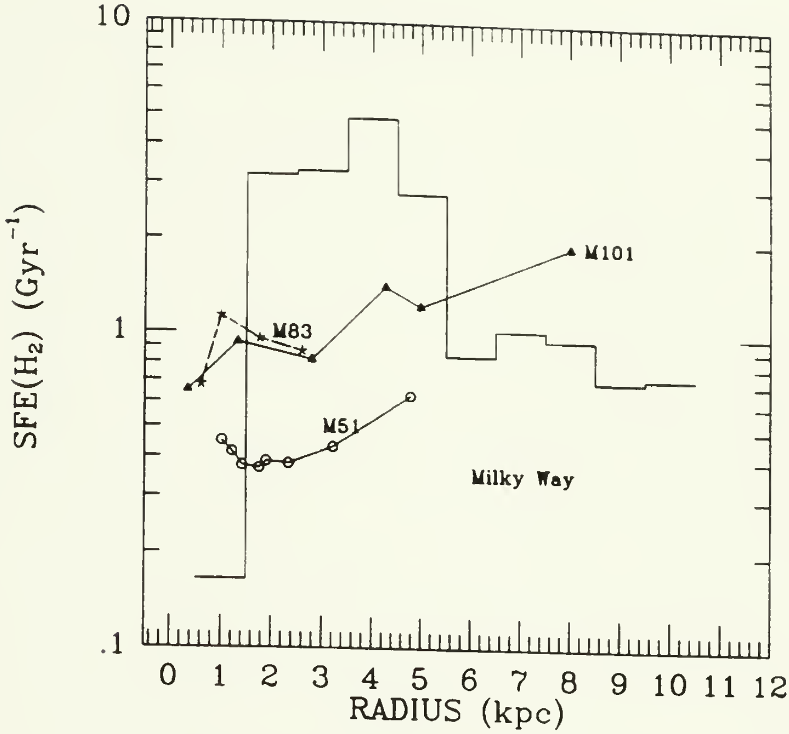

10
1
.1
SFE(H2) (Gyr-1)
0 1 2 3 4 5 6 7 8 9 10 11 12
RADIUS (kpc)
M101
M83
M51
Milky Way

a ▲ b ▼

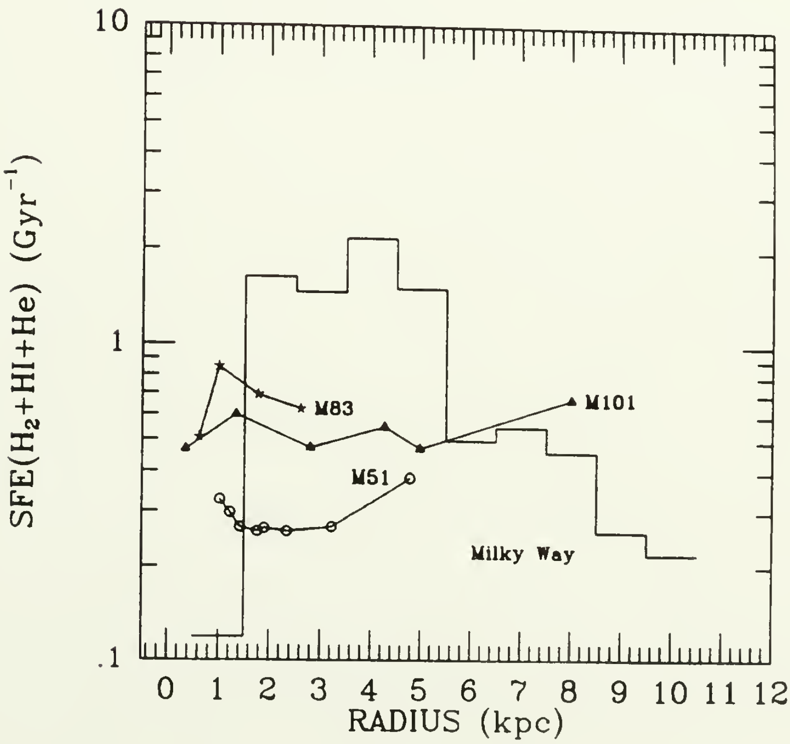

10
1
.1
SFE(H2+HI+He) (Gyr-1)
0 1 2 3 4 5 6 7 8 9 10 11 12
RADIUS (kpc)
M83
M101
M51
Milky Way

Figure 3–12

Annular-averaged starbirth intensities *vs.* H_2, HI, and total gas surface densities in M101 and other disk galaxies.

a. Starbirth intensity *vs.* H_2 surface density.

b. Starbirth intensity *vs.* HI surface density.

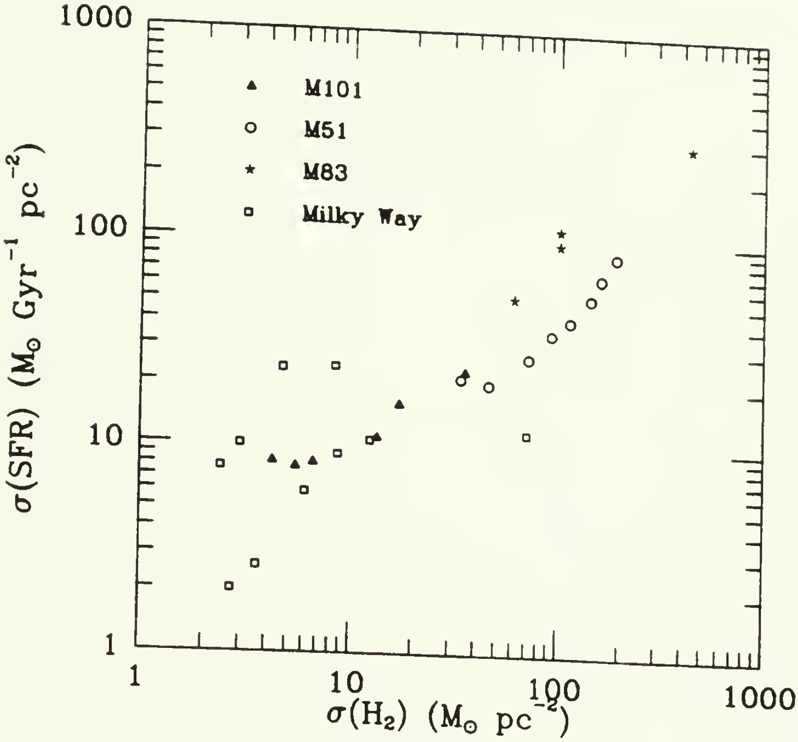

M101
M51
M83
Milky Way
1000
100
10
1
1
10
100
1000
σ(SFR) (M⊙ Gyr⁻¹ pc⁻²)
σ(H₂) (M⊙ pc⁻²)

a ▲ **b ▼**

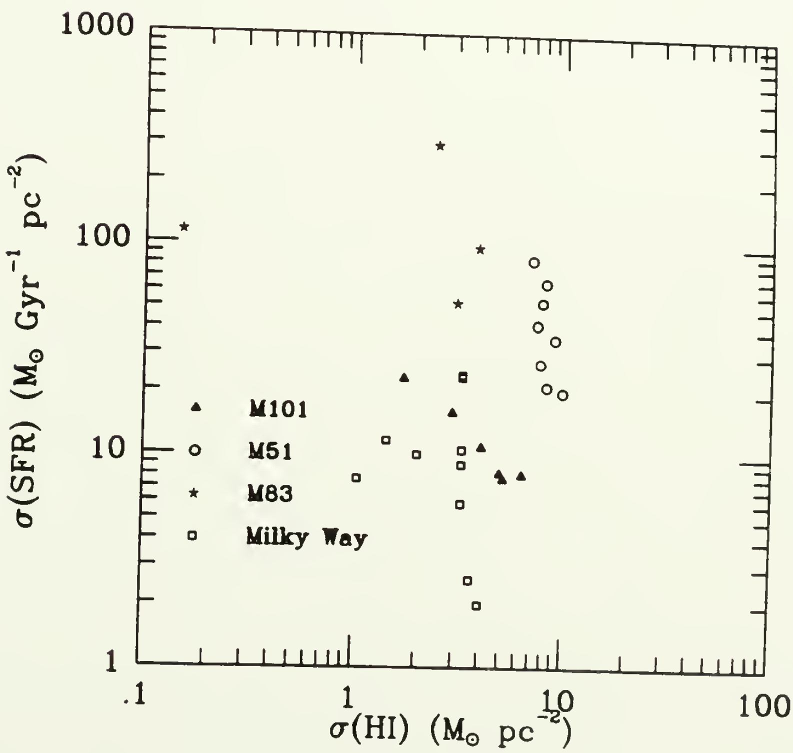

M101
M51
M83
Milky Way
1000
100
10
1
.1
1
10
100
σ(SFR) (M⊙ Gyr⁻¹ pc⁻²)
σ(HI) (M⊙ pc⁻²)

Figure 3-12 (cont.)

c. Starbirth intensity *vs.* total gas surface density. The mean intensity and surface density (within a circle of 30" radius) for the supergiant HII region complex, NGC 5461, has been plotted along with the annular averages.

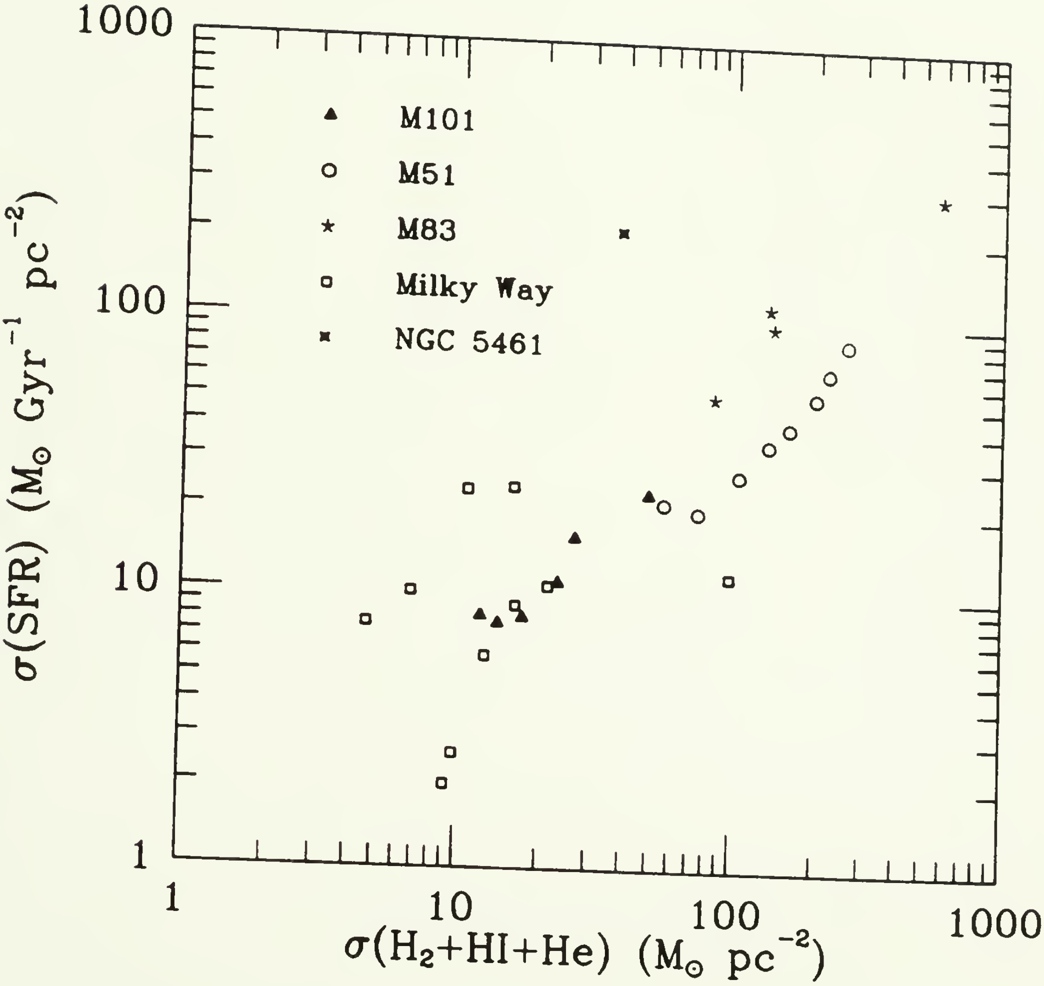
1000
100
10
1
1
10
100
1000
M101
M51
M83
Milky Way
NGC 5461
σ(SFR) (M⊙ Gyr⁻¹ pc⁻²)
σ(H₂+HI+He) (M⊙ pc⁻²)

C

Figure 3–13

Radial distributions of Hα and red-continuum emission from individual HII regions. Each pixel corresponds to a radial displacement of 0.81". The Hα and red-continuum "counts" refer to log I(Hα) (erg cm^{-2} s^{-1} $arcsec^{-2}$) and log $I_{\lambda}(\lambda 6563)$ (erg cm^{-2} s^{-1} arcsec−2 Å) respectively. The sequence of 4 HII regions spans the range of intensities and signal-to-noise ratios that is present in the observed sample of 385 HII regions.

a. The radial distributions of Hα and λ6563 emission from HII region #287 (also known as S3 and H40; see Tables 3-4 and 3-5).

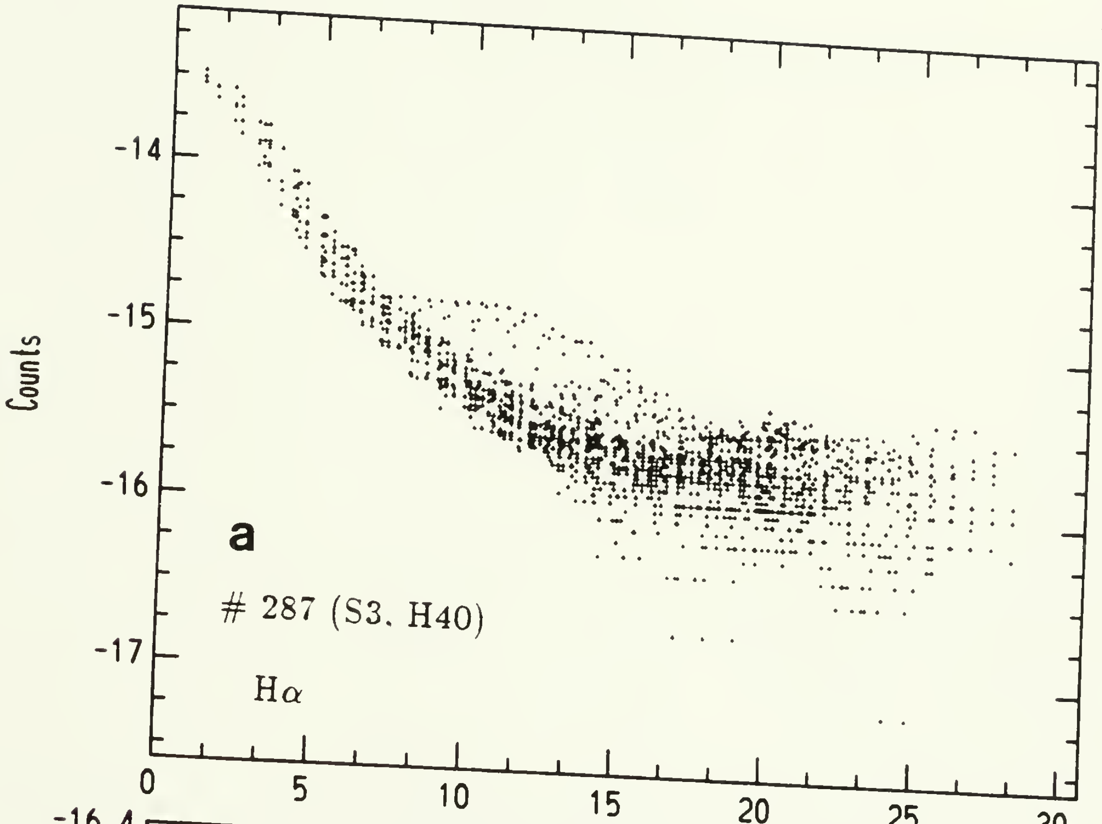
-14
-15
-16
-17
Counts
a
287 (S3, H40)
Hα
0
5
10
15
20
25
30

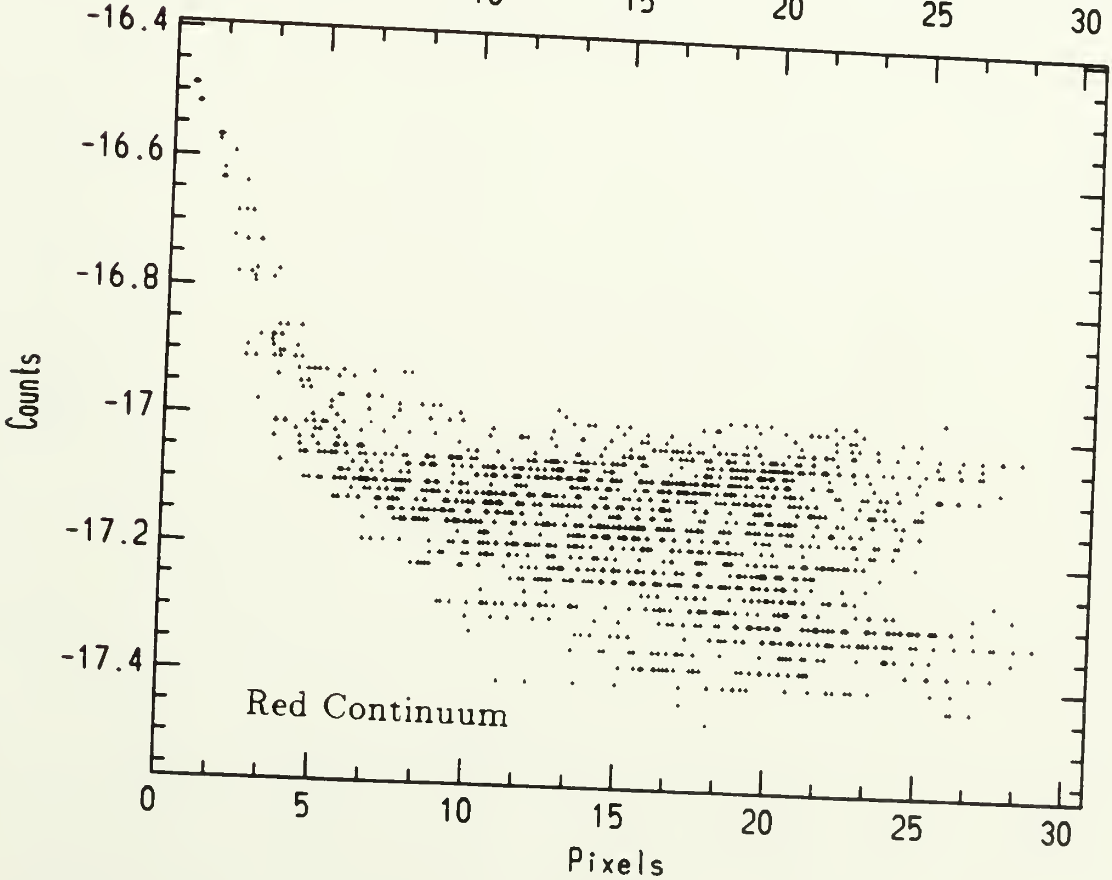
-16.4
-16.6
-16.8
-17
-17.2
-17.4
Counts
Red Continuum
0
5
10
15
20
25
30
Pixels

Figure 3-13 (cont.)

b. The radial distributions of Hα and λ6563 emission from HII region #303 (also known as S4; see Tables 3-4 and 3-5).

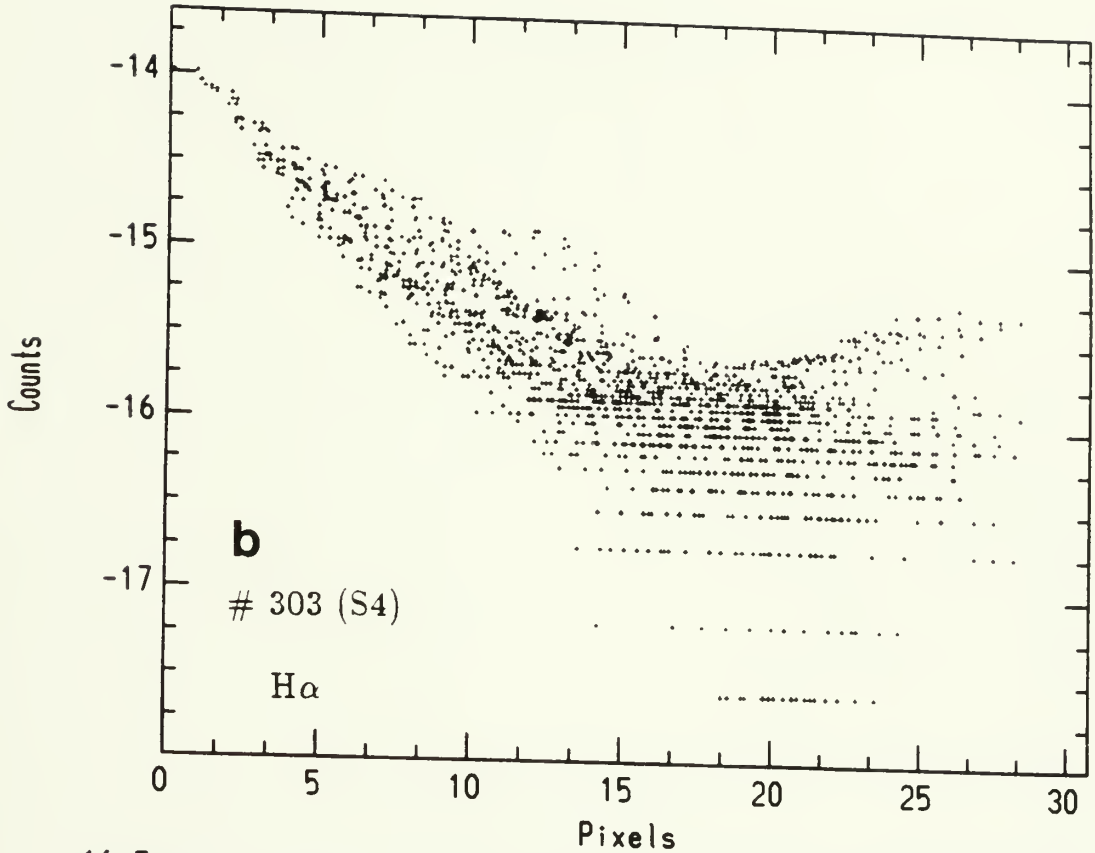
b
303 (S4)
Hα
Counts
-14
-15
-16
-17
0
5
10
15
20
25
30
Pixels

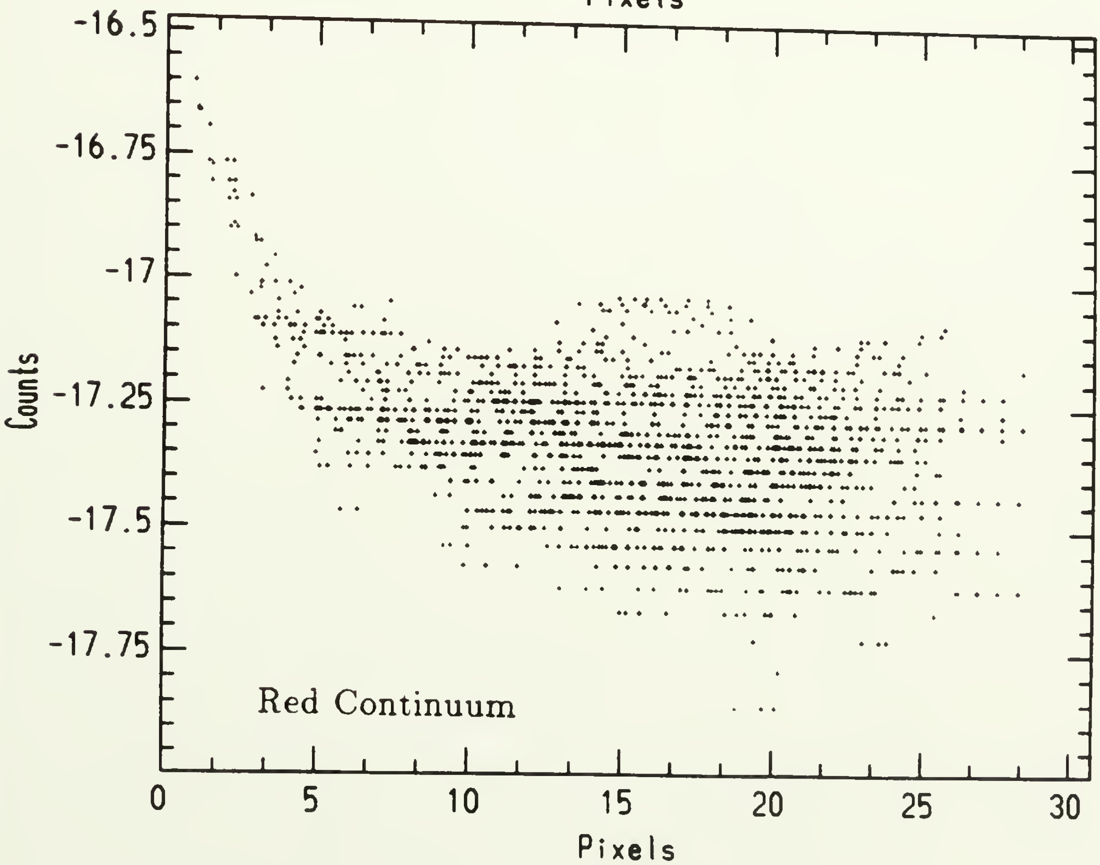
Red Continuum
Counts
-16.5
-16.75
-17
-17.25
-17.5
-17.75
0
5
10
15
20
25
30
Pixels

Figure 3-13 (cont.)

c. The radial distributions of Hα and λ6563 emission from HII region #242 (see Tables 3-4 and 3-5).

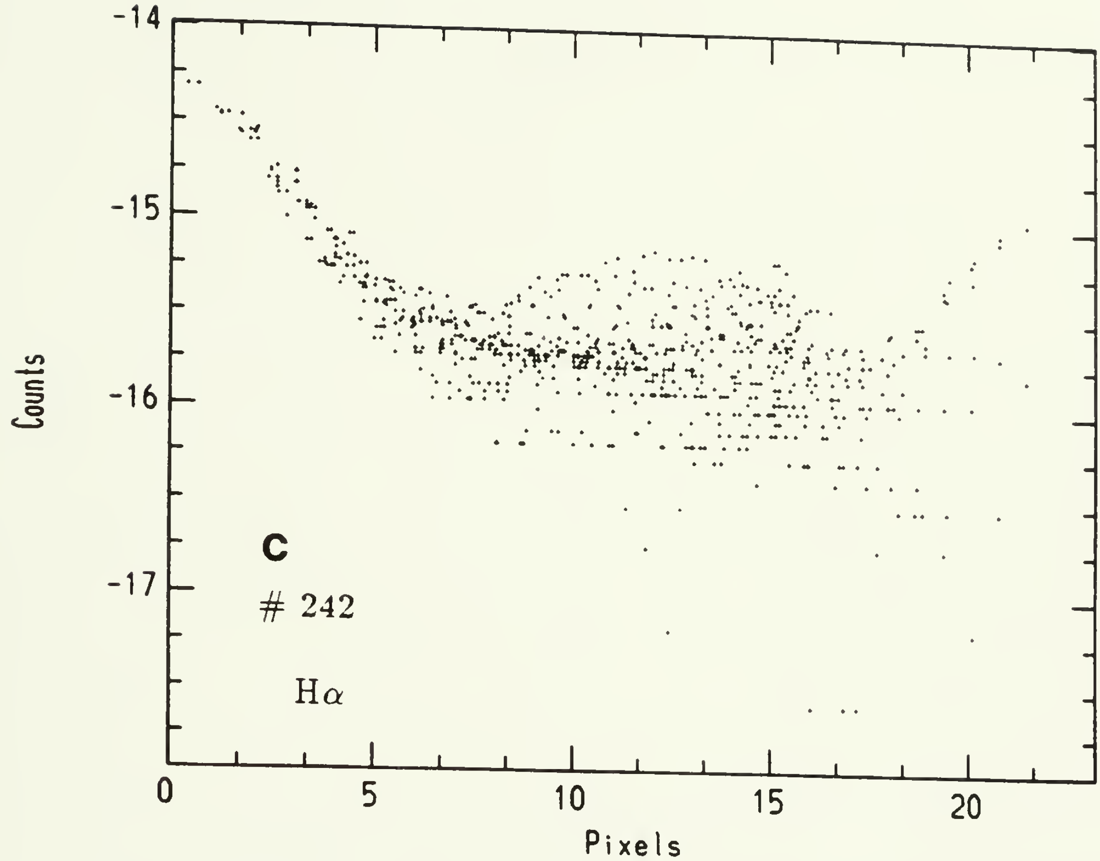
-14
-15
-16
-17
Counts
C
242
Hα
0
5
10
15
20
Pixels

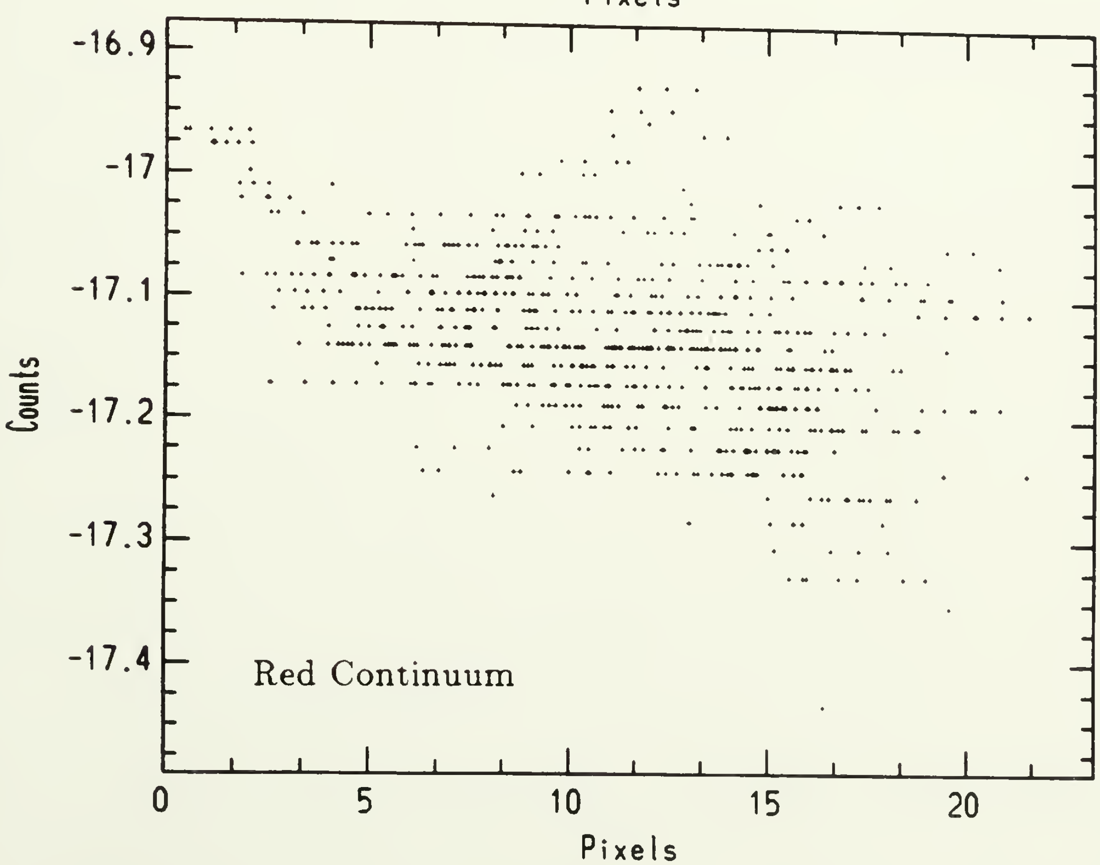
-16.9
-17
-17.1
-17.2
-17.3
-17.4
Counts
Red Continuum
0
5
10
15
20
Pixels

Figure 3-13 (cont.)

d. The radial distributions of Hα and λ6563 emission from HII region #259 (see Tables 3-4 and 3-5).

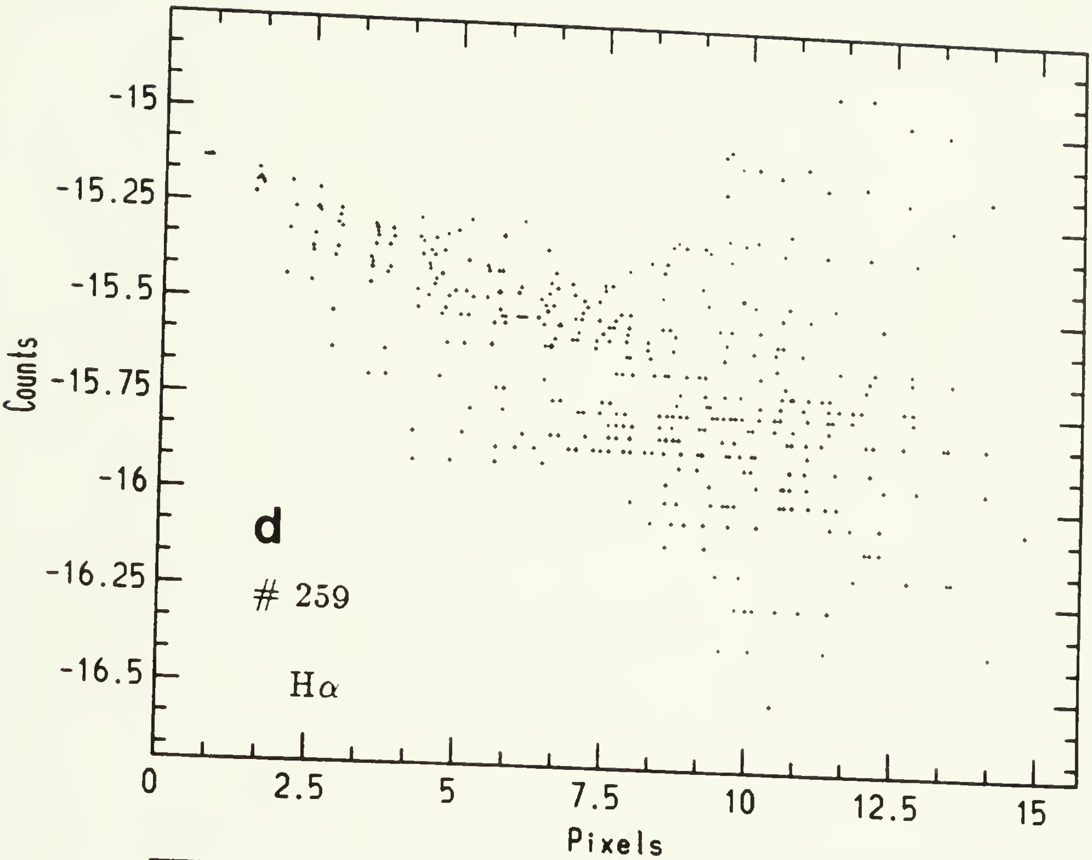

-15
-15.25
-15.5
-15.75
-16
-16.25
-16.5
Counts
d
259
Hα
0
2.5
5
7.5
10
12.5
15
Pixels

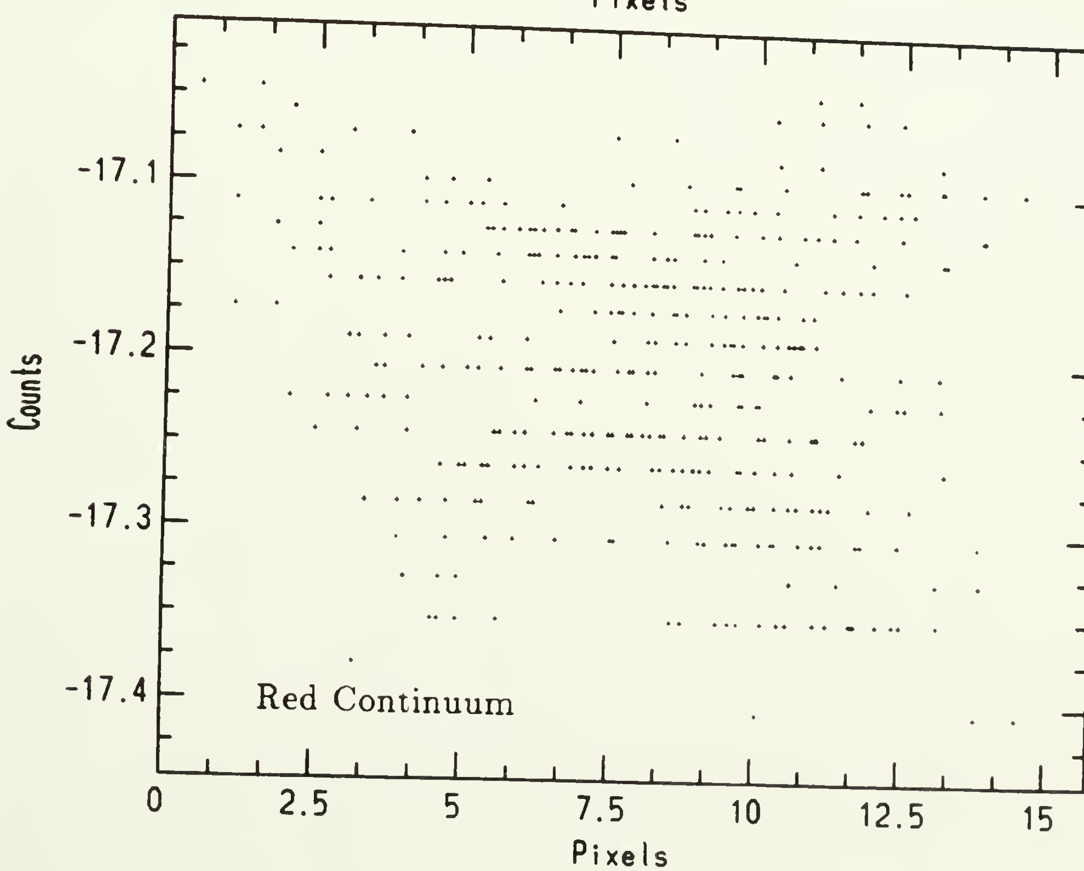

-17.1
-17.2
-17.3
-17.4
Counts
Red Continuum
0
2.5
5
7.5
10
12.5
15
Pixels

Figure 3–14

Identifications and locations of HII regions in the inner galaxy.

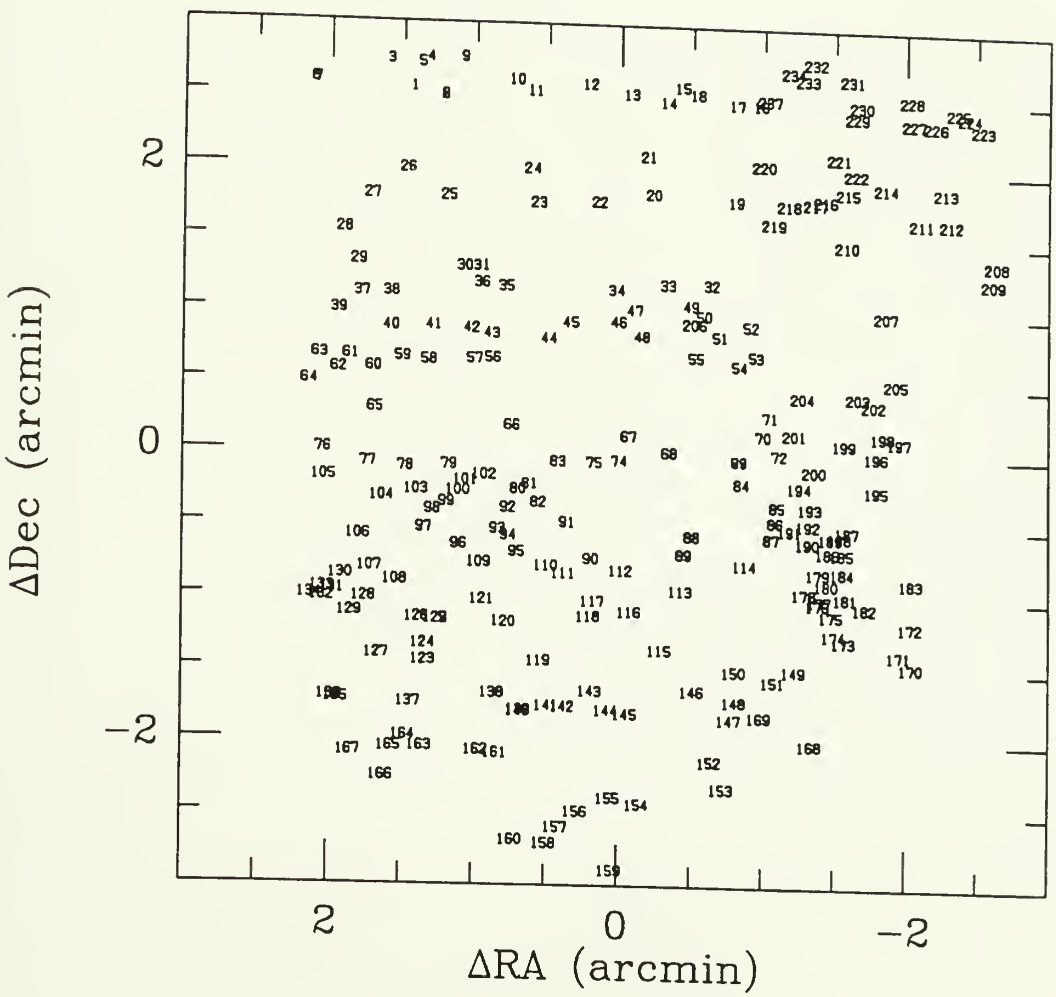
ΔDec (arcmin)
2
0
−2
ΔRA (arcmin)
2
0
−2

Figure 3–15

Identifications and locations of HII regions in the eastern arms. For clarity, HII regions with red continuum surface brightnesses below the 1σ level in the subtracted background (1.4×10^{-18} $erg\ cm^{-2}\ s^{-1}\ arcsec^{-2}$ Å^{-1}) have been excluded from the plot.

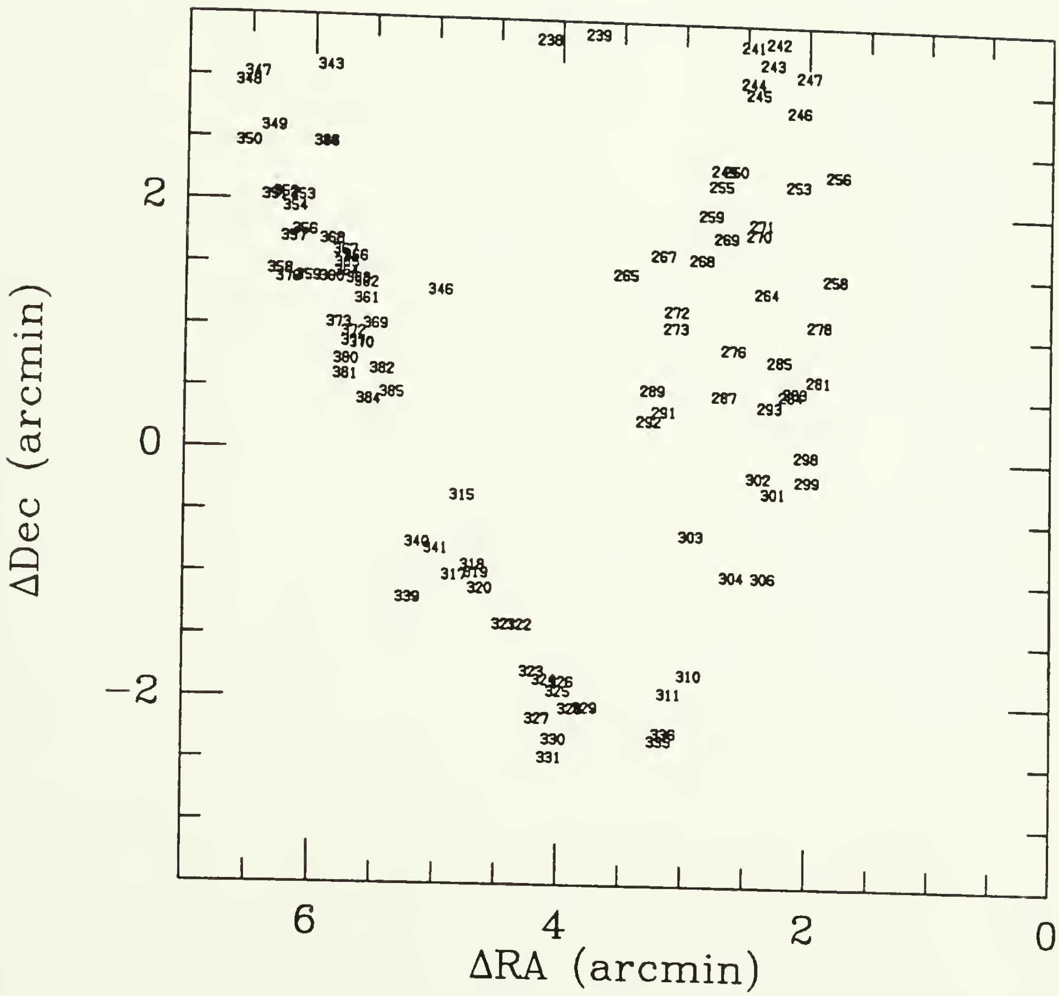
ΔDec (arcmin)
ΔRA (arcmin)
2
0
−2
6
4
2
0

Figure 3–16

Photograph of the combined fields and the locations of HII regions in the combined fields. Every HII region is mapped. The circles are locations from the inner galaxy image. The stars are locations from the eastern arms image. Some redundancy in the overlapping fields is evident, thus confirming the registration between the images.

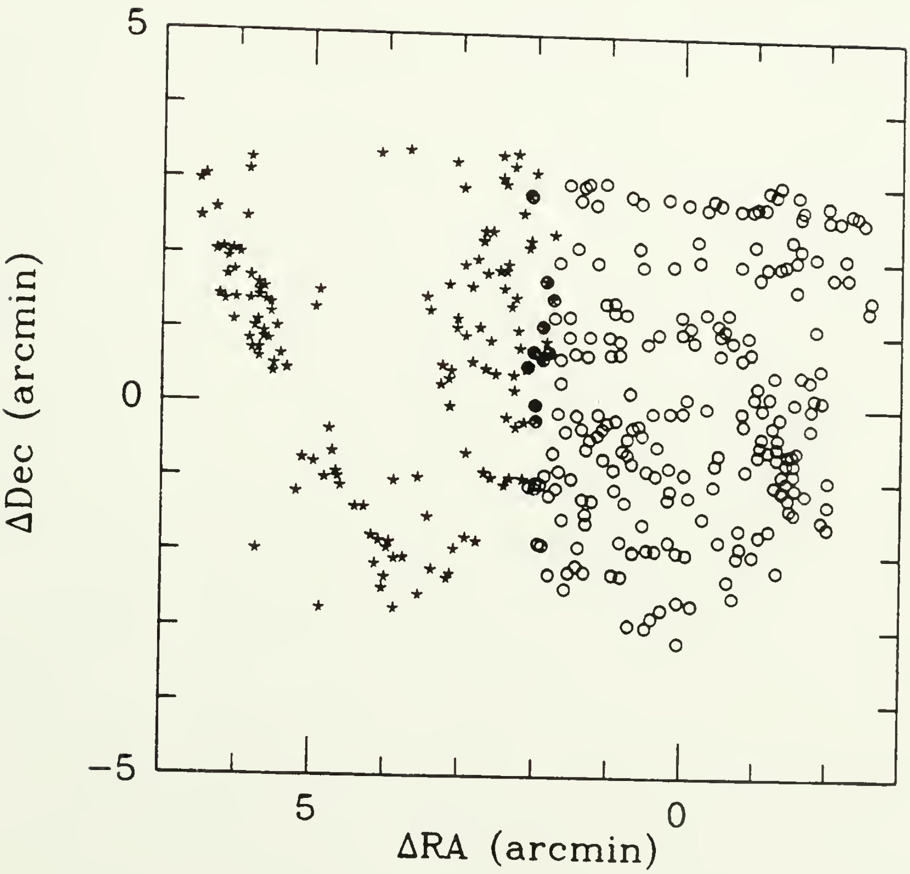
5
0
−5
5
0
ΔDec (arcmin)
ΔRA (arcmin)

Figure 3–17

Frequency distributions of HII region radii. The top plot shows the statistics for the "total" measured radius — whether blended or unblended. The bottom plot shows the statistics for the "unblended" radii. The error bars are based on Poisson counting statistics.

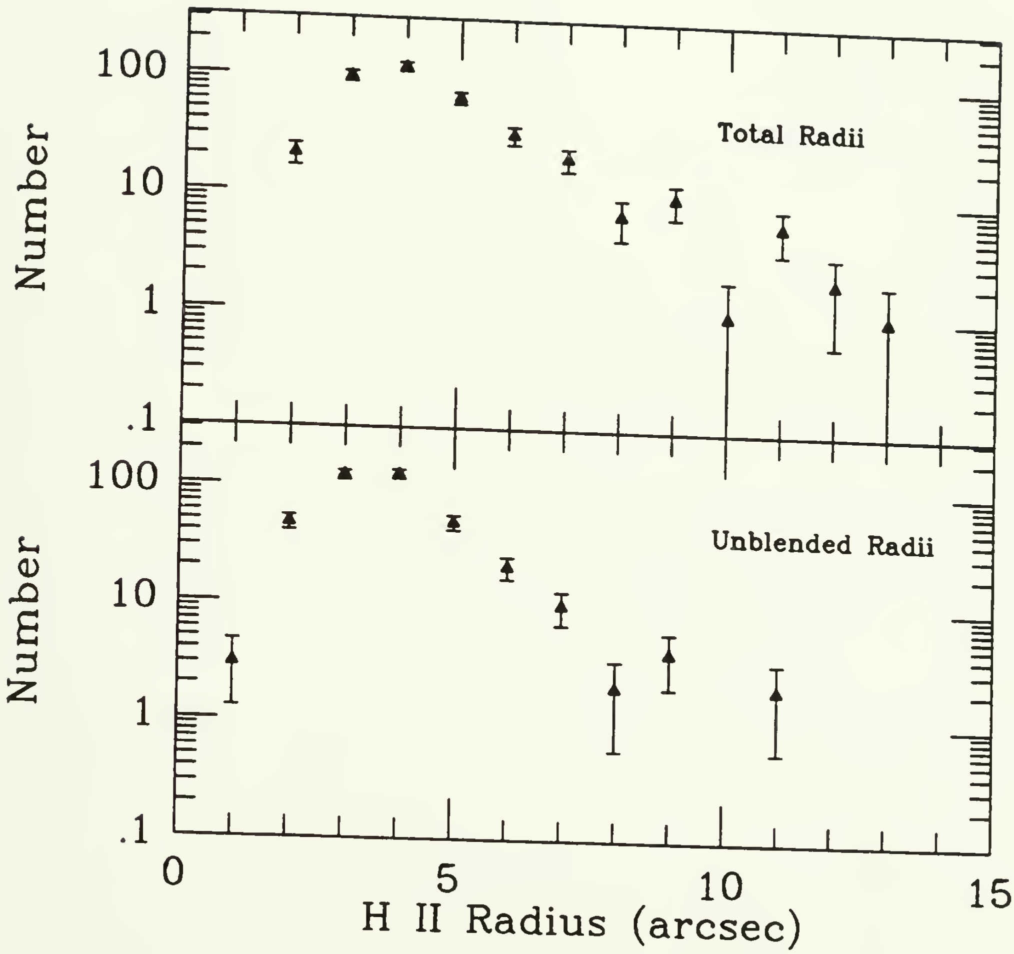
Total Radii
Unblended Radii
Number
Number
100
10
1
.1
100
10
1
.1
0
5
10
15
H II Radius (arcsec)

Figure 3–18

Radial "curves of growth" for the Hα and red-continuum emission from the 4 HII regions in Figure 3-13. "Curves of growth" for the Hα equivalent width are also plotted. The red-continuum fluxes refer to the ionizing clusters, the background starlight of the ambient galaxy having been subtracted.

a. "Curves of growth" for HII region #287.

b. "Curves of growth" for HII region #303.

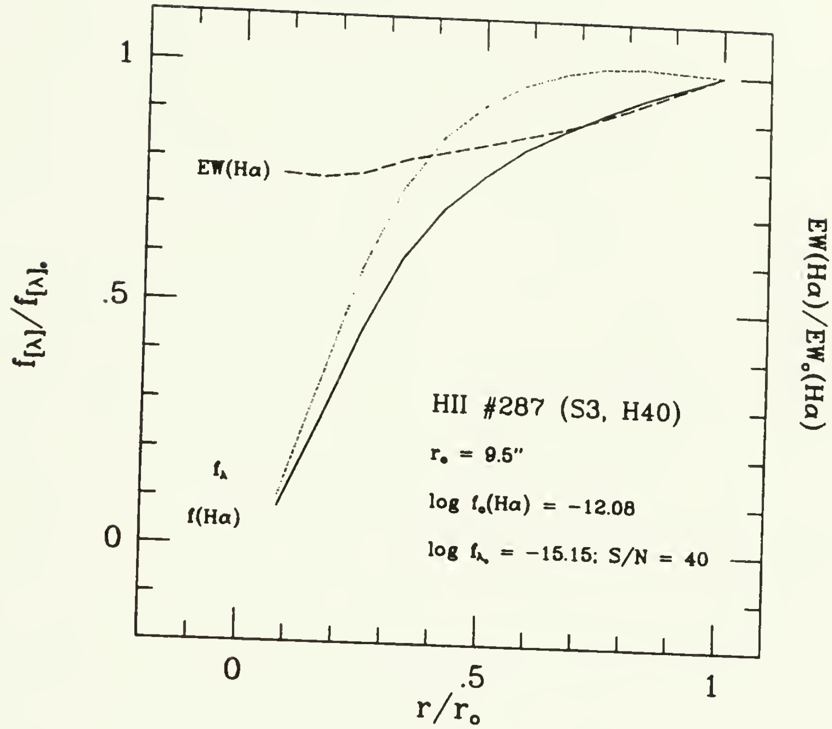
1
.5
0
$f_{[\lambda]}/f_{[\lambda]_o}$
EW(Hα)
f_λ
f(Hα)
HII #287 (S3, H40)
r_o = 9.5"
log f_o(Hα) = −12.08
log f_{λ_o} = −15.15; S/N = 40
0
.5
1
r/r_o
EW(Hα)/EW$_o$(Hα)

a ▲ b ▼

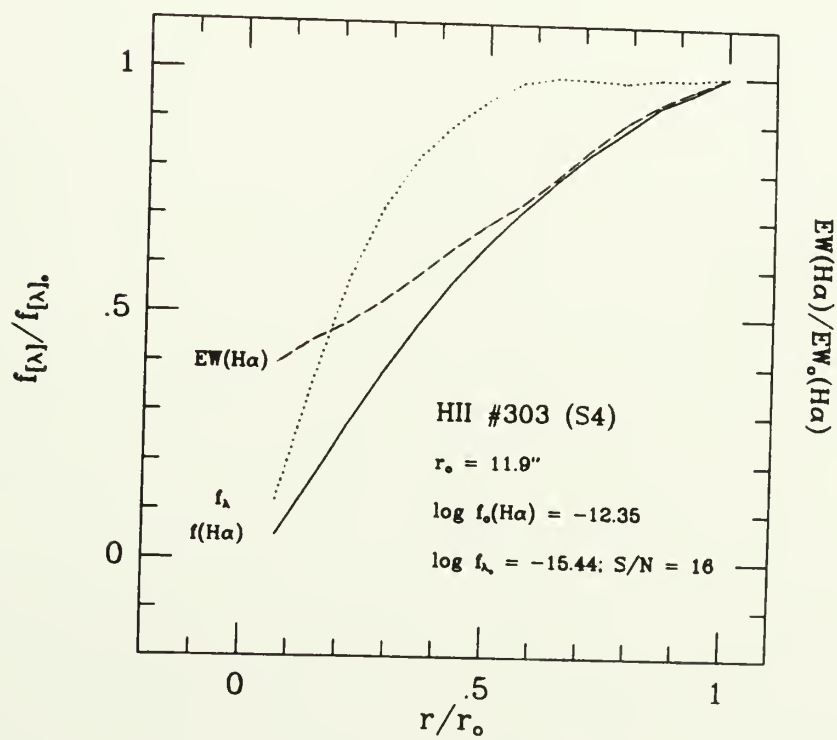
1
.5
0
$f_{[\lambda]}/f_{[\lambda]_o}$
EW(Hα)
f_λ
f(Hα)
HII #303 (S4)
r_o = 11.9"
log f_o(Hα) = −12.35
log f_{λ_o} = −15.44; S/N = 16
0
.5
1
r/r_o
EW(Hα)/EW$_o$(Hα)

Figure 3-18 (cont.)

c. "Curves of growth" for HII region #242.

d. "Curves of growth" for HII region #259.

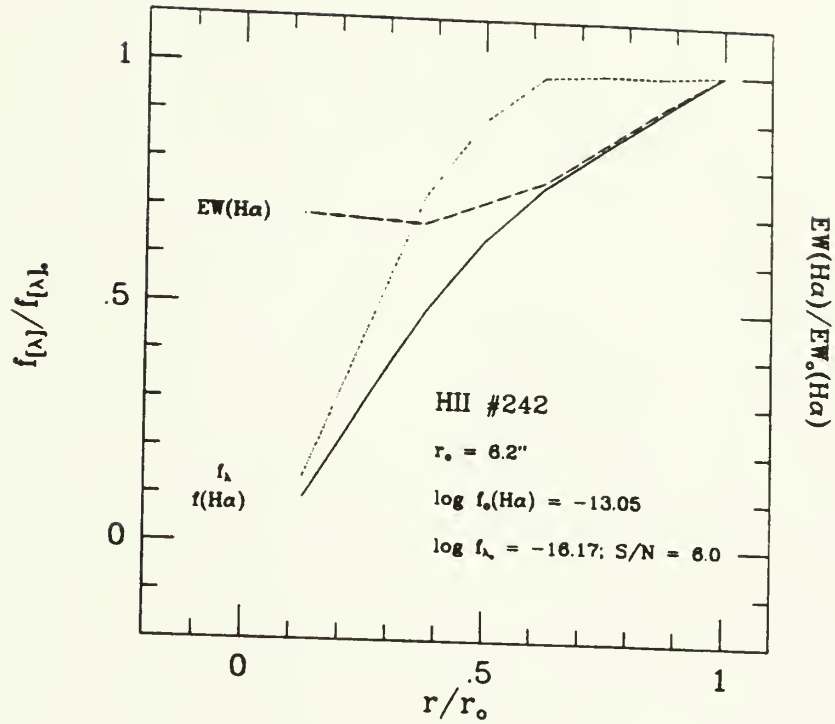

1
.5
0
EW(Hα)
$f_{[\lambda]}/f_{[\lambda]_o}$
f_λ
f(Hα)
HII #242
r₀ = 6.2"
log f₀(Hα) = −13.05
log f_λ = −16.17; S/N = 6.0
EW(Hα)/EW₀(Hα)
0
.5
1
r/r₀

c ▲ d ▼

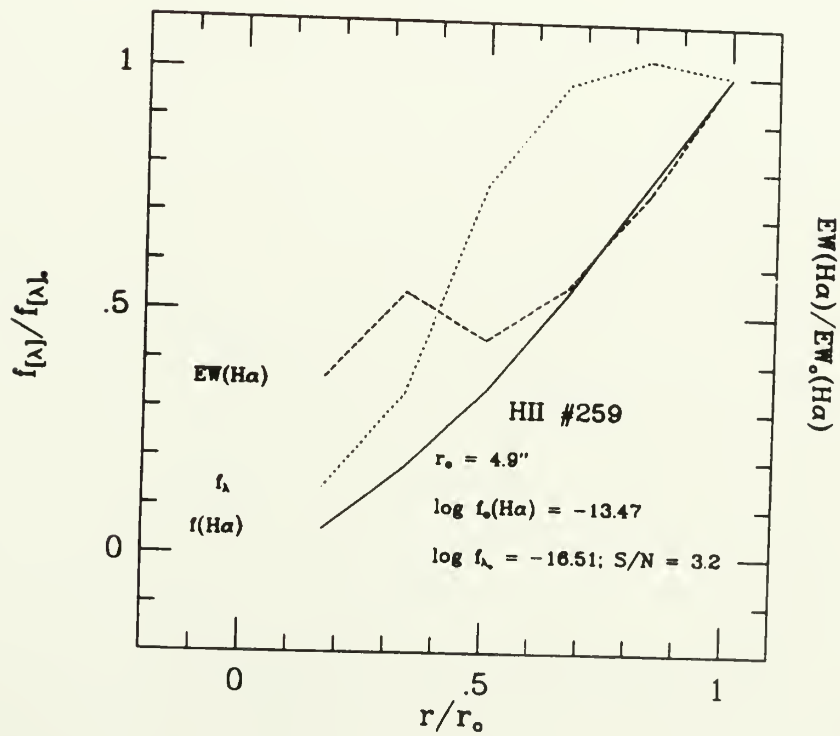

1
.5
0
EW(Hα)
$f_{[\lambda]}/f_{[\lambda]_o}$
f_λ
f(Hα)
HII #259
r₀ = 4.9"
log f₀(Hα) = −13.47
log f_λ = −16.51; S/N = 3.2
EW(Hα)/EW₀(Hα)
0
.5
1
r/r₀

Figure 3–19

Hα luminosity functions for inner and outer disk (differential format). The binning is in logarithmic intervals of 0.25. The upper histogram shows the luminosity function for the 290 HII regions within 5 kpc of the nucleus. The lower histogram shows the luminosity function for the 95 HII regions between 5 and 10 kpc from the nucleus. The error bars are based on Poisson counting statistics.

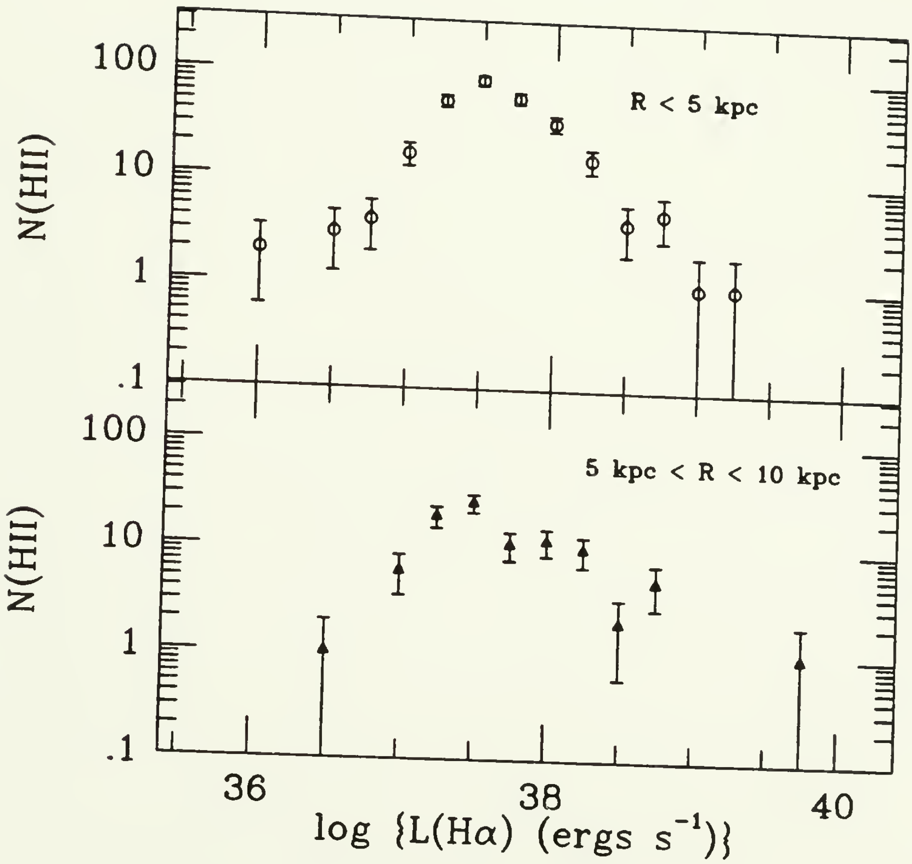

100
10
1
.1
N(HII)
R < 5 kpc
100
10
1
.1
N(HII)
5 kpc < R < 10 kpc
36
38
40
log {L(Hα) (ergs s⁻¹)}

Figure 3–20

Hα luminosity functions for the inner and outer disk (cumulative format). The cumulative luminosity function plots $N(logL \geq logL_\circ)d(logL)$ in logarithmic bins of 0.25. Each luminosity function has been normalized to the total number of HII regions that is involved. The circles denote the statistics for the 95 HII regions between 5 and 10 kpc from the nucleus. The triangles denote the statistics for the 290 HII regions within the 5 kpc radius. The error bars are based on Poisson counting statistics.

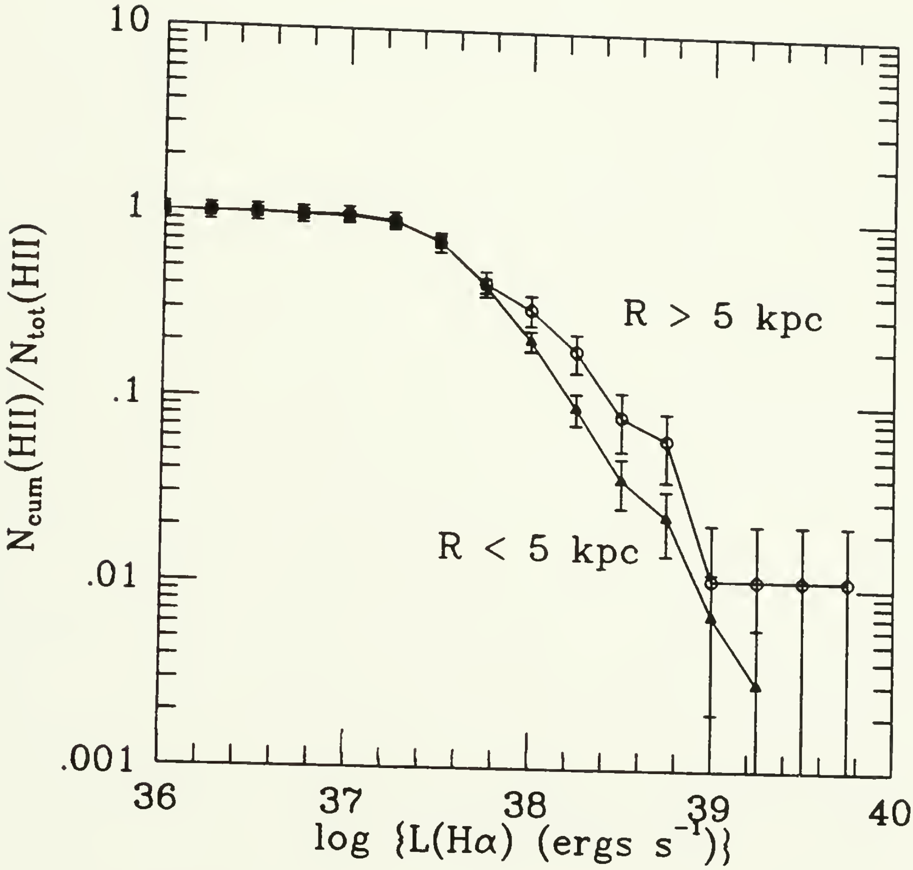
10
1
.1
.01
.001
36
37
38
39
40
$N_{cum}(HII)/N_{tot}(HII)$
log {L(Hα) (ergs s^{-1})}
R > 5 kpc
R < 5 kpc

Figure 3–21

$H\alpha$ luminosity functions (complete sample) in both differential and cumulative form. All 385 HII regions with measurable $H\alpha$ fluxes are included. Error bars are based on Poisson counting statistics. The upper plot shows the differential luminosity function $N(logL)d(logL)$, where the binning is in logarithmic intervals of 0.25. The lower plot shows the cumulative luminosity function. $N(logL \geq logL_{\circ})d(logL)$.

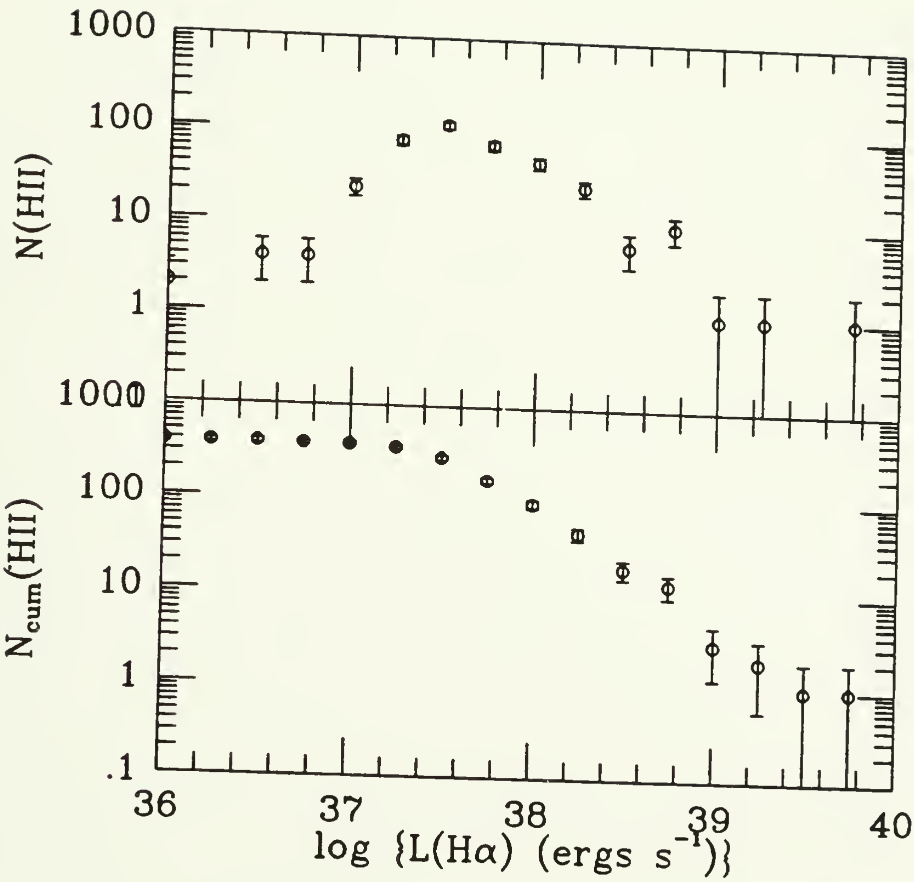

N(HII)
N_{cum}(HII)
1000
100
10
1
.1
36
37
38
39
40
log {L(Hα) (ergs s^{-1})}

Figure 3–22

Galactocentric distribution of Hα and red continuum luminosities.

Galactocentric distribution of Hα and red continuum luminosities for the 102 HII regions which have detectable red-continuum emission ($S/N \geq 5.0$).

a. Galactocentric distribution of Hα luminosities.

b. Galactocentric distribution of red-continuum luminosity densities.

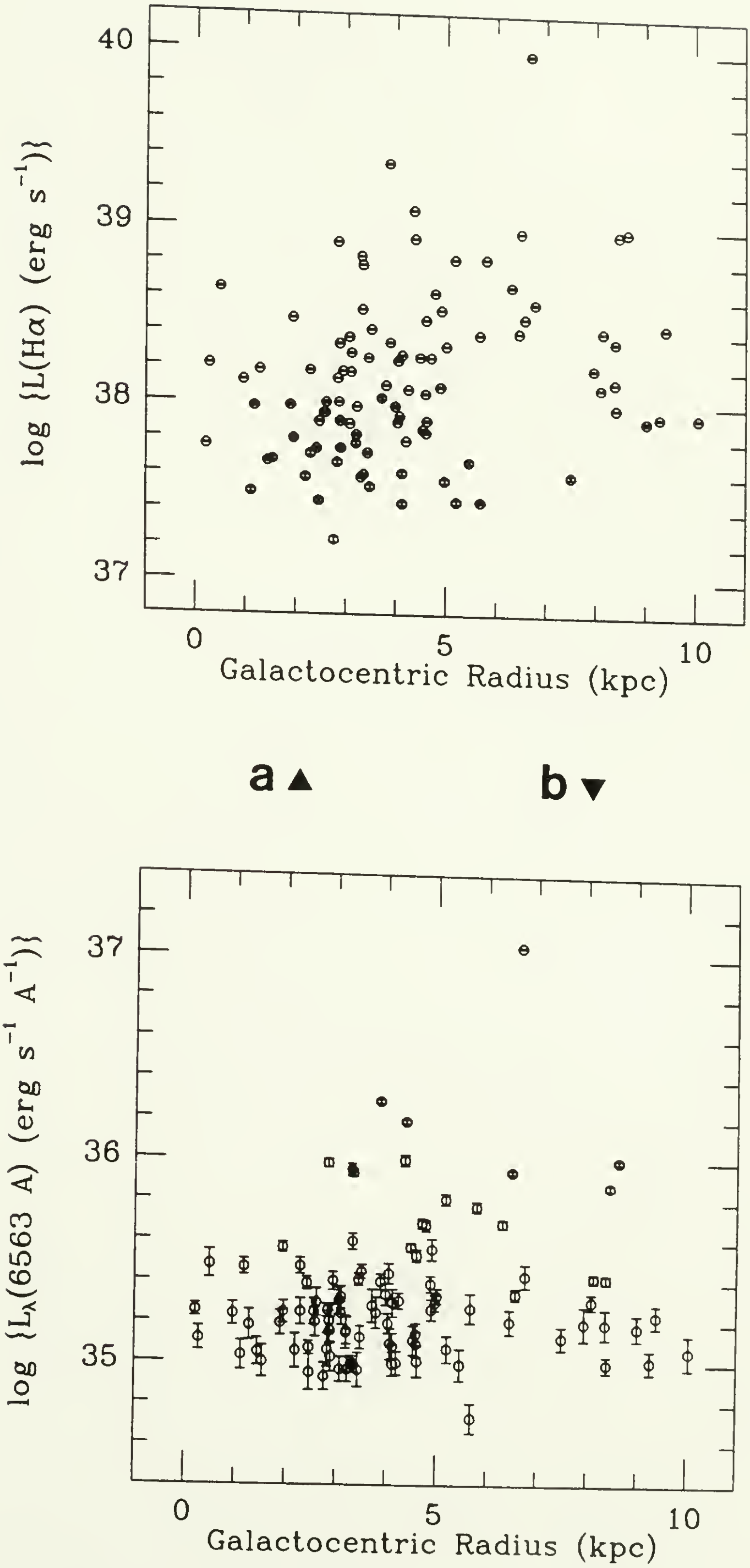
40
39
38
37
log {L(Hα) (erg s^{-1})}
0
5
10
Galactocentric Radius (kpc)
a ▲
b ▼
37
36
35
log {L$_\lambda$(6563 A) (erg s^{-1} A^{-1})}
0
5
10
Galactocentric Radius (kpc)

Figure 3–23

Hα versus red-continuum luminosities. Includes all 102 HII regions with red-continuum emission above the 5-sigma level of the ambient disk. Error bars are based on noise in the subtracted sky and red-continuum backgrounds.

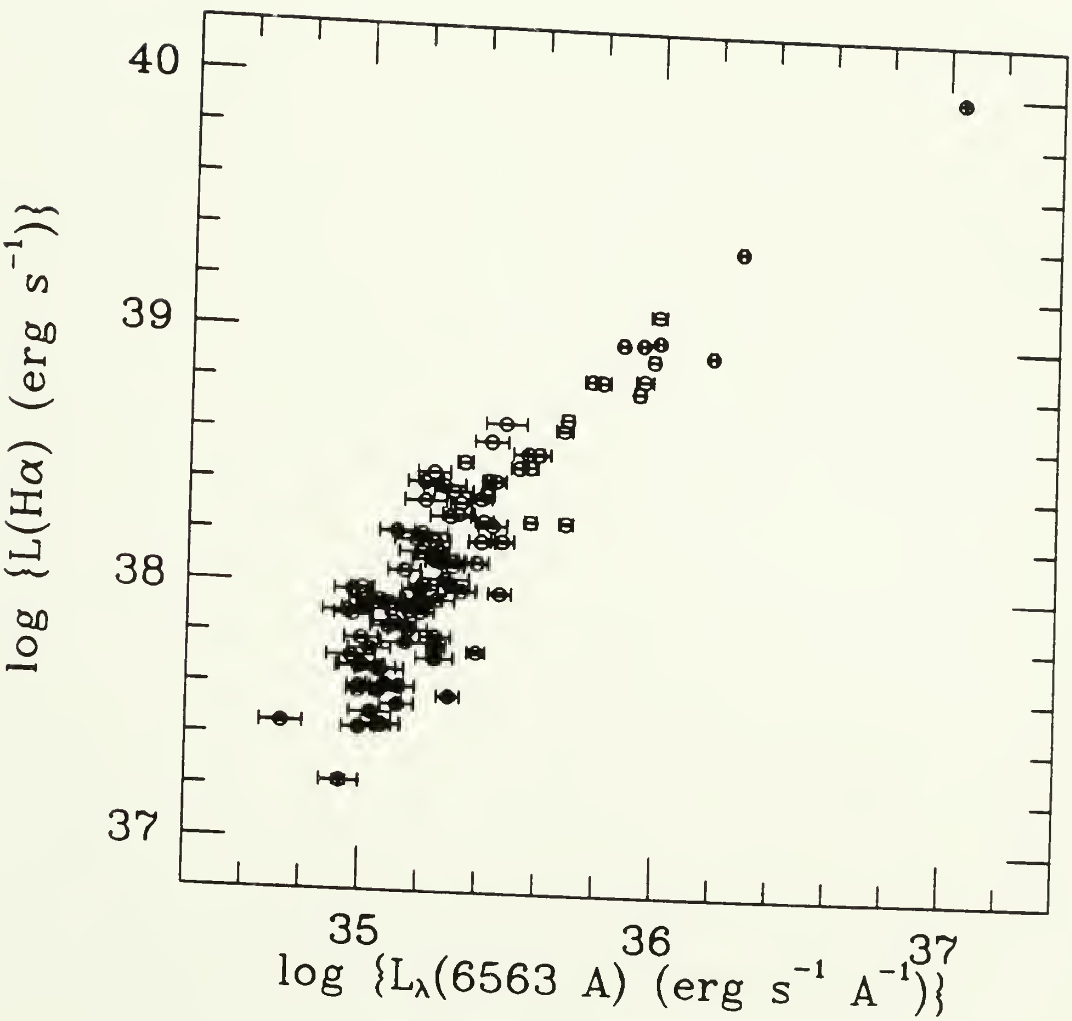
40
39
38
37
35
36
37
log {L(Hα) (erg s⁻¹)}
log {Lλ(6563 A) (erg s⁻¹ A⁻¹)}

Figure 3–24

Galactocentric distribution of Hα equivalent widths (without prior elimination of continuum emission from ambient disk). $L_\lambda(total)$ includes light from the ionizing cluster, any spiral arm enhancement, and the underlying disk. The resulting equivalent width is especially sensitive to the ratio of current-epoch to past-averaged star forming activity.

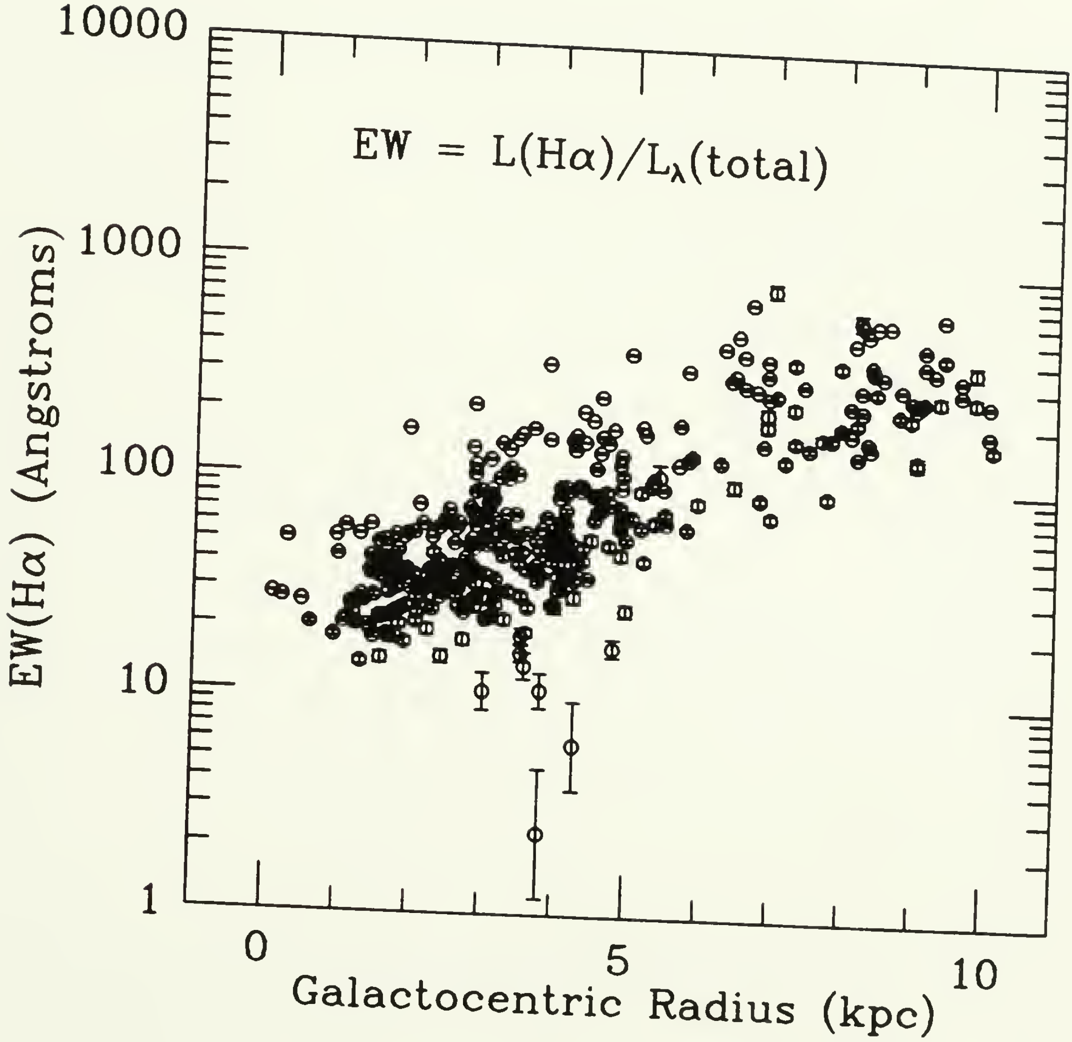

EW = L(Hα)/Lλ(total)
10000
1000
100
10
1
EW(Hα) (Angstroms)
0
5
10
Galactocentric Radius (kpc)

Figure 3–25

Galactocentric distribution of Hα equivalent widths (after elimination of continuum emission from ambient disk).

a. Galactocentric distribution of Hα equivalent widths, where L_λ(arm) includes light from the ionizing cluster and any spiral arm enhancement — the underlying disk light having been modeled via annular-averaged photometry and removed.

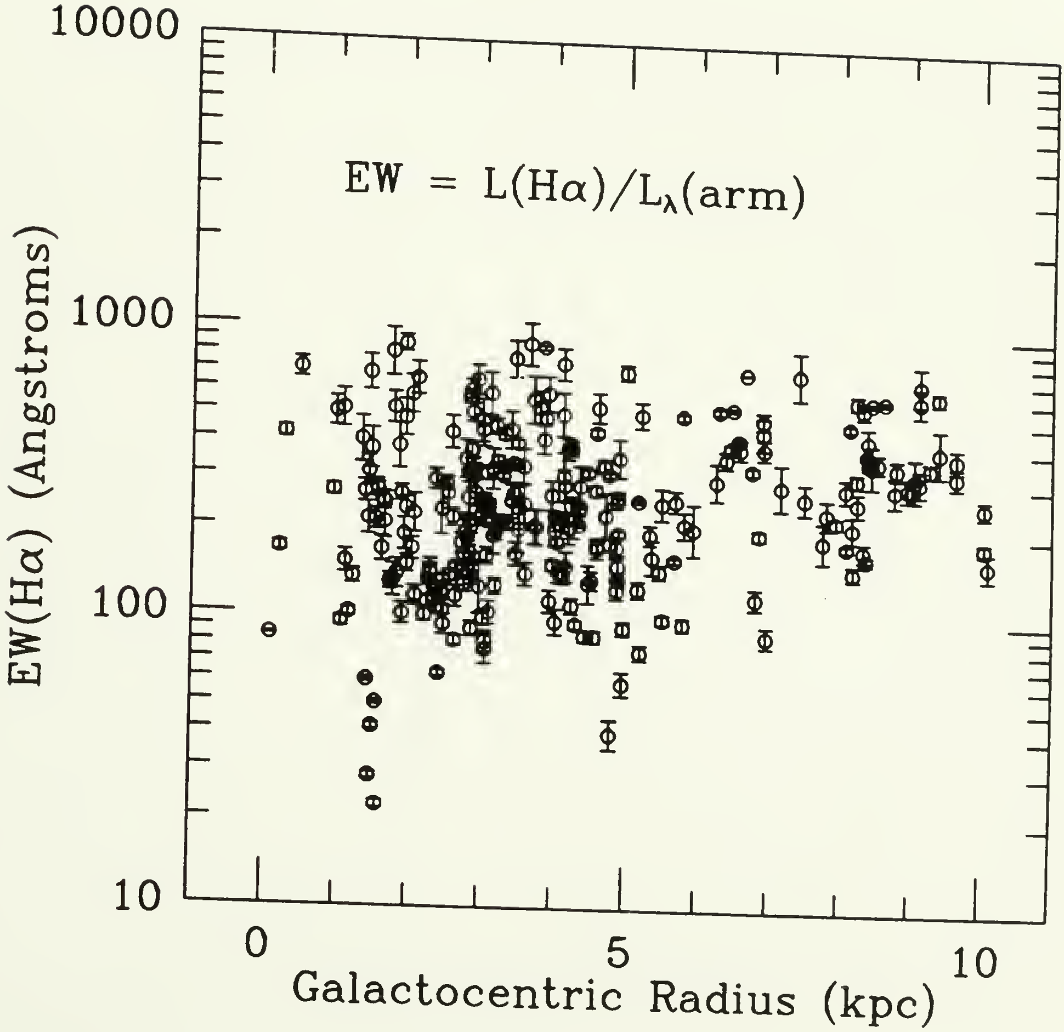
EW = L(Hα)/Lλ(arm)
10000
1000
100
10
EW(Hα) (Angstroms)
0
5
10
Galactocentric Radius (kpc)

Figure 3-25 (cont.)

b. Galactocentric distribution of Hα equivalent widths, where L_λ(cluster) includes light from the ionizing cluster only — the background disk and arms having been removed by subtracting a median-smoothed image from the original red-continuum image. All clusters with signal-to-noise ratios ≥ 5 are shown.

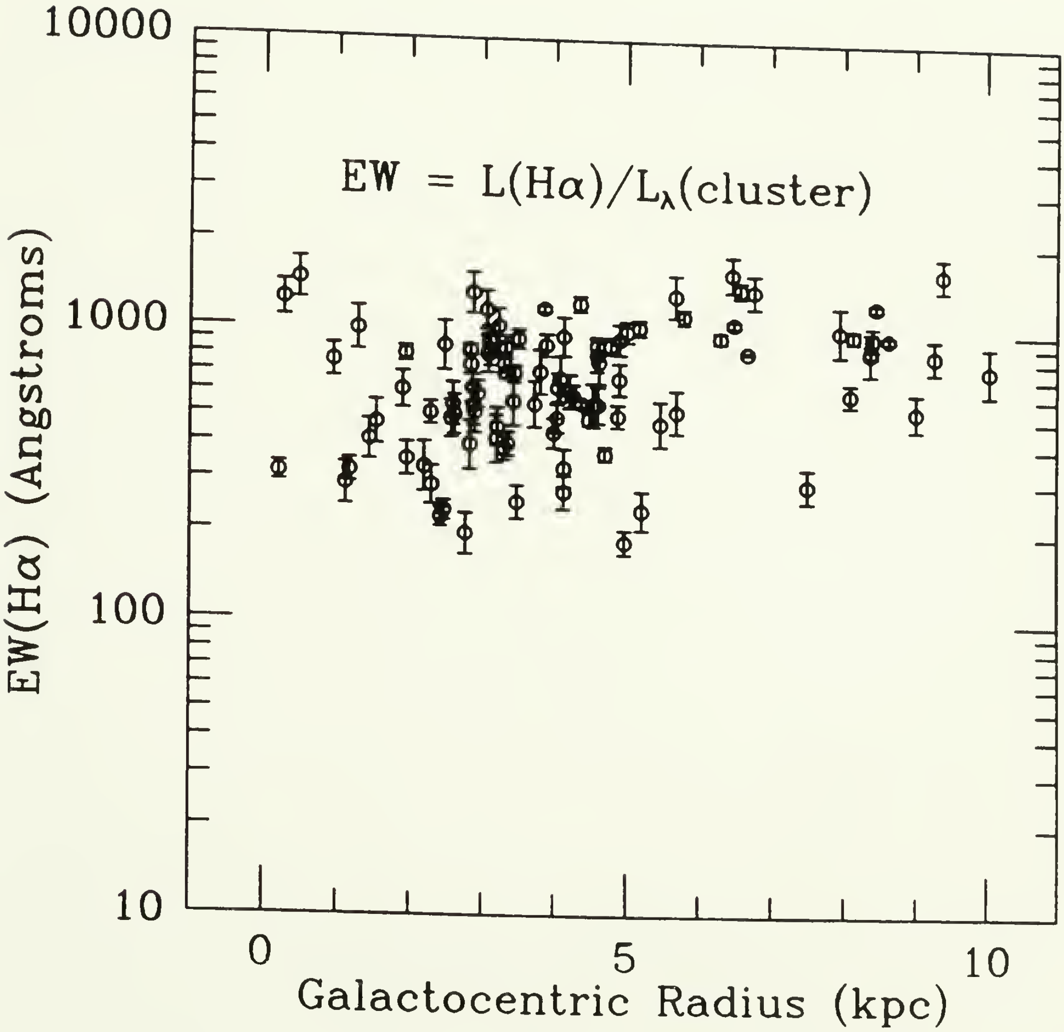

EW = L(Hα)/Lλ(cluster)
10000
1000
100
10
EW(Hα) (Angstroms)
0
5
10
Galactocentric Radius (kpc)

Figure 3-25 (cont.)

c. Galactocentric distribution of Hα equivalent widths, where L_λ(cluster) includes light from the ionizing cluster only — the background continuum having been determined individually for each and every HII region (from visual inspection of radial surface-brightness plots) and subtracted. All clusters with $S/N \geq 5$ are shown.

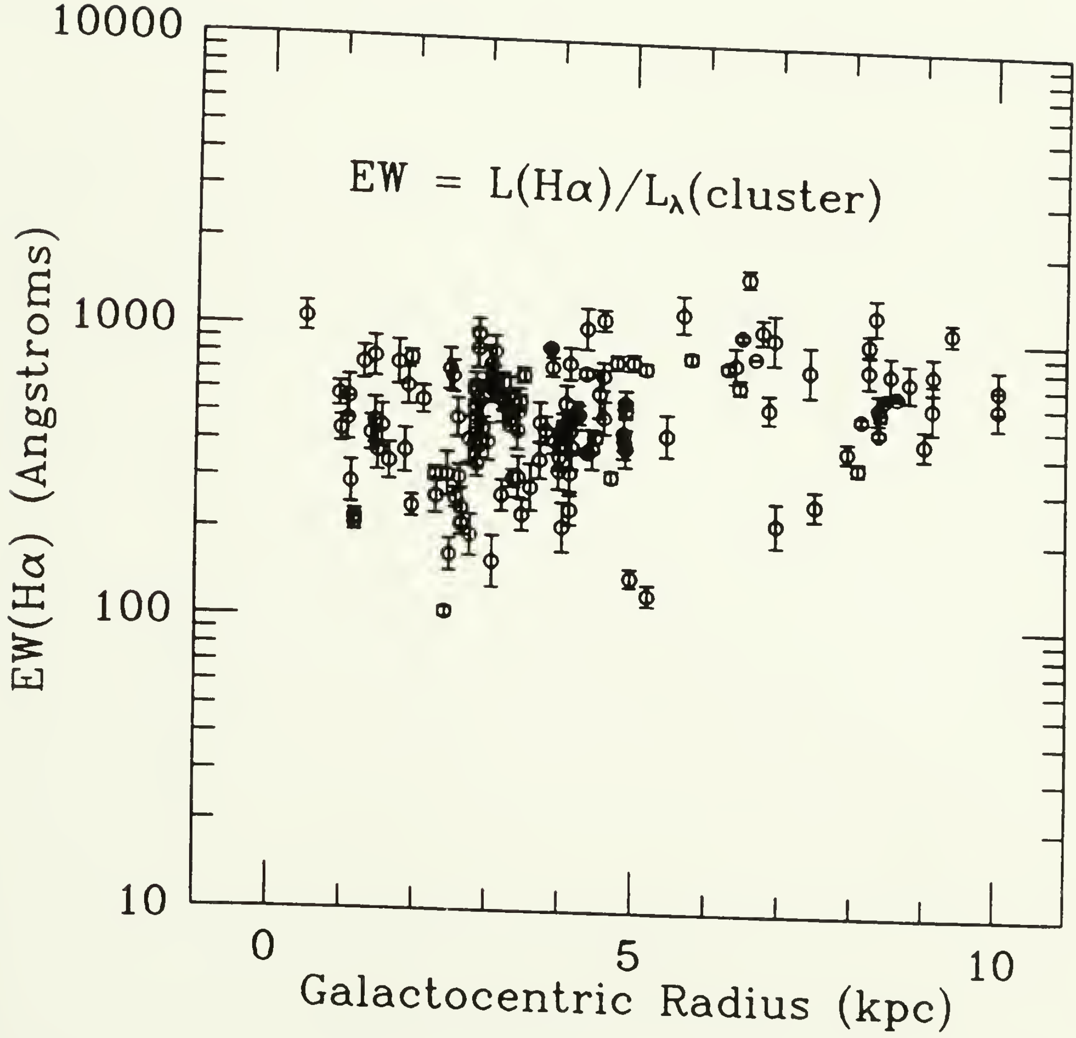
EW = L(Hα)/Lλ(cluster)
EW(Hα) (Angstroms)
10000
1000
100
10
0
5
10
Galactocentric Radius (kpc)

Figure 3–26

Theoretical effects of dust on Hα and red-continuum fluxes. The dust is assumed to be uniformly mixed with the ionized gas, while the continuum-emitting stars are assumed to be segregated on the backside of the HII region. This sort of morphology is similar to that produced by a "champagne-flow" expansion of ionized gas away from the ionizing star in the direction of least resistance. If the stars, gas, and dust are *all* uniformly mixed, then the attenuation of the Hα flux would be identical to that of the red-continuum flux, and the Hα equivalent width would be constant with dust optical depth. By contrast, the "champagne-flow" morphology (if viewed with the stars on the backside) results in a dust-dependent differential in the observed line and continuum fluxes (as shown in **a**) and hence a strong dependence of the Hα equivalent width on the dust optical depth (as shown in **b**).

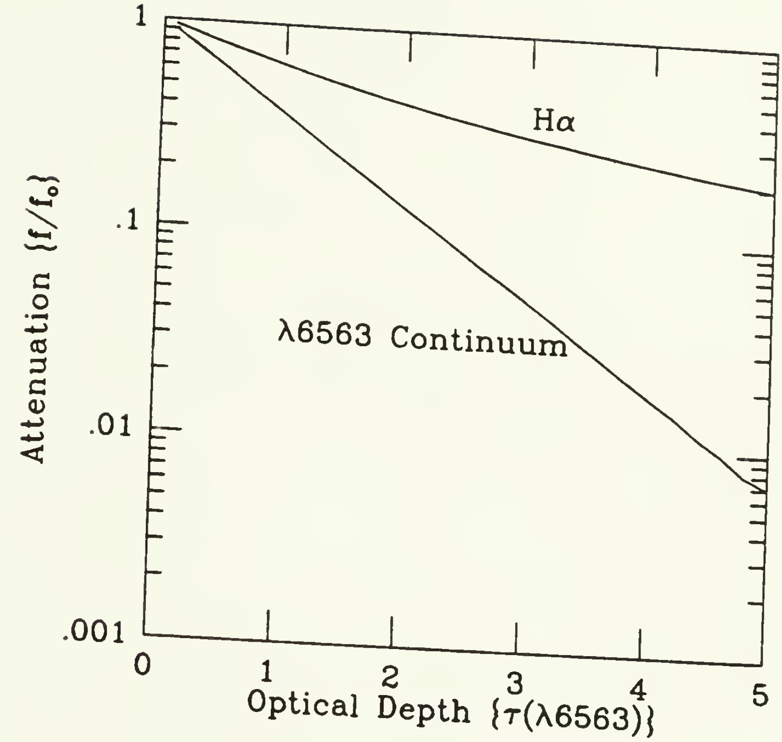
1
.1
.01
.001
Attenuation {f/f₀}
Hα
λ6563 Continuum
0
1
2
3
4
5
Optical Depth {τ(λ6563)}

a ▲ b ▼

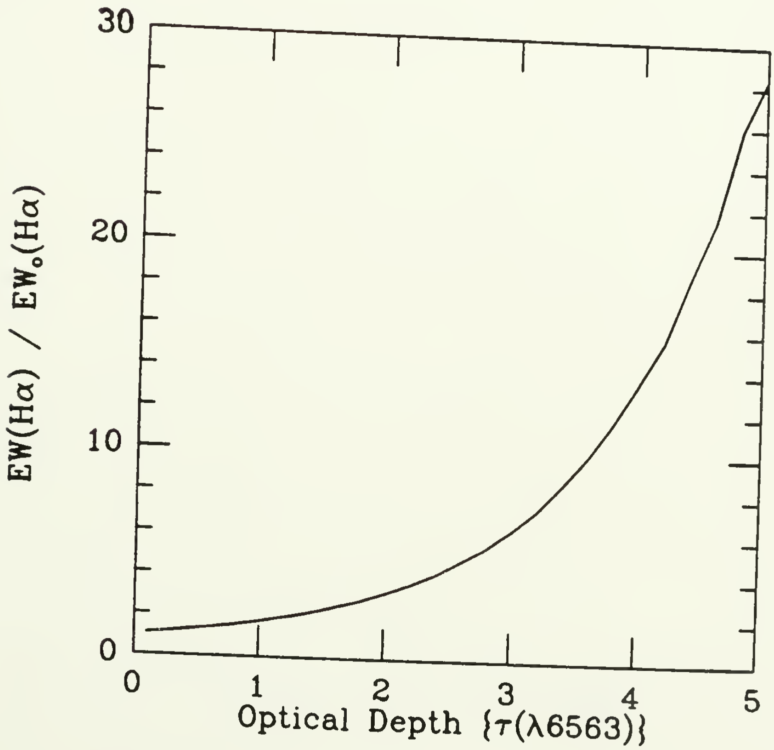
30
20
10
0
EW(Hα) / EW₀(Hα)
0
1
2
3
4
5
Optical Depth {τ(λ6563)}

Figure 3–27

Galactocentric distributions of cluster color and nebular extinction.

a. The galactocentric distribution of the ionizing clusters' (λ6563 - λ8380) colors, where contamination from the old stellar disk has been removed. The plotted sample includes those clusters with red continua greater than 5-sigma above the dispersion in the old disk. The error bars represent the quadrature sums of the standard errors at both wavelengths. The colors are plotted with the bluer values towards the top. Colors redder than 0.5 are thought to be the consequences of reddening by dust.

b. The galactocentric distribution of nebular extinctions as determined from the observed ratio of Hα and Hβ fluxes. The ratios were culled from a variety of references (Searle 1971; Smith 1975; Shields and Searle 1978; McCall *et al.* 1982; Rayo *et al.* 1982; Davidson *et al.* 1985). Although each ratio was computed from observations with the same size aperture, the sample of ratios involves observations with different size apertures.

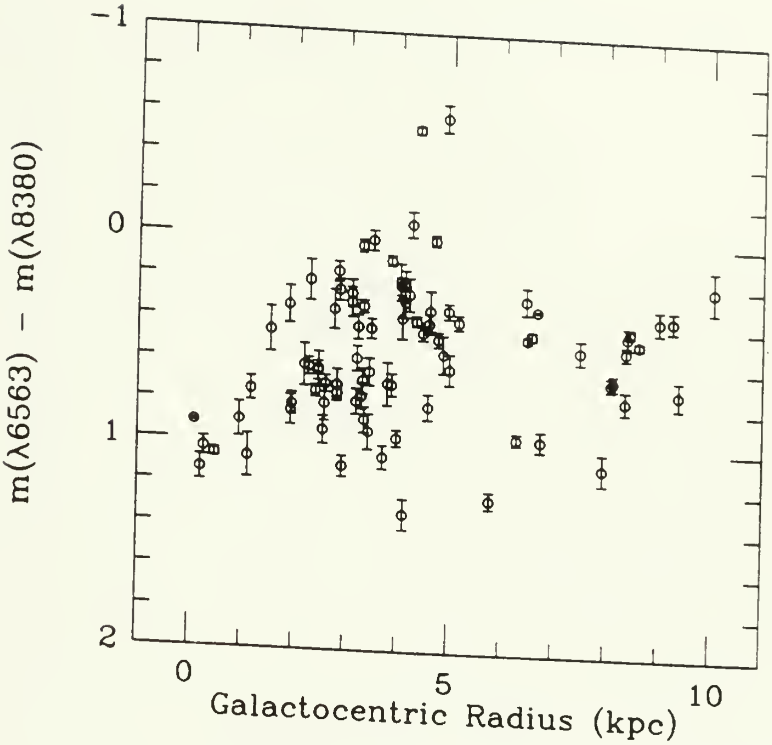
m(λ6563) − m(λ8380)
Galactocentric Radius (kpc)

a ▲ b ▼

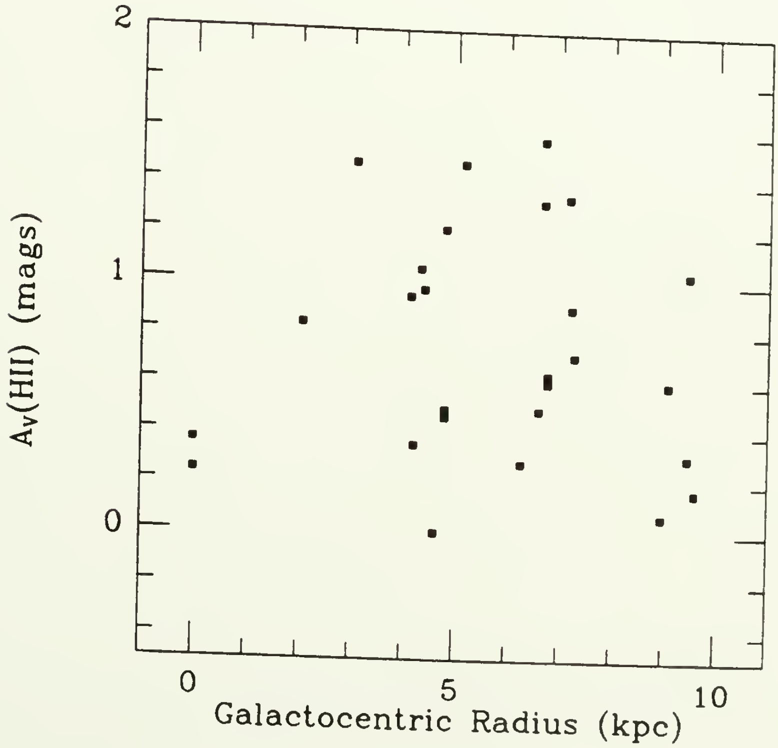
A_V(HII) (mags)
Galactocentric Radius (kpc)

Figure 3–28

Cluster colors versus Hα equivalent widths. The plotted sample includes all clusters with red continua greater than 5-sigma above the dispersion in the ambient disk. The format of this diagram follows that of traditional "color-color" diagrams, such that the EWs increase (become "hotter") towards the left and the (λ6563 − λ8380) color grows bluer towards the top. If *both* the color and the EW were systematically affected by the presence of dust, there would be a strong correlation between the two quantities. This is not evident.

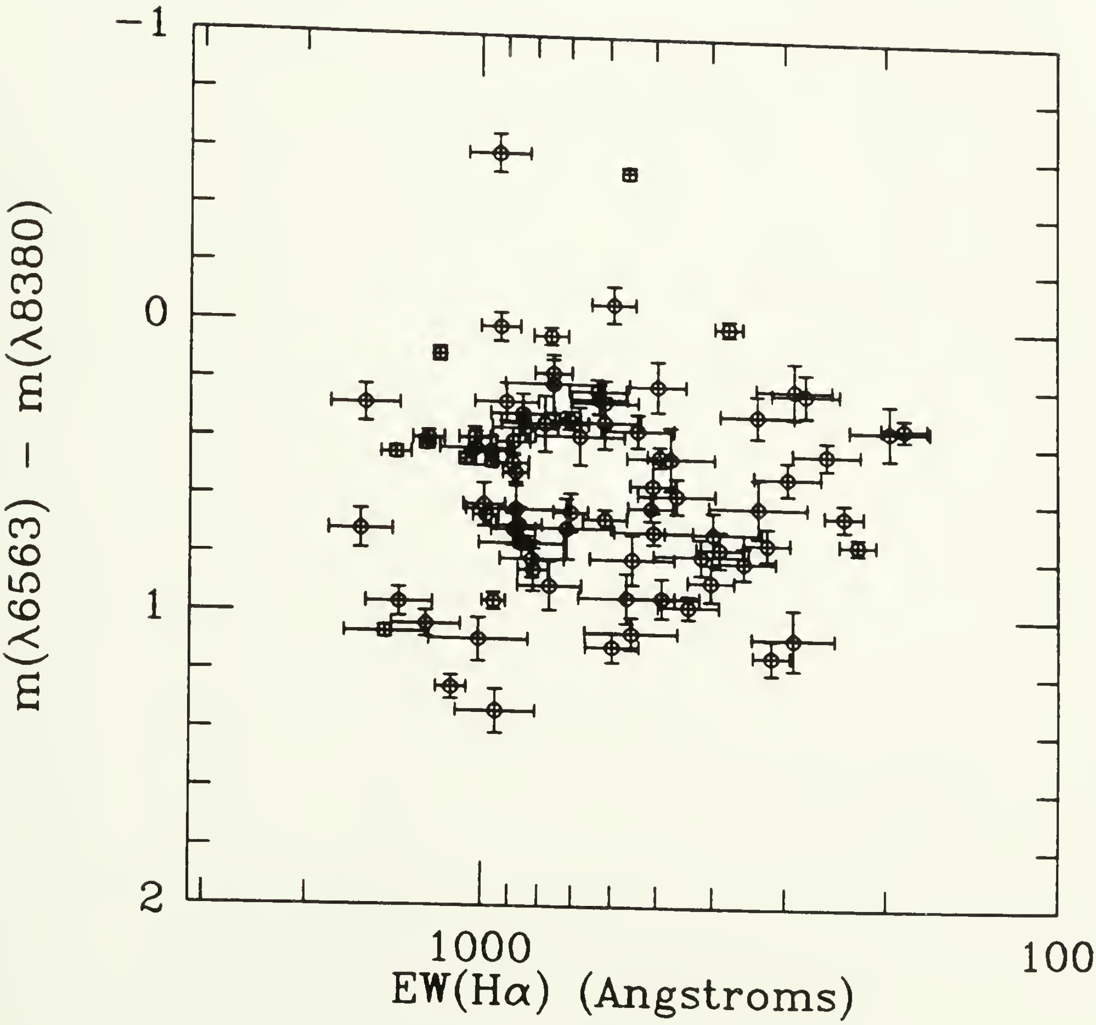

−1
0
1
2
m(λ6563) − m(λ8380)
1000
100
EW(Hα) (Angstroms)

Figure 3–29

Galactocentric distribution of Hα equivalent widths of blue clusters.

Galactocentric distribution of Hα equivalent widths after having excluded all clusters with ($\lambda 6563 - \lambda 8380$) colors redder than 0.5.

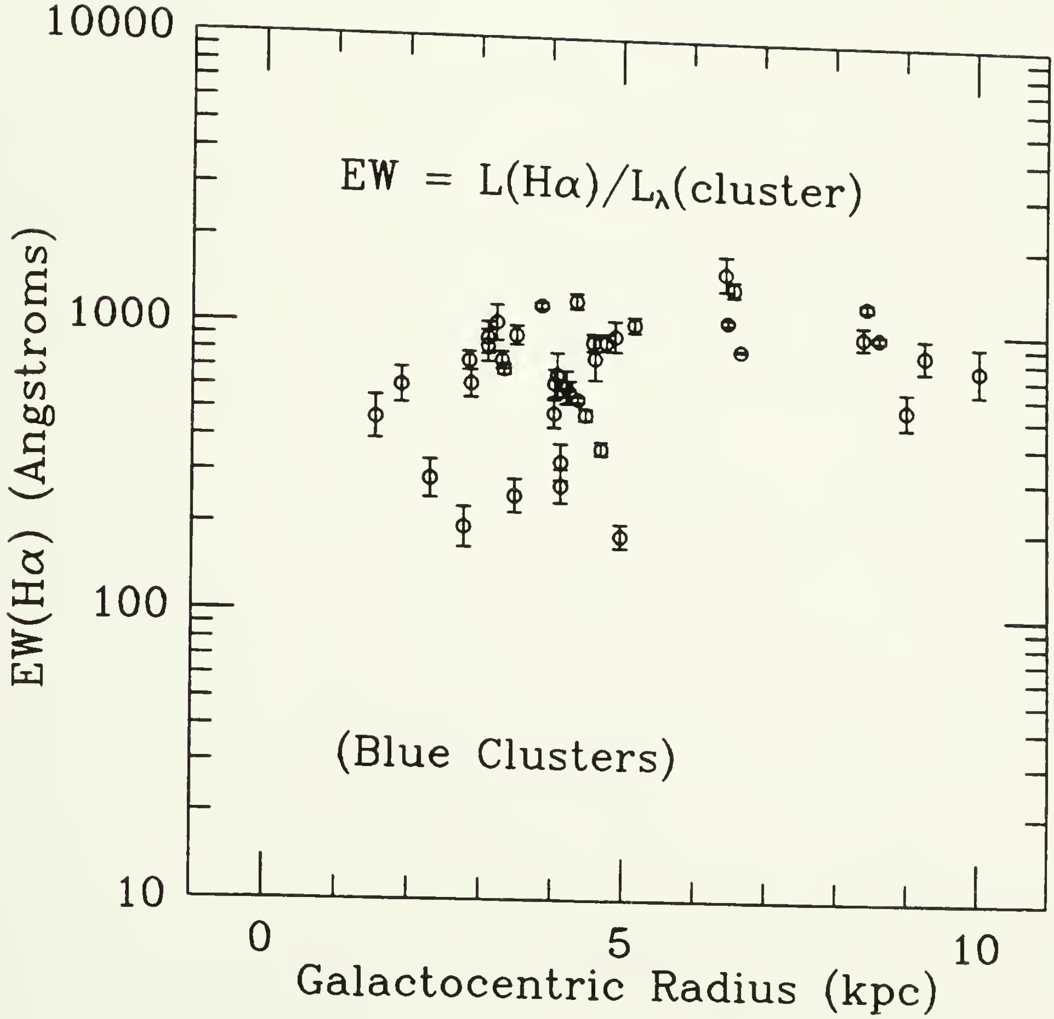
10000
1000
100
10
EW(Hα) (Angstroms)
EW = L(Hα)/Lλ(cluster)
(Blue Clusters)
0
5
10
Galactocentric Radius (kpc)

Figure 3–30

Modeled dependence between the Hα equivalent width and the upper stellar mass limit. EW_* refers to the line-to-continuum ratio when only the stellar continuum is considered. The values plotted here are based on the results of A. Campbell which were derived from the ZAMS population synthesis program described in Terlevich and Melnick (1985). EW_{tot} refers to the line-to-continuum ratio after the nebular continuum and the effects of nebular dust are incorporated. The fraction of ionizing luminosity that *is not* absorbed by dust is represented by β. The typical densities and gas-to-dust ratios found in giant extragalactic HII regions suggest that $\beta \approx 0.5$ (Spitzer 1978).

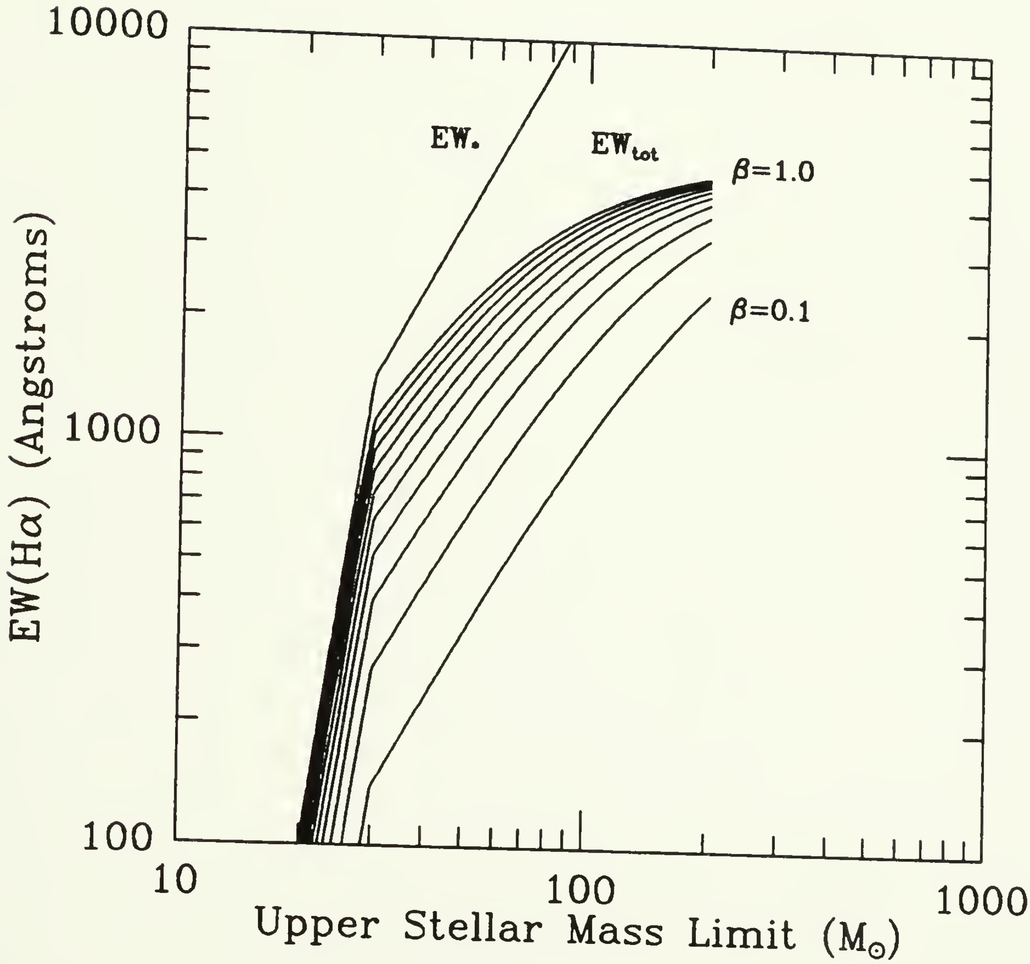

EW*
EW$_{tot}$
β=1.0
β=0.1
EW(Hα) (Angstroms)
10000
1000
100
10
100
1000
Upper Stellar Mass Limit (M$_\odot$)

Figure 3–31

Galactocentric distribution of Hα equivalent widths (combined data sets). The circles with error bars denote the equivalent widths that were obtained in the present study after excluding all significantly reddened clusters ($[\lambda6563 - \lambda8380] > 0.5$). The stars were derived from the spectroscopic data of Searle (1971), where some attempt had been made to isolate the starlight of the ionizing cluster from that of the ambient disk. The triangles are from the spectroscopy of Torres-Peimbert *et al.* (1989).

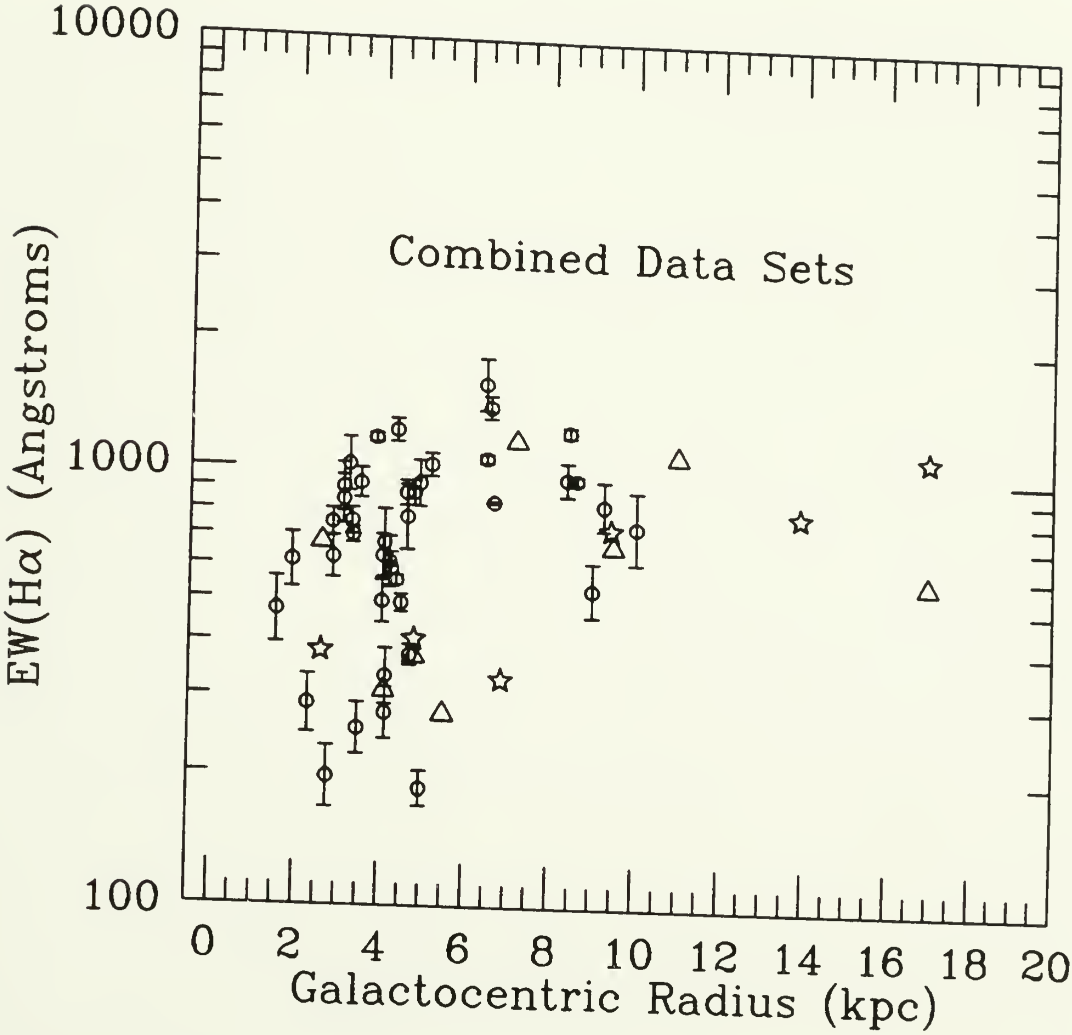
Combined Data Sets
10000
1000
100
EW(Hα) (Angstroms)
0
2
4
6
8
10
12
14
16
18
20
Galactocentric Radius (kpc)

Figure 3–32

"Temperature-Luminosity" diagrams using EW(Hα) as an index of cluster effective temperature. Increasing values of EW(Hα) go to the left, in accordance with "traditional" temperature-luminosity diagrams. The sample includes all clusters with red continua greater than 5-sigma above the dispersion in the ambient disk.

a. Hα luminosity versus Hα equivalent width.

b. Red-continuum luminosity density versus EW(Hα).

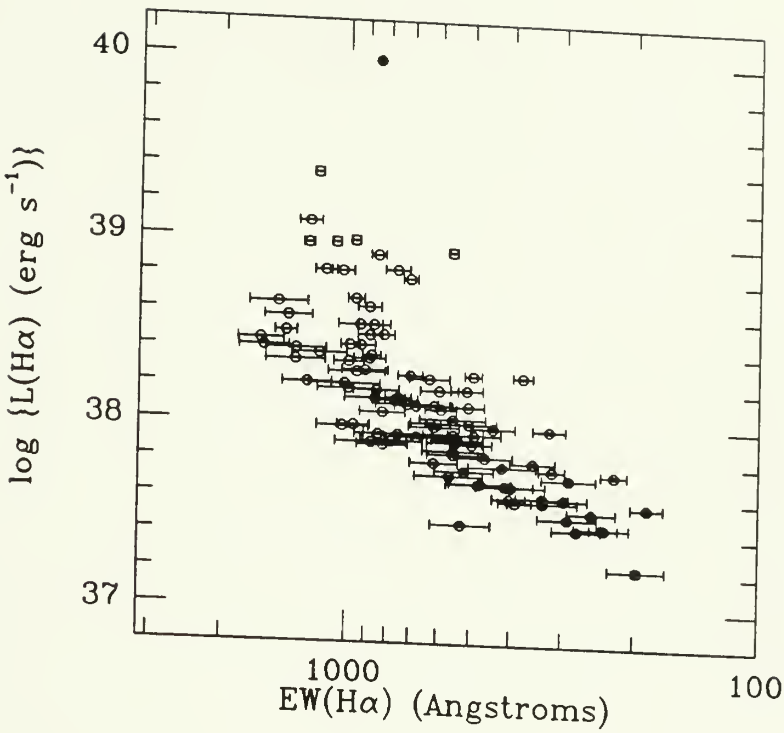
40
39
38
37
log {L(Hα) (erg s⁻¹)}
1000
100
EW(Hα) (Angstroms)

a ▲ **b ▼**

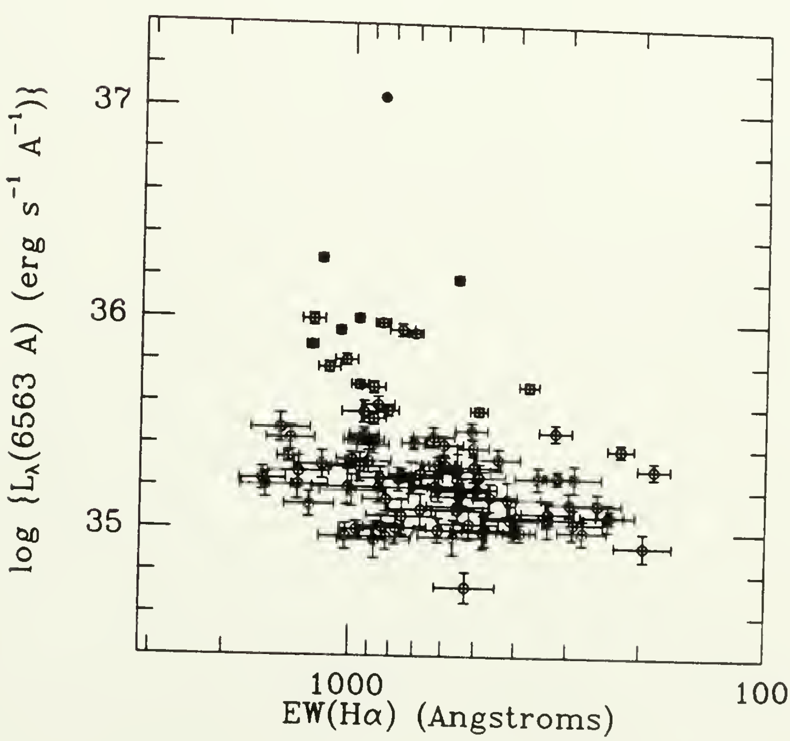
37
36
35
log {Lλ(6563 A) (erg s⁻¹ A⁻¹)}
1000
100
EW(Hα) (Angstroms)

Figure 3–33

"Temperature-Luminosity" diagram for blue clusters.

"Temperature-Luminosity" diagram for clusters with ($\lambda6563 - \lambda8380$) colors bluer than 0.5 and hence minimally reddened by dust. The Hα equivalent width is used as a tracer of the cluster effective temperature and is plotted against the Hα luminosity.

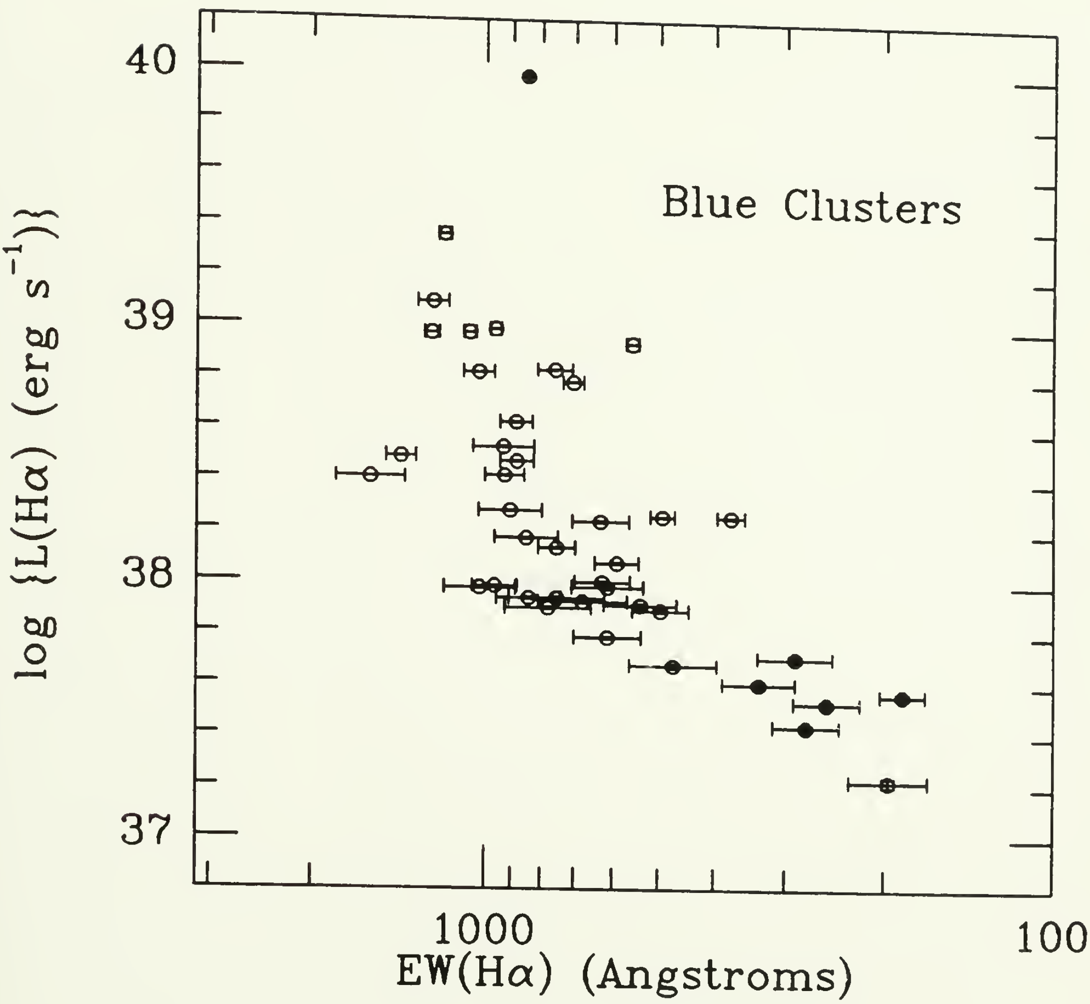
Blue Clusters
40
39
38
37
log {L(Hα) (erg s^{-1})}
1000
100
EW(Hα) (Angstroms)

CHAPTER 4

M82

4.1 *Abstract*

Red Hα and R-band CCD images of the starburst galaxy M82 are compared with corresponding near-infrared [SIII] and I-band imagery. Enhancements in the continuum-subtracted [SIII]/Hα flux ratio are evident along an arc that includes the nuclear "dust lanes" visible at Hα and two especially enhanced regions on opposite sides of the bursting nucleus. If interpreted as the consequences of reddening by dust, the [SIII]/Hα flux enhancements indicate the presence of obscured ionized gas, much of which is distributed immediately beyond the nuclear 1 kpc. The arclike morphology of the obscuration as well as the strong peripheral extinction can be explained by invoking a circumnuclear ring of dust that is highly inclined to the line of sight. Comparisons with other tracers of dust and gas are made in an effort to test the proposed scenario. Although some of the comparisons are ambiguous, most of them reinforce the picture of a circumnuclear "dusty chimney" that has been shaped by the starburst and is now collimating the subsequent eruptions.

4.2 *Introduction*

The classic "starburst" galaxy M82 (NGC 3034) has been a rich hunting ground for many types of emissive phenomena. The central kpc of this Irr II/Amorphous-class system is renowned for its bright continuum emission at far-infrared and radio wavelengths and for its powerful spectral-line emission at red, infrared and millimeter wavelengths. Most of this luminous activity has been attributed to a mega-burst of star formation that has recently occurred in the galaxy's nucleus (see reviews by Telesco [1988] and Sofue [1988]).

According to the "starburst" scenario, the radio continuum emission is dominated by synchrotron processes arising from the acceleration of electrons by the many supernovae that have detonated. The most recent detonations appear as discrete knots on high-resolution VLA maps (Kronberg *et al.* 1985).

The FIR continuum represents the dust which has absorbed the $3 \times 10^{10}\ L_{\odot}$ output from the newborn stars and which is now reradiating this luminosity at a temperature of 45 K (Telesco and Harper 1980; Joy *et al.* 1987). The 10 μm infrared continuum comes from hotter dust ($T \approx 150\ K$) adjacent to the hottest stars (Rieke *et al.* 1980). The infrared emission lines of hydrogen (Brα and Brγ), [NeII] 12.8 μm, [SIII] 18.7 and 33.4 μm, [OIII] 52 and 88 μm, and [NIII] 57 μm trace the $\sim 10^8\ M_{\odot}$ of gas that has been ionized by the new-born hot stars and which is now almost completely filling the volume of the nucleus (Simon *et al.* 1979; Rieke *et al.* 1980; Beck *et al.* 1978; Houck *et al.* 1984; and Duffy *et al.* 1987 respectively). The ionized component is also evident in a recent mapping of the 3.3 mm continuum (Carlstrom 1988), where thermal Brehmstrahlung processes are believed to outshine the nonthermal synchrotron processes. Also at mm wavelengths, the line emission from ^{12}CO, ^{13}CO, HCN, and HCO^{+} delineate the distribution of the remnant molecular gas at successively increasing densities (Lo *et al.* 1987; Nakai *et al.* 1987; Stark and Carlson 1982; Stark and Wolff 1979; Rickard *et al.* 1977; Carlstrom 1988).

Beyond the nucleus along the galaxy's minor axis, unusual Hα emitting plumes (Lynds and Sandage 1963; Williams *et al.* 1984), diffuse soft X-ray emission (Watson, Stanger, and Griffiths 1984; Kronberg *et al.* 1985), and anomolous optical emission-line ratios (McCarthy *et al.* 1987) attest to the presence of a hot (10^7 K) bipolar outflow which is shock heating the swept-up ISM to temperatures of $\sim 10^4$ K (Chevalier and Clegg 1985; McCarthy *et al.* 1987). The non-circular velocity field of the ionized gas filaments along the minor axis also seems to be consistent with some sort of outflow scenario (Williams *et al.* 1984; Bland and Tully 1988).

Recent single-aperture observations of the ^{12}CO 2.6 mm emission from M82 have revealed "spur-like structures" of molecular gas extending more than 0.5 kpc above and below the galaxy's major axis on opposite sides of the kpc-size central starburst (Nakai *et al.* 1987). These investigators have modeled their observations in terms of a molecular gas cylinder — seen edge-on — which surrounds the mostly ionized starburst region. Their so-called "dusty chimney" has been shaped by the energetic outflow of gas that is being driven by the windy

OB stars and shocking supernovae therein. Along the minor axes, the outflowing gas has met comparatively little opposition thus creating the Hα plumes and unusual gas kinematics that are observed above and below the galaxy's highly inclined disk. Along the major axis, however, the gas has encountered quiescent gas in the disk thus leading to a cylindrically symmetric pile-up. This simple picture has been supplemented by high-resolution observations of CO and 2.12 μm H_2 in emission and of 21 cm HI in absorption (Lo *et al.* 1987; Telesco 1988 and references therein), which show bipolar enhancements — suggestive of a "ring" of gas — interior to the "walls" of the dusty chimney.

In this Chapter, evidence for circumnuclear obscuration is presented. The association of this obscuration with observed enhancements in the CO, HI, and H_2 emission lends further credence to the idea of a "dusty chimney" having been shaped by a ring-shaped starburst and which is now collimating the subsequent eruptions. The obscuration is derived from a well-resolved comparison of the galaxy's Hα emission with its corresponding near-infrared [SIII] emission. Enhancements in the longer wavelength [SIII] emission (9532 Å) relative to the Hα emission are attributed to the reddening effects of dust. Such an interpretation has been found to be fairly reliable, as long as other effects influencing the [SIII]/Hα flux ratio (*e.g.* the metallicity and excitation) are taken into account (see Figure 4–1). Previous comparisons of [SIII] and Hα emission from dust-rich galaxies include an imaging study of NGC 253 (Waller, Kleinmann, and Ricker 1988) and an imaging survey of 5 other infrared-bright galaxies including M82 (Young, Kleinmann, and Allen 1988). Kennicutt and Pogge (1989) have re-observed the latter 5 galaxies using a long-slit spectrograph and CCD detector in an effort to verify the unusually high [SIII]/Hα intensity ratios reported by Young *et al.* (1988). The present Chapter concentrates on M82 and, in particular, on the circumnuclear distribution of obscuration that is traced by the observed enhancements in the [SIII] emission.

Table 4-1 lists the basic properties of M82 that will be adopted throughout the remainder of this Chapter. The new observations are presented in the form of images, contour diagrams, and major axis scans. The observed emission.

the derived extinctions, and the de-reddened emission, are discussed in the context of other available tracers of gas and dust.

4.3 *Observations and Reductions*

A summary of the CCD imagery obtained for this study is provided in Table 4-2. The Hα, [SIII], R and I-band images were obtained at the Cassegrain focus of the McGraw-Hill Observatory 1.3-m telescope on Kitt Peak during clear weather.[1] The imaging device was the "MASCOT" CCD camera developed at MIT (Meyer and Ricker 1980), a dual-chip system which enables a variety of simultaneous observing modes. I did not take advantage of this versatility and simply imaged on one of the chips — a TI 4849 virtual phase CCD (Luppino *et al.* 1987) which had replaced the poorer quality chip used in similar observations of NGC 253 (see Waller *et al.* [1988]). Although the full chip size is 584 × 390 pixels, only 476 × 390 worth was saved after recording and trimming. Of this amount, approximately 15 percent was vignetted by the beam splitter in the MASCOT camera. With the $f/13.5$ secondary in place, the resolution per pixel is 0.81", and the unvignetted field of view is approximately $5' \times 5'$. The following sections will be concerned with the central $2' \times 2'$ of the unvignetted field — where M82's starburst nucleus and high-latitude plumes are located.

Imaging at Hα was conducted using an interference filter (#1276, λ6563) kindly loaned by Kitt Peak National Observatory. With a $\Delta\lambda = 36$ Å bandpass, this filter is sufficiently broad to accomodate the galaxy's systemic redshift of 4.8 Å as well as the ± 3 Å shifting due to the galaxy's disturbed velocity field (O'Connell and Mangano 1978; Williams *et al.* 1984). Near the nucleus ("knot A" of O'Connell and Mangano [1978]), the filter passes $H\alpha(\lambda_o 6563)$ with 0.75 transmissivity, $[NII](\lambda_o 6584)$ with 0.16 transmissivity, and $[NII](\lambda_o 6548)$ with 0.67 transmissivity. From the emission-line velocities and [NII]/Hα line ratios measured by O'Connell and Mangano (1978), I estimate the net contamination

---

[1] The McGraw-Hill Observatory is operated by Dartmouth College, Massachusetts Institute of Technology, and the University of Michigan, with partial support from the National Science Foundation, the Alfred P. Sloan Foundation, and McGraw-Hill, Inc.

from [NII] to be 41 ± 11 percent in emission and 25 ± 4 percent in the present Hα imagery, depending on position in the galaxy. Referring to O'Connell and Mangano's specific measurements, the estimated levels of *detected* [NII] contamination are 26 percent in knot A, 28 percent in knot C (12" SW of A), 35 percent in knot E (11" W of A), 21 percent in knot F (30" W of A), 27 percent in the northern filaments (12" - 25" N of A), and 22 percent in the southern filaments (12" - 36" S of A).

Imaging at [SIII] was conducted with a Barr Associates interference filter ($\lambda 9532$, $\Delta\lambda 43$) kindly loaned by George Ricker. Contamination by the Pa8 line ($\lambda_0 9546$) within the bandpass is expected to be negligible (Dennefeld and Stasinska 1982). The effect of telluric H_2O absorption on the variously Doppler-shifted [SIII] emission could be significant, but to first order it can be corrected by referral to measurements of a similarly affected calibration star. Imaging of the red and near-infrared continua was conducted using the resident "R-band" and "I-band" filters at McGraw-Hill Observatory. Their wavelengths of peak transmissivity and FWHM bandpasses are similar to those of the Mould system R and I filters commonly used at Kitt Peak.

Images of the subdwarf standard star $BD + 26°2606$ (Oke and Gunn 1983) were obtained immediately after imaging the galaxy. Like other subdwarfs of spectral type sdF, this star has a relatively clean spectrum with few absorption features at red wavelengths. Additional observations of the subdwarf standard $BD + 17°4708$ were also made thus providing a check on the calibration process. Images of an illuminated screen inside the dome were taken through each filter at the beginning of each night for the purpose of flattening the background variations in the galaxy images.

Initial processing of the CCD imagery was accomplished using the Mountain Photometry Code package at Kitt Peak headquarters. Bias averaging and subtraction as well as flatfield division were performed automatically using the standard algorithm. Because of the relatively short exposure times that were involved, darkframe subtraction was found to be unnecessary. Further processing, including image arithmetic, median filtering, and synthetic aperture photometry, was conducted at the Universities of Massachusetts and Washington using the Image Reduction and Analysis Facility (IRAF) software created at Kitt Peak National Observatory.

All measured fluxes were corrected for atmospheric extinction, using the airmass at the time of observation and Beer's Law:

$$R_\circ = R\ 10^{0.4K_\lambda sec\ z}, \tag{4-1}$$

where $R_\circ$ denotes the corrected count rate per pixel as expressed in $ADU\ s^{-1}$, z is the zenith distance, $K(\lambda6563) = 0.1$, and $K(\lambda9532) = 0.05$ as estimated from CCD observations of Landolt standards taken at Kitt Peak during 1986 (Bushouse, private communication). Synthetic aperture photometry on the images of the sdF-type standard star $BD + 26°2606$ yielded the following conversions between flux and count rate (after bias subtraction, flatfield division, and atmospheric extinction correction):

$$f(H\alpha)(erg\ cm^{-2}\ s^{-1}) = 4.0 \times 10^{-14} R_\circ(\lambda6563,\ \Delta\lambda36)(ADU\ s^{-1}), \tag{4-2}$$

$$f([SIII])(erg\ cm^{-2}\ s^{-1}) = 4.1 \times 10^{-13} R_\circ(\lambda9532,\ \Delta\lambda43)(ADU\ s^{-1}), \tag{4-3}$$

$$f_\lambda(\lambda6563)(erg\ cm^{-2}\ s^{-1}\ \mathring{A}^{-1}) = 4.2 \times 10^{-17} R_\circ(R\ band)(ADU\ s^{-1}), \tag{4-4}$$

$$f_\lambda(\lambda9532)(erg\ cm^{-2}\ s^{-1}\ \mathring{A}^{-1}) = 2.4 \times 10^{-17} R_\circ(I\ band)(ADU\ s^{-1}). \tag{4-5}$$

Nearly identical conversions were obtained using $BD + 17°4708$ as the calibrator.

A final check on the calibrations was made from photometry of the star $AGK3 + 690428 = BD + 70°587$ which appears in the images of M82 approximately 2 arcminutes to the southwest of M82's nucleus. The [SIII] image was the only one not to saturate on this star, and so I could only check on the [SIII] calibration. The *Catalogue of Stellar Identifications* (1977)[2] lists this star as a

---

[2] Based on data retrieved from SIMBAD, database of the Strasbourg, France, astronomical Data Center.

G5 spectral type with magnitudes of B = 10.5 and V = 9.4 and proper motions of $\mu_\alpha = -0.016'' \; yr^{-1}$ and $\mu_\delta = -0.020'' \; yr^{-1}$. The resulting [SIII] calibration, based on the star's extrapolated 9532 Å flux density (Johnson 1966; Kurusz 1979) and photometry of the [SIII] image, agrees with the subdwarf calibrations to within 10 percent (if $BD + 70°587$ is a main sequence star). The calibration would exceed the subdwarf calibration by almost a factor of two, however, if $BD + 70°587$ turns out to be a giant. The proper motion of this star is consistent with it being 160 pc away at an absolute magnitude of 4.5, which would designate it as being a G5V-IV star. Therefore, the calibrations appear to be in good agreement. Spectrophotometric observations of $BD + 70°587$ at optical and near-infrared wavelengths would be necessary to better calibrate the M82 data.

Additional uncertainty in the derived fluxes stem from the noise in the subtracted sky backgrounds. The resulting uncertainties are estimated to be $\delta I(H\alpha) \approx 2.0 \times 10^{-16} erg \; cm^{-2} \; s^{-1} \; arcsec^{-2}$, $\delta I([SIII]) \approx 4.5 \times 10^{-16} erg \; cm^{-2} \; s^{-1} \; arcsec^{-2}$, $\delta I_\lambda(\lambda 6563) \approx 4.0 \times 10^{-18} erg \; cm^{-2} \; s^{-1} \; arcsec^{-2} \; Å^{-1}$, and $\delta I_\lambda(\lambda 9532) \approx 3.0 \times 10^{-18} erg \; cm^{-2} \; s^{-1} \; arcsec^{-2} \; Å^{-1}$. These uncertainties correspond to approximately 10 percent of the subtracted sky values.

To obtain Hα images that are free from contamination by the stellar and nebular continua, appropriately sky-subtracted, shifted and scaled R-band images were subtracted from the original sky-subtracted Hα-band images (see Appendix B). The scaling was determined from synthetic aperture photometry of foreground stars in the field of M82 and from photometry of the standard stars. The two methods gave scaling factors that agreed to within 10 percent. Similar processing of the I-band and [SIII] image was done to obtain a pure [SIII] emission-line image. To obtain red-continuum images that are free from contamination by the Hα emission line, subtraction of scaled Hα-band images from the R-band images was performed, where the scaling was determined from the relative bandwidths of the Hα and R-band filters (see Appendix B).

As a check on the image processing, I have compared the Hα flux from the inner $1.5' \times 1.5'$ of M82 with the flux obtained from the same region by McCarthy *et al.* (1987). After correcting the detected flux for a 20 percent contamination by [NII], I derive an Hα flux of $4.5 \times 10^{-11} erg \; cm^{-2} \; s^{-1}$, agreeing with that measured by McCarthy *et al.* to within 5 percent. Good agreement is also found between the Hα equivalent widths that I measure in the central knots and those measured spectroscopically by O'Connell and Mangano (1978). Lastly, I have compared the spectroscopic intensities measured by Kennicutt and Pogge (1989) with the corresponding intensities in the present imagery. Kennicutt and Pogge measured the [SIII] and Hα+[NII] intensities in M82 along an E-W oriented slit (180" × 4.5" in size) that was positioned 10" North of the 2.2 μm nucleus. They report a peak [SIII]/Hα+[NII] intensity ratio of 1.2 which corresponds to I([SIII])/I(Hα) ≈ 2.0; I obtain a peak intensity ratio of 1.9 along the same E-W cut. The consistency between these measurements contrasts strongly with the results of Young *et al.* (1988) who obtain I([SIII])/I(Hα) ≈ 6 along the same E-W cut. Kennicutt and Pogge argue that insufficient continuum emission was subtracted from the 144 Å-bandwidth [SIII] imagery of Young *et al.*, thus leading to their much higher measured [SIII] intensities and [SIII]/Hα intensity ratios.

4.4 *Emission-Line Morphology*

Figure 4–2 shows the Hα and [SIII] images of M82 that were obtained after having subtracted off the contaminating continuum emission from the narrowband CCD images. Figure 4–3 shows the corresponding contour diagrams of Hα and [SIII] surface brightness. These diagrams are similar to those produced by Young *et al.* (1988) except for the 2 - 3 times lower [SIII] surface brightnesses that I find on opposite sides of the nucleus along the major axis (see previous Section).

The 3 most obvious distinctions between the [SIII] and Hα images are:

• The [SIII] emission shows a lens-like distribution consistent with the appearance of a highly inclined disk galaxy, whereas the Hα emission is not nearly as extended along the major axis. This morphological difference extends beyond the major axis to high latitudes, where the radiation is thought to arise from scattering by dust grains (Mathis 1973; Visvanathan and Sandage 1974).

• The inner Hα emission is structured into discrete "knots" separated by lanes of darkness (O'Connell and Mangano *et al.* 1978), whereas the [SIII] emission is more smoothly distributed. Even the two central bright spots in the [SIII] image are less prominent relative to their neighboring emission.

• The centroids of the two [SIII] bright spots are displaced 4" northwest of the Hα counterparts.

All of these differences can be understood as consequences of the greater obscuration suffered by the *Hα* emission. The distribution of this obscuration — and of the obscuring dust — is discussed in the following section.

4.5 *Circumnuclear Obscuration*

To investigate the structure of obscuration in the starbursting region of M82, I have divided the [SIII] image by the Hα image. According to the relationships illustrated in Figure 4–1, regions with higher [SIII]/Hα flux ratios should be tracing larger amounts of reddening and hence obscuration. The resulting "flux ratio" image and contour diagram are shown in Figures 4–4 and 4–5(a) respectively. The image format most clearly shows the striking correspondence between the lanes of darkness in the Hα image and the ridges of enhanced [SIII] in the [SIII]/Hα image. *If the dark lanes are, in fact, consequences of obscuration, then the Hα "knots" which they outline are probably not discrete objects (cf. O'Connell and Mangano 1978) but rather exposed portions of a much larger ionized region.*

Both the image and the contour diagram show the strongest [SIII] enhancements on opposite sides of the nucleus. These "circumnuclear" enhancements are well within the 3-sigma boundary of the [SIII] emission and can therefore be regarded as being real. The highest [SIII]/Hα flux ratios (1.5 - 2.0) are approximately 5 times higher than the ratios that characterize most individual HII regions (see Figure 4–1).[3] Together with the nuclear ridges, the circumnuclear enhancements define a shallow arc which rises from the major axis roughly 50"

[3] Young *et al.* (1988) obtain 2 - 3 times higher [SIII]/Hα flux ratios for the NE enhancement. This difference is mostly due to the higher amounts of [SIII] surface brightness that they find in this region. The SW enhancement is also greater by a factor of 1.5 - 2.0 in their data, again due to higher values of the [SIII] surface brightness.

(790 pc) southwest of the nucleus, culminates about 10" (160 pc) to the northwest of the nucleus, and falls back to the major axis about 40" (630 pc) northeast of the nucleus. Such an arc is consistent with the model of a *circumnuclear ring of obscuring dust* that is highly inclined to the line of sight. The displacement of the arc from the major axis implies an inclination of roughly 80°, with the near side of the ring lying to the Northwest and with the farside hidden in the Southeast. The thickness of the arc (~25" or ~400 pc) implies a toroidal geometry with an inner radius of ~18" (230 pc) and an outer radius of ~40" (630 pc). The lack of farside obscuration would be due to the farside dust lying *behind* most of the ionized gas. Alternatively, the arc of extinction could be tracing a half-shell of gas and dust which has been shaped by the central burst. The southern half of the shell would then be absent, thus implying a major eruption having occurred towards the South. This scenario, however, has trouble explaining why the [SIII]/Hα flux enhancements are greatest on opposite sides of the nuclear region, unless the shell is especially weak along the minor axis. In its favor are recent high resolution maps of HI 21 cm emission which show arc-like lobes of atomic gas to the northeast and northwest of the central starburst just beyond the obscuring arc (Yun *et al.* 1988).

To translate the [SIII]/Hα flux ratios into visual extinctions, it is necessary to adopt a "nominal" [SIII]/Hα flux ratio that is free of any reddening effects. Examination of Figure 4–5 shows that the lowest flux ratios appear to the South and are in the range of 0.2 ± 0.1. These ratios also exist in the data of Young *et al.* (1988), even though a higher nominal ratio of 0.5 is adopted by them for dereddening purposes. Such low ratios have also been found in HII regions of the Large Magellanic Cloud (Dennefeld and Stasinska 1983). Examination of Figure 4–1 indicates that these ratios are associated with low O/H abundance ratios of about 2.0×10^{-4} which, in turn, imply [NII]/Hα flux ratios of 0.04 ± 0.02 (McCall *et al.* 1985; see also Chapter 3). Spectroscopic observations of M82 by McCarthy *et al.* (1987) give much higher [NII]/Hα flux ratios of 0.5, however, which are more typical of solar abundances (O/H $\approx 7.0 \times 10^{-4}$). Therefore the "near-solar" abundances inferred from the [NII]/Hα flux ratios in M82 appear to be inconsistent with the "Magellanic-type" [SIII]/Hα flux ratios that are evident to the south of the nucleus. Line emission due to processes other than photoionization by OB-type stars could be contributing to the anomolously low [SIII]/Hα flux ratios that are observed (McCarthy *et al.* 1987). Faced with this perplexing situation, I have chosen to derive the following extinctions based on a reddening-free [SIII]/Hα flux ratio equal to 0.2. My reasons for this choice are that (a) a higher value would lead to the derivation of negative extinctions to the south of the nucleus, which would be unphysical, and (b) the extinction depends on the *ratio* of the observed flux ratio against the nominal flux ratio and is therefore insensitive to the physical origin of the nominal flux ratio and to systematic offsets in the two ratios due to possible calibration error. Spatial variations in the nominal flux ratio are presumed to be negligible. This presumption could be in error, however, if different ionization and excitation processes are operating at different sites.

Visual extinctions were derived from the observed [SIII]/Hα flux ratios according to

$$A_v = 7.5[log\{f([SIII])/f(H\alpha)\} - log\{f_\circ([SIII])/f_\circ(H\alpha)\}], \qquad (4-6)$$

where $f_\circ([SIII])/f_\circ(H\alpha) = 0.2$, and where a reddening law similar to that found in the solar neighborhood has been adopted (*i.e.*, van der Hulst curve No. 15; *cf.* Johnson 1965). Figure 4–5(b) shows the resulting spatial distribution of visual extinctions. The extinctions range between $A_v = 0$ and $A_v = 7$, the highest value corresponding to an optical depth of dust at 9532 Å of 2.5. The regions of greatest extinction are located beyond the central starburst, near the extremities of the shallow "arc." Such peripheral enhancements in the obscuration are consistent with the "limb darkening" effects that would be created by an inclined annulus of dust.

It is interesting to compare the above-derived extinctions with the corresponding continuum-band surface brightnesses at red and near-infrared wavelengths (see Figure 4–6). Both continuum-band images show a band of darkening that diagonals across the major axis approximately 20" NE of the nucleus. This feature closely matches the region of highest extinctions as determined from the [SIII]/Hα ratios. The (λ6563 – λ9532) color of this feature (see Figure 4–7) is between 1.0 and 1.2, or roughly 0.4 magnitudes redder than the rest of the disk. Since $E(B-V) \approx E(\lambda6563 - \lambda9532)$, the corresponding increase in visual extinction would be 1.2 mag. If the inner disk of M82 has an intrinsic composite spectrum similar to that of an F8-type star ($(B-V)_\circ \approx 0.5$ [O'Connell and Mangano 1978]), the total extinction would be about 2.8 mag. This is roughly a factor of 2.5 lower than the peak extinctions determined from the [SIII]/Hα flux ratios. Because the stars are distributed throughout the disk and the ionized gas is more concentrated towards the center of the disk, a difference in the derived extinctions is to be expected. An idealized geometry which has the obscuring dust coextensive with the stars (so that the attenuation of the starlight goes as $[1 - e^{-\tau}]/\tau$) but foreground to the ionized gas (so that the emission-line attenuation goes as $e^{-\tau}$) would lead to stellar and nebular extinctions that differ by a factor of ~3.

To the SW of the nucleus, the continuum imagery show other less prominent dust lanes, one of which is coincident with a peak in the nebular extinction. This region — 40" from the nucleus — is not nearly as reddened as the NE dust lane, its ($\lambda6563 - \lambda9532$) color being only about 0.9. The corresponding visual extinction would be about 1.9 mag., or roughly 3 times lower than that derived from the nebular lines. The rest of the disk has $(\lambda6563 - \lambda9532) \approx 0.7 - 0.8$ which would correspond to an extinction of about 1.3 mag. This agrees to within 0.2 mag with previous estimates based on (B - V) colors (O'Connell and Mangano 1978 and references therein).

4.6 *Nuclear Obscuration*

Near the 2.2 μm nucleus, the derived extinction is about 5 magnitudes. This is somewhat higher than the extinctions of $A_v \approx 3$ that have been derived from comparisons of the Hα and shorter-wavelength Hβ fluxes from the same region (O'Connell and Mangano 1978 and references therein; McCarthy *et al.* 1987) but is considerably lower than the 14 – 25 mag. of extinction that have been obtained from ratios of the longer-wavelength Brα and Brγ fluxes (Willner *et al.* 1977; Simon *et al.* 1979; Rieke *et al.* 1980). Such wavelength-dependent extinctions have also been found in the nucleus of NGC 253 (Waller *et al.* 1988). The increase of computed visual extinction with sampled mean wavelength is consistent with the presence of a limiting optical depth of dust ($\tau_\lambda \approx 1 - 3$), beyond which the emission is no longer detectable. Radiative transfer models with uniformly mixed dust and ionized gas, or nonuniform foreground dust, can reproduce the threshold optical depths that are observed (Mathis 1983).

An additional check on the nuclear extinction can be made by comparing the [SIII] 0.9532 μm flux from the central 25" with the corresponding [SIII] 18.7 μm flux observed by Houck *et al.* (1984). The theoretical $\lambda 0.9532/\lambda 18.7$ ratio of emissivities has been found to depend weakly on the electron density but to vary significantly with electron temperature. At densities of $\sim 10^2\ cm^{-3}$, the ratio has been calculated to range from 0.97 at $T_e = 7500K$ to 2.7 at $T_e = 15,000K$ (Hippelein and Goudis 1986). The observed ratio of fluxes is 0.29. A comparison of this ratio with the theoretical values — assuming $\tau(18.7\mu m)/\tau(9.7\mu m) = 0.6$ (Herter *et al.* 1981) and the near-infrared reddening curve of Rieke and Lebofsky (1985) — yields extinctions of 9.2, 14.0, and 16.9 mag. at electron temperatures of 7500 K, 10,000 K, and 15,000 K respectively. These extinctions agree reasonably well with the extinction derived by Simon *et al.* (1979) from their Brackett-line observations. An even higher extinction of 20 mag. can be derived from a comparison of the mid-infrared 18.7 and 33.4 μm lines of [SIII] (Houck *et al.* 1984) (after setting the electron density equal to 210 cm^{-3}, as determined by Duffy *et al.* [1987] from observations of the density-sensitive [OIII] 52 μm/88 μm line ratio). These various measures of extinction further corroborate the "skin-depth" effect of wavelength-limited penetrating powers, as it applies to the dusty nucleus of M82.

4.7 *Extinction Corrections*

The derived extinctions at 6563 Å and 9532 Å have been used to correct the distributions of [SIII] and Hα emission according to

$$f_\circ = f 10^{0.4 A_\lambda}. \qquad (4-7)$$

The resulting "extinction-free" distributions of line emission are shown as images in Figure 4–8 and as contour diagrams in Figure 4–9. It should be noted that the innermost regions near the 2 μm nucleus could be significantly brighter than these figures indicate. The Brα and Brγ measurements of Simon *et al.* (1979) and Rieke *et al.* (1980) suggest that the extinction-free Hα surface brightness here is more like 5×10^{-12} $erg\ cm^{-2}\ s^{-1} arcsec^{-2}$, or roughly 3-7 times greater than the contoured value. The 3.3 mm continuum emission from the central $20'' \times 30''$ (Carlstrom 1988) also suggests ~$3\times$ higher fluxes (if the continuum is dominated by thermal Brehmstrahlung emission, as claimed). Furthermore, the major axis of the "extinction-corrected" Hα emission near the nucleus appears significantly displaced from the major axis as defined by the 3.3 mm and 2.2 μm emission. This displacement is a possible indication that the nuclear extinction corrections have missed the mark.

Beyond the innermost regions, the extinction-corrected emission is distributed in a pronounced bar or disk-like configuration which extends along the major axis out to a radius of almost 1 kpc. This contrasts strongly with the original Hα morphology whose major axis extent is less than 0.5 kpc. The total corrected Hα flux within the $2' \times 2'$ field of view is $f_\circ(H\alpha) = 5.9 \times 10^{-10}$ $erg\ cm^{-2}\ s^{-1}$, or 3 times the flux within the inner $20'' \times 30''$ and roughly 9.7 times the uncorrected value. At an assumed distance of 3.25 Mpc, the total Hα luminosity is then $L(H\alpha) = 7.5 \times 10^{41}$ $erg\ s^{-1}$, and the total ionizing luminosity is $N_i = 5.6 \times 10^{53}$ $photons\ s^{-1}$ (assuming Case B recombination at an electron temperature of 10,000 K [Osterbrock 1974]). If the ionizing radiation field is produced by hot OB-type stars, and if a Salpeter-type IMF is adopted (see Appendix A), the resulting star formation rate would be $SFR = 6.7\ M_\odot\ yr^{-1}$. Letting this activity be distributed in a disk of 1 kpc radius, I estimate the mean starbirth surface density to be $\sigma(SFR) = 2133\ M_\odot\ pc^{-2}\ Gyr^{-1}$, or roughly twice that measured in NGC 253 (Waller *et al.* 1988) and about 50 times higher than those inferred for the nuclei of M101 and the Milky Way (see Chapter 6). Addition of the heavily obscured ionized gas detected at Brα and 3.3 mm would approximately double these figures. Further adjustments towards higher values would be necessary, if the dust is absorbing a significant fraction of the ionizing photons (*cf.* Smith *et al.* 1978).

A complete re-evaluation of these stellar birthrates would be required, if the [SIII] and Hα line emission arise from physical processes other than photoionization by OB-type stars (McCarthy *et al.* 1987). Such nonstellar ionization, however, would create an unusually low value for the infrared excess (IRE) as defined by

$$IRE_{bol} = L_{bol}/N_i h\nu(Ly\alpha). \tag{4-8}$$

Adopting $L_{bol} = 3.9 \times 10^{10}\ L_\odot$ (Rice *et al.* 1988) and $N_i = 9.7 \times 10^{53}$ (which includes the heavily obscured component), I compute an IRE equal to 9.4. Similar IREs have been measured for high-mass star forming regions in the Milky Way (Caux *et al.* 1984). This consistency weakens the argument that wind-driven shocks provide the bulk of the ionization (*cf.* McCarthy *et al.* 1987). The fact that the FIR emission is extended (Joy *et al.* 1987) further argues against a point-like "monster" ionizing the gas and warming the dust. One is therefore left with an extended distribution of hot stars as the dominant source of ionization and infrared luminosity. The unusual "low ionization" spectral-line ratios that have been observed (McCarthy *et al.*) could be due to *strong outflows* of the photo-ionized gas smearing out the H^+ transition zone, *i.e.* the Stromgren radius, and thereby enlarging the regime of excited low-ionization species (A. Raga, private communication).

4.8 *Comparisons with Other Tracers of Gas and Dust*

In Figure 4–10, a scan of the visual extinction across the major axis is plotted along with high-resolution scans of the CO, Brγ, and H_2 (2.12 μm) emission as well as the HI 21 cm absorption. Several correspondences between the visual extinction and the other tracers of gas and dust are evident. In particular, the two enhancements in molecular hydrogen emission seem to coincide with peaks in the visual extinction. These two peaks (located 14" NE and 16" SW of the nucleus) are also seen in the CO and HI distributions. However, there are other peaks in the visual extinction that do not have any apparent counterparts. The most notable of these is located 40" SW of the nucleus. It is possible that this region was poorly sampled at the other wavelengths, however. The larger-scale mappings of CO by Sutton *et al.* (1983), Oloffson and Rydbeck (1984), Young *et al.* (1984), and Nakai *et al.* (1987) all show robust emission in this area.

Figure 4–11 compares the two-dimensional distribution of extinction with Nakai *et al.*'s (1987) 16"-resolution map of CO emission. Although the two distributions are dissimilar in appearance, the ridge lines of CO emission intersect some of the most obscured regions in the extinction map. According to Nakai *et al.* (1987), these ridge lines delineate the "walls" of the "dusty chimney" as seen in projection. It is worth noting that two more ridge lines can be drawn — one in the SE that intersects the major axis 10" NE of the nucleus, and another in the SW that intersects the heavily obscured region 40" SW of the nucleus. This latter ridge of CO emission is also evident in the 26"-resolution mapping by Sutton *et al.* (1983). Indeed, a more consistent picture would have an inner two-lobed structure of gas and dust with a radius of 10" - 15" and an outer "wall" with a NE displacement of 20" - 30" and a SW displacement 30" - 40". The greatest visual extinctions would then be associated with the limb-darkening effects of an outer ring, from which the outer "walls" diverge. The 3-dimensional distributions of gas and dust could be a lot more complicated than this simple picture allows, however.

In Figure 4–12 the "extinction-corrected" Hα emission from the inner $20'' \times 30''$ is plotted to the same scale as the 3.3 mm, 10 μm, CO, HI, and 2.2 μm emission. Correspondences between the Hα and the other tracers of ionized gas and warm dust are evident. The Hα, 3.3 mm, and 10 μm emission are all strongest 12" to the SW of the 2.2 μm nucleus. This site is also brightest at Brα (Simon *et al.* 1979).

Several lines of evidence are now pointing towards the presence of a small two-lobed structure ($R \approx 200$ pc) in the center of M82. The lobes are made up of molecular, neutral, and ionized gasses, as traced by the H_2, CO, HI, and HII emission that has been observed. The spatial relationships between the various gas phases remain uncertain, however. The new interferometric maps of CO emission have adequate spatial resolution for the comparison but are ambiguous with regard to what the CO emission is really tracing. The HI absorption-line map is more easily interpreted in this regard. The H_2 (2.12 μm), Brα, and Brγ observations are barely above the noise and should therefore be regarded with caution (D. Depoy, private communication). The well-resolved 3.3 mm continuum emission includes unknown contributions of nonthermal synchrotron emission and thermal reradiation by dust along with the thermal Brehmstrahlung emission from the ionized gas. Lastly, the "extinction-corrected" map of Hα emission that is presented here is well-resolved and well above the noise. However, it suffers from large uncertainties in the near-nuclear extinctions which, in turn, imply large uncertainties in the "extinction-corrected" morphologies.

With these difficulties in mind, one can still note a segregation between the ionized and neutral components. The sense of this segregation is that the tracers of ionized gas and warm dust lie interior to the CO and HI lobes, with the H_2 emission perhaps delineating the transition zone (Telesco 1988). Improved observations of the near-infrared tracers of ionized and molecular hydrogen, conducted with the newly available infrared arrays (D. Depoy, private communication), will no doubt help to untangle the various components of the ISM near M82's nucleus.

4.9 *Discussion*

The two-lobed structure near M82's nucleus is suggestive of a ring (Nakai *et al.* 1987) or of tightly-wound spiral arms (Lo *et al.* 1987) seen at high inclination. Similar ring-like structures of molecular, atomic, and ionized gas have been observed around the nuclei of several face-on barred spirals (Combes 1988). One of the best observed examples of the "ringed barred" class of galaxies is NGC 1097 which shows Hα "hot spots" encircling the nucleus at a radius of 700 pc (Meaburn *et al.* 1981). This circumnuclear ring is also evident in the radio continuum (Wolstencroft *et al.* 1984), at 10 μm (Telesco and Gatley 1981), and in CO (Gerin *et al.* 1988; Combes 1988). Combes (1988) ascribes the ring to an inner Lindblad resonance (ILR) that has been set up inside the stellar bar. As the bar perturbation transfers angular momentum outward via spiral density waves, dissipative material falls inward and piles up at the ILR. Perhaps the gaseous structures in M82's nucleus are consequences of similar dynamics.

Beyond the inner 30" (500 pc), are two regions of enhanced visual extinction (inferred from enhanced [SIII]/Hα flux ratios) which are intersected by "ridge-lines" of enhanced CO emission. These two regions seem to be the limb-darkened extremities of an obscuring arc of dust. If the CO ridges or "spurs" truly represent wind driven "walls" of molecular gas, then the arc would correspond to the ring-like intersection between the walls and the ambient disk. The greatest pile-up of gas and dust should be in the disk and hence in the ring. This is evident from the distribution of visual extinctions but is not apparent in the CO maps. Further compromising the ring interpretation, is a recent high-resolution map of the 21 cm HI emission (Yun, Ho, and Lo 1989) which shows the greatest concentrations of circumnuclear HI to the northeast and northwest of the central starburst just beyond the obscuring arc. Unlike the CO "spurs," the HI concentrations are not symmetric about the major axis. Instead, the HI seems to be tracing the remnant of a superbubble, which burst towards the Southeast but is still intact to the Northwest. The obscuring arc could therefore represent the inner portions of such a shell remnant.

Although these comparisons do not lead to a well-defined morphology, they reinforce the picture of a circumnuclear pile-up of dust and gas that has been shaped by the starburst and is now collimating the subsequent eruptions. They therefore support the "dusty chimney" scenario — with the "chimney" possibly being more open to the southeast than to the northwest of the major axis. The estimated mass of the pile-up, based on the distribution of extinctions and a standard N_H/A_v conversion, is roughly 4×10^8 $M_\odot$, or about half of the dynamical mass within this region. This estimate most closely matches the H_2 mass that is obtained from an "optically thick" interpretation of the CO flux measurements (Young and Scoville 1984). The energy spent in displacing the mass to a mean radius of 500 pc is estimated at $\sim 10^{56}$ ergs, or about the same as the thermal energy of the x-ray emitting gas (Watson *et al.* 1984) and the kinetic energy of the Hα filaments (Bland and Tully 1988). Higher-resolution maps of the CO and HI in the *disk* of M82 will be needed to better delineate the mass distribution and energetics of this circumnuclear pile-up.

References

Beck, S. C., Lacy, J. H., Baas, F., and Townes, C. H. 1978, *Ap. J.*, **226**, 545.

Bettoni, D. and Galleta, G. 1982, *Astr. Ap.*, **113**, 344.

Bland, J. and Tully, R. B. 1988, *Nature*, **334**, 43.

Carlstrom, J. E. 1988, in *Galactic and Extragalactic Star Formation*, eds. R. E. Pudritz and M. Fich (Dordrecht: Kluwer Academic Publ.), p. 571.

Caux, E., Puget, J. L., Serra, G., Gispert, R., and Ryter, C. 1984, *Astr. Ap.*, **144**, 37.

Chevalier, R. A. and Clegg, A. W. 1985, *Nature*, **317**, 44.

Combes, F. 1988, in *Galactic and Extragalactic Star Formation*, eds. R. E. Pudritz and M. Fich (Dordrecht: Kluwer Academic Publ.), p. 475.

Crawford, M. K., Genzel, R., Townes, C. H., and Watson, D. M. 1985, *Ap. J.*, **291**, 755.

Dennefeld, M. and Stasinska, G. 1983, *Astr. Ap.*, **118**, 234.

Duffy, P. B., Erickson, E. F., and Haas, M. R. 1987, *Ap. J.*, **315**, 68.

Gerin, M., Nakai, N., and Combes, F. 1988, *Astr. Ap.*, submitted.

Houck, J. R., Shure, M. A., Gull, G. E., and Herter, T. 1984, *Ap. J. (Letters)*, **287**, L204.

Johnson, H. L. 1965, *Ap. J.*, **141**, 170.

Johnson, H. L. 1966, *Ann. Rev. Astr. Ap.*, **4**, 193.

Joy, M., Lester, D. F., and Harvey, P. M. 1987, *Ap. J.*, **319**, 314.

Kennicutt, R. C. and Pogge, R. W. 1989, *A. J.*, in press.

Klein, U., Wielebinski, R., and Morsi, H. W. 1988, *Astr. Ap.*, **190**, 41.

Kronberg, P. P., Biermann, P., and Schwab, F. R. 1985, *Ap. J.*, **291**, 693.

Kurusz, R. L. 1979, *Ap. J. Suppl.*, **40**, 1.

Lo, K. Y., Cheung, K. W., Masson, C. R., Phillips, J. G., Scott, S. L., and Woody, D. P. 1987, *Ap. J.*, **312**, 574.

Luppino, G. A., Ceglio, N. M., Doty, J. P., Ricker, G. R., and Vallerga, J. V. 1987, *Opt. Eng.*, **26**, 1048.

Lynds, C. R. and Sandage, A. R. 1963, *Ap. J.*, **137**, 1005.

Mathis, J. S. 1983, *Ap. J.*, **267**, 119.

McCall, M. L., Rybski, P. M., and Shields, G. A. 1985, *Ap. J. Suppl.*, **57**, 1.

McCarthy, P. J., Heckman, T., and van Breugel, W. 1987, *A. J.*, **92**, 264.

Meaburn, J., Terett, D. L., Theokas, A., and Walsh, J. R. 1981, *M. N. R. A. S.*, **195**, 39.

Meyer, S. S. and Ricker, G. R. 1980, *Applications of Digital Imaging to Astronomy*, SPIE Proceedings No. 264 (Bellingham, WA: SPIE), p. 38.

Nakai, N., Hayashi, M., Handa, T., Sofue, Y., Hasagawa, T., and Sasaki, M. 1987, *Publ. Astr. Soc. Japan*, **39**, 685.

O'Connell, R. W. and Mangano, J. J. 1978, *Ap. J.*, **221**, 62.

Oke, J. B. and Gunn, J. E. 1983, *Ap. J.*, **266**, 713.

Olafsson, H. and Rydbeck, G. 1984, *Astr. Ap.*, **136**, 17.

Osterbrock, D. E. 1974, *Astrophysics of Gaseous Nebulae* (San Francisco: Freeman).

Rice, W., Lonsdale, C. J., Soifer, B. T., Neugebauer, G., Koplan, E. L., Lloyd, L. A., de Jong, T., and Habing, H. J. 1988, *Ap. J. Suppl.*, **68**, 91.

Rickard, L. J., Palmer, P., Turner, B. E., Morris, M., and Zuckerman, B. 1977, *Ap. J.*, **214**, 390.

Rieke, G. H., Lebofsky, M. J., Thompson, R. J., Low, F. J., and Tokunaga, A. T. 1980, *Ap. J.*, **238**, 24.

Rieke, G. H. and Lebofsky, M. J. 1985, *Ap. J.*, **288**, 618.

Sandage, A. R. 1961, *The Hubble Atlas of Galaxies*, (Washington, D. C.: Carnegie Institution of Washington).

Sandage, A. R. and Tammann, G. A. 1981, *A Revised Shapley-Ames Catalog of Bright Galaxies* (Washington, D. C.: Carnegie Institution).

Schmidt, G. D., Angel, J. R. P., and Cromwell. R. H. 1976, *Ap. J.*, **208**, 888.

Simon, M., Simon, T., and Joyce, R. R. 1979, *Ap. J.*, **227**, 64.

Smith, L. F., Biermann, P., and Mezger, P. G. 1978, *Astr. Ap.*, **66**, 65.

Sofue, Y. 1988, in *Galactic and Extragalactic Star Formation*, eds. R. Pudritz and M. Fich (Dordrecht: Kluwer Academic Publ.), p. 409.

Stark, A. A. and Wolff, R. S. 1979, *Ap. J.*, **229**, 118.

Stark, A. A. and Carlson, E. R. 1984, *Ap. J.*, **279**, 122.

Sutton, E. C., Masson, C. R., and Phillips, T. G. 1983, *Ap. J. (Letters)*, **275**, L49.

Tammann, G. A. and Sandage, A. R. 1968, *Ap. J.*, **151**, 825.

Telesco, C. and Harper, D. A. 1980, *Ap. J.*, **235**, 392.

Telesco, C. M. and Gatley, I. 1981, *Ap. J. (Letters)*, **247**, L11.

Telesco, C. M. 1988, *Ann. Rev. Astr. Ap.*, **26**, 343.

Visvanathan, N. and Sandage, A. R. 1972, *Ap. J.*, **176**, 57.

Waller, W. H., Kleinmann, S. G., and Ricker, G. R. 1988, *A. J.*, **95**, 1057.

Watson, D. M., Stanger, V., and Griffiths, R. E. 1984, *Ap. J.*, **286**, 144.

Weliachew, L., Fomalont, E. B., and Greisen, E. W. 1984, *Astr. Ap.*, **137**, 335.

Williams, T. B., Caldwell, N., and Schommer, R. A. 1984, *Ap. J.*, **281**, 579.

Willner, S. P., Soifer, B. T., Russell, R. W., Joyce, R. R., and Gillett, F. C. 1977, *Ap. J. (Letters)*, **217**, L121.

Wolstencraft, R. D., Tully, R. B., and Perley, R. A. 1984, *M. N. R. A. S.*, **207**, 889.

Young, J. S. and Scoville, N. Z. 1984, *Ap. J.*, **287**, 153.

Young, J. S., Kleinmann, S. G., and Allen, L. E. 1988, *Ap. J. (Letters)*, **334**, L63.

Yun, M. S., Ho, P. T. P., and Lo, K. Y. 1988, *B. A. A. S.*, **20**, 1001.

Table 4–1
Adopted Properties of M82

Type[a,b]	IrrII/Amorphous
R. A.(1950)[c]	$09^h\ 51^m\ 43.9^s$
Declination(1950)[c]	69° 55' 01"
Radial velocity (heliocentric)[d]	214 km s^{-1}
Position angle of major axis[e]	65°
Inclination[e]	81.5°
Distance[f]	3.25 Mpc

[a] Sandage 1961

[b] Sandage and Tammann 1981

[c] The position of the 2.2 μm infrared peak (Rieke *et al.* 1980)

[d] Olofsson and Rydbeck 1984; Sutton *et al.* 1983

[e] Lynds and Sandage 1963

[f] Tammann and Sandage 1968

Table 4–2

Observing Log

Telescope		MHO 1.3m @ $f/13.5$
Pixel size		0.81"
Field of view		5' × 6'
	6/19/86	
Filter	[SIII]	"I"
$\lambda_\circ$	9532 Å	8380 Å
FWHM	43 Å	2050 Å
Integration time	1633s	(103 × 2)s
	6/21/86	
Filter	Hα	"R"
$\lambda_\circ$	6563 Å	6040 Å
FWHM	36 Å	1504 Å
Integration time	340s	20s

Figures

Figure 4–1

[SIII]/Hα flux ratios in galactic and extragalactic HII regions.

a. Observed correlation between the [SIII]/Hα flux ratio and the visual extinction. The plotted data are taken from McGregor *et al.*'s (1984) observations of compact HII regions in the Milky Way. Their estimates of extinction are based on the observed infrared colors of the individual HII regions. The circles denote [SIII]/Hα flux ratios based on measurements of the blended emission from [SIII]λ9532 + Pa8λ9546. The stars are based on measurements of the unblended [SIII]λ9069 emission which has been scaled up to the predicted 9532 Å value by multiplying by $\frac{A_{\lambda 9532} h\nu_{\lambda 9532}}{A_{\lambda 9069} h\nu_{\lambda 9069}} = 2.44$. The "zero-point" (extinction-free) [SIII]/Hα flux ratio for compact HII regions appears to be lower than is observed in classical and giant HII regions (see next panel).

b. Measured and modeled correlations between the dereddened [SIII]/Hα flux ratio and the O/H abundance ratio. The plotted data are taken from Dennefeld and Stasinska's (1983) observations of classical and giant HII regions in the Milky Way and nearby galaxies. Corrections for extinction are based on measurements of the Balmer decrement. The circles represent galactic HII regions. The triangles and squares respectively denote HII regions of the Large and Small Magellanic Clouds. The star represents the blue compact galaxy Pox 4. The plotted curve is derived from the "theoretical sequence" of giant extragalactic HII regions as modeled by McCall *et al.* (1985). The offset between the measured and modeled correlations may be due to an offset between the model-dependent O/H ratios derived by Dennefeld and Stasinska (1983) and the corresponding O/H ratios that are plugged into the "theoretical sequence" of McCall *et al.* (1985). For reference, Dennefeld and Stasinska ascribe O/H = 3.47×10^{-4} to the Orion nebula.

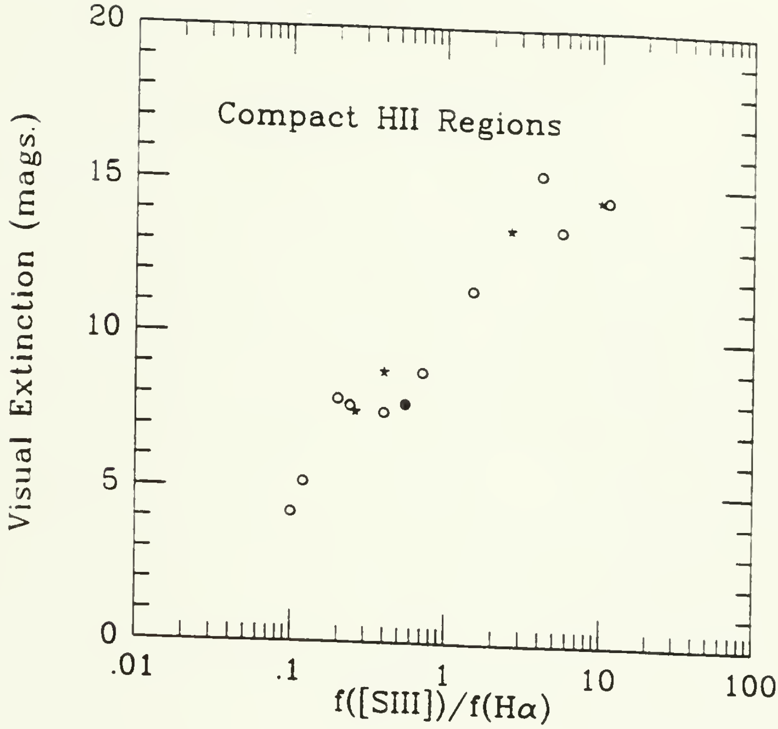
Compact HII Regions
Visual Extinction (mags.)
20
15
10
5
0
.01
.1
1
10
100
f([SIII])/f(Hα)

a ▲ **b ▼**

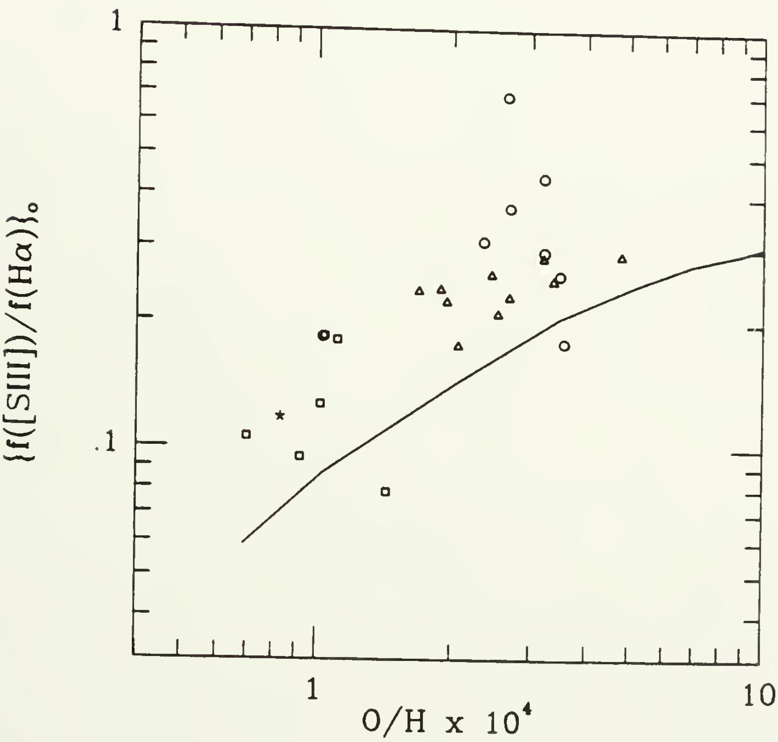
{f([SIII])/f(Hα)}₀
1
.1
1
10
O/H x 10⁴

Figure 4–2

CCD images of M82 in the light of Hα and [SIII]. Each image is a logarithmic representation of the surface brightness in the respective spectral line. The pixel size is 0.81" and the total field of view is $1.7' \times 1.7'$ (1.6 kpc × 1.6 kpc).

a. Continuum-subtracted Hα emission.

b. Continuum-subtracted [SIII] emission.

a ▲ b ▼

Figure 4–3

Contour diagrams of the Hα and [SIII] emission from M82. The pixel size is 0.81" and total field of view is $2' \times 2'$ (1.9 kpc $\times$ 1.9 kpc). The filled triangle denotes the position of the 2.2 μm stellar nucleus, where reference has been made to the accurate positions of several optical "knots", as determined by Bettoni and Galletta (1982). The Hα emission (**a**) is contoured logarithmically beginning at 10^{-15} $erg\ cm^{-2}\ s^{-1}\ arcsec^{-2}$ with contour intervals of 0.25 dex. The [SIII] emission (**b**) is contoured beginning at $10^{-15.5}$ $erg\ cm^{-2}\ s^{-1}\ arcsec^{-2}$ with contour intervals of 0.25 dex. A 3×3 pix boxcar smoothing function has been applied in the contouring, except in the two lowest contours of the [SIII] image — where cruder smoothing has been applied to increase the signal-to-noise.

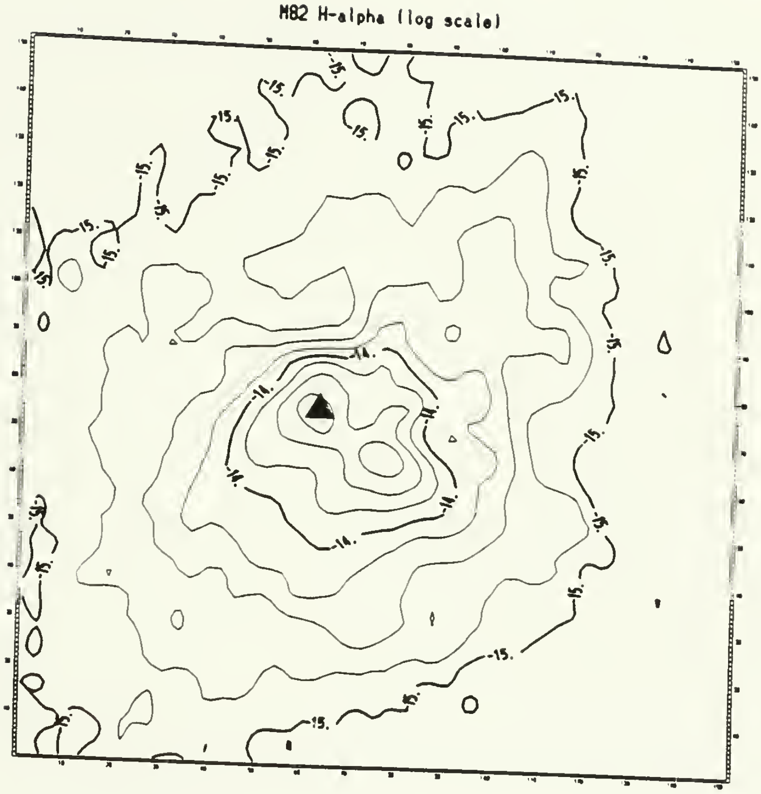

a ▲ b ▼

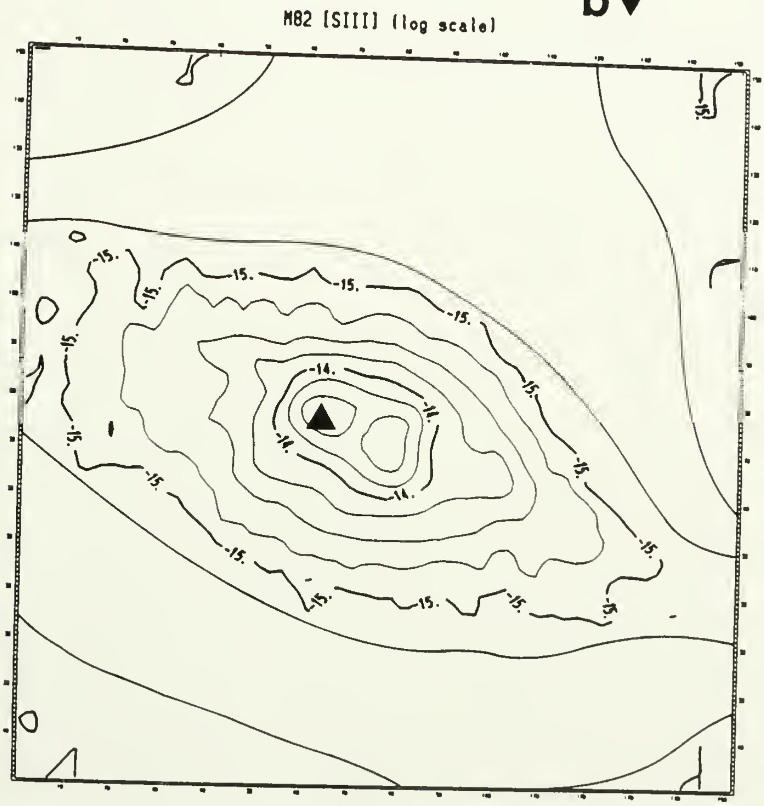

Figure 4–4

Imagery of the [SIII]/Hα flux ratio compared with the Hα emission. Field of view is $1.7' \times 1.7'$ (1.6 kpc $\times$ 1.6 kpc). Enhancements in the [SIII]/Hα flux ratio (**b**) are depicted as regions of darkness. Note that many of these regions are identical to the dark lanes that break up the Hα (and red continuum) emission (**a**) into an assemblage of "knots" (*cf.* O'Connell and Mangano 1982). Also note the dark regions on opposite sides of the Hα emitting nucleus.

a ▲ b ▼

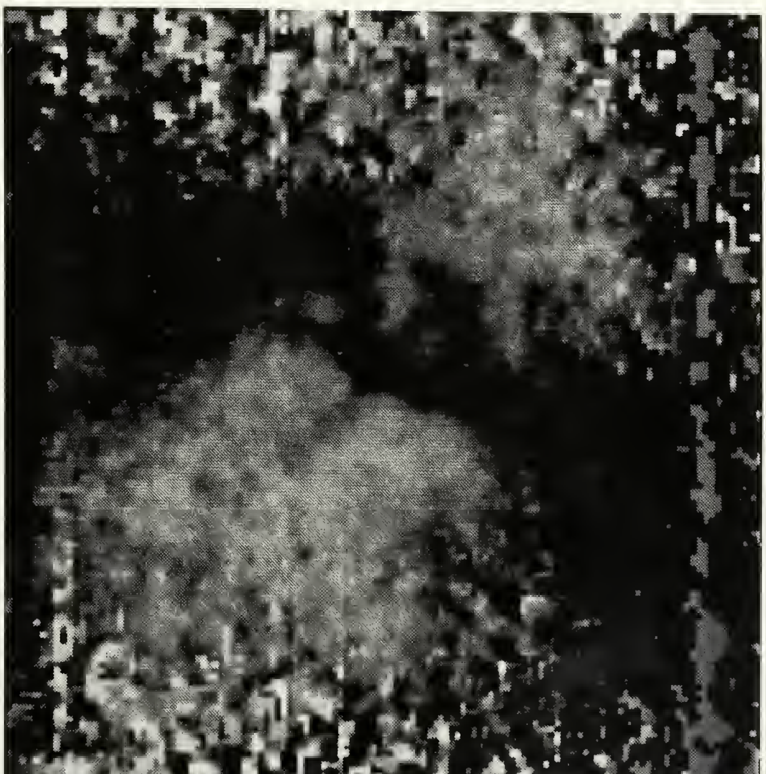

Figure 4–5

Contour diagrams of the [SIII]/Hα flux ratio and the computed visual extinction. Field of view is $2' \times 2'$ (1.9 kpc $\times$ 1.9 kpc). Only those regions having [SIII] surface brightnesses higher than 1.3×10^{-15} $erg\ cm^{-2}\ s^{-1}\ arcsec^{-2}$ (3-sigma above the noise in the subtracted sky background) are plotted. The [SIII]/Hα diagram (**a**) is contoured from 0.0 to 2.0 in intervals of 0.2. The diagram of visual extinctions (**b**) is contoured from 1.0 to 7.0 mag. in intervals of 1.0 mag. The visual extinctions have been computed assuming an extinction-free [SIII]/Hα flux ratio of 0.2 (see text). The filled triangle designates the position of the 2.2 μm stellar nucleus.

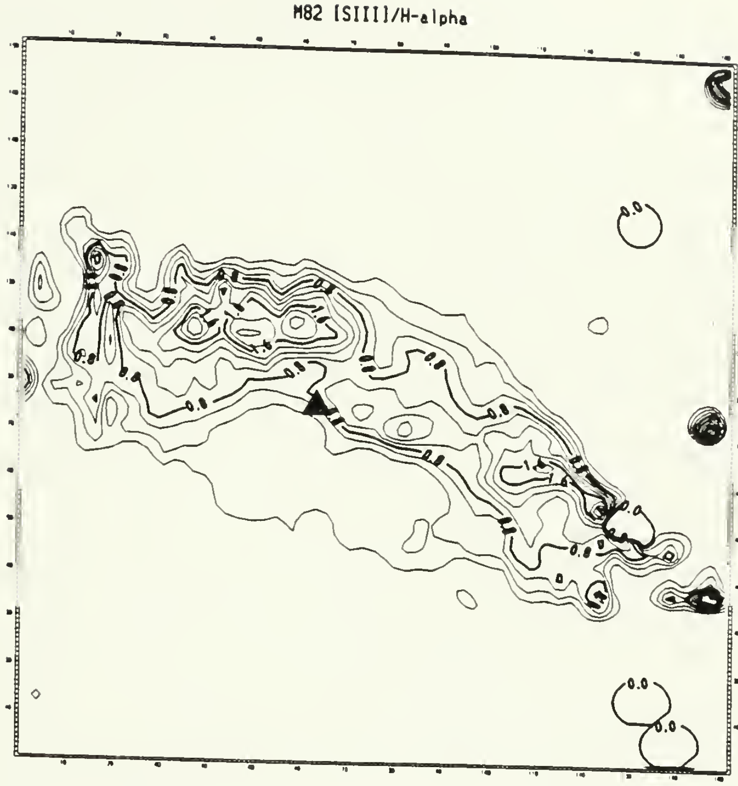

a ▲ b ▼

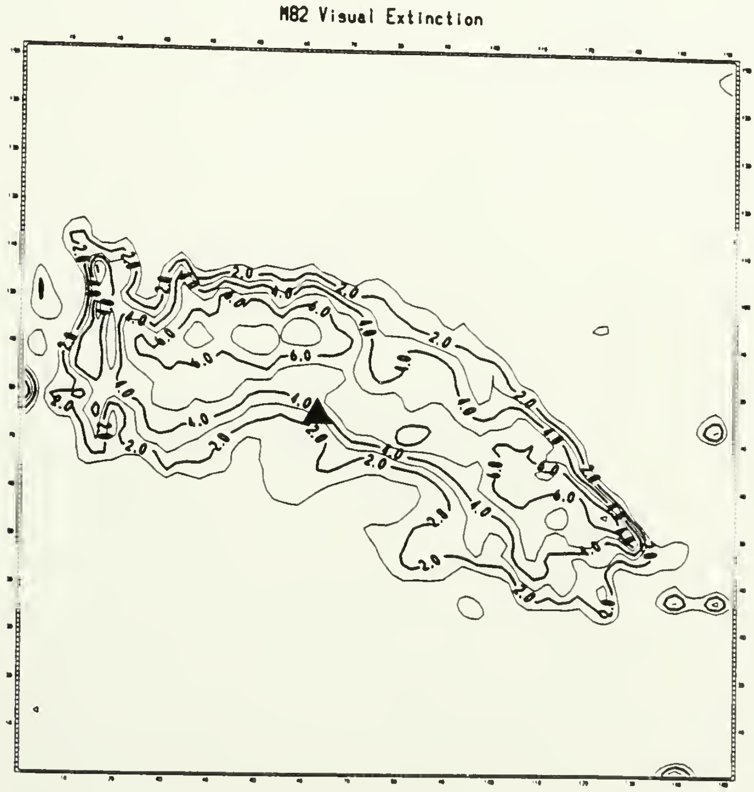

Figure 4–6

Red and near-infrared continuum emission from M82. Field of view is $2' \times 2'$ (1.9 kpc $\times$ 1.9 kpc). The red (λ6563) (**a**) and near-infrared (λ9532) (**b**) continua are contoured logarithmically beginning at $10^{-16.5}$ $erg\ cm^{-2}\ s^{-1}\ arcsec^{-2}$ Å^{-1} with contour intervals of 0.1 dex.

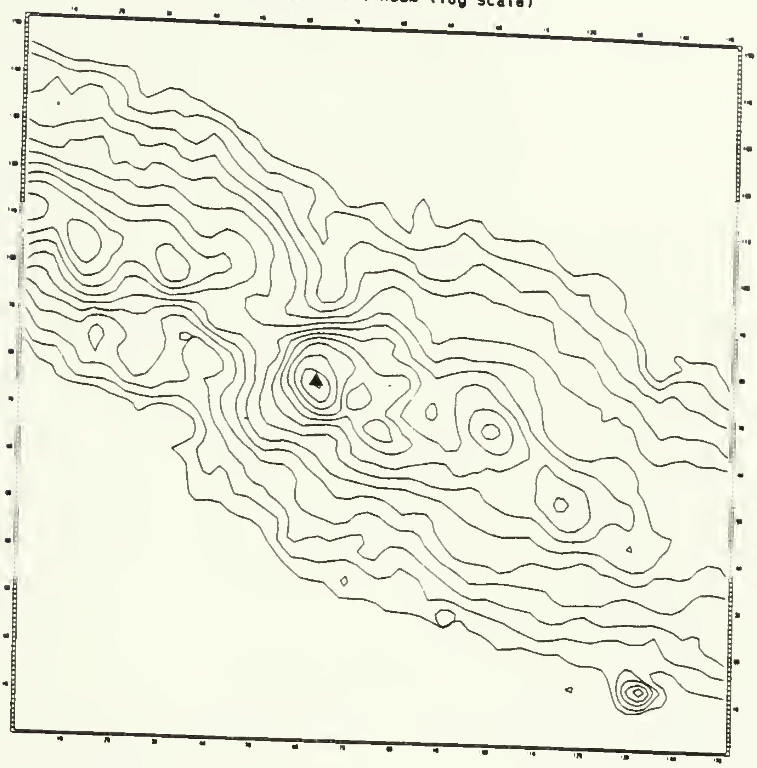
M82 6563A Continuum (log scale)

a ▲ b ▼

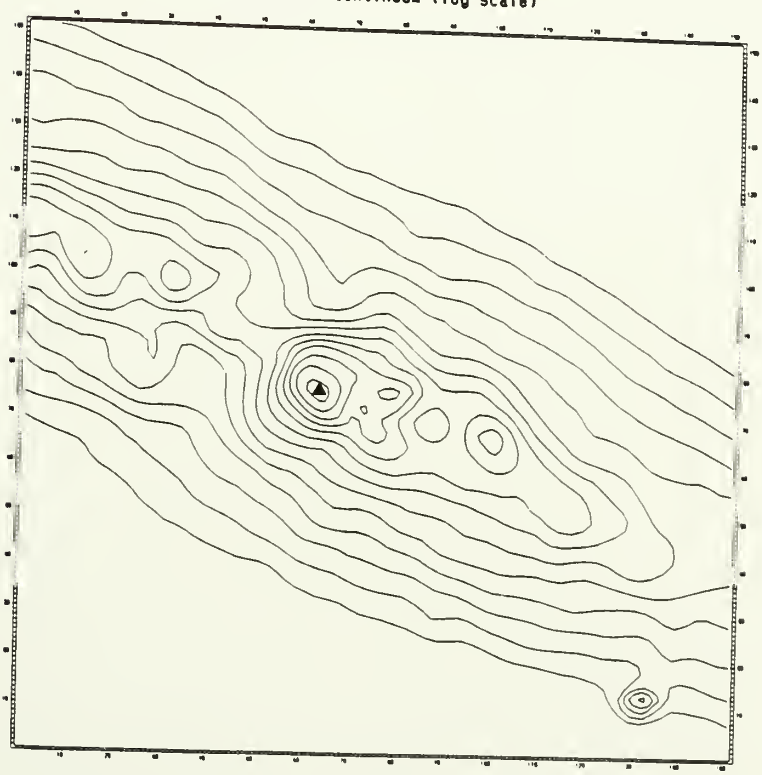
M82 9532A Continuum (log scale)

Figure 4–7

Continuum-band color across M82. Field of view is $2' \times 2'$ (1.9 kpc × 1.9 kpc). The ($\lambda6563 - \lambda9532$) color (**a**) is contoured from 0.6 to 1.3 mag. in intervals of 0.1 mag. The corresponding color of Vega has been set equal to zero. Crowding of the contours near the periphery is an artifact of having apodized the continuum images at the 3-sigma level. For comparison, the distribution of nebular extinction is included (**b**).

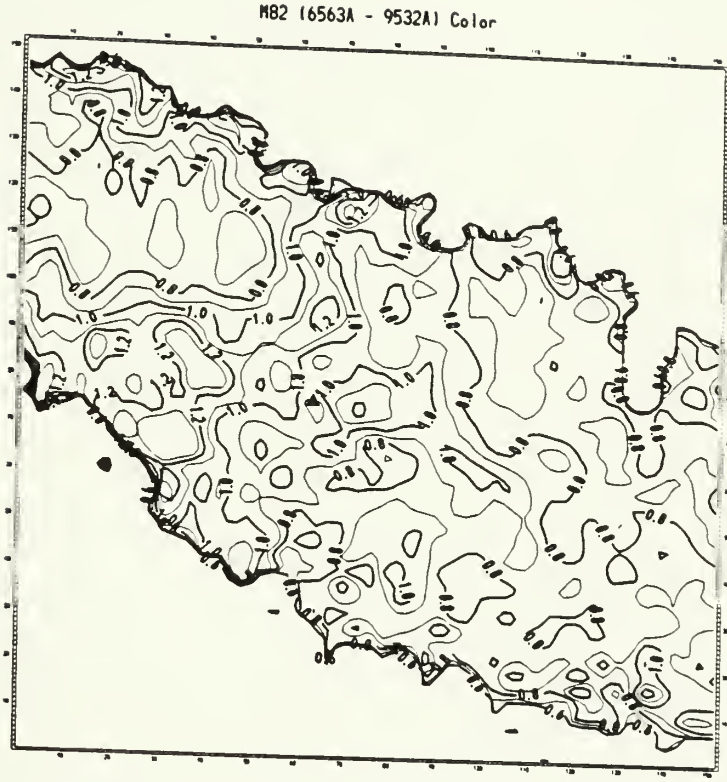

a ▲ b ▼

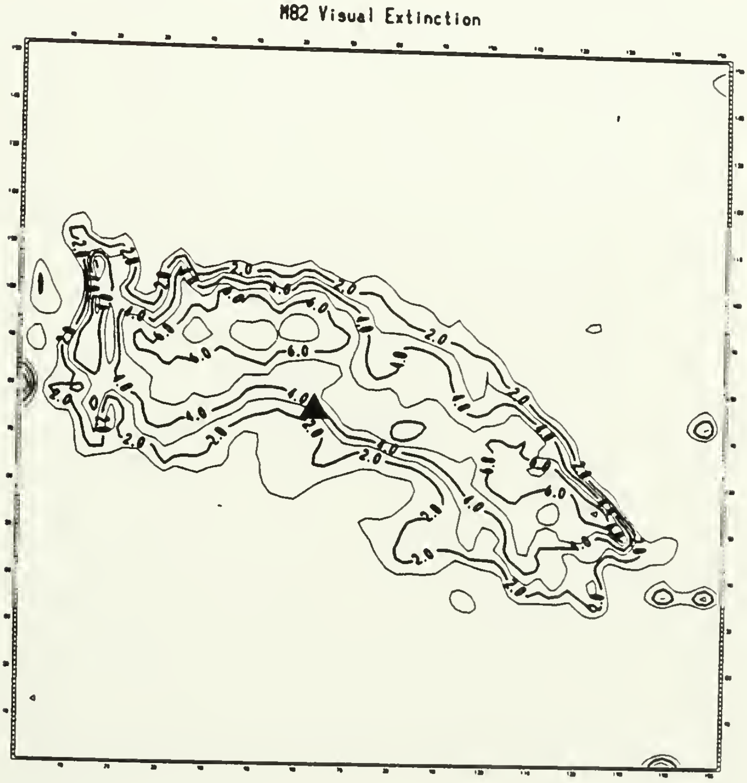

Figure 4–8

Extinction-corrected images of the Hα emission. Field of view is $1.7' \times 1.7'$ (1.6 kpc $\times$ 1.6 kpc). The emission is displayed at two different contrast levels, the lowest (**a**) being logarithmically scaled and the highest (**b**) being linearly scaled. These images show the straightforward application of the extinction correction to the entire Hα image. No apodization at the 3-sigma level has been applied. Therefore spurious enhancements are evident beyond the main body of the galaxy.

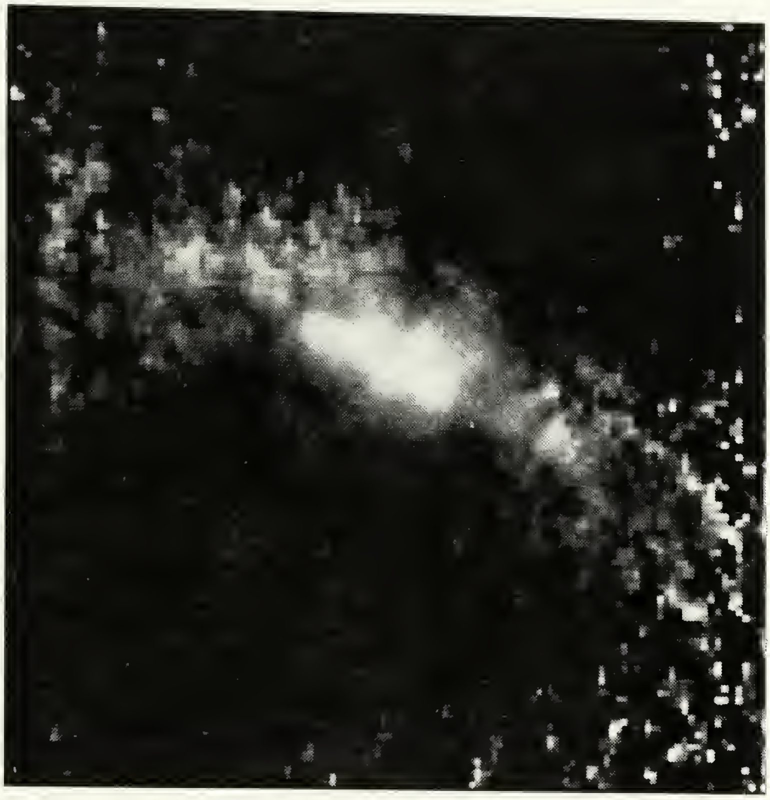

a ▲ b ▼

Figure 4–9

Extinction-corrected contour diagrams of the Hα and [SIII] emission. Field of view is $2' \times 2'$ (1.9 kpc × 1.9 kpc). Apodization of the [SIII] image at the 3-sigma level has been applied, so that there is no extinction correction beyond the lowest [SIII] contour. Note the identical morphologies of the Hα (**a**) and [SIII] (**b**) emission in the central $30'' \times 20''$. The surface brightness in both spectral lines is contoured logarithmically in intervals of 0.25 dex. The filled triangle designates the position of the 2.2 μm stellar nucleus. Note that the "corrected" Hα emission and the centroid of the 2.2 μm emission do not share the same major axis. This may be due to underestimated extinctions having been applied near the nucleus.

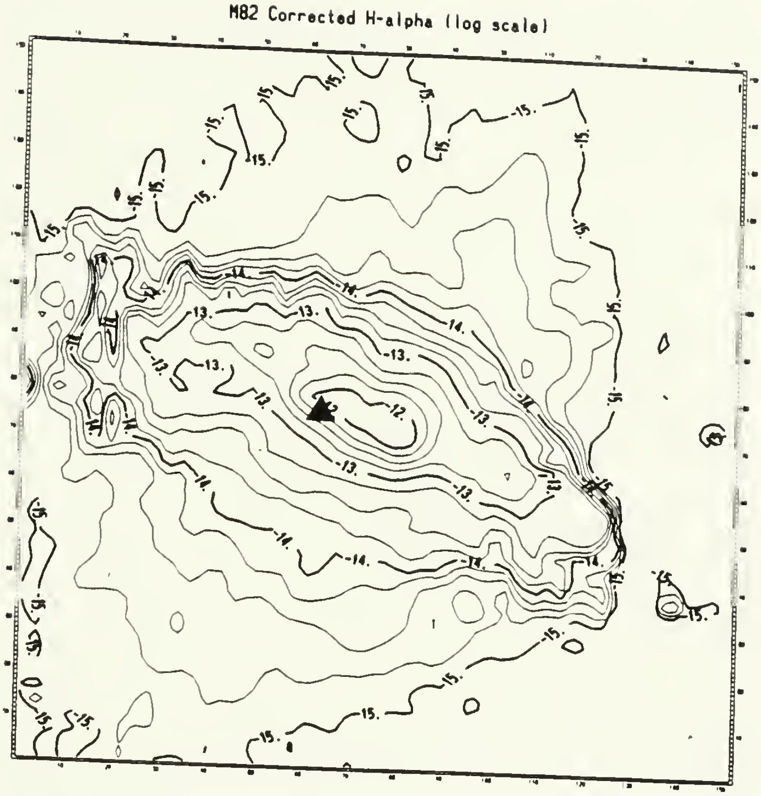
M82 Corrected H-alpha (log scale)

a ▲ b ▼

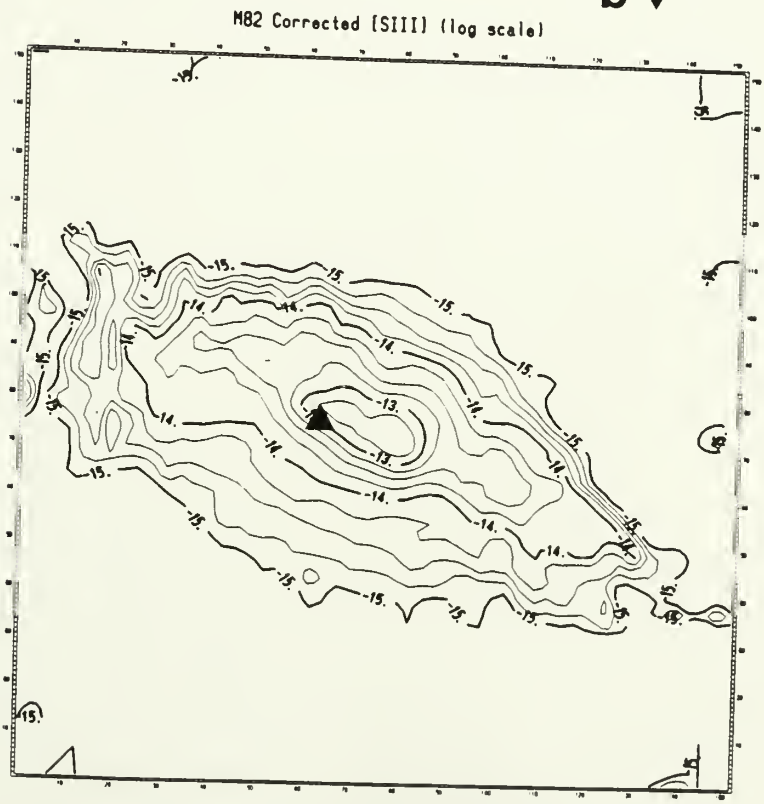
M82 Corrected [SIII] (log scale)

Figure 4–10

Major axis scans of the visual extinction along with other tracers of gas and dust. The scan of visual extinction represents a 8" average across the minor axis. The scans of CO and HI emission are taken from Lo *et al.* (1987) and references therein, where similar minor-axis extents are involved. The scans of Brγ emission and of the H_2 [S(1)]/Brγ flux ratio are taken from Telesco (1988) and references therein.

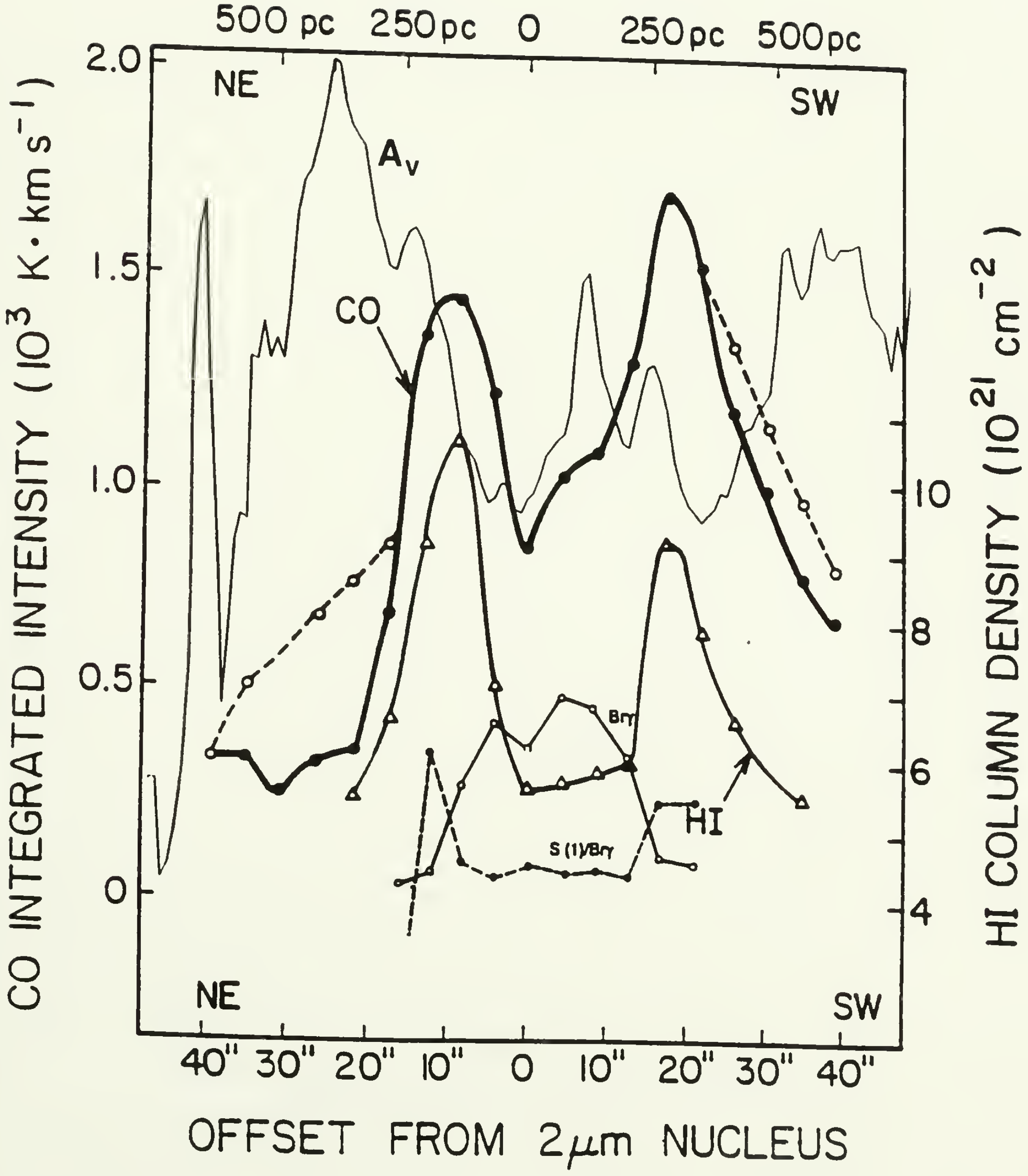

500 pc 250pc 0 250pc 500pc
NE
SW
A$_V$
CO
Brγ
S(1)/Brγ
HI
NE
SW
2.0
1.5
1.0
0.5
0
10
8
6
4
40" 30" 20" 10" 0 10" 20" 30" 40"
OFFSET FROM 2μm NUCLEUS
CO INTEGRATED INTENSITY (10^3 K·km s^{-1})
HI COLUMN DENSITY (10^{21} cm^{-2})

Figure 4–11

The ^{12}CO emission and visual extinction compared to the same scale. The ^{12}CO map (**a**) is from Nakai *et al.* (1987), where the resolution is 16". The mildly curved long dashes trace the CO "ridges," as noted by Nakai *et al.*. The short dashes and steeply curved long dashes have been added by the present author who sees evidence for more ridges. These various ridges intersect some of the most obscured regions in the map of visual extinctions (**b**).

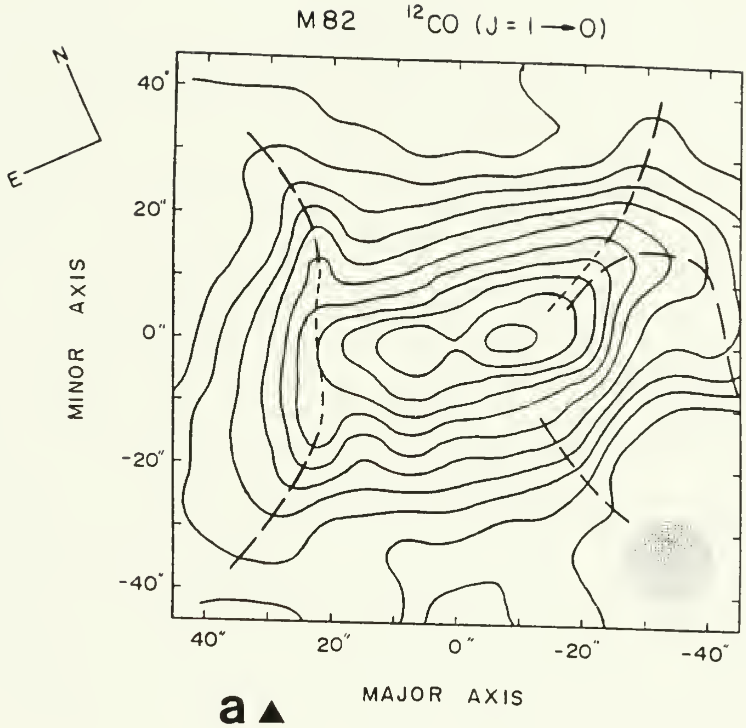
M82 ^{12}CO (J = 1 → 0)
N
E
40"
20"
0"
-20"
-40"
MINOR AXIS
MAJOR AXIS

a ▲

b ▼

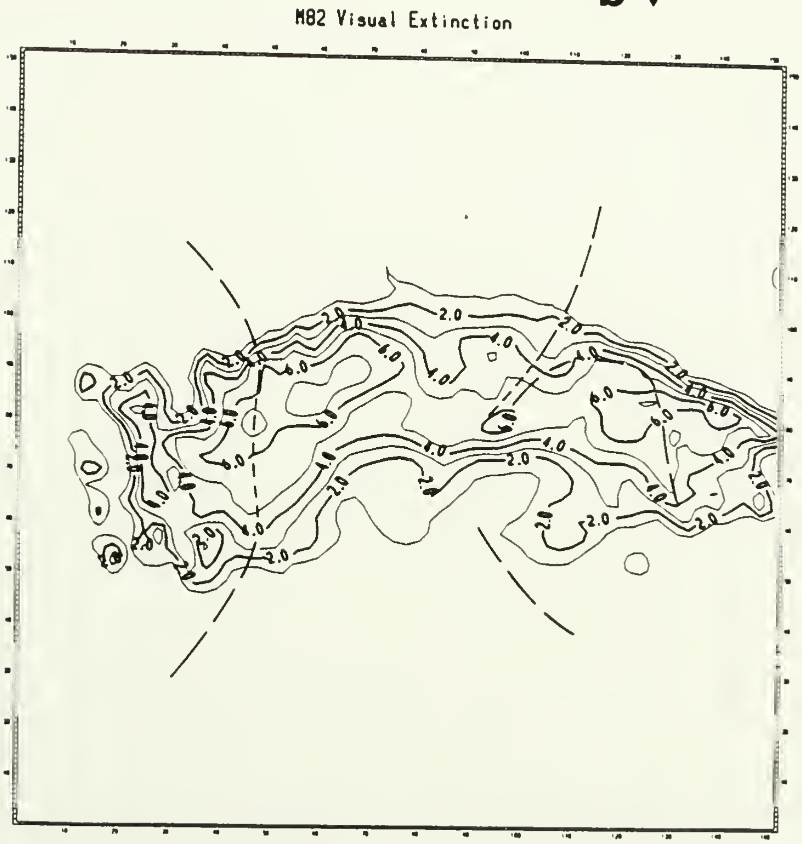
M82 Visual Extinction
2.0
4.0
6.0

Figure 4–12

The extinction-corrected Hα emission and other tracers of gas, dust, and stars. Only the inner $60'' \times 30''$ of the Hα emission is shown. The surface brightness is plotted logarithmically beginning at 10^{-13} $erg\ cm^{-2}\ s^{-1}\ arcsec^{-2}$ with contour intervals of 0.1 dex. The 3.3 mm continuum interferometric map is taken from Carlstrom (1988). The 2.2 μm and 10 μm continuum maps are from Rieke *et al.* (1980). The ^{12}CO emission is from the interferometric mapping by Lo *et al.* (1987). The map of HI optical depth with positions of two OH masers (crosses) is from Weliachew *et al.* (1984).

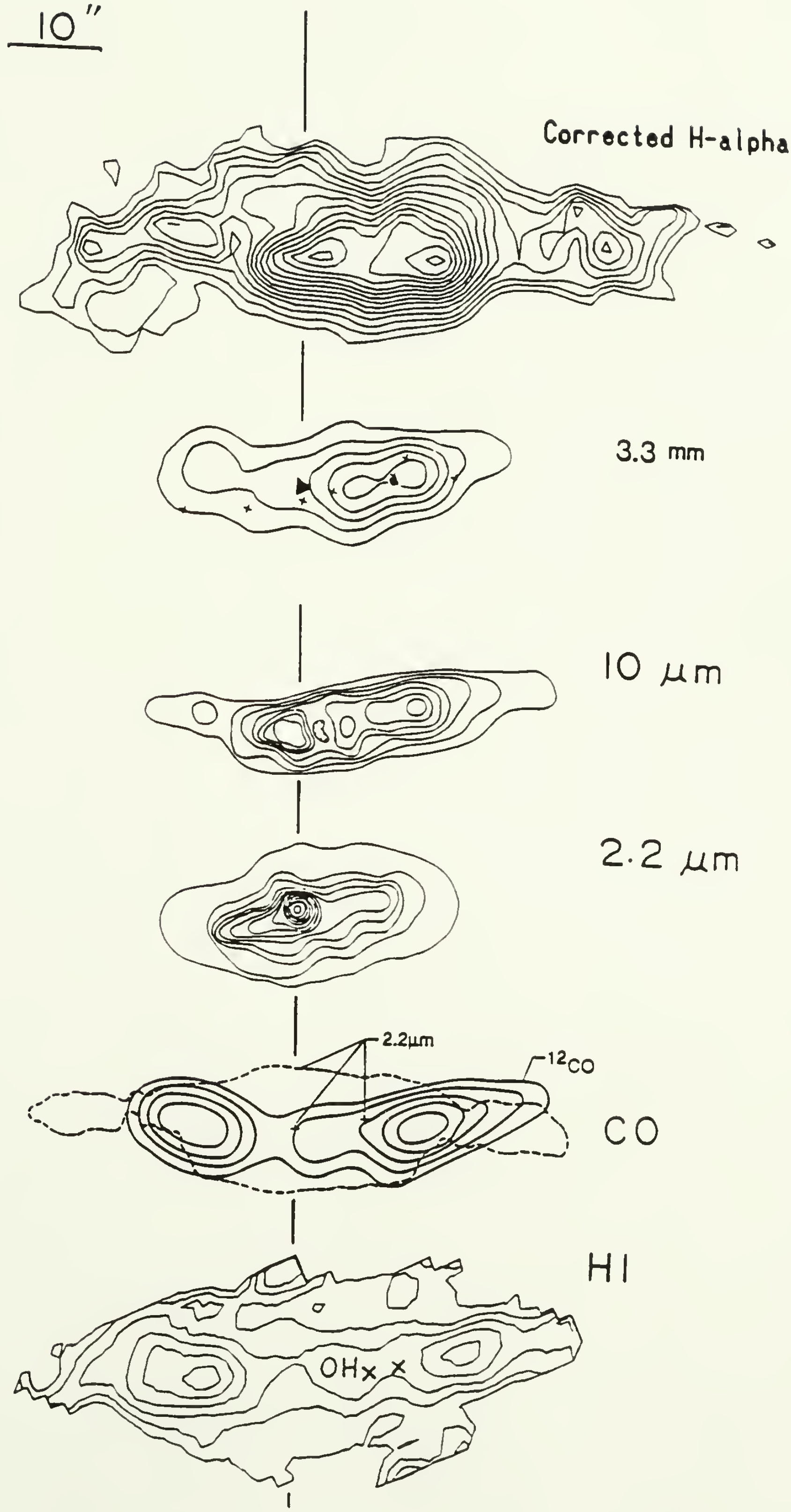
10″
Corrected H-alpha
3.3 mm
10 μm
2.2 μm
2.2μm
12CO
CO
HI
OH

CHAPTER 5

NGC 1569

5.1 *Abstract*

Hα, R, and I-band CCD images of the "post-eruptive" irregular galaxy NGC 1569 are presented. The discovery of two arclike structures of diffuse Hα emission located more than a kpc beyond the star-forming bar is reported. These features are used to estimate an age for the near-nuclear starburst that created them along with other filamentary and armlike structures previously seen in Hα photographs. Considerations of likely outflow geometries and kinematics lead to an estimated age of 10 – 30 Myr, agreeing with the age that Israel and de Bruyn (1988) derive based on considerations of synchrotron losses in the nonthermal radio spectrum.

The gravitational and kinetic energies associated with the Hα arcs are estimated to be orders of magnitude higher than can be provided by a single supernova explosion. Coherent outbursts involving thousands of supernovae each could explain the diffuse Hα features without exceeding the starbirth rate inferred from the total Hα luminosity of the galaxy.

Comparisons between the line and continuum imagery show the inner bar to be populated with HII regions of high Hα equivalent width and blue color. These regions are located on opposite sides of the brightest continuum emission which, in turn, is offset from the dynamical nucleus as defined by the outer B and V isophotes. A starburst history incorporating these observations is proposed and discussed.

5.2 *Introduction*

NGC 1569 (VII Zw 16, Arp 210) is a Magellanic-type irregular galaxy located in a relatively nearby and uncrowded part of the M81/IC342/Maffei grouping of galaxies (Tully and Fisher 1987). Its unusual Hα emitting morphology prompted Zwicky (1971) to classify it as a "post-eruptive system similar to M82." Since then, NGC 1569 has been the subject of many observational studies involving photographic imagery of the Hα filaments (Hodge 1974), Fabry-Perot interferometry of the Hα velocity field (de Vaucouleurs *et al.* 1974; de Vaucouleurs 1981), aperture synthesis mapping of the radio continuum emission (Seaquist and Bignell 1976; Condon 1983; Israel and de Bruyn 1988), 21 cm mapping of the HI emission (Reakes 1980), 2.6 mm observations of the ^{12}CO emission (Young *et al.* 1984), and UV-IR photometry of the starlight (see literature review by W. van Driel as presented by Israel [1988]). The picture that has emerged is of a small, relatively nearby irregular galaxy, rich in HI, poor in metallicity, extremely bright at Hα, and very blue in broadband colors. Despite its low mass, it has recently undergone a strong burst of star formation, whose repurcussions are evident throughout the electromagnetic spectrum. The burst appears to have produced a bipolar outflow of ionized gas that is directed perpendicular to the highly inclined disk (de Vaucouleurs *et al.* 1974). Such intense activity from a relatively unevolved system in many ways mimics the global starbursts that are thought to have characterized the beginnings of earlier-type galaxies such as the Milky Way and M31 (Sandage 1986; see also Chapter 2). Therefore, the ability to study the NGC 1569 starburst at close range represents a valuable opportunity to better understand the early stages of galaxy evolution and perhaps to better diagnose the "primordial" galaxies that are just now becoming detectable at high redshift.

In this chapter I present further evidence for a major starburst having erupted $1 - 3 \times 10^7$ years ago from the nucleus of NGC 1569. The evidence is in the form of Hα emitting arcs of ionized gas, whose displacement from the bursting center are used to estimate the burst age. The most recent high-mass star formation is explored by analyzing the Hα, R-band, and I-band imagery. The brightest Hα emission and bluest colors are found to be well-matched with one another but significantly displaced from the once-bursting nucleus. The relative displacements, ages, and burst strengths are discussed in the context of the galaxy's recent history.

Table 5-1 lists the properties of NGC 1569 that are adopted in this chapter. As usual, the most controversial property is the distance. The distance that I have adopted is based on the observation of *resolved* blue stars in NGC 1569 that have B magnitudes of 20.2 (Ables 1971). By applying a calibration of the absolute magnitude of the brightest blue stars as a function of M_B of the parent galaxy, Arp and Sandage (1985) derive an apparent distance modulus of $(m - M)_B = 29.0 \pm 1.0$ mag. (see also Ables [1971] and de Vaucouleurs *et al.* [1974] who obtain similar results). From multicolor photometry and spectroscopy of the neighboring star BD $+64°450$, Israel (1988) derives a large foreground reddening to the star of $E(B-V) = 0.55$ and to the galaxy of $E(B-V) = 0.56$. The resulting extinction-corrected distance modulus is then $(m - M)_\circ = 26.7 \pm 0.6$ which corresponds to a distance of 2.2 ± 0.6 Mpc.

At this distance, the mysterious central objects A and B (first noted by Ables [1971]) would have absolute blue magnitudes of -13.3 and -12.5 mag respectively. By contrast, 30 Doradus has $M_B \approx -10.3$ mag. Therefore, the central objects are either super-star clusters ~5 times more luminous than 30 Doradus (Arp and Sandage 1985) or simply foreground blue stars (Ables 1971). The spatial coincidence between objects A and B and the photometric nucleus (see Section 5.5), along with the *composite hot supergiant* spectral classifications for both objects (A2 I – B0 I), and the similarities between the radial velocities of A, B, and the HI centroid of NGC 1569 (Arp and Sandage 1985) provide additional reasons for choosing the resident supercluster interpretation. Any larger distance (*e.g.* Hunter *et al.* 1982) would make the clusters even more luminous and difficult to explain. High-resolution imaging and spectroscopy of A and B by the Hubble Space Telescope will be helpful in pinning down the true properties of these intriguing objects, without confusion from the ambient galaxy light.

The adopted position angle of the major axis and inclination of the disk are based on the outer B and V isophotes as mapped by Ables (1971). The inclination appears as an important ingredient along with the distance when computing the displacements and kinematic ages of the arcs.

5.3 *Observations and Reductions*

A summary of the CCD imagery obtained for this study is provided in Table 5-2. The Hα, R, I, and [SIII]-band images were obtained at the Cassegrain focus of the Kitt Peak #1 0.9-m telescope during clear weather.[1] With the $f/7.5$ secondary in place, the resolution on the RCA-3 CCD chip is 0.86" per pixel, and the field of view is approximately $7.3' \times 4.5'$. Care was taken to point the telescope, so that the nearby 10th magnitude star BD +64°450 would be just north of the field of view and therefore out of harm's way. This meant missing out on imaging the northerly extremities of NGC 1569 as well. However, inspection of the wider-field photographic images of Hodge (1974) indicates that very little nebular emission has been missed. The following sections will be concerned with the $3' \times 3'$ portion of the image that contains all of the detected Hα emission features.

Imaging at Hα was conducted using an interference filter (#810, λ6563) provided by Kitt Peak. The transmission characteristics of this filter combined with the 1.7 Å blueshift of NGC 1569 results in the transmission of Hα($\lambda_\circ$6563) with 0.73 transmissivity, [NII]($\lambda_\circ$6584) with 0.16 transmissivity, and [NII]($\lambda_\circ$6548) with 0.46 transmissivity. The net contamination from [NII] is expected to be 10 percent in emission (Kennicutt and Kent 1983) and 4 percent in the present imagery. All subsequent Hα fluxes are corrected for this effect.

Imaging at R and I bands was conducted with the Mould R and I filters that are commonly used at Kitt Peak. An attempt was made to image at [SIII](λ9532) using a 144 Å bandwidth filter centered on 9540 Å. The resulting image suffered from strong fringing, however, with only the brightest HII region rising sufficiently above the noise for further analysis.

To calibrate the galaxy imagery, images of the sdOp-type standard star BD +28°4211 (Stone 1977) were obtained through all filters. Images of an illuminated screen inside the dome were taken through each filter at the beginning of the night for the purpose of flattening the background variations in the galaxy images.

Initial processing of the CCD images — including bias averaging and subtraction, darkframe subtraction, and flatfield averaging and division — was carried out at Kitt Peak using the Mountain Photometry Code package. Further

[1] Kitt Peak National Observatory is operated by the Association of Universities for Research in Astronomy, Inc., under contract with the National Science Foundation.

processing — including image arithmetic, median filtering, synthetic aperture photometry, and contouring — was conducted at the University of Washington using the Image Reduction and Analysis Facility (IRAF) software created at Kitt Peak National Observatory. Synthetic aperture photometry on the images of the standard star yielded the following conversions between flux and count rate (after bias subtraction, flatfield division, and atmospheric extinction correction):

$$f(H\alpha)(erg\ cm^{-2}\ s^{-1}) = 1.7 \times 10^{-14} R_\circ(\lambda 6563,\ \Delta\lambda 38)(ADU\ s^{-1}), \qquad (5-1)$$

$$f_\lambda(\lambda 6563)(erg\ cm^{-2}\ s^{-1}\ \AA^{-1}) = 1.4 \times 10^{-17} R_\circ(R\ band)(ADU\ s^{-1}), \qquad (5-2)$$

$$f([SIII])(erg\ cm^{-2}\ s^{-1}) = 4.2 \times 10^{-14} R_\circ(\lambda 9540,\ \Delta\lambda 144)(ADU\ s^{-1}), \qquad (5-3)$$

$$f_\lambda(\lambda 9532)(erg\ cm^{-2}\ s^{-1}\ \AA^{-1}) = 1.3 \times 10^{-17} R_\circ(I\ band)(ADU\ s^{-1}). \qquad (5-4)$$

Uncertainty in the derived fluxes primarily comes from the noise in the subtracted sky backgrounds. The resulting uncertainties are estimated to be δ I(Hα) $\approx 3.9 \times 10^{-17}$ erg cm^{-2} s^{-1} arcsec^{-2}, δ $I_\lambda(\lambda 6563) \approx 3.9 \times 10^{-19}$ erg cm^{-2} s^{-1} arcsec^{-2} Å^{-1}, δ I([SIII]) $\approx 4.1 \times 10^{-16}$ erg cm^{-2} s^{-1} arcsec^{-2}, and $\delta I_\lambda(\lambda 9532) \approx 4.3 \times 10^{-19}$ erg cm^{-2} s^{-1} arcsec^{-2} Å^{-1}. For the narrow-band images, the uncertainties correspond to approximately 5 percent of the subtracted sky value; and for the broad-band images, the uncertainties correspond to about 1 percent of the subtracted backgrounds.

To create an Hα image that is free from contamination by the stellar and nebular continua, an appropriately sky-subtracted, shifted and scaled R-band image was subtracted from the original sky-subtracted Hα-band image (see Appendix B). The scaling was determined from synthetic aperture photometry of foreground stars in the field of NGC 1569. Similar processing of the I-band and [SIII]-band image was done to obtain a pure [SIII] emission-line image, weak as it was. To obtain a red-continuum image that is free from contamination by the Hα emission line, a scaled Hα-band image was subtracted from the R-band image, where the scaling was determined from the relative bandwidths of the Hα and R-band filters (see Appendix B).

As a check on the image processing, I have compared the Hα flux from the $3' \times 3'$ field surrounding NGC 1569 with the flux measured photoelectrically by Kennicutt and Kent (1983) through a 3 arcminute diameter aperture. After correcting the detected flux for a 4 percent contamination by [NII], I derive an Hα flux of $(2.03 \pm 0.12) \times 10^{-11}$ $erg\ cm^{-2}\ s^{-1}$, which is 11 percent lower than Kennicutt and Kent's value of $(2.26 \pm 0.23) \times 10^{-11}$ $erg\ cm^{-2}\ s^{-1}$. Within the uncertainties, the two values are in good agreement.

5.4 *Morphologies, Fluxes, and Colors*

Figure 5–1 shows the Hα and red-continuum images of NGC 1569 that were obtained after having subtracted off contaminating continuum emission from the Hα-band image and contaminating line emission from the R-band image. Immediately apparent is the enormous difference in emission morphologies. While the red continuum emission is dominated by a central barlike feature, the Hα emission is lumpier, off-center with respect to the stellar "bar," and far more extended at low surface brightness levels. Contour diagrams of the stellar continuum (Figure 5–2) and Hα emission (Figure 5–3) help to show these differences with even greater clarity.

5.4.1 *Diffuse Hα Emission*

The extended Hα emission is particularly striking in its similarity to the Hα plumes and filaments that emanate from the more powerful M82 starburst. Both systems of extended emission are currently thought to be the byproducts of recent eruptions from the respective nuclei. The NGC 1569 system is characterized by a bright arm-like feature to the West, filamentary structures radiating outwards from the North and South, and two arc-like swatches of emission with large southern displacements from the nucleus. All but the last two features have been previously noted (*cf.* Hodge 1974; de Vaucouleurs *et al.* 1974). Unlike the classic HII regions, the diffuse emission is not associated with any ionizing star clusters. This is most clearly shown in the map of Hα equivalent widths (*i.e.* line-to-continuum ratios) (Figure 5–4), where the regions of diffuse emission show up as dramatic enhancements in line emission relative to the ambient continuum emission.

The most prominent extended feature is the western "Arm" that begins 27" to the West of object A and curves southward for a total displacement of about 1.1 arcmin. It has projected dimensions of 640 pc $\times$ 213 pc and has an ionization requirement equivalent to 1.1×10^{51} Lyman continuum photons per second. The source of this ionization could be either UV photons from hot stars in the bright central bar or energetic collisions from encounters between outflowing hot gas and cooler ambient gas. The twisted morphology that is evident in the present Hα imagery and in previous photographs (Hodge 1974), is reminiscent of the "corkscrew" structure seen by Williams *et al.* (1984) in the northern plume of M82. Both structures may represent the limb-brightened "walls" that separate the hot outflowing gas from the cool neutral gas exterior to the outflow (*cf.* Sofue 1988). Neutral hydrogen observations of NGC 1569 seem to corroborate this picture, showing a large arm-like HI feature that lies *exterior* to the Hα arm and which extends for more than 3 arcmin (Reakes 1980).

The velocity field of the Arm is remarkably uniform, averaging -8 ± 5 $km\ s^{-1}$ with respect to the systemic velocity of 77 $km\ s^{-1}$. If the Arm represents gas flowing outwards from the bar in a direction perpendicular to the inclined disk, then the measured radial velocity would correspond to a flow velocity of 18 $km\ s^{-1}$. This is less than one-tenth the flow velocity of M82's "corkscrew" as computed from similar considerations (Williams *et al.* 1984). It is also barely supersonic, thus constraining the energy available for shock heating. Spectroscopic observations of collisionally-excited emission lines (*e.g.* the [SII] ($\lambda\lambda$6717, 6731) doublet) from this feature will be necessary, before a reliable discrimination of the ionizing source can be accomplished.

The ray-like filaments in the North and South can be traced back to a common origin that includes objects A and B. This was first noted in a sketch by de Vaucouleurs *et al.* (1974), based on the photographs of Hodge (1974), and is corroborated by the present CCD imagery. A strict straight-line backtracking of the filamentary trajectories results in a convergence circle 6" in diameter located 2.5" West of object B, but many of the filaments are obviously curved, so this should not be taken very seriously.

The radial velocity field in the filamentary regions shows a strong gradient, with the northern filaments redshifted and the southern filaments blueshifted with respect to the systemic velocity (de Vaucouleurs 1981; note that an *oppositely directed* gradient is reported in de Vaucouleurs *et al.* 1974). The deviation from systemic velocity steadily rises with increasing displacement from the nucleus, reaching a maximum detected deviation of 60 $km\ s^{-1}$ in the North. If the filaments represent gas flowing perpendicular to the inclined disk, then the measured deviations in radial velocity correspond to a maximum outflow velocity of 132 $km\ s^{-1}$. This dispersion is roughly half that of M82's filamentary system (Williams *et al.* 1984).

As in M82, the velocity gradient along the minor axis of NGC 1569 can be attributed to ionized gas in polar orbits or in outflow. De Vaucouleurs *et al.* (1974) have modeled the motions in terms of a *biconical outflow*, whereby the Hα filaments are located on the *surfaces* of the cones — the southern filaments tracing the farside of the southern cone, and the northern filaments tracing the nearside of the northern cone.[2] The authors neglected to note that the biconical outflows would have to accelerate, or the opening angle of the cones would have to increase with distance in order for the model to fit the observations (K. H. Bohm, private communication). Either of these considerations are possible, and so the biconical outflow scenario is far from disqualified. Nowhere is there evidence for a decrease in radial velocities with increasing distance from the nucleus. This observation will be used in dating the more distant "arcs."

The faintest Hα features of a diffuse nature are the two arclike segments to the south of the nucleus. Although the innermost arc is evident on a deep Hα photograph by Hodge (1974), no mention of it has yet to appear in the literature. The outermost arc seems to have eluded detection until now. The contour

---

[2] This situation would be reversed using the velocity field of de Vaucouleurs (1981).

diagram in Figure 5–3 shows both arcs to be roughly concentric, with radii of curvature consistent with a common focus near objects A and B. The innermost arc ("Arc 1") has projected dimensions of approximately 747 pc $\times$ 267 pc and has an ionization budget equivalent to 2.2×10^{50} Lyman continuum photons per second. It appears to be part of a much larger arc that includes the western Arm. The outer arc ("Arc 2") is significantly fainter, appearing at the 1-2 sigma level in the present image. It is clearly evident in the raw Hα-band CCD image, however, and thus cannot be an artifact of the image processing. It is approximately 640 pc $\times$ 214 pc in projected size and is ionized by the equivalent of 8.3×10^{49} Lyman continuum photons per second. Arc 2 does not seem to be a part of any larger diffuse structure. If both arcs were ejected from the nucleus perpendicular to the disk, their current displacements would be 1.2 kpc and 1.5 kpc respectively. The biconical model of de Vaucouleurs *et al.* (1974) would place them on the farside of the southern cone with slightly larger displacements of 1.3 kpc and 1.6 kpc respectively.

5.4.2 *HII Regions and their Ionizing Star Clusters*

Visual inspection of the high surface-brightness portions of the Hα image shows the bar of NGC 1569 to be populated with a clutter of HII regions. The region around objects A and B is relatively devoid of such regions, but on either side of the objects — and especially to the West of them — discrete knots of Hα emission are clearly evident. Several of these knots are not round but appear more like closely bunched hot-dog buns. The silhouetting effects of dust lanes could be causing these distortions, by breaking up the light from a single HII region into a small gathering of luminous "buns." Some dust lanes are evident in the continuum images, but none are coincident with the suspect dust lanes in the Hα image. B-band imagery may be more successful in bringing out these anticipated features.

Table 5-3 lists the prominent HII regions in NGC 1569 along with their positions, sizes, and cross-references. This list is far from complete (see Hodge and Kennicutt 1983) but represents only those HII regions, whose sizes and Hα fluxes could be measured with some degree of reliability. Table 5-4 lists the fluxes and equivalent widths for these objects. The Hα equivalent widths of the ionizing clusters are computed by subtracting off the continuum light of the ambient galaxy and then dividing the Hα flux by the remaining cluster light. The cluster equivalent width is sensitive to the hardness of a cluster's radiation field and hence to the cluster's stellar population at the high-mass end. The equivalent widths measured in NGC 1569 average to about (950 ± 200) Å with a dispersion of 600 Å. Similar values have been found in the outer arms of M101 (see Chapter 3). They imply the presence of relatively high-mass stars ($M_* \geq 40\ M_\odot$) in the ionizing clusters (A. Campbell, private communication). This inference is corroborated by the spectroscopic detection of high-excitation species such as HeI(λλ5876, 6678, 7065) and [ArIII](λ7136) (Kennicutt and Kent 1983).

The brightest HII region in NGC 1569 is located 90 pc to the West of object A. Listed as #2 in Table 5-3, it coincides with the strongest radio continuum source (A) mapped by Seaquist and Bignell (1976). This HII region was the only one bright enough to rise above the noise in the [SIII] image. The measured [SIII]/Hα flux ratio is 0.10, which after correction for foreground reddening, amounts to $f([SIII])/f(H\alpha) = 0.06$, or roughly 6 times lower than that measured in the Orion nebula (Dennefeld and Stasinska 1983). Such a low ratio is consistent with a high-excitation, low-metallicity HII region similar to those observed in the Small Magellanic Cloud (Dennefeld and Stasinska 1983; see also Figure 4-1).

The Hα luminosity of the brightest HII region is $9 \times 10^{39}\ erg\ s^{-1}$ (after correction for Galactic foreground obscuration) which implies an ionizing luminosity of 6.6×10^{51} Lyman continuum photons per second, or the equivalent of 660 O6 V stars (Panagia 1973). By comparison, 30 Doradus in the LMC is almost identical in Hα luminosity (ignoring internal absorption), whereas NGC 5461 in M101 is approximately 2 times more powerful (Kennicutt 1984; see also Chapter 3). Varying considerations of distance and internal absorption will juggle these values by factors of 2-3. More important to note is that NGC 1569 is *currently* experiencing high-mass star formation on a scale comparable with the supergiant HII regions in M101.

The *total* Hα luminosity from NGC 1569 is 3.7×10^{40} $erg\ s^{-1}$ which corresponds to a Lyman continuum luminosity of 2.8×10^{52} photons s^{-1} and an extrapolated starbirth rate of 0.33 $M_{\odot}\ yr^{-1}$ (assuming the IMF of Kennicutt [1983]; see also Appendix A). Such figures are remarkably similar to those measured in the NGC 5461 and NGC 5462 HII-region *complexes* (Viallefond *et al.* 1982; see also Chapter 3). The size of NGC 1569's active "bar" (1.1 kpc $\times$ 0.3 kpc in the plane of the sky) is also strikingly similar to the dimensions of the supergiant HII complexes in M101. These resemblances could be merely coincidental or, perhaps, profoundly natural consequences of some common physical process inherent to the starburst phenomenon. Further insight will require a much larger sample of starbursting regions than is considered here (*cf.* Kennicutt 1984; see also Chapter 6).

5.4.3 *Continuum Morphology and Colors*

The red-continuum image shown in Figure 5–1 is characterized by a bright bar-like structure with some indications of silhouetting dust in the northeast portion. Beyond the "bar," individual stars can be resolved. Photometry of these stars is marginally feasible with the present imagery, though I have not yet attempted it. Imaging at a smaller pixel resolution than 0.86" would be preferable for this purpose. A large enough sample of stars with measured fluxes and colors would enable a spectroscopic parallax to be determined for the galaxy. This would be a tremendous improvement over the present distance determination which is based on the magnitude of the brightest resolved stars and the assumption that they are red supergiants.

The contour diagrams of the red and near-infrared surface brightness show a concentration of emission centered on objects A and B. This same concentration of surface brightness is also evident at 2.2 μm (Israel 1988). Ables (1971) points out that the outer B and V contours *are not* centered on A and B but are, instead, centered on a fainter region 20" to the SE of object A. Therefore, the inner concentration probably does not represent the dynamical center of the galaxy but is, instead, a relatively young assemblage of stars in orbit around the dynamical center.

The spatial distribution of ($\lambda 6563 - \lambda 9532$) color in NGC 1569 is depicted in Figure 5–5. Two effects are clearly visible from this mapping. The first is the excellent correspondence between the regions of bluest color and the HII regions shown in Figure 5–3. This strengthens the impression that *the most recent high-mass star formation is occurring exterior to the nuclear region inhabited by objects A and B.* The second effect is the reddening of the color with increasing distance from the "bar." Similar changes in ($B - V$) color were observed by Ables (1971) who notes that such behavior is characteristic of Magellanic irregular galaxies. The redder colors in the outer galaxy are probably not tracing increasing column densities of dust. This would imply increasing column densities of HI which is not seen (Reakes 1980). Instead, the redder colors are probably tracing redder (and older) stars. This age differential is consistent with the outer starlight being off center with respect to the inner (younger) starlight, the two populations not having yet equilibrated.

5.5 *Dating the Hα Arcs*

One way to estimate the age of the nuclear starburst in NGC 1569 is to evaluate the kinematic ages of the remnant ejecta. The two arcs are especially useful for this purpose, because their large angular displacements from the nucleus provide an excellent "lever arm" with which to calculate spatial displacements. Although the kinematic histories of the arcs are completely unknown, one can make some educated guesses based on the radial velocities that are observed along the minor axis.

The Hα velocity field of de Vaucouleurs (1981) shows a strong gradient across the minor axis, with blueshifts in the South increasing to 40 $km\ s^{-1}$ above the systemic value at a displacement of 30" from the nucleus (The velocity field of de Vaucouleurs *et al.* [1974] shows the same gradient but of opposite sign.) Because the radial velocities seem to plateau at larger displacements, a first order approximation would be to keep the velocity of the arcs constant in time and equal to the highest observed value interior to them. The absence of decelerating motion and the possibility of further accelerations beyond 30" from the nucleus suggests that the constant velocity approximation will tend to err on the side of overestimating the ages. Of course, actual measurements of the velocity field out to and including the arcs would be preferable to the above approximations.

If the arcs resulted from outflows along the minor axis, the 40 $km\ s^{-1}$ radial velocity translates to an 88 $km\ s^{-1}$ outflow velocity, and the angular displacements of the two arcs translate to 1.17 and 1.46 kpc respectively. The resulting kinematic ages are 13.0 and 16.5 Myr respectively. If, instead, the distant arcs trace the farside of a cone whose axis is tilted 27° towards us, and whose opening angle is 130° (as in the model of de Vaucouleurs *et al.* [1974]), then the outflow velocity is 61 $km\ s^{-1}$, and the displacements are 1.32 and 1.65 kpc respectively. The resulting kinematic ages would then be 22 and 27 Myr respectively.

These estimates for the age of the nuclear starburst are well matched with the age that Israel and de Bruyn (1988) estimate based on the last major injection of energetic electrons into the ISM. Noting that the non-thermal radio emission from NGC 1569 has a high-frequency cutoff at 8 ± 1 GHz, Israel and de Bruyn ascribe the cutoff to a sharp decrease in relativistic electron injection rates about 5 Myr ago followed by synchrotron radiation losses at frequencies above 8 GHz. Their estimate for the mean age of the electron-injecting supernova outbursts is 10-20 Myr.

5.6 *Energetics of the Arcs*

5.6.1 *Ionization Requirements*

In the absence of diagnostic spectra, it is virtually impossible to determine the source of ionization for the arcs. However, one can still estimate the Lyman continuum production rate that hot stars near the nucleus would need to ionize these distant regions. If it is much higher than that currently measured in the brightest HII regions, then ionization by shock-heating will begin to look more attractive.

For simplicity, I let the arcs be modeled as segments of spherical surfaces that are centered on the nucleus. They intercept the ionizing radiation from the nucleus according to the fractional areas that they fill. Further simplifying, I let the areas of the arcs be equal to the square of their longest dimension. The Hα fluxes from Arc 1 and Arc 2 imply ionization rates of $2.2 \times 10^{50}\ s^{-1}$ and

$8.3 \times 10^{50}\ s^{-1}$ respectively. These two rates are consistent with photoionization from a source near the nucleus, if that source has a Lyman continuum luminosity of $6.9 \times 10^{51}\ s^{-1}$ (to adequately illuminate Arc 1) or $5.4 \times 10^{51}\ s^{-1}$ (to adequately illuminate Arc 2). These ionizing luminosities are nearly identical to that measured in the brightest HII region in the "bar" ($N_i = 6.6 \times 10^{51}\ s^{-1}$). They all require the equivalent of ~600 O6 V stars. Therefore, the ionization requirements for the arcs can be easily provided by a population of hot stars similar to those that are ionizing the brightest HII regions. Whether this population coincides with objects A and B remains unclear, though the spectra of Arp and Sandage (1985) seem to be a little too "soft" to provide the required UV luminosity.

5.6.2 *Gravitational and Kinetic Energies*

One way to estimate the mechanical energy expended during the nuclear starburst is to estimate the gravitational and kinetic energies associated with the ejected arcs. This requires determining the masses of the arcs which, in turn, requires some knowledge of the ionized gas density. For hydrogen in ionization equilibrium, the condition of equilibrium can be stated as

$$N_i = \alpha_B\ n_{H^+}\ n_e\ V, \qquad (5-5)$$

where the ionization rate, N_i is determined from the Hα luminosity, the recombination coefficient for hydrogen at $T = 10^4\ K$ is $\alpha_B = 2.6 \times 10^{-13}\ cm^3\ s^{-1}$ (Osterbrock 1974), and the volume, V, refers to that which is *completely filled* by the ionized gas (rather than the total volume associated with the emitting region). This statement can be rewritten in terms of the mass and density of ionized hydrogen according to

$$N_i = \frac{M_{H^+}\ n_{H^+}\ \alpha_B}{m_H}, \qquad (5-6)$$

as long as the density of free electrons is nearly equal to the density of free protons.

The mass of ionized hydrogen is therefore

$$M_{H^+} = \frac{N_i \, m_H}{n_{H^+} \, \alpha_B}, \tag{5 - 7}$$

where the density, n_{H^+}, refers to the density of ionized gas specific to the Hα emitting regions rather than the density averaged over the volume of the entire emitting feature.

If observations of the density-sensitive [SII] or [OI] doublet transitions are available, it is possible to estimate the density from the measured flux ratio of one or the other flux doublet. Such observations are lacking for the diffuse emission in NGC 1569. The polar plumes in M82, however, have been observed at [SII], resulting in densities that range between 30 and 100 cm^{-3} (McCarthy *et al.* 1987). Considerations of the pressure equilibrium that may operate between the HI and HII phases in NGC 1569, along with the observed HI column densities near the arcs (Reakes 1980) result in much lower densities of 0.1 to 0.5 cm^{-3}. These low values cannot yet be ruled out with the available data.

With the estimated range of possible densities ranging from 0.1 to 100 cm^{-3}, the computed masses of ionized hydrogen in Arc 1 and Arc 2 are $7.2 \times 10^{(3-6)}$ $M_\odot$ and $1.4 \times 10^{(3-6)}$ $M_\odot$ respectively, the lowest exponents referring to the highest density (and lowest volume filling fraction). The corresponding gravitational energies are $1.7 \times 10^{(50-53)}$ $ergs$ and $5.2 \times 10^{(49-52)}$ $ergs$ respectively. An assumed outflow velocity of 88 $km\ s^{-1}$ yields kinetic energies of $8.3 \times 10^{(50-53)}$ $ergs$ and $3.1 \times 10^{(50-53)}$ $ergs$ respectively.

These estimates of gravitational and kinetic energy indicate that for $n_{H^+} \sim 100\ cm^{-3}$, a single supernova of energy 10^{51} ergs would be barely sufficient to eject one of the arc segments. However, lower densities would require up to 1000 supernova explosions per arc segment. The ejection of the western Arm along with Arc 1 as part of a single coherent eruption would require even more energy. Inefficient coupling of the supernova energy to mechanical motions of the gas is also likely, thus increasing the energy requirements even further. Anticipated coupling efficiencies are in the 1 to 5 percent range (Spitzer 1978), so the least amount of energy required to expel Arc 1 would be equivalent to about 50 supernova explosions.

Despite the large uncertainties inherent to estimating the masses of the ionized ejecta. the computed energy requirements are sufficiently constrained to indicate that *each arc was powered by more than one supernova explosion.* The actual number of detonations per arc ranges between 10 (for Arc 2 assuming $n_{H^+} = 100\ cm^{-3}$ and 5% coupling efficiency) and 10^5 (for Arc 1 assuming $n_{H^+} = 0.1\ cm^{-3}$ and 1% coupling efficiency).

In the Milky Way the estimated rate of supernova explosions is roughly 1 every 25 years or 40,000 per Myr. Scaling NGC 1569's supernova activity according to its smaller current star formation rate (one-tenth that of the Milky Way) produces an estimated supernova rate of 4000 per Myr. The nuclear starburst $\sim 10^7$ yrs ago probably involved a significantly higher supernova rate than this. Therefore, the possibility of a coherent ($\Delta t \leq 1\ Myr$) salvo of $\sim 10^3$ supernovae from the nucleus producing each of the observed arc segments is not so farfetched. Indeed, similar arguments have been used to explain the kpc-size "supershells" that are evident in 21 cm maps of the Milky Way and in deep Hα images of the LMC (Kulkarni and Heiles 1988 and references therein).

From the nonthermal radio luminosity that they measure in NGC 1569, Israel and de Bruyn (1988) estimate the non-thermal energy content to be about $4.4 \times 10^{54}\ ergs$. Approximately 5×10^5 supernova remnants could account for this energy (Woltjer 1972). The corresponding supernova rate would have been about 25,000 per Myr (assuming a burst period of 20 Myr), or about 6 times the current estimated rate. The starbirth rate would have been enhanced by the same factor, amounting to 2 $M_\odot\ yr^{-1}$.

5.7 *Discussion*

5.7.1 *A Starburst History*

The data presented here and elsewhere seem to be converging on a common scenario for the recent history of NGC 1569. Approximately 10 to 30 Myr ago, the nucleus of this gas-rich dwarf experienced a sudden increase of high-mass star formation. The starburst seems not to have been provoked by any encounters with other galaxies. The nearest large galaxy, IC 342, is more than 200 kpc away from NGC 1569, and hence has been well beyond interaction range for more than a Gyr. The possibility of an encounter with an intergalactic gas cloud (which would have fueled the burst) cannot be ruled out, however.

The starburst occurred near but not in the nucleus as defined by the isophotes of the older stellar population. The resulting stellar population currently dominates the inner galaxy at optical and near-infrared wavelengths. Associated with the center of the young stellar population are objects A and B, whose luminosities and spectra qualify as super-star clusters, ~5 times brighter than the 30 Doradus cluster.

The starburst created supernovae at a rate of approximately 25,000 per Myr, which corresponds to a starbirth rate of about 2 $M_\odot\ yr^{-1}$ assuming an IMF similar to the one operating in the Milky Way. The supernovae have injected the ISM with relativistic electrons whose synchrotron emission is observed at radio frequencies. A rapid dropoff in the supernova production rate approximately 5 Myr ago is responsible for the observed dropoff in nonthermal emission at frequencies above 8 GHz.

The supernovae have also produced massive outflows of gas along the galaxy's minor axis. Some of this gas continues to be ionized, because it is visible in the light of Hα. Photoionization from hot stars in the "bar" or collisional ionization from interactions between the outflowing gas and cooler gas in the "halo" could explain this activity. Near the bar, the outflow is characterized by ray-like filaments of ionized gas which can be traced backwards to a small region near objects A and B. The outflow appears to accelerate with increasing distance from the bar. Alternatively, the faster ejecta could have simply attained greater displacements.

Farther out, the interaction of the outflow with ambient gas in the halo has produced armlike bunchings of Hα emitting ionized gas and 21-cm emitting neutral gas that reach southwards from the western end of the bar. The Hα "Arm" along with "Arc 1" to the South appear to be segments of a vast bubble that was blown out by a coherent salvo of supernova detonations about 13 Myr ago. About 2 Myr earlier, another eruption of supernovae occurred producing the more distant "Arc 2." Hundreds to thousands of supernovae were probably responsible for creating each of the observed bubble segments.

High-mass star formation continues today ($\tau \leq 5Myr$), as evidenced by the Hα emitting HII regions and their underlying blue clusters. The HII regions are located in the bar on opposite sides of the once bursting nucleus. The most active star-forming region, located to the West of objects A and B, includes an HII region equivalent in Hα luminosity to the 30 Doradus HII region. The ongoing starbirth activity throughout the bar is strikingly similar in size, intensity, and stellar population to that seen in the supergiant HII region complexes NGC 5461 and NGC 5462 in M101. Though still impressive, the present activity is several times lower than that experienced during the heyday of the starburst. Declining activity is expected to ensue at the extremities of the bar until the nucleus cools off and fills up again with cool star forming gas.

In its 15 Gyr lifetime, NGC 1569 could have experienced 6 starbursts equal in intensity to the most recent one. Each burst would have been characterized by a starbirth rate of 2 $M_\odot\ yr^{-1}$, a duration of 20 Myr, and a cycling time of 2 Gyr. This episodic star-forming history would have led to a lifetime-averaged starbirth rate of 0.017 $M_\odot\ yr^{-1}$ with a total accumulation of $16 \times 10^7\ M_\odot$ in the form of stars and stellar remnants (see Tables 5-1 and 5-5).

5.7.2 *Uncertainties and Future Directions*

The scenario presented here is appealing in its self consistency. However, major gaps exist in the picture which, once exposed, may completely alter our perception of what is going on. For starters, the intensity of the burst is poorly known, being based (in this Chapter) on the luminosity of the nonthermal radiation from cooling supernova remnants. Using UV, optical, and near-infrared fluxes plus the evolving models of Larson and Tinsley (1978), Israel (1988) obtains a starbirth rate during the burst of $0.3 \pm 0.1\ M_\odot\ yr^{-1}$. Similarly low birthrates can be derived from the galaxy's bolometric luminosity ($L_{bol} \approx 1.2 \times 10^9\ L_\odot$) using standard conversions (*cf.* Telesco 1988). These birthrates closely resemble the "current epoch" birthrate which I derive from the Hα luminosity. Therefore, the "major burst" $\sim 10^7$ yrs ago may have been less titanic than I have painted and more like the activity of the last few million years.

The cycling time between bursts would then be more like 0.3 Gyr instead of the 2 Gyr cycling time implied by the higher starbirth rate.

The ensuing outflows of hot gas have yet to be mapped in X-rays, even though a bright, resolved source was detected by the Einstein satellite at a position close to objects A and B (Fabbiano *et al.* 1982). Further mapping at higher X-ray sensitivity would be necessary to confirm a hot outflow in NGC 1569 similar to those observed in NGC 253 and M82.

The other gas phases are also in need of better observations. The diffuse ionized gas — including the Arm and the arcs — have yet to be observed spectroscopically. Whether they are photo or shock-ionized remains completely unknown. The radial velocities of the arcs also awaits spectroscopic determination. Such low surface-brightness measurements, though difficult, could be crucial to finding a satisfactory solution to the overall Hα velocity field. Right now, the available data can be satisfied by *either* a bipolar outflow of suitable geometry and kinematic history or windings of ionized gas in polar orbit about the major axis.

The HI has yet to be mapped at a resolution better than 2 arcmin. Therefore the distribution of neutral gas near the bar remains unresolved. In the starburst scenario, the outward blowing winds and supernova eruptions should have created pile-ups of HI and H_2 gas on opposite sides of the nucleus (as appears to be the case in M82 [see Chapter 4]). High resolution HI emission and absorption-line mapping, interferometric CO mapping (at extremely high sensitivity to offset the low CO emissivity [Young *et al.* 1984]), and near-infrared imaging of the shock-excited H_2 emission would go far to better delineate the various phases of the ISM near the bar.

Lastly, objects A and B remain enigmatic. High-resolution imaging and spectroscopy of these compact nuclear sources should finally tell us whether they are super-star clusters, forged from the gaseous implosion that brought on the starburst, or simply foreground imposters. The Hubble Space Telescope will be most helpful in this regard.

References

Ables, H. D. 1971, *Publ. U. S. Naval Obs. Sec. Ser XX (IV)*, 61.

Arp, H. C. and Sandage, A. R. 1985, *A. J.*, **90**, 1163.

Condon, J. J. 1983, *Ap. J. Suppl.*, **53**, 459.

Dennefeld, M. and Stasinska, G. 1983, *A. J.*, **118**, 234.

de Vaucouleurs, G., de Vaucouleurs, A., and Pence, W. 1974, *Ap. J. (Letters)*, **194**, L119.

de Vaucouleurs, G., de Vaucouleurs, A., and Corwin, H. G. 1976, *Second Reference Catalogue of Bright Galaxies* (Austin: Univ. of Texas Press).

de Vaucouleurs, G. 1981, *Sky & Telescope*, **62**, 406.

Fabbiano, G., Feigelson, E., and Zamorani, G. 1982, *Ap. J.*, **256**, 397.

Hodge, P. W. 1974, *Ap. J. (Letters)*, **191**, L21.

Hodge, P. W. and Kennicutt, R. C. 1983, *A. J.*, **88**, 296.

Hunter, D. A., Gallagher, J. S., and Rautenkranz, D. 1982, *Ap. J. Suppl.*, **49**, 53.

Israel, F. P. 1988, *Astr. Ap.*, **194**, 24.

Israel, F. P. and de Bruyn, A. G. 1988, *Astr. Ap.*, **198**, 109.

Kennicutt, R. C. 1983, *Ap. J.*, **272**, 54.

Kennicutt, R. C. 1984, *Ap. J.*, **287**, 116.

Kennicutt, R. C. and Kent, S. M. 1983, *A. J.*, **88**, 1094.

Kulkarni, S. R. and Heiles, C. 1988, in *Galactic and Extragalactic Radio Astronomy* (2nd edition), eds. G. L. Verschuur and K. I. Kellermann (New York: Springer-Verlag), p. 95.

Larson, R. B. and Tinsley, B. M. 1978, *Ap. J.*, **219**, 46.

McCarthy, P. J., Heckman, T., and van Breugel, W. 1987, *A. J.*, **93**, 264.

Osterbrock, D. E. 1974, *Astrophysics of Gaseous Nebulae*, (San Francisco: Freeman).

Panagia, N. 1973, *A. J.*, **78**, 930.

Reakes, M. 1980, *M. N. R. A. S.*, **192**, 297.

Sandage, A. R. 1986, *Astr. Ap.*, **161**, 89.

Sandage, A. R. and Tammann, G. A. 1981, *A Revised Shapley-Ames Catalog of Bright Galaxies* (Washington, D. C.: Carnegie Institution).

Seaquist, E. R. and Bignell, R. C. 1976, *Astr. Ap.*, **48**, 421.

Sofue, Y. 1988, in *Galactic and Extragalactic Star Formation*, eds. R. Pudritz and M. Fich (Dordrecht: Kluwer Academic Publ.), p. 409.

Spitzer, L. 1978, *Physical Processes in the Interstellar Medium* (New York: John Wiley and Sons), p. 260.

Stone, R. P. S. 1977, *Ap. J.*, **218**, 767.

Telesco, C. M. 1988, *Ann. Rev. Astr. Ap.*, **26**, 343.

Tully, R. B. and Fisher, J. R. 1987, *Nearby Galaxies Atlas* (Cambridge: Cambridge University Press).

Viallefond, F., Goss, W. M., and Allen, R. J. 1982, *Astr. Ap.*, **115**, 373.

Williams, T. B., Caldwell, N., and Schommer, R. A. 1984, *Ap. J.*, **281**, 579.

Woltjer, L. 1972, *Ann. Rev. Astr. Ap.*, **10**, 129.

Young, J. S., Gallagher, J. S., and Hunter, D. A. 1984, *Ap. J.*, **276**, 476.

Zwicky, F. 1971, *Catalogue of Selected Compact Galaxies and Post-Eruptive Galaxies* (Zurich: Speich).

Table 5–1

Adopted Properties of NGC 1569

Type[a,b]	SmIV/ IBm
R. A. (1950)[a]	$04^h\ 26^m\ 05^s$
Declination (1950)[a]	64° 44' 24"
Galactic longitude[a]	143.69°
Galactic latitude[a]	11.24°
Radial velocity (heliocentric)[c]	-77 km s^{-1}
Position angle of major axis[d]	116°
Inclination[d]	63°
E(B - V)[e]	0.56 mag.
$(B - V)_\circ$ [d,e]	0.23 mag.
$B_\circ$ [d,e]	9.64 mag.
Distance[e]	2.2 Mpc
Holmberg radius[b,e]	1.44' (925 pc)
$L_\circ$(UV+opt.)[e]	$1.2 \times 10^9\ L_\odot$
L(FIR)[e]	$7 \times 10^8\ L_\odot$
M(HI)[c,e]	$11 \times 10^7\ M_\odot$
$M(H_2)$[e,f]	$2 \times 10^7\ M_\odot$
M(dynamic)[c,e]	$33 \times 10^7\ M_\odot$
M_*	$15 \times 10^7\ M_\odot$

[a] Sandage and Tammann 1981 (RSA)

[b] de Vaucouleurs *et al.* 1976 (RC2)

[c] Reakes 1980

[d] Ables 1971

[e] Israel 1988 and references therein

[f] Young *et al.* 1984

Table 5–2

Observing Log

Telescope	KPNO #1 0.9m @ $f/7.5$
Detector	RCA-3 CCD
Pixel size	0.86"
Field of view	7.3' × 4.5'
Date	10/22/85

Filter	Hα	R	I	[SIII]
$\lambda_\circ$	6563 Å	6500 Å	8290 Å	9540 Å
FWHM	38 Å	1283 Å	1947 Å	144 Å
Integration time	2400 s	600 s	600 s	2400 s

Table 5–3

Positions and Sizes of HII Regions and Other Features

Name (1)	α(1950) (2)	δ(1950) (3)	ΔX" (4)	ΔY" (5)	R" (6)	Id (7)
A	4:26:03.7	64:44:29	0.0	0.0	4.4/1.1	Ables
B	4:26:04.5	64:44:23	5.2	6.0	4.3/1.0	
1	4:25:59.9	64:44:45	-24.2	15.9	(2.9)	HK(50)
2	4:26:02.4	64:44:31	-8.2	1.8	(6.4)/3.2	SB(A), HK(45)
3	4:26:03.5	64:44:26	-0.9	-3.0	(5.2)	SB(c)
4	4:26:03.7	64:44:18	-0.1	-10.7	(3.8)	HK(43)
5	4:26:04.8	64:44:35	6.8	6.4	3.4	SB(E), HK(36)
6	4:26:06.0	64:44:16	14.5	-12.5	(4.3)	HK(29)
7	4:26:07.6	64:44:19	24.8	-9.9	8.3	SB(F), HK23
8	4:26:09.6	64:44:00	37.7	-28.8	6.0	HK(11)
9	4:26:10.8	64:44:10	45.5	-19.3	5.2	HK(7)
10	4:26:10.9	64:43:55	46.3	-34.0	3.4	HK(8)
11	4:26:12.0	64:44:00	53.2	-28.8	4.5	HK(4)
12	4:26:14.5	64:43:52	69.6	-37.4	5.6	HK(2)
Arm	4:25:58.2	64:44:31	-35.1	1.9	(60×20)	HK(50)
Arc 1	4:26:06.1	64:42:51	15.4	-97.6	(70×25)	
Arc 2	4:26:05.8	64:42:27	13.7	-121.7	(60×20)	

Table 5-3 (cont.)

Explanation of Columns for Table 5-3

(1) The object's designation. A and B denote the puzzling blue continuum sources near the nucleus of NGC 1569. The numbers denote Hα emitting HII regions as identified by the author. The arm and arcs are Hα emitting features with no corresponding enhancements in the continuum. They are therefore not *classic* HII regions with underlying star clusters.

(2) Right ascension based on the offset, ΔX, from object A and the R. A. of object A determined by Ables (1971). The position of the arm refers to its brightest part.

(3) Declination based on the offset, ΔY, from object A and the declination of object A determined by Ables (1971).

(4) Offset in Right Ascension from object A, measured in arcseconds, in the detector plane (not on the celestial sphere).

(5) Offset in Declination from object A, measured in arcseconds, in the detector plane.

(6) Radius of object in arcseconds. For objects A and B, both the background-limited radius and halfwidth at half-maximum are given. For the HII regions (except for the brightest one) only the background-limited radius is given. Values in parentheses indicate the presence of blending by neighboring sources. For the Arm and arcs, approximate dimensions are given.

(7) Cross-referenced identification of the feature. Ables refers to the optical continuum sources of Ables (1971). SB refers to the radio continuum sources of Seaquist and Bignell (1976). There is an error in this latter reference with regard to the position of SB(A). Their map shows the correct declination to be 64° 44' 32". HK refers to the Hα sources identified by Hodge and Kennicutt (1983).

Table 5–4

Hα Fluxes and Equivalent Widths

Name (1)	log f(Hα) (2)	EW(tot) (3)	EW(cl) (4)	log $L_{\circ}$(Hα) (5)	log N_i (6)
1	-13.22	121	1225	38.05	49.92
2	-11.32	304	734	39.95	51.82
3	-11.69	103	283	39.58	51.45
4	-12.22	218	(1244)	39.05	50.92
5	-12.22	213	989	39.05	50.92
6	-12.37	80	203	38.90	50.77
7	-11.67	167	1835	39.60	51.47
8	-12.42	191	608	38.85	50.72
9	-12.55	175	787	38.72	50.59
10	-12.88	258	2035	38.39	50.26
11	-12.76	222	(8443)	38.51	50.38
12	-12.91	269	859	38.36	50.23
Arm	-12.10	98	(···)	39.17	51.04
Arc 1	-12.79	61	(···)	38.48	50.35
Arc 2	-13.22	3564	(···)	38.05	49.92

Table 5-4 (cont.)

Explanation of Columns for Table 5-4

(1) The object's designation. See Table 5-3 for cross-references.

(2) Logarithm of the Hα flux, as measured in units of erg cm^{-2} s^{-1}.

(3) The Hα equivalent width, *i.e.* the line-to-continuum flux ratio, as measured in units of Angstroms. The red continuum involved here includes *both* the young cluster light and the older light from the ambient galaxy.

(4) The Hα equivalent width pertaining to the ionizing cluster, in units of Angstroms. The red continuum involved here includes *only* the young cluster light. Values in parentheses are uncertain due to difficulties in segregating the cluster and ambient continuum components.

(5) Logarithm of the extinction-corrected Hα luminosity, in units of erg s^{-1}. A uniform extinction of $A_{H\alpha} = 1.24$ mag. has been assumed.

(6) Lyman continuum photon production rate in units of photons s^{-1}.

Table 5–5

Derived Properties of NGC 1569

Fluxes and Colors	
(observed)	
$f(H\alpha)$	2.04×10^{-11} erg cm^{-2} s^{-1}
$\langle EW(H\alpha) \rangle$	150 Å
$\langle \lambda 6563$ - $\lambda 9532 \rangle$	0.63 mag.
(corrected)	
$f_\circ(H\alpha)$	6.43×10^{-11} erg cm^{-2} s^{-1}
$L_\circ(H\alpha)$	3.73×10^{40} erg s^{-1}
$\langle \lambda 6563$ - $\lambda 9532 \rangle_\circ$	0.07 mag.
Birthrates and Depletion Timescales	
(lifetime averaged)	
$\langle MLR \rangle^a_{15Gyr}$	0.01 $M_\odot$ yr^{-1}
τ(gas)	18.0 Gyr
(currently measured)	
$SFR_\circ$	0.33 $M_\odot$ yr^{-1}
$MLR^a_\circ$	0.21 $M_\odot$ yr^{-1}
$\tau_\circ$(gas)	0.85 Gyr

[a] MLR refers to the mass lockup rate in low mass stars and stellar remnants. For the Kennicutt IMF, it is 0.63 times the star formation rate (SFR). $\langle MLR \rangle_{15Gyr}$ refers to the rate obtained from dividing a galaxy's nongaseous mass (presumed to be in the form of stars and stellar remnants) by its lifetime (presumed to be 15 Gyr).

Figures

Figure 5–1

CCD imagery of the Hα and red continuum emission from NGC 1569. North is up and East is to the left. The total field of view in each image is $3' \times 3'$ (1.9 kpc $\times$ 1.9 kpc). Each image is a logarithmic representation of surface brightness.

a. NGC 1569 in the light of Hα. Continuum emission within the Hα filter bandpass has been eliminated by scaling and subtracting an R-band image from the Hα-band image. Some continuum features persist however, including the two incompletely subtracted stars to the South and one especially bright star to the East. The western "Arm" and northern and southern filaments are evident here, but the southern "arcs" are too faint to show up in this representation.

b. The inner "bar" of NGC 1569 at red wavelengths. Contaminating Hα emission within the R filter bandpass has been eliminated by scaling and subtracting an Hα-band image from the R-band image (see Appendix B). The sharp ray to the North is due to scattered light from the bright foreground star BD +64°450 falling on the CCD chip. Individual stars are evident in the galaxy just outside of the bright central region. A dust lane is also evident in the northeast part of the bar.

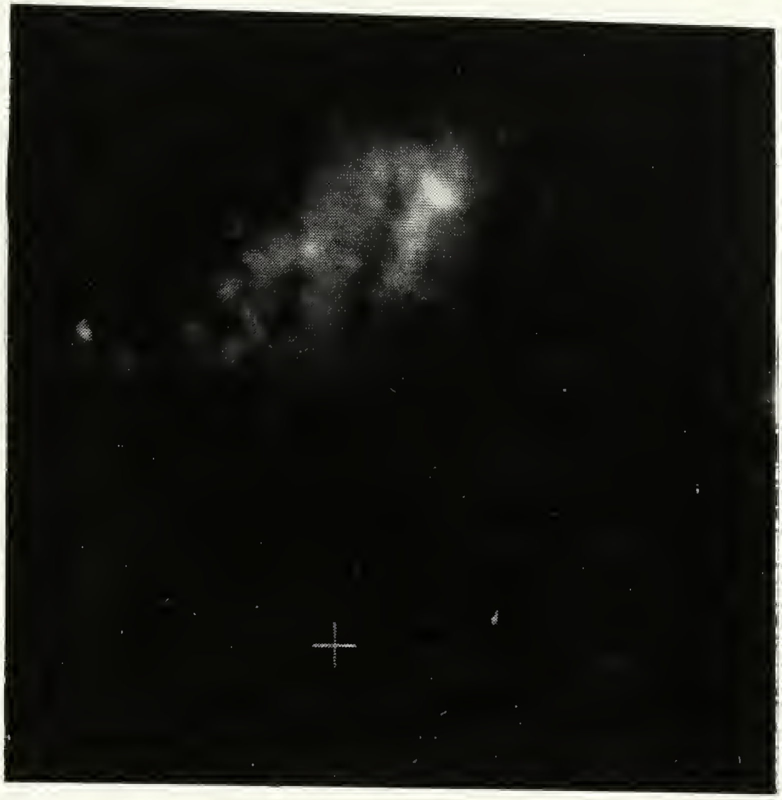

a ▲ b ▼

Figure 5–2

Contour diagrams of the red and near-infrared continuum emission from NGC 1569. The pixel size is 0.86", and the total field of view is $3' \times 3'$ (1.9 kpc $\times$ 1.9 kpc). The red (λ6563) (**a**) and near-infrared (λ9532) (**b**) continua are contoured logarithmically beginning at the 3-sigma level of surface brightness (10^{-18} erg cm^{-2} s^{-1} arcsec^{-2} Å^{-1} with contour intervals of 0.1 dex. The two star-like objects near the nucleus have been labeled in accordance with Ables (1971). Scattered light from the star BD $-64^{\circ}450$ is evident to the north of object A.

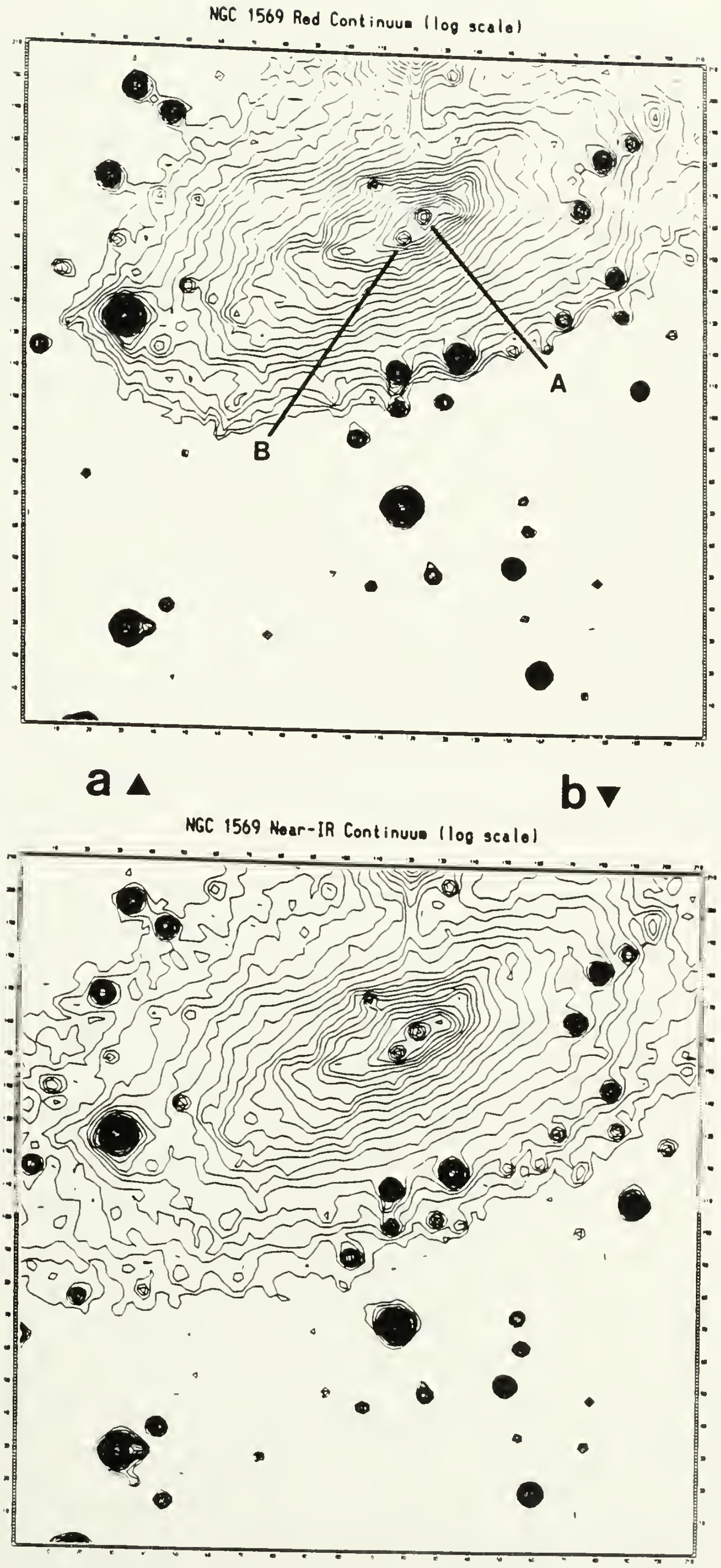
NGC 1569 Red Continuum (log scale)
A
B
a ▲
b ▼
NGC 1569 Near-IR Continuum (log scale)

Figure 5–3

Contour diagrams of the Hα emission from NGC 1569. Same field of view as before. The Hα emission is contoured logarithmically with contour intervals of 0.25 dex.

a. The data have been smoothed via a 4 pix × 4 pix "boxcar" algorithm before plotting. This is done to bring out the fainter emission to the South. The contouring begins at the 1-sigma level ($10^{-16.5}$ erg cm^{-2} s^{-1} arcsec^{-2}) with the major logarithmic values labeled.

b. The data have been plotted with minimal smoothing, so that greater detail can be shown. The contouring begins at the 3-sigma level (10^{-16} erg cm^{-2} s^{-1} arcsec^{-2}). The filled circle and triangle denote the positions of objects A and B respectively. Some filamentary structure is evident to the north and south of the brightly emitting bar.

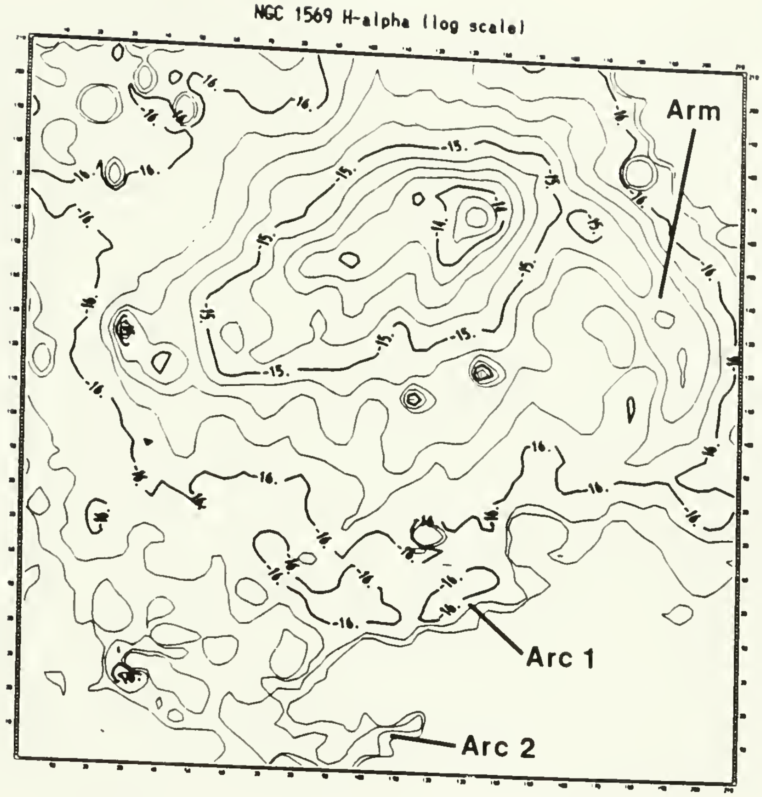
NGC 1569 H-alpha (log scale)
Arm
Arc 1
Arc 2
-15.
-16.

a ▲ b ▼

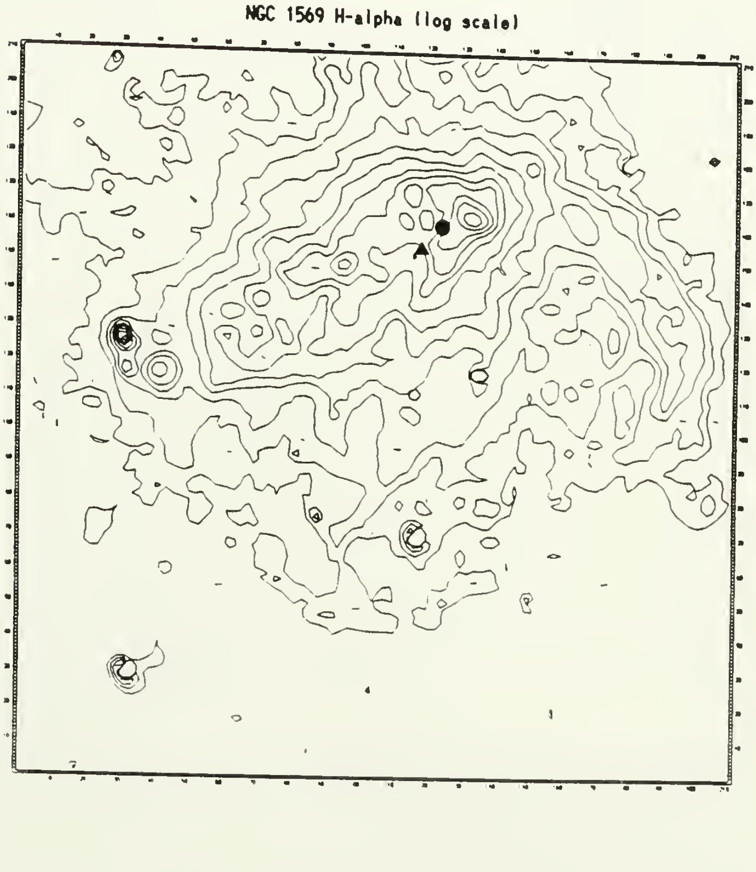
NGC 1569 H-alpha (log scale)

Figure 5–4

Representations of the Hα equivalent width in NGC 1569. Same field of view as before. Being a line-to-continuum emission ratio, the Hα equivalent width highlights regions where (1) the contrast between recent star formation and past-averaged star formation is especially strong, and where (2) diffuse emission with no stellar counterpart is evident. The filled circle and triangle denote the positions of objects A and B respectively.

a. Image of the Hα equivalent width. HII regions in the bar, the diffuse Arm to the West, and the diffuse arc segments to the South are especially prominent.

b. Contour representation of the Hα equivalent width, showing enhancements at the locations of the HII regions, the Arm, and Arc 1.

a ▲ b ▼

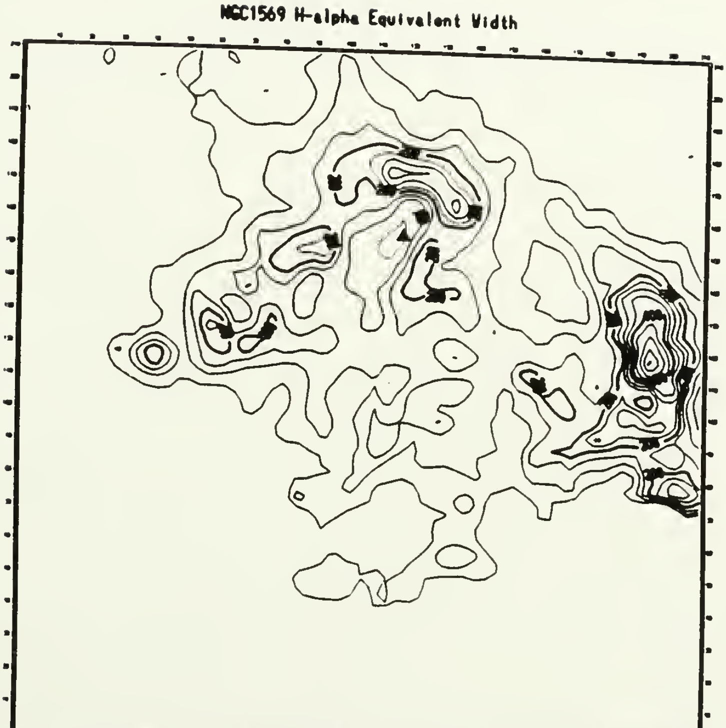

Figure 5–5

Contour diagrams of the continuum color in NGC 1569. Same field of view as before. The ($\lambda 6563 - \lambda 9532$) color is plotted with contour intervals of 0.05 mag.

a. The ($\lambda 6563 - \lambda 9532$) color within the 3-sigma boundary of the corresponding red and near-infrared images. Color reddens from the inside out. The colors near the 3-sigma boundary get as red as ($\lambda 6563 - \lambda 9532$) = 0.85 mag. (after correction for foreground Galactic reddening of 0.56 mag.). The filled circle and triangle denote objects A and B respectively. Note the contaminating effects caused by the scattered light from BD $+64^{\circ}450$ located just north of the field of view.

b. The ($\lambda 6563 - \lambda 9532$) color of the star forming bar. Labeled contours denote colors after correction for Galactic foreground reddening. The bluest colors coincide with the brightest HII regions.

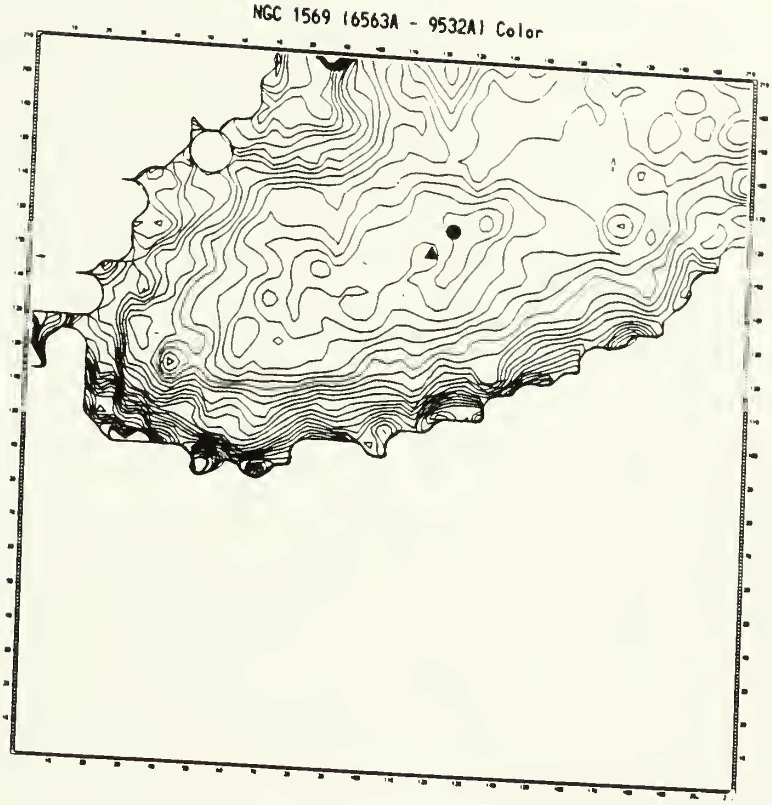
NGC 1569 (6563A - 9532A) Color

a ▲

b ▼


NGC 1569 (6563A - 9532A) Corrected Color

CHAPTER 6

SUMMATION

6.1 *Abstract*

The three galaxies are compared with one another and with 3 other nearby galaxies in terms of their starbirth intensities, their starbirth efficiencies, their ionizing stellar populations, and their possible starbirth histories. The annular-averaged starbirth intensities are strongly correlated with the H_2 surface density, where $\sigma(SFR) \propto \sigma(H_2)^{1.0}$, and with the total gas surface density, where $\sigma(SFR) \propto \sigma(gas)^{1.1}$. The mean starbirth intensity in the starburst galaxy, M82, is 370 times higher than the mean intensities in M101 and the Milky Way; the starbirth efficiency in M82 is 12 times higher than the mean efficiencies in M101 and the Milky Way. The giant HII regions in M101 show significant variations in $H\alpha$ equivalent width as a function of both galactocentric radius and $H\alpha$ luminosity. These variations can be attributed to changes in the initial upper mass limits of the ionizing clusters. The ionizing stellar populations in early-type, late-type, and starburst galaxies are discussed in terms of these results. Crude indices of the galaxies' starbirth histories indicate temporally declining starbirth intensities in M101 and the Milky Way but currently "bursting" starbirth intensities in M82 and NGC 1569.

6.2 *Introduction*

In the preceding three chapters, I have presented CCD imagery and photometric results on three nearby late-type galaxies. The key aims have been (1) to determine how the starbirth intensity (*i.e.* star formation rate per unit area) and ambient gas surface density are typically related, (2) to determine how the efficiency of star formation might vary as a function of environment, and (3) to determine how ionizing stellar populations might vary in their content as a function of environment. These 3 questions are intertwined, in that one requires knowledge of the relevant Initial Mass Function (IMF) of the ionizing stellar populations before being able to estimate starbirth rates and efficiencies from tracers of the high-mass star forming activity(*e.g.* Hα and FIR fluxes). If the IMF varies in an uncertain way, comparisons of starbirth rates and efficiencies within and between galaxies also become ambiguous. Such appears to be the case within M101 at least and may also apply to the other galaxies in the sample. Nevertheless, the comparisons are still revealing in what they tell us about the relative vigor of *high-mass* star formation as a function of environment. This should be kept in mind, when examining the figures in this Chapter.

6.3 *Starbirth Intensities*

Starbirth rates computed from observed tracers of high-mass stars are critically dependent on the IMF that is adopted (see Appendix A). They are also dependent on the distance that is adopted. Although the problem of the IMF cannot be avoided, it is possible to get around the problem of uncertain distances. By using the *surface density* of the starbirth rate, the distance dependence drops out. I call this surface density the "starbirth intensity." Figure 6–1 shows the galactocentric profiles of starbirth intensity for the three galaxies. All intensities are based on the Lyman continuum luminosities inferred from dereddened H-line measurements and the "extended Miller-Scalo" IMF of Kennicutt (1983) (see Appendix A). For comparison, the starbirth intensities in M51, M83, and the Milky Way are also plotted. Although the starbirth intensity is independent of distance, its galactocentric profile is not. That is because the radial distance is distance dependent. Therefore, the individual profiles are subject to being squeezed or stretched along the x-axis, depending on changes in the adopted distances. The profiles for M82 and NGC 1569 are flat straight lines, because all of the ionizing starbirth activity within these galaxies occurs inside the binning radius of 1 kpc.

As Figure 6–1 shows, the starbirth intensity varies by almost 3 orders of magnitude, with M101 and the Milky Way scudding along the bottom at ~10 $M_\odot\ Gyr^{-1}\ pc^{-2}$, and with M82 flying high at ~4000 $M_\odot\ Gyr^{-1}\ pc^{-2}$. The intensity of NGC 1569 is similar to those of the NGC 5461 and NGC 5462 supergiant HII-region complexes in M101 (see Chapter 2). The bump in M101's profile is due to the disproportionate contributions of these complexes to the annular-averaged intensities at R = 5.5 - 7.5 kpc (having imaged and measured only 1/6 of the entire annulus at these radii). The *total* starbirth rates of the four galaxies are not nearly as disparate as the starbirth intensities. At the adopted distances, they range from 0.33 $M_\odot\ yr^{-1}$ for NGC 1569 to 11.6 $M_\odot\ yr^{-1}$ for M82.

6.4 *Starbirth Efficiencies*

Like the starbirth intensities, the starbirth efficiencies do not depend on the adopted distance to a galaxy. Defined here as the ratio of the starbirth intensity and the ambient gas surface density, *i.e.*

$$SFE = \sigma(SFR)/\sigma(gas). \qquad (6-1)$$

this "star formation efficiency" is sometimes called the normalized or specific star formation rate and is expressed in units of Gyr^{-1}. In computing starbirth efficiencies, it is necessary to compare identically resolved annular measures of the starbirth intensity and gas surface density. This is often done by smoothing the Hα imagery with a Gaussian "beam" of equal size as the corresponding HI and CO beams before conducting the photometry. Figure 6–2 shows the galactocentric profiles of the starbirth efficiency for the four galaxies, after having performed the necessary smoothing. For comparison, the resolution-matched annular-averaged efficiencies in M51, M83, and the Milky Way are also plotted. Again, the x-extents of the profiles are subject to distant-dependent changes. Although the starbirth intensities vary over a 2.6 dex range, the starbirth efficiencies vary by less than 1.6 dex. *Therefore 90 percent of the variations in the starbirth intensity can be attributed to variations in the available gas content.* The remaining variations are either due to real fluctuations in stellar fecundity or to variations in the high-mass IMF. For now, it is best to conclude that real variations in the high-mass star forming efficiency exist between galaxies, with the high-intensity "starburst" galaxies such as M82 comprising the high-efficiency regime.

The relationship between starbirth intensity and gas surface density can be further explored in terms of both the annular-averaged measurements and the globally-averaged measurements. Figure 6–3 shows the resolution-matched annular-averaged starbirth intensities plotted against the H_2, HI, and total gas surface densities. Annular-averaged measurements for M51, M83, and the Milky Way are also plotted. Casual inspection reveals strong correlations between $\sigma(SFR)$ and $\sigma(H_2)$ as well as between $\sigma(SFR)$ and $\sigma(H_2 + HI + He)$. By contrast, little correlation is evident between $\sigma(SFR)$ and $\sigma(HI)$. Least-squares regressions give

$$log\ \sigma(SFR) = (-0.74 \pm 2.45) + (3.51 \pm 5.33) log\ \sigma(HI), \qquad (6-2)$$

with a correlation coefficient, r_c, of 0.23 yielding a correlation significance level of only 0.77,

$$log\ \sigma(SFR) = (0.04 \pm 0.33) + (0.97 \pm 0.24) log\ \sigma(H_2), \qquad (6-3)$$

with $r_c = 0.78$ yielding a correlation significance level exceeding 0.999, and

$$log\ \sigma(SFR) = (-0.47 \pm 0.36) + (1.13 \pm 0.22) log\ \sigma(gas), \qquad (6-4)$$

with $r_c = 0.82$ again yielding a correlation significance level exceeding 0.999. The intercepts, slopes, and standard deviations of these least-squares fits are all based on having run the regressions in both directions. The near-linear dependences on H_2 and total gas agree (to within the uncertainties) with the conclusions of Kennicutt (1989) who obtained $\sigma(SFR) \propto \sigma(gas)^{1.3\pm0.3}$, based on similar annular-averaged measurements in 15 nearby galaxies.

Table 6 lists the globally-averaged properties of the 3 galaxies along with those of the Milky Way. This table highlights the differences in starbirth intensity, starbirth efficiency, and current-epoch *vs.* past-averaged starbirth activity that exist between "normal" and "starbirth" galaxies. Least-squares regressions between $\sigma(SFR)$ and $\sigma(gas)$ for this small sample yields

$$log\ \sigma(SFR) = (0.01 \pm 0.74) + (1.48 \pm 0.56) log\ \sigma(H_2), \qquad (6-5)$$

where $r_c = 0.90$ yielding a correlation significance level of 0.90, and

$$log\ \sigma(SFR) = (-1.05 \pm 0.18) + (1.74 \pm 0.10) log\ \sigma(gas), \qquad (6-6)$$

where $r_c = 0.997$ yielding a correlation significance level of 0.998. Here, the non-linear dependences on H_2 and total gas surface density reflect the higher starbirth efficiencies of NGC 1569 and M82. Similar "nonlinear" behavior is evident in the spiral arms of M51 and M83 (Lord 1987; Vogel *et al.* 1988), in the supergiant HII region complex NGC 5461 (see Chapter 3), in the center of NGC 253 (Waller *et al.* 1988), and in larger samples of "normal" and "starburst" galaxies, where the FIR luminosities were used to trace the star formation rates (Sanders *et al.* 1988; Young 1988). Possible explanations for such non-linear enhancements in starbirth activity are discussed in Chapter 2 (see "Laws' of Star Formation" [Section 2.7]).

6.5 *Ionizing Stellar Populations*

The most insight regarding the stellar populations that underly giant HII regions was obtained from M101 (see Chapter 3). The Hα and red-continuum photometry of several hundred HII regions in this galaxy revealed subtle but significant variations with galactocentric radius. Within 5 kpc of the nucleus, the Hα luminosity function shows proportionately fewer high-luminosity HII regions than are evident in the outer arms. Moreover, the galactocentric distribution of Hα equivalent widths appears depressed inside of R = 5 kpc. These effects can be attributed to a "softening" of the stellar radiation fields that power the inner-galaxy HII regions. A simple model of the ionizing stellar populations leads to consistent results for an IMF slope of 2.9 ± 0.3 and initial upper mass limits that vary by a factor of 1.3 to 1.7. Whatever the specific form of the IMF is, we are still left with fewer high-mass stars powering the inner galaxy HII regions. This alone is enough to compromise (by factors of $\sim$2) computations of starbirth rates and efficiencies based on tracers of high-mass star formation (*e.g.* Hα and FIR luminosities).

Although previous studies of the HII regions in M101 have found changes in spectral "excitation" (and, by inference, varying cluster IMFs) that appear correlated with the metallicity gradient (Viallefond *et al.* 1982), the galactocentric variations in the Hα equivalent width reported here show closer similarities with the profiles of the differential rotation, shear rate, and tidal acceleration in the disk. The sense is to have lower equivalent widths, where the shear flow and tidal stress are higher. This opens up the possibility of *dynamical effects* governing the formation of clusters and of the stars therein. Although more comprehensive measurements will be necessary to verify such a link in M101, there is some evidence for dynamical effects constraining the stellar populations in other galaxies.

Early-type galaxies with large bulges exert strong tidal stresses and create severe shearing in the disk. They would be expected, therefore, to be lacking in bright ionizing clusters of high effective temperature. Such appears to be the case in the disk of M31 (Hodge 1987), though more work needs to be done in this regard. By contrast, Scd and irregular-type galaxies should be characterized by extremely bright HII regions of high excitation. This again appears to be the case, as demonstrated by the HII regions in the LMC, M33, and NGC 1569 (see Chapter 5). The Hα luminosities and equivalent widths of NGC 1569's HII regions are remarkably similar to those measured in the *outer arms* of M101. Indeed the entire galaxy could be mistaken for one of M101's supergiant HII region complexes! Apparently, the outer disk of M101 and the inner bar of NGC 1569 are similarly conducive to the creation of high-mass, high-temperature clusters.

The stellar populations that power the ionizing activity in M82 are confused by the older stars in the galaxy's dense center. Indeed, the task of isolating the young cluster light from that of the galaxy's nucleus and bulge was more than could be attempted with the present data. The dust that obscures so much in this galaxy serves only to confound such efforts.

Considerations of the Brackett-line emission and near-infrared starlight from the central (8") region of M82 have led to stellar population models that are lacking in both high and low-mass stars (Rieke *et al.* 1980). The uncertainties associated with dereddening the continuum light and breaking it up into dwarf, giant, and supergiant components, however, make the final conclusions dubious. I find myself impressed by the enormous ionizing and FIR luminosities from such a small package ($R \leq 1$ kpc). Disregarding non-thermal "engines," the most economical way to supply this power is with bright clusters containing high-mass stars. The correlation between Hα luminosity and Hα equivalent width, as found in M101, is worth noting in this regard. There, the brighter HII regions contain the hotter, more massive stars. If the same correlation holds in starburst nuclei, such as in M82, then extremely high-mass stars should be present. The likely presence of a rigidly rotating bar in the center of M82 further implies relatively low shearing stresses and, perhaps, an accreting environment biased towards forming enormous clusters with fully populated upper stellar mass limits. The enormous clusters certainly seem to be there.

6.6 *Starbirth Histories*

A simple way of gauging the starbirth history of a galaxy is to compare its current-epoch starbirth rate with its lifetime-averaged starbirth rate. The current-epoch birthrate is usually based on a tracer of the massive star formation activity (*e.g.* the Hα or FIR flux), while the lifetime-averaged birthrate is based on the integrated mass of stars along with an assumed age for the galaxy. The integrated mass of stars can be estimated by subtracting the residual gaseous mass from the dynamical mass and then multiplying this difference by a factor (of order unity) that compensates for the mass returned to the ISM via stellar winds and supernova explosions. To avoid problems associated with distance ambiguities, I have used starbirth intensities (*i.e.* surface densities), thus deriving $\sigma(SFR)$ for the current-epoch birthrate and $\langle\sigma(SFR)\rangle_{15\ Gyr}$ for the lifetime-averaged birthrate. The ratio of these two birthrates for the Milky Way, M101, M82, and NGC 1569 is listed in Table 6-1.

A common way to model the starbirth history of a disk galaxy is to assume exponentially varying starbirth rates or intensities, such that

$$\sigma(SFR) = \sigma_o(SFR)\ e^{\pm(t-t_o)/\tau}, \qquad (6-7)$$

where $t - t_o$ is the star forming age of the galaxy, and τ is the e-folding timescale (*cf.* Gusten and Mezger 1982; Kennicutt 1983; Scalo 1986). For decaying exponentials, τ corresponds to the e-folding gas depletion timescale

$$\tau = (f\ SFE)^{-1}, \qquad (6-8)$$

where SFE is the starbirth efficiency (which is constant in such a model) and f is the fractional mass that stays locked up in low-mass stars and stellar remnants ($f \approx 0.65$ for a Salpeter-type IMF, see Appendix A). The near-linear relationship between starbirth intensities and gas surface densities that is evident among the 6 galaxies implies a near constant starbirth efficiency and hence supports the use of such an exponential model.

Both M101 and the Milky Way have current-epoch birthrates that are about 1/3 of their lifetime-averaged birthrates, thus implying some sort of temporal decline in their starbirth activity. *If* the starbirth rates in these galaxies have been declining exponentially, then the ratio of current-epoch to lifetime-averaged birthrates is

$$\frac{\sigma(SFR)}{\langle\sigma(SFR)\rangle} = \frac{(t - t_o)e^{-(t-t_o)/\tau}}{\tau(1 - e^{-(t-t_o)/\tau})}. \qquad (6-9)$$

For star-forming ages of 10 to 15 Gyr, the measured ratios in M101 and the Milky Way would imply e-folding gas depletion timescales of 8 Gyr and *initial* starbirth rates that are 3.5 to 6.5 times higher than they are today. These estimates should be compared with the *current-epoch* starbirth efficiencies in M101 and the Milky Way which predict much shorter e-folding gas depletion timescales of 2.9 and 2.1 Gyr respectively (see Table 6-1), initial starbirth rates that are 25 and 33 times higher than the current-epoch birthrates, and star-forming ages of 9.3 and 7.3 Gyr respectively. Such discrepancies indicate that there are problems with the exponential model and/or the derived star forming properties. Two possible complications are highlighted below.

• The starbirth histories are episodic, and the current epoch represents a more intense phase than would be predicted from the exponentially decaying model. The episodic possibility is not without precedent. Both M82 and NGC 1569 show strong evidence for episodic starbirth histories. Not only do they have current-epoch starbirth rates that are many times *higher* than their lifetime-averaged birthrates, but they also show evidence for supernovae-driven outbursts. In the case of NGC 1569, the ionized relics of the outburst can be used to date the eruption at 10 - 30 Myr. This provides a strong precedent for episodic "starburst" activity occurring on temporal scales of at least 10^7 years and on spatial scales of at least a kpc.

In M101 and the Milky Way, the episodic modes of starbirth activity would have to prevail over timescales of at least 10^8 years and on spatial scales of $\sim$10 kpc. Such large-scale variations in a galaxy's starbirth history would have many consequences, including bumps in the frequency distributions of stellar age, mass, and metallicity. In the Milky Way (within a few kpc of the Sun), the frequency distribution of F and G dwarf ages indicates that the starbirth rate has varied by factors of 10 over intervals of 0.4 Gyr, with 5σ enhancements having occurred 7 and 5 Gyr ago as well as within the last 0.4 Gyr (*cf.* Scalo 1987). A similar enhancement could be occurring in the disk of M101.

• The current-epoch starbirth rates are significantly overestimated, thus leading to the discrepancy in e-folding gas depletion timescales. A common depletion timescale of 5 Gyr would result from the birthrate ratio (Eq. 6-9) and starbirth efficiency (Eq. 6-8), if the current-epoch starbirth rates were 2.3 times lower (*i.e.* 1/7 of the lifetime-averaged rates). This would also match the depletion timescale that results from considerations of the current-epoch gas fraction, $\sigma(gas)/\sigma(tot)$ (see Table 6-1), where

$$\sigma(gas) = \sigma(tot)\, e^{-(t-t_o)/\tau}, \qquad (6-10)$$

and where a star-forming age of 15 Gyr is assumed. The lower birthrates would require a lower $\sigma(SFR)/I(H\alpha)$ conversion which, in turn, would entail an IMF that is flatter or biased towards higher mass stars than the IMF prescribed by Kennicutt (1983) (see Table A-1 in Appendix A).

The available evidence for IMF-based overestimations of the starbirth rates is ambiguous but difficult to dismiss (*cf.* Gusten and Mezger 1982; Scalo 1986). In M101, the Hα emission follows a much flatter galactocentric profile than the red continuum emission. This immediately indicates a significant difference between the galactocentric distributions of current-epoch massive star formation and past-averaged star formation in M101. Either the radial distribution of star formation has truly varied over time, or the IMF is spatially skewed so that the $\sigma(SFR)/I(H\alpha)$ conversion should be lower in the outer galaxy. This latter possibility is supported by the higher Hα equivalent widths that are found beyond 5 kpc of the nucleus (see Chapter 3). The higher equivalent widths are probably tracing IMFs with higher upper mass limits and/or flatter slopes. Such variations in the IMF will lead to lower $\sigma(SFR)/I(H\alpha)$ conversions (see Table A-1 in Appendix A) thus reducing the discrepancies in depletion timescales.

It is not at all clear whether birthrate or IMF variations are responsible for the discrepancy in estimated gas depletion times in M101 and the Milky Way and for the different galactocentric distributions of Hα and red continuum emission in M101. Other nearby disk galaxies, such as M31 and the Milky Way, show galactocentric concentrations of current-epoch massive star formation that are similarly at odds with the mass distributions in the underlying disks. Understanding these large-scale departures from the past-averaged starbirth record remains a important challenge to those wishing to determine evolutionary behavior from crude tracers of current-epoch and lifetime-averaged star formation.

References

Bloeman, J. B. G. M., Strong, A. W., Blitz, L., Cohen, R. S., Dame, T., Grabelsky, D. A., Hermen, W., Lebrun, F., Mayer-Hasselwander, H. A., and Thaddeus, P. 1986, *Astr. Ap.*, **154**, 25.

Bosma, A., Goss, W. M., and Allen, R. J. 1981, *Astr. Ap.*, **93**, 106.

Gusten, R. and Mezger, P. G. 1982, *Vistas in Astronomy*, **26**, 159.

Hodge, P. 1987, *Pub. A. S. P.*, **99**, 915.

Israel, F. P. 1988, *Ap. J.*, **194**, 24.

Kennicutt, R. C. 1983, *Ap. J.*, **272**, 54.

Kennicutt, R. C. 1989, *Ap. J.*, in press.

Lord, S. 1987, Ph.D. Thesis, University of Massachusetts.

Nakai, N., Hayashi, M., Handa, T., Sofue, Y., Hasagawa, T., and Sasaki, M. 1987, *Publ. Astr. Soc. Japan*, **39**, 685.

Rieke, G. H., Lebofsky, M. J., Thompson, R. I., Low, F. J., and Tokunaga, A. T. 1980, *Ap. J.*, **238**, 24.

Sanders, D. B., Soifer, B. T., Elias, J. H., Madore, B. F., Matthews, K., Neugebauer, G., and Scoville, N. Z. 1988, *Ap. J.*, **325**, 74.

Sanders, D. B., Solomon, P. M., and Scoville, N. Z. 1984, *Ap. J.*, **276**, 182.

Scalo, J. M. 1986, *Fundam. Cosmic Phys.*, **11**, 1.

Scalo, J. M. 1987, in *Starbursts and Galaxy Evolution*, ed. T. X. Thuan, T. Montmerle, and J. T. T. Van (Gif Sur Yvette: Editions Frontieres), p. 445.

Scoville, N. Z., Soifer, B. T., Neugerbauer, G., Young, J. S., Matthews, K., and Yerka, J. 1985, *Ap. J.*, **289**, 129.

Solomon, P. M., Barrett, J., Sanders, D. B., and de Zafra, R. 1983, *Ap. J. (Letters)*, **266**, L103.

Viallefond, F., Goss, W. M., and Allen, R. J. 1982, *Astr. Ap.*, **115**, 373.

Vogel, S. N., Kulkarni, S. R., and Scoville, N. Z. 1988, *Nature*, **334**, 402.

Waller, W. H., Kleinmann, S. G., and Ricker, G. R. 1988, *A. J.*, **95**, 1057.

Young, J. S., Gallagher, J. S., and Hunter, D. A. 1984, *Ap. J.*, **276**, 476.

Young, J. S. and Scoville, N. Z. 1984, *Ap. J.*, **287**, 153.

Young, J. S. 1988, in *Galactic and Extragalactic Star Formation*, eds. R. E. Pudritz and M. Fich (Dordrecht: Kluwer Academic Publ.), p. 579.

Table 6–1

Globally-Averaged Properties of the Galaxies

Galaxy	M.W.[a]	M101[b]	M82[c]	NGC 1569[d]
Type	Sbc	Sc	Amorph.	Sm
$\sigma(tot)$ ($M_\odot$ pc^{-2})	446	427	955	105
$\sigma(HI)$ ($M_\odot$ pc^{-2})	2.9	5.1	19.1	35.0
$\sigma(H_2)$ ($M_\odot$ pc^{-2})	7.3	7.7	318	6.4
$\sigma(gas)$ ($M_\odot$ pc^{-2})[e]	13.6	17.0	458	55.0
$\sigma(gas)/\sigma(tot)$	0.03	0.04	0.48	0.52
$\sigma(SFR)$ ($M_\odot$ pc^{-2} Gyr^{-1})	10.5	9.16	3690	105
SFE(H_2) (Gyr^{-1})	1.44	1.19	11.6	16.4
SFE(gas) (Gyr^{-1})	0.77	0.54	8.06	1.91
τ(gas)[f] (Gyr)	2.1	2.9	0.2	0.8
$\frac{\sigma(SFR)}{\langle\sigma(SFR)\rangle_{15Gyr}}$	0.36	0.33	111	31.5

Table 6-1 (cont.)

Explanation of Notes for Table 6-1

[a] All Galactic mass densities and starbirth intensities concern the inner R $\leq$ 10 kpc, where the Solar Circle is set at R = 10 kpc. $\sigma(H_2)$ and $\sigma(HI)$ are from Sanders *et al.* (1984) and references therein. The $\sigma(H_2)/I(CO)$ conversion of Bloeman *et al.* (1986) is used instead of the original conversion, however. $\sigma(SFR)$ is based on Lyman continuum luminosities of Gusten and Mezger (1982) and $\sigma(SFR)/\sigma(N_i)$ conversion of Kennicutt (1983).

[b] All M101 mass densities and starbirth intensities concern the inner R $\leq$ 5.7 arcmin, or R $\leq$ 8 kpc for an assumed distance of 4.8 Mpc. $\sigma(tot)$ is derived from the rotation curve of Bosma *et al.* (1981). $\sigma(H_2)$ and $\sigma(HI)$ are from Solomon *et al.* (1983) and references therein, with the $\sigma(H_2)/I(CO)$ conversion of Bloeman *et al.* (1986) replacing the original conversion.

[c] All M82 mass densities and starbirth intensities concern the inner R $\leq$ 1.1 arcmin, or R $\leq$ 1.0 kpc for an assumed distance of 3.2 Mpc. $\sigma(tot)$, $\sigma(H_2)$, and $\sigma(HI)$ are from Young and Scoville (1984) and references therein.

[d] All NGC 1569 mass densities and starbirth intensities concern the inner R $\leq$ 1.6 arcmin, or R $\leq$ 1.0 kpc for an assumed distance of 2.2 Mpc. $\sigma(tot)$ and $\sigma(HI)$ are from Reakes (1980). $\sigma(H_2)$ is from Israel (1988) who used the single CO observation (50" beam) of Young *et al.* (1984) plus a $\times 4$ higher $N(H_2)/I(CO)$ conversion (to compensate for low metal abundance) as well as a $\times 3$ spatial scaling factor (based on the ratio of the total FIR luminosity to that from the central 50").

[e] Total gas mass densities include estimated contributions from HII and from He.

[f] The gas depletion timescale, τ(gas), is based on a constant star formation rate according to $\tau(gas) = \sigma(gas)/(f\ \sigma(SFR))$, where f corresponds to the fractional mass that stays locked up in low-mass stars and stellar remnants. For a Salpeter-type IMF, $f \approx 0.65$. If a constant star formation efficiency is assumed, τ(gas) corresponds to the gas depletion e-folding time.

Figures

Figure 6–1

Galactocentric distributions of the starbirth intensity. The star formation intensities are plotted as surface densities in the plane of each galaxy. All values of $\sigma(SFR)$ are based on the $\sigma(SFR)/\sigma(N_i)$ conversion of Kennicutt (1983). The $\sigma(N_i)$ values for M83 and M51 are based on the $I(H\alpha)$ data in Lord (1987); and the $\sigma(N_i)$ values are based on the thermal radio continuum data in Gusten and Mezger (1982). The profiles for M82 and NGC 1569 are represented as flat straight lines, because of the 1 kpc binning radius and the lack of significant Hα emission beyond this radius.

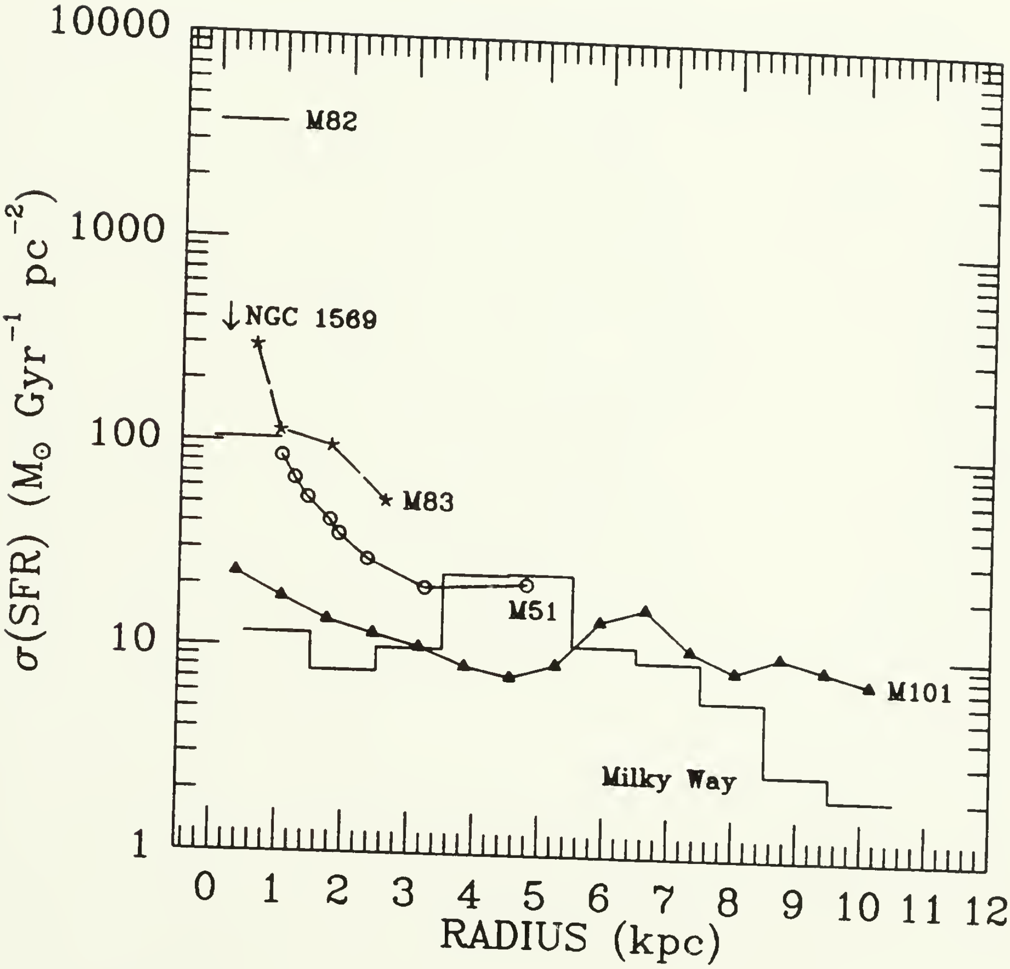

10000
1000
100
10
1
σ(SFR) (M⊙ Gyr⁻¹ pc⁻²)
M82
↓NGC 1569
M83
M51
M101
Milky Way
0 1 2 3 4 5 6 7 8 9 10 11 12
RADIUS (kpc)

Figure 6–2

Galactocentric distributions of the starbirth efficiency. The starbirth efficiencies in M83 and M51 are based on the annular-averaged Hα, CO, and HI data in Lord (1987); the efficiencies for the Milky Way are based on the radio continuum data in Gusten and Mezger (1982) and the CO and HI data in Sanders *et al.* (1984). Each starbirth efficiency involves a starbirth intensity and gas surface density of matching resolution. Considerations of the IMF and extinction-dependent conversion between I(Hα) and σ(SFR), as well as the uncertain conversion between I(CO) and $\sigma(H_2)$ indicate that the plotted SFEs are absolutely certain to within a factor of about 3 (or $\pm$ 0.5 dex as plotted here) and self-consistent to within a factor of about 2 (or $\pm$ 0.3 dex as plotted here).

a. Galactocentric profiles of the starbirth efficiency with respect to the H_2 surface density alone.

b. Galactocentric profiles of the starbirth efficiency with respect to the total gas surface density.

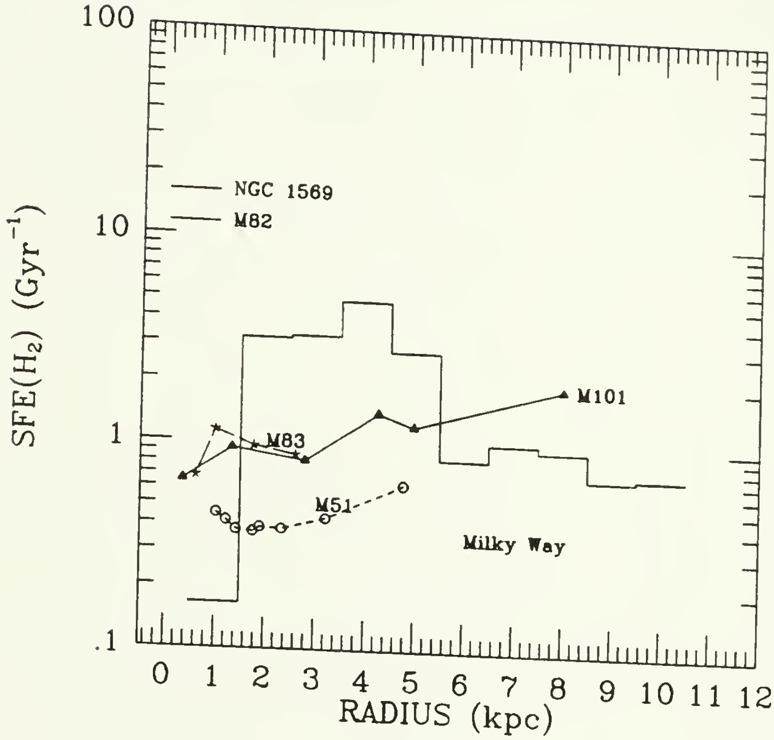
100
10
1
.1
SFE(H$_2$) (Gyr^{-1})
NGC 1569
M82
M101
M83
M51
Milky Way
0 1 2 3 4 5 6 7 8 9 10 11 12
RADIUS (kpc)

a ▲ b ▼

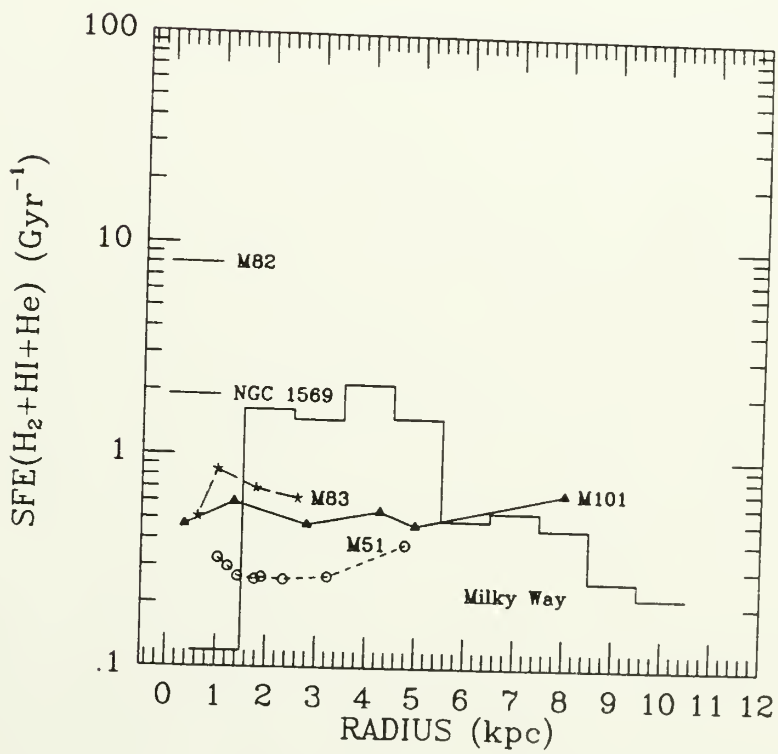
100
10
1
.1
SFE(H$_2$+HI+He) (Gyr^{-1})
M82
NGC 1569
M83
M101
M51
Milky Way
0 1 2 3 4 5 6 7 8 9 10 11 12
RADIUS (kpc)

Figure 6–3

Annular-averaged starbirth intensities *vs.* H_2, HI, and total gas surface densities in 6 galaxies. Each point involves a starbirth intensity and gas surface density of matching resolution.

a. Starbirth intensity *vs.* H_2 surface density.

b. Starbirth intensity *vs.* HI surface density.

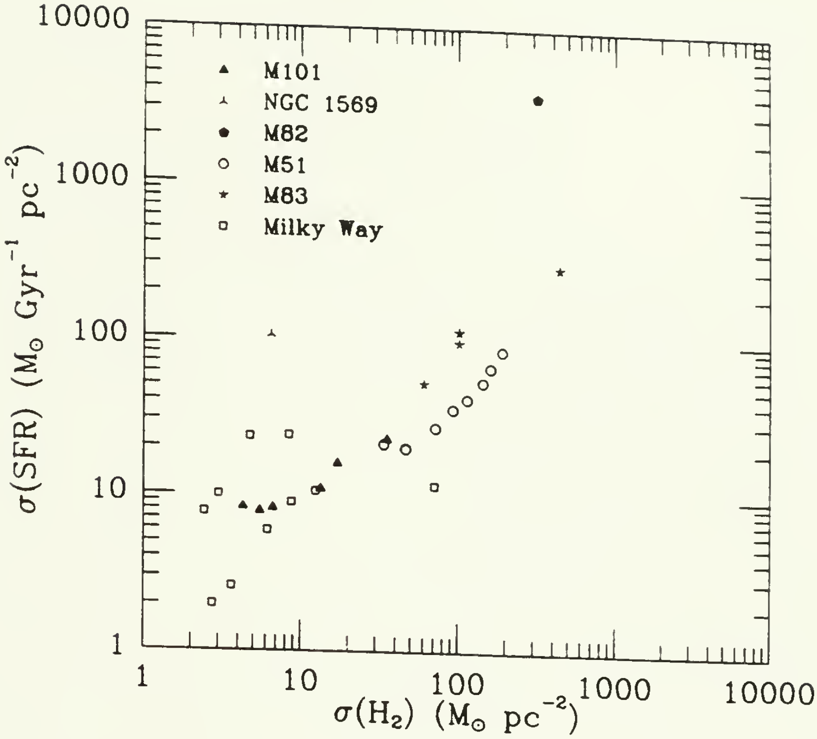
M101
NGC 1569
M82
M51
M83
Milky Way
σ(SFR) (M⊙ Gyr⁻¹ pc⁻²)
σ(H₂) (M⊙ pc⁻²)
10000
1000
100
10
1
1
10
100
1000
10000

a ▲

b ▼

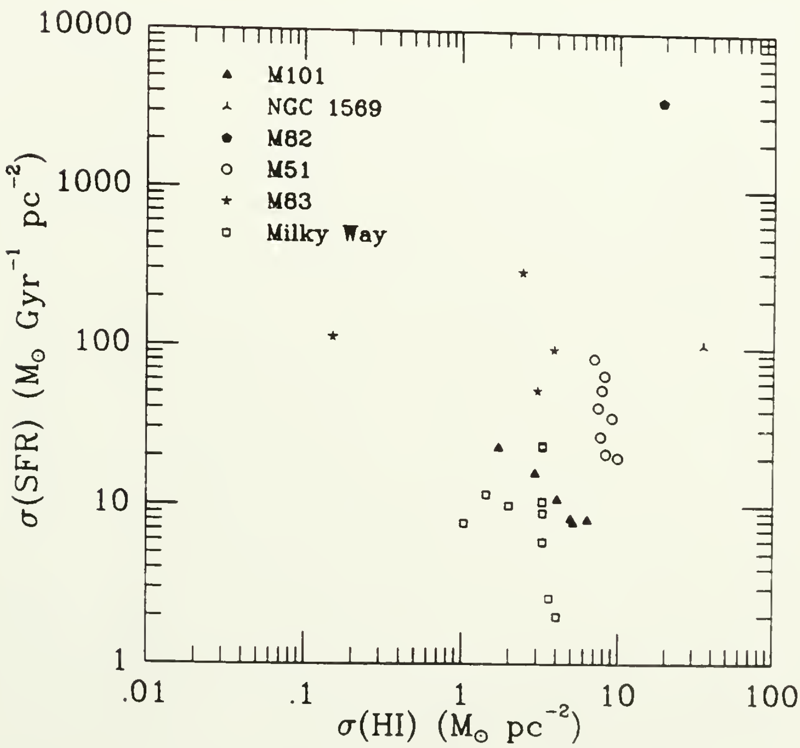
M101
NGC 1569
M82
M51
M83
Milky Way
σ(SFR) (M⊙ Gyr⁻¹ pc⁻²)
σ(HI) (M⊙ pc⁻²)
10000
1000
100
10
1
.01
.1
1
10
100

Figure 6–3 (cont.)

c. Starbirth intensity *vs.* total gas surface density.

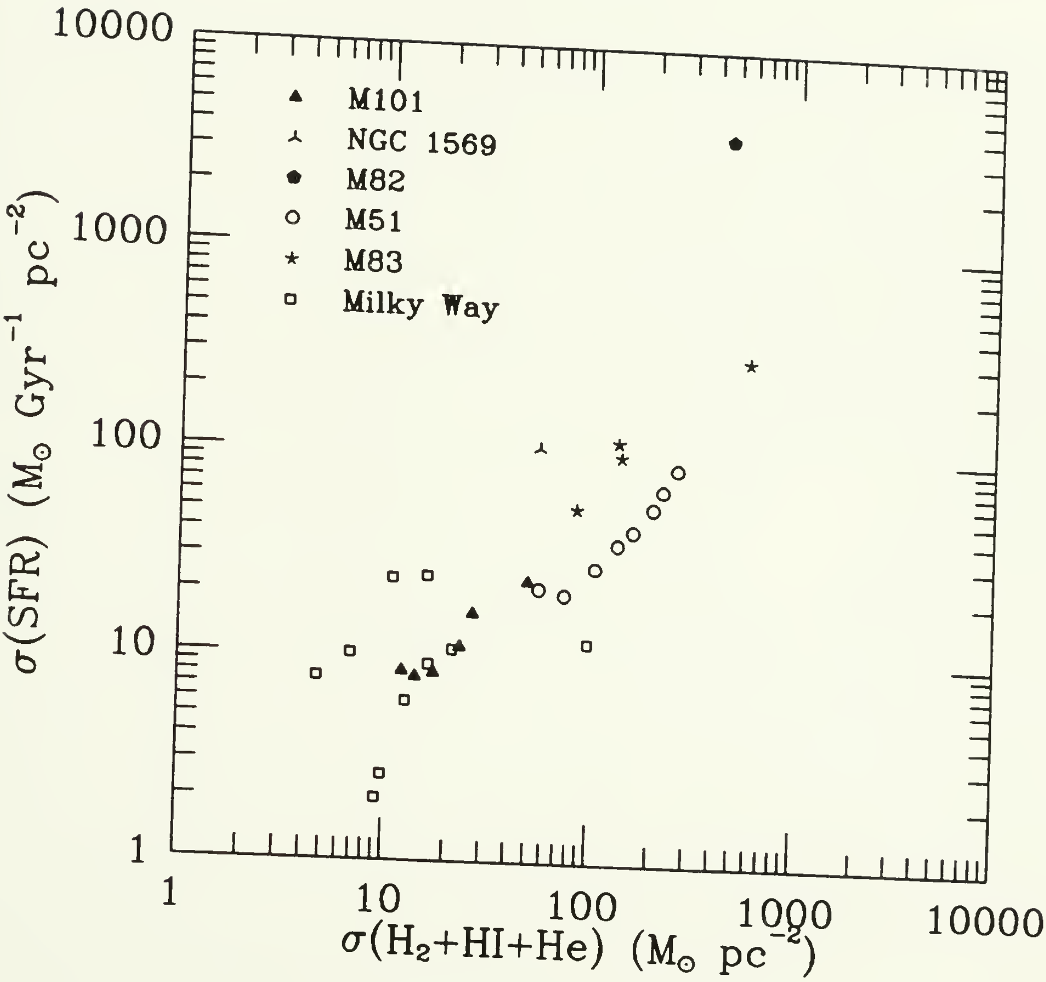
M101
NGC 1569
M82
M51
M83
Milky Way
10000
1000
100
10
1
σ(SFR) (M⊙ Gyr⁻¹ pc⁻²)
1
10
100
1000
10000
σ(H₂+HI+He) (M⊙ pc⁻²)

C

APPENDIX A

COMPUTATION OF STAR FORMATION RATES

To demonstrate how one obtains star formation rates from varying ionizing luminosities, it is convenient to express all relevant variables as power laws. In this tutorial demonstration I have chosen the following power laws...

Initial Mass Function (Salpeter 1955):

$$N(M)dM = KM^{-2.35}dM \qquad (A-1)$$

Ionizing Luminosity (Panagia 1973):

$$N_i\,(M) = 3.8 \times 10^{42}\ M^{3.86} \quad (M > 32\ M_\odot) \qquad (A-2)$$

$$N_i\,(M) = 2.4 \times 10^{35}\ M^{8.67} \quad (9 < M < 32\ M_\odot) \qquad (A-3)$$

Main Sequence Lifetime (Mihalas and Binney 1981):

$$\tau(M) = 10^{10} M^{-2.2} yrs \qquad (A-4)$$

where all masses are in solar units.

From these power laws, one can model the emerging luminosity of ionizing photons as a mass and lifetime-weighted integral of the individual ionizing stars (see also Gallagher *et al.* 1984).

$$N_i(tot) = \dot{N}(> 9M_\odot)\ \frac{\int_9^{M_u} N(M)\ N_i\ (M)\ \tau(M)\ dM}{\int_9^{M_u} N(M)\ dM} \qquad (A-5)$$

Here the stellar birthrate, $\dot{N}\ (> 9M_\odot)$, corresponds to only those stars contributing to the ionization. Solving for this birthrate in terms of the observable N_i, one gets

$$\dot{N}(> 9M_\odot) = N_i\ \frac{\int_9^{M_u} N(M)\ dM}{\int_9^{M_u} N(M)\ N_i\ (M)\ \tau(M)\ dM} \qquad (A-6)$$

Upon plugging in the above power laws and solving the integrals, the birthrate conversion becomes for two choices of the upper mass limit (M_u)

$$\dot{N}\ (> 9M_\odot) = 2.01 \times 10^{-55}\ N_i \quad (M_u = 100\ M_\odot) \qquad (A-7)$$

and

$$\dot{N}\ (> 9M_\odot) = 3.35 \times 10^{-55}\ N_i \quad (M_u = 60\ M_\odot) \qquad (A-8)$$

Extrapolation of this birthrate to include the non-ionizing stars can be formulated as

$$\dot{N}(tot) = \dot{N}(> 9M_\odot)\ \frac{\int_{M_l}^{M_u} N(M)\ dM}{\int_{9}^{M_u} N(M)\ dM} \qquad (A-9)$$

If one chooses a lower mass limit of 0.1 $M_\odot$, the extrapolated conversion becomes

$$\dot{N}(tot) = 9.2 \times 10^{-53}\ N_i \quad (M_u = 100\ M_\odot) \qquad (A-10)$$

and

$$\dot{N}(tot) = 16.0 \times 10^{-52}\ N_i \quad (M_u = 60\ M_\odot). \qquad (A-11)$$

To compute the star formation rate in $M_\odot$/yr, one multiplies the birthrate by the mean mass in the model stellar population, *i.e.* $SFR = \dot{N}(tot)\,\langle M\rangle$, where the mean mass is determined from

$$\langle M\rangle = \frac{\int_{M_l}^{M_u} N(M)\ M\ dM}{\int_{M_l}^{M_u} M\ dM} \qquad (A-12)$$

For the Salpeter IMF with $M_l = 0.1\ M_\odot$ and the two choices of M_u, the mean masses are both very close to 0.35 $M_\odot$, and so the final conversions are

$$SFR\ (M_\odot\ yr^{-1}) = 3.2 \times 10^{-53}\ N_i\ (photons\ s^{-1}) \quad (M_u = 100\ M_\odot) \qquad (A-13)$$

and

$$SFR\ (M_\odot\ yr^{-1}) = 5.5 \times 10^{-53}\ N_i\ (photons\ s^{-1}) \quad (M_u = 60\ M_\odot) \qquad (A-14)$$

Note that the lower M_u produces a somewhat higher conversion. That is because the dependence of ionizing luminosity (N_i) on M is much steeper than the dependence of stellar number (N) on M, leading to the need for disproportionately more ionizing stars with the lower M_u. This enhancement near M_u is then extrapolated to lower masses, leading to a higher overall SFR.

If one repeated the previous work using a two step IMF of the form

$$N(M)dM = KM^{-2.35}dM \quad (M > 1M_\odot) \qquad (A-15)$$

$$N(M)dM = KM^{-1.4}dM \quad (0.1 < M < 1M_\odot), \qquad (A-16)$$

the resulting conversion would be lower by a factor of 1.6, giving

$$SFR\ (M_\odot\ yr^{-1}) = 1.95 \times 10^{-53}\ N_i\ (photons\ s^{-1}) \quad (M_u = 100\ M_\odot) \qquad (A-17)$$

$$SFR\ (M_\odot\ yr^{-1}) = 3.29 \times 10^{-53}\ N_i\ (photons\ s^{-1}) \quad (M_u = 60\ M_\odot) \qquad (A-18)$$

The flattening of the IMF at lower masses leads to lower conversions, because one is always extrapolating *downward* from the well-constrained high-mass SFR to the model-dependent low-mass SFR. A flatter IMF at low masses means that there will be fewer low mass stars per high mass star thus leading to a lower overall SFR.

Kennicutt (1983) found that a two-step IMF of the form

$$N(M)dM = KM^{-2.5}dM \quad (1.0 < M < 100\ M_\odot) \qquad (A-19)$$

$$N(M)dM = KM^{-1.4}dM \quad (0.1 < M < 1.0\ M_\odot) \qquad (A-20)$$

could best reproduce the colors and Hα equivalent widths observed in 170 nearby spiral and irregular galaxies. The conversion that he calculates, using a more sophisticated treatment of the mass and age dependent ionizing luminosities, is again a factor of 1.6 lower —

$$SFR\ (M_\odot\ yr^{-1}) = 1.2 \times 10^{-53}\ N_i\ (photons\ s^{-1}) \quad (M_u = 100\ M_\odot). \qquad (A-21)$$

This conservatively low conversion (compared to the Miller-Scalo equivalent) is adopted throughout the body of the present dissertation. To compare with other IMFs, Kennicutt includes the following table, where the conversions are normalized to the Kennicutt ($M_u = 100$) value.

Table A-1: Star Formation Rate Conversions

IMF	M_u			
	30	60	100	200
Miller-Scalo	8.01	4.05	3.35	2.55
Kennicutt	3.78	1.44	1.0	0.53
Shallow($\alpha = 2$)	1.44	0.43	0.26	0.11

Kennicutt refers to his own IMF as an " extended Miller-Scalo IMF." He also notes that his computed conversions for the Salpeter IMF are virtually identical.

If one is simply interested in the total mass of newborn stars, one can assume that all stars are on the zero-age main sequence (*i.e.* a single coeval burst of star formation), and so formulate

$$M_* = N_*(tot)\,\langle M\rangle \qquad (A-22)$$

where

$$N_*(tot) = \frac{N(tot)}{N(>9M_\odot)}\,N(>9M_\odot) \qquad (A-23)$$

and where

$$N(>9M_\odot) = N_i\,\frac{\int_9^{M_u} N(M)\,dM}{\int_9^{M_u} N(M)\,N_i(M)\,dM} \qquad (A-24)$$

as in the previous treatment, with all the time dependences removed. For a Salpeter IMF, the resulting conversions are

$$M_*(M_\odot) = 1.49\times10^{-46}\,N_i\,(photons\ s^{-1}) \quad (0.1-60\ M_\odot) \qquad (A-25)$$

$$M_*(M_\odot) = 3.81\times10^{-47}\,N_i\,(photons\ s^{-1}) \quad (0.1-100\ M_\odot) \qquad (A-26)$$

These conversions can be regarded as conservative because evolution of the ZAMS population will naturally lead to lower ionizing luminosities.

Increasing the lower mass limit from 0.1 $M_\odot$ to 0.5, 1.0, 5.0, and 10.0 $M_\odot$ has the effect of reducing the mass and SFR conversions by factors of 1.4, 2.0, 4.3, and 7.0 respectively (if the upper mass limit is fixed at 60 $M_\odot$).

Raising M_l has an even greater effect on the conversions which pertain to the mass that is forever locked up in the stars. For lower mass limits of 0.1, 0.5, 1.0, 5.0, and 10.0 $M_\odot$, the mass lockup conversions are reduced by 1.6, 2.3, 4.4, 16.7, and 26.0 respectively (see Sandage 1986).

References

Gallagher, J. S., Hunter, D. A., and Tutukov, A. V. 1984, *Ap. J.*, **284**, 544.

Kennicutt, R. C. 1983, *Ap. J.*, **272**, 54.

Mihalas, D. and Binney, J. 1981, *Galactic Astronomy* (San Francisco: W. H. Freeman and Co.).

Panagia, N. 1973, *A. J.*, **78**, 930.

Salpeter, E. E. 1955, *Ap. J.*, **121**, 161.

Sandage, A. 1986, *Astr. Ap.*, **161**, 89.

APPENDIX B

EMISSION-LINE AND CONTINUUM FLUXES FROM NARROW AND BROAD-BAND IMAGERY

Gaseous emission nebulae (HII regions) and their exciting stars are rich sources of information on photoionization, chemical enrichment, hydrodynamics, and star formation processes. One fruitful way to study HII regions is by imaging them through various optical filters, so that the spectral-line and continuum emissions can be isolated and measured. To do so usually requires an "on-line" image taken through a narrow-band filter (which passes some spectral emission line plus whatever continuum emission that fits within the narrow bandpass) as well as an "off-line" image taken through a filter of similar bandwidth but displaced in wavelength so as not to pass the spectral-line emission. By carefully scaling and digitally subtracting the "off-line" image from the "on-line" image, one can produce a spectral-line image that is free of any contamination by the continuum (see the excellent review by Jacoby *et al.* [1987]). This image, in turn, can be compared with the "off-line" continuum image for purposes of computing line-to-continuum ratios (*i.e.* equivalent widths) and so gauging the excitation of the nebula by the underlying stars.

Often, however, the continuum emission from HII regions and their underlying star clusters is considerably weaker than the spectral-line emission, thus requiring frustratingly long exposure times at the telescope in order to obtain decent signal-to-noise ratios. One way around this dilemma is to replace the narrow-band "off-line" filter by a broad-band filter that passes lots of continuum emission plus (alas) any spectral-line emission falling within the broad bandpass. If one spectral emission line dominates the bandpass, however, it is still possible to isolate the line and continuum components. In the following sections, this capability is developed theoretically and then demonstrated using the Orion nebula as an example.

B.1 *Theoretical Basis*

The effect of filtering and detecting the light from a cosmic source is to introduce a wavelength dependent detector efficiency η_λ which can be regarded as the product of the filter transmissivity T_λ times the unfiltered instrumental response ρ_λ, *i.e.*

$$\eta_\lambda = T_\lambda \, \rho_\lambda. \qquad (B-1)$$

The detector efficiency produces a weighting of the line and continuum emission which can be formally expressed as an integral over the bandpass.

$$R_\circ = \int_{\Delta\lambda} \eta_\lambda(line) f_\lambda(line) d\lambda + \int_{\Delta\lambda} \eta_\lambda(cont) f_\lambda(cont) d\lambda. \qquad (B-2)$$

where $R_\circ$ denotes the measured count rate in units of ADU s^{-1} (after correction for atmospheric absorption) and f_λ is the line or continuum flux density. By assuming that both the detector efficiency and continuum flux density are constant over the bandpass, one can approximate the formal integrals as simple products involving constant detector efficiencies and effective bandwidths.

For the sake of illustration, consider the effect of filtering the light through wide (W) and narrow (N) bandpasses, both of which are centered on an emission line. The detected count rates through the two filters are

$$R_\circ(W) = \eta(W) \, [f(line) + bw(W) \, f_\lambda(cont)] \qquad (B-3)$$

and

$$R_\circ(N) = \eta(N) \, [f(line) + bw(N) f_\lambda(cont)] \qquad (B-4)$$

where bw(W) and bw(N) are the FWHM bandwidths of the two filters, $\eta(W)$ and $\eta(N)$ are the detection efficiencies through the two different filters in units of ADU s^{-1} $/erg\ cm^{-2}\ s^{-1}$ and where it is assumed that the spectrum of the source has negligible slope across the wide band

$$\frac{\Delta f_\lambda(cont)}{< f_\lambda(cont) >} \ll 1. \qquad (B-5)$$

Using a standard star, or region in the target field containing no Hα emission, one can *scale* the broad-band image to the narrow-band image by equalizing the counts, such that

$$R_\circ(N) - c \, R_\circ(W) = 0 \qquad (B-6)$$

or equivalently

$$[\eta(N)\ bw(N)\ -\ c\ \eta(W)\ bw(W)]\ \ f_\lambda(cont)\ =\ 0 \qquad (B-7)$$

Therefore, the scaling factor, c, can be formulated as

$$c\ =\ \frac{\eta(N)\ bw(N)}{\eta(W)\ bw(W)}. \qquad (B-8)$$

In principle, the scale factor should be determinable from a priori knowledge of the chip's wavelength-dependent quantum efficiencies, the filter transmissivities, and filter bandwidths. However, it is most often determined by equalizing the observed count rates from a region containing only continuum emission, *e.g.* from an isolated star.

For a line-emitting HII region, the scaling and image subtraction will yield positive definite results. From equations B-3 and B-4,

$$\begin{aligned} R_\circ(N)\ -\ c\ R_\circ(W) = \ & \eta(N)\ f(line)\ +\ \dots \\ & \eta(N)\ bw(N)\ f_\lambda(cont)\ -\ \dots \\ & c\ \eta(W)\ f(line)\ -\ \dots \\ & c\ \eta(W)\ bw(W)\ f_\lambda(cont) \end{aligned} \qquad (B-9)$$

which can be simplified to

$$R_\circ(N)\ -\ c\ R_\circ(W)\ =\ f(line)\,[\eta(N)\ -\ c\ \eta(W)\,]. \qquad (B-10)$$

Solving for the line flux gives

$$f(line)\ =\ \frac{[R_\circ(N) - c\ R_\circ(W)]}{[\eta(N) - c\ \eta(W)]} \qquad (B-11)$$

or

$$f(line)\ =\ \frac{[R_\circ(N) - c\ R_\circ(W)]}{\eta(N)[1 - bw(N)/\ bw(W)]} \qquad (B-12)$$

where $\eta(N)$ and $\eta(W)$ are determined by observing a calibration star. If the N filter is much narrower than the W filter, the above formulation reduces to the more intuitive

$$f(line)\ \approx\ \frac{[R_\circ(N)\ -\ c\ R_\circ(W)]}{\eta(N)}. \qquad (B-13)$$

The emission-line equivalent width is defined as the ratio of the line flux by the continuum flux density at the line's central wavelength, or

$$EW(line) = f(line)/\ f_\lambda(cont), \tag{B-14}$$

and is expressed in units of Angstroms. Having just derived the means of obtaining the emission-line flux $f(line)$, we now need to obtain the continuum flux $f_\lambda(cont)$ from the line-contaminated R-band image. Again from equations B-3 and B-4, we get

$$\frac{R_\circ(W)}{\eta(W)} - \frac{R_\circ(N)}{\eta(N)} = f_\lambda(cont)[bw(W) - bw(N)] \tag{B-15}$$

so that the continuum flux is

$$f_\lambda(cont) = \frac{R_\circ(W)\ \eta(N) - R_\circ(N)\ \eta(W)}{\eta(W)\ \eta(N)[bw(W) - bw(N)]} \tag{B-16}$$

which upon rearrangement of terms becomes

$$f_\lambda(cont) = \frac{[R_\circ(W)\ \eta(N)/\ \eta(W)] - R_\circ(N)}{\eta(N)\ bw(W)[1 - bw(N)/\ bw(W)]}. \tag{B-17}$$

The line to continuum ratio is then

$$\frac{f(line)}{f_\lambda(cont)} = \frac{[R_\circ(N) - c\ R_\circ(W)]\ [\eta(N)\ bw(W)]}{[\eta(N)][R_\circ(W)\ \eta(N)/\ \eta(W) - R_\circ(N)]} \tag{B-18}$$

or more simply

$$EW(line) = \frac{[R_\circ(N) - c\ R_\circ(W)]\ bw(N)}{c\ [R_\circ(W) - R_\circ(N)\ \eta(W)/\ \eta(N)]}. \tag{B-19}$$

This can be re-expressed in terms of the relative bandwidths as

$$EW(line) = \frac{[R_\circ(N) - c\ R_\circ(W)]\ bw(N)}{[c\ R_\circ(W) - R_\circ(N)\ bw(N)/\ bw(W)]}. \tag{B-20}$$

Note that if the wide-band image is replaced by an "off-line" continuum-band image, then the equivalent width reduces to

$$EW(line) = \frac{[R_\circ(N) - c\ R_\circ(cont)]\ bw(N)}{[c\ R_\circ(cont)]}, \tag{B-21}$$

as anticipated.

B.2 *Practical Application: The Orion Nebula*

To test whether the formulations derived in the previous section actually succeed at separating the line and continuum components, I have applied equations B-13 and B-17 to Hα and R-band images of the Orion nebula. This object provides an especially good test of the technique, because its R-band emission is strongly contaminated by the Hα line. The CCD images were taken October 23, 1986 using the 0.9 m telescope at Kitt Peak.[1] At $f/7.5$, the 0.9 m telescope and RCA-3 CCD detector combination produce a pixel size of 0.86" and a total field of view of $7.3' \times 4.5'$.

Figure B–1(**a**) shows the Orion nebula imaged for 2 seconds through a narrow-band Hα filter (λ = 6563 Å, $\Delta\lambda$ = 38 Å). The CCD image is dominated by the nebula's Hα spectral-line emission, but also includes continuum emission from the underlying stars and from the nebulosity itself. Figure B–1(**b**) shows the nebula and stars imaged for 1 second through a broad-band Mould R filter (λ = 6500 Å, $\Delta\lambda$ = 1283 Å). The image contains strong contributions from both the stellar continuum and nebular line emission. The brightest stars have saturated the CCD chip resulting in anomolously low counts and spurious "rays" emanating from these sites.

By scaling and subtracting the R-band image [B-1(**b**)] from the Hα image [B-1(**a**)] according to equation B-13, I obtain an emission-line image that is almost completely free of contamination by the red continuum. This is shown in Figure B–2(**a**). The elimination of continuum light can be gauged by noting the disappearance of the unsaturated stars above the horizontal black line (a bad pixel column) and in the lower left-hand corner. The bright stars in the central "trapezium" cluster and just below the straight ionization front were saturated in the R-band image, however, thus leading to their incomplete subtraction.

---

[1] Kitt Peak National Observatory is operated by the Association of Universities for Research in Astronomy, Inc., under contract with the National Science Foundation.

By scaling and subtracting the Hα-band image [B-1(**a**)] from the R-band image [B-1(**b**)] according to equation B-17, re-expressed as

$$f_\lambda(6563) \approx \frac{c\, R_\circ(R) - R_\circ(H\alpha)[bw(H\alpha)/\, bw(R)]}{bw(H\alpha)\; \eta(H\alpha)}, \qquad (B-22)$$

I get a continuum-band image that is virtually free of contamination by the Hα line. This is shown in figure B–2(**b**) and should be compared with the original R-band image, Figure B–1(**b**). The meager nebulosity that remains (seen here in high contrast) is 8.7 times weaker than the nebulosity in the original R-band image and roughly 5500 times weaker per unit wavelength than the corresponding Hα emission (after correcting the Hα image for 10 percent contamination by [NII] within the 38 Å bandpass). In other words, the nebular component of the Hα equivalent width is $EW_{neb}(H\alpha) \approx 5500$ Å. This estimation of the nebular equivalent width is consistent with expectations based on considerations of recombination-line, free-free continuum and 2-photon continuum emission from a gas at $T_e \approx 7500K$ (*cf.* Osterbrock 1974; A. Campbell, private communication).

References

Jacoby, G. H., Quigley, R. J., and Africano, J. L. 1987, *Pub. A. S. P.*, **99**, 672.

Osterbrock, D. E. 1974, *Astrophysics of Gaseous Nebulae*, (San Francisco: Freeman), pp. 59-77.

Figures

Figure B–1

Hα and R-band CCD images of the Orion nebula. The field of view is approximately $7.3' \times 4.5'$.

a. Orion nebula and ionizing star cluster through Hα filter (λ = 6563 Å, $\Delta\lambda$ = 38 Å). The CCD image is dominated by the nebula's Hα spectral-line emission, but also includes continuum emission from the underlying stars and from the nebulosity itself.

b. Orion nebula and cluster through broad R-band filter (λ = 6500 Å, $\Delta\lambda$ = 1283 Å). The image contains strong contributions from both the stellar continuum and nebular line emission. The brightest stars have saturated the CCD chip resulting in anomolously low counts and spurious "rays" emanating from these sites.

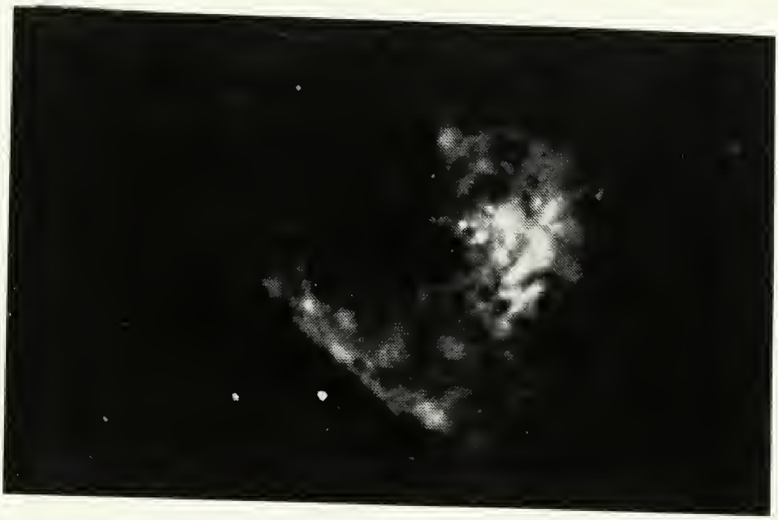

a ▲ b ▼

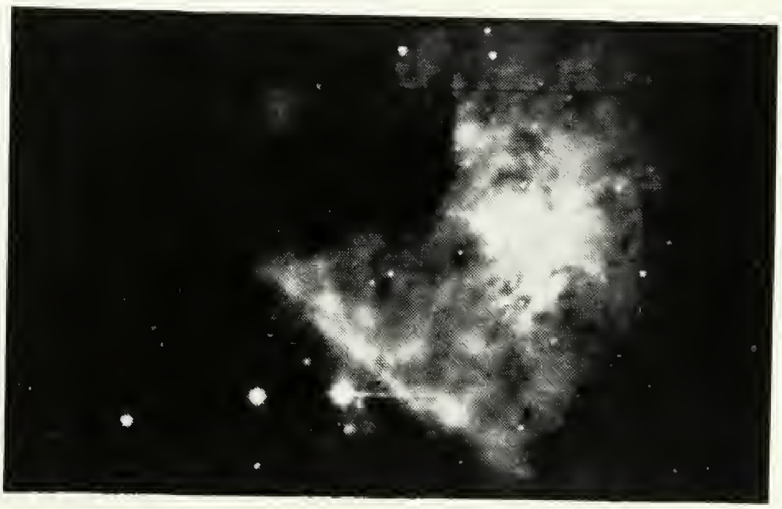

Figure B–2

Decontaminated emission-line and continuum images of the Orion nebula.

a. Orion nebula in the light of Hα (except for those sites where the R-band image was saturated). This image was made by appropriately scaling and subtracting the R-band image from the Hα-band image. Note the disappearance of the unsaturated stars above the horizontal black line and in the lower left-hand corner.

b. Orion cluster and nebulosity in the red continuum. This image was made by appropriately scaling and subtracting the Hα-band image from the R-band image. Note that most of the nebular emission seen in the R-band image is now gone. The remaining nebulosity is seen here in high contrast. Free-free emission and scattering by dust are the most likely radiation processes that are contributing to the nebular continuum.

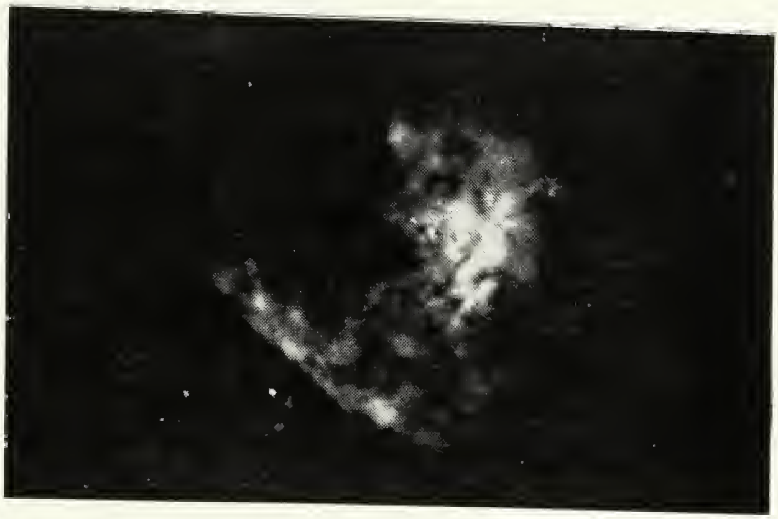

a ▲ b ▼

BIBLIOGRAPHY

Ables, H. D. 1971, *Publ. U. S. Naval Obs. Sec. Ser XX (IV)*, 61.

Allen, C. W. 1973, *Astrophysical Quantities*, (London, The Athlone Press).

Allen, R. J., van der Hulst, J. M., Goss, W. M., and Huchtmeier. W. 1978, *Astr. Ap.*, **64**, 359.

Allen, R. J. and Goss, W. M. 1979, *Astr. Ap. Suppl.*, **36**, 135.

Aller, L. H. and Liller, W. 1959, *Ap. J.*, **130**, 45.

Arp, H. C. and Sandage, A. R. 1985, *A. J.*, **90**, 1163.

Baron, E. and White, S. D. M. 1987, *Ap. J.*, **322**, 585.

Beck, S. C., Lacy, J. H., Baas, F., and Townes, C. H. 1978, *Ap. J.*, **226**, 545.

Beck, S. C. and Beckwith, S. V. 1984, *M. N. R. A. S.*, **207**, 671.

Beichman, C. A. 1987, *Ann. Rev. Astr. Ap.*, **25**, 521.

Bettoni, D. and Galleta, G. 1982, *Astr. Ap.*, **113**, 344.

Binney, J. and Tremaine, S. 1987, *Galactic Dynamics* (New Jersey: Princeton University Press).

Bland, J. and Tully, R. B. 1988, *Nature*, **334**, 43.

Blitz, L., Israel, F. P., Neugebauer, G., Gatley, I., Lee, T. J., and Beattie, D. H. 1981, *Ap. J.*, **249**, 76.

Blitz, L. and Glassgold, A. E. 1982, *Ap. J.*, **252**, 481.

Bloeman, J. B. G. M., Strong, A. W., Blitz, L., Cohen, R. S., Dame, T., Grabelsky, D. A., Hermen, W., Lebrun, F., Mayer-Hasselwander, H. A., and Thaddeus, P. 1986, *Astr. Ap.*, **154**, 25.

Bosma, A., Goss, W. M., and Allen, R. J. 1981, *Astr. Ap.*, **93**, 106.

Bothun, G. D., Impey, C. D., Malin, D. F., and Mould, J. R. 1987, *A. J.*, **94**, 23.

Bowers, R. L. and Deeming, T. 1984, in *Astrophysics II [Interstellar Matter and Galaxies]* (Boston: Jones and Bartlett).

Burnham, R. 1978, *Burnham's Celestial Handbook*, **Vol. 3**, (New York: Dover).

Bushouse, H. 1985, *NOAO Newsletter, No. 4*, p. 14.

Bushouse, H. A. 1986, *A. J.*, **91**, 255.

Campbell, A., Terlevich, R., and Melnick, J. 1987, *M. N. R. A. S.*, **223**, 811.

Campbell, A. 1988, *Ap. J.*, **335**, 644.

Carlstrom, J. E. 1988, in *Galactic and Extragalactic Star Formation*, eds. R. E. Pudritz and M. Fich (Dordrecht: Kluwer Academic Publ.).

Caux, E., Puget, J. L., Serra, G., Gispert, R., and Ryter , C. 1984, *Astr. Ap.*, **144**, 37.

Chevalier, R. A. and Clegg, A. W. 1985, *Nature*, **317**, 44.

Cohen, R. S., Dame, T. M., Garay, G., Montani, J., Rubio, M., and Thaddeus, P. 1988, *Ap. J. (Letters)*, **331**, L95.

Combes, F. 1988, in *Galactic and Extragalactic Star Formation*, eds. R. E. Pudritz and M. Fich (Dordrecht: Kluwer Academic Publ.).

Comte, G., Monnet, G., and Rosado, M. 1979, *Astr. Ap.*, **72**, 73.

Condon, J. J. 1983, *Ap. J. Suppl.*, **53**, 459.

Condon, J. J., Condon, M. A., Gisler, G., Puschell, J. J. 1982, *Ap. J.*, **252**, 102.

Cook, K., Aaronson, M., and Illingworth, G. 1986, *Ap. J. (Letters)*, **301**, L45.

Crawford, M. K., Genzel, R., Townes, C. H., and Watson, D. M. 1985, *Ap. J.*, **291**, 755.

Davidson, K., Humphreys, R. M., and Blaha, C. 1985, *A. J.*, **90**, 192.

DeGioia-Eastwood, K., Grasdalen, G. L., Strom, S. E., and Strom, K. M. 1985, *Ap. J.*, **278**, 564.

Dennefeld, M. and Stasinska, G. 1983, *Astr. Ap.*, **118**, 234.

Dennefeld, M. 1986, *Astr. Ap.*, **157**, 267.

Devereux, N. 1987, *Ap. J.*, **323**, 91.

de Vaucouleurs, G., de Vaucouleurs, A., and Pence, W. 1974, *Ap. J. (Letters)*, **194**, L119.

de Vaucouleurs, G., de Vaucouleurs, A., and Corwin, H. 1976, *Second Reference Catalogue of Bright Galaxies*, (Austin: The University of Texas Press).

de Vaucouleurs, G. 1978, *Ap. J.*, **224**, 710.

de Vaucouleurs, G. 1979, *Astr. Ap.*, **79**, 274.

de Vaucouleurs, G. 1981, *Sky & Telescope*, **62**, 406.

Diaz, A. I., Pagel, B. E. J., and Terlevich, E. 1985, *M. N. R. A. S.*, **214**, 41.

Djorgovski, S. 1985, *Pub. A. S. P.*, **97**, 1119.

Djorgovski, S., Strauss, M. A., Perley, R. A., Spinrad, H., and McCarthy, P. 1987, *A. J.*, **93**, 1318.

Donas, J. and Deharveng, J. M. 1984, *Astr. Ap.*, **140**, 325.

Dopita, M. A. 1985, *Ap. J. (Letters)*, **295**, L5.

Duffy, P. B., Erickson, E. F., and Haas, M. R. 1987, *Ap. J.*, **315**, 68.

Elmegreen, B. G. 1979, *Ap. J.*, **231**, 372.

Elmegreen, D. M., and Elmegreen, B. G. 1984, *Ap. J. Suppl.*, **54**, 127.

Evans, I. N. 1986, *Ap. J.*, **309**, 544.

Fabbiano, G., Feigelson, E., and Zamorani, G. 1982, *Ap. J.*, **256**, 397.

Fabbiano, G. and Trinchieri, G. 1984, *Ap. J.*, **286**, 491.

Ferris, T. 1980, *Galaxies* (San Francisco: Sierra Club Books).

Fierro, J., Torres-Peimbert, S., and Peimbert, M. 1986, *Pub. A. S. P.*, **98**, 1032.

Foukal, P. 1972, *Ap. J.*, **172**, 591.

Foukal, P. 1973, *Pub. A. S. P.*, **86**, 211.

Gallagher, J. S., Hunter, D. A., and Tutukov, A. V. 1984, *Ap. J.*, **284**, 544.

Gehrz, R. D., Sramek, R. A., and Weedman, D. W. 1983, *Ap. J.*, **267** , 551.

Gerin, M., Nakai, N. and Combes, F. 1988, *Astr. Ap.*, submitted.

Gunn, E., Struper, L. L., and Tinsley, B. M. 1981, *Ap. J.*, **249**, 48.

Gusten, R. and Mezger, P. G. 1982, in *Vistas in Astronomy*, **26**, 159.

Hawarden, T. G., Mountain, C. M., Lessett, S. K., and Poxley, P. J. 1986, *M. N. R. A. S.*, **221**, 41P.

Heyer, M. H., Vrba, F. J., Snell, R. L., Schloerb, F. P., Strom, S. E., Goldsmith, P. F., and Strom, K. M. 1987, *Ap. J.*, **321**, 855.

Hill, J. K., Bohlin, R. C., and Stecher, T. P. 1984, *Ap. J.*, **277**, 542.

Hodge, P. W. 1969, *Ap. J. Suppl.*, **18**, 73.

Hodge, P. W. 1974, *Ap. J. (Letters)*, **191**, L21.

Hodge, P. W. 1983, *Ap. J.*, **264**, 470.

Hodge, P. W. 1987a, *Pub. A. S. P.*, **99**, 724.

Hodge, P. W. 1987b, *Pub. A. S. P.*, **99**, 915.

Hodge, P. W. and Kennicutt, R. C. 1983, *Ap. J.*, **267**, 563.

Hodge, P. W. and Kennicutt, R. C. 1983, *A. J.*, **88**, 296.

Hodge, P. W. and Kennicutt, R. C. 1988, unpublished.

Hoskins, M. A. 1963, *William Herschel and the Construction of the Heavens*, (London: Oldbourne Book Co.).

Houck, J. R., Shure, M. A., Gull, G. E., and Herter, T. 1984 , *Ap. J. (Letters)*, **287**, L204.

Humphreys, R. M. and Aaronson, M. 1987, *Ap. J. (Letters)*, **318**, L69.

Hunter, D. A., Gallagher, J. S., and Rautenkranz, D. 1982, *Ap. J. Suppl.*, **49**, 53.

Israel, F. 1988, *Astr. Ap.*, **194**, 24.

Israel, F. and de Bruyn, A. G. 1988, *Astr. Ap.*, **198**, 109.

Israel, F. and Kennicutt, R. C. 1980, *Ap. Letters*, **21**, 1.

Jacoby, G. H., Hunter, D. A., and Christian, C. A. 1984, *Ap. J. Suppl.*, **56**, 257.

Jeans, Sir J. H. 1928, *Astronomy and Cosmogony* (Cambridge: Cambridge University Press).

Jensen, E. B., Strom, K. M., and Strom, S. E. 1976, *Ap. J.*, **209**, 748.

Jensen, E. B., Talbot, R. J., and Dufour, R. J. 1981, *Ap. J.*, **243**, 716.

Johnson, H. L. 1965, *Ap. J.*, **141**, 170.

Johnson, H. L. 1966, *Ann. Rev. Astr. Ap.*, **4**, 193.

Joy, M., Lester, D. F., and Harvey, P. M. 1987, *Ap. J.*, **319**, 314.

Kahn, F. D. 1974, *Astr. Ap.*, **37**, 149.

Kaufman, M., Bash, F. N., Kennicutt, R. C., and Hodge, P. W. 1987, *Ap. J.*, **319**, 61.

Keel, W. C. 1984, *Ap. J.*, **282**, 75.

Keel, W. C., Kennicutt, R. C., Hummel, E., and van der Hulst, J. M. 1985, *A. J.*, **90**, 708.

Kennicutt, R. C. 1983, *Ap. J.*, **272**, 54.

——. 1984, *Ap. J.*, **287**, 116.

——. 1989, *Ap. J.*, in press.

Kennicutt, R. C. and Hodge, P. W. 1980, *Ap. J.*, **241**, 573.

Kennicutt, R. C. and Kent, S. M. 1983, *A. J.*, **88**, 1094.

Kennicutt, R. C., Keel, W. C., van der Hulst, J. M., Hummel, E., and Roettiger, K. A. 1987, *A. J.*, **93**, 1011.

Kennicutt, R. C., and Chu, Y. 1988, *A. J.*, **95**, 720.

Kennicutt, R. C., Keel, W. C., and Blaha, C. A. 1989, *A. J.*, **97**, 1022.

Kennicutt, R. C. and Pogge, R. W. 1989, *A. J.*, in press.

Klein, U., Wielebinski, R., and Morsi, H. W. 1988, *Astr. Ap.*, **190**, 41.

Knapp, G. R. 1987, *Pub. A. S. P.*, **99**, 1134.

Kronberg, P. P., Biermann, P., and Schwab, F. R. 1985, *Ap. J.*, **291**, 693.

Kulkarni, S. R. and Heiles, C. 1988, in *Galactic and Extragalactic Radio Astronomy* (2nd edition) eds. G. L. Verschuur and K. I. Kellermann (New York: Spinger-Verlag), p. 95.

Kurusz, R. L. 1979, *Ap. J. Suppl.*, **40**, 1.

Larson, R. B. 1982, *Mon. Not. R. astr. Soc.*, **200**, 159.

——. 1985, *M. N. R. A. S.*, **214**, 379.

——. 1986, *M. N. R. A. S.*, **218**, 409.

——. 1987a, in *Starbursts and Galaxy Evolution*, ed. J. Montmerle and J. T. T. Van (Yvette, France: Editions Frontieres).

——. 1987b, in *Globular Cluster Systems in Galaxies*, IAU Symp. No. 126, ed. A. G. D. Philip and J. E. Grindlay (Dordrecht: D. Reidel).

——. 1987c, *American Scientist*, **75**, 376.

——. 1988, in *Galactic and Extragalactic Star Formation*, ed. R. E. Pudritz and M. Fich (Dordrecht: D. Reidel).

Larson, R. B. and Tinsley, B. M. 1978, *Ap. J.*, **219**, 46.

Lequeux, J. 1980, in *Star Formation* (Sauverny: Geneva Observatory).

Lo, K. Y., Cheung, K. W., Masson, C. R., Phillips, T. G. , Scott, S. L., and Woody, D. P. 1987, *Ap. J.*, **312**, 574.

Lord, S. D. 1987, Ph. D. Thesis, University of Massachusetts.

Lucretius 55 BC, *De Rerum Natura*, trans. Cyril Bailey 1972 (Oxford: Clarendon Press).

Luppino, G. A., Ceglio, N. M., Doty, J. P., Ricker, G. R., and Vallerga, J. V. 1987, *Opt. Eng.*, **26**, 1048.

Lynds, B. T. 1980, *Ap. J.*, **238**, 17.

Lynds, C. R. and Sandage, A. R. 1963, *Ap. J.*, **137**, 1005.

Maeder, A. and Meynet, G. 1988, *Astr. Ap. Suppl.*, **76**, 411.

Maloney, P. and Black, J. H. 1988, *Ap. J.*, **325**, 389.

Mathis, J. S. 1983, *Ap. J.*, **267**, 119.

McCall, M. L., Rybski, P. M., and Shields, G. A. 1985, *Ap. J. Suppl.*, **57**, 1.

McCarthy, P. J., Heckman, T., and van Breugel, W. 1987, *A. J.*, **92**, 264.

McCarthy, P., Spinrad, H., Djorgovski, S., Strauss, M., van Breugel, W., and Liebert, J. 1987, *Ap. J.(Letters)*, **319**, L39.

McGregor, P. J., Persson, S. E., and Cohen, J. G. 1984, *Ap. J.*, **286**, 609.

Meaburn, J., Terett, D. L., Theokas, A., and Walsh, J. R. 1981, *M. N. R. A. S.*, **195**, 39.

Melnick, J. 1986, *Astr. Ap.*, **153**, 235.

Meyer, S. S. and Ricker, G. R. 1980, *Applications of Digital Imaging to Astronomy*, SPIE Proceedings No. 264 (Bellingham, WA: SPIE).

Mihalas, D. and Binney, J. 1981, *Galactic Astronomy* (San Francisco: W. H. Freeman and Co.).

Miller, G. E. and Scalo, J. M. 1979, *Ap. J. Suppl.*, **41**, 513.

Nakai, N., Hayashi, M., Handa, T., Sofue, Y., Hasagawa, T., and Sasaki, M. 1987, *Publ. Astr. Soc. Japan*, **39**, 685.

Narlikar, J. V. 1983, *Cosmology* (Boston: Jones and Bartlett).

Norman, C. A. 1987 in *Star Formation in Galaxies* (NASA Conf. Publ. 2466) ed. C. J. Lonsdale Persson (Wash., D. C.: U. S. Govt. Print. Off.).

O'Connell, R. W. and Mangano, J. J. 1978, *Ap. J.*, **221**, 62.

O'Connell, R. W. 1986, *Pub. A. S. P.*, **98**, 163.

Oke, J. B. and Gunn, J. E. 1983, *Ap. J.*, **266**, 713.

Olafsson, H. and Rydbeck, G. 1984, *Astr. Ap.*, **136**, 17.

Osterbrock, D. E. 1974, *Astrophysics of Gaseous Nebulae* (San Francisco: Freeman).

Pagel, B. E. J. 1986, *Highlights of Astronomy* General Assembly of the IAU, **7**, 551.

Panagia, N. 1973, *A. J.*, **78**, 930.

Persson, C. J. L. and Helou, G. 1987, *Ap. J.*, **314**, 513.

Pence, W. D. 1980, *Ap. J.*, **239**, 54.

Pence, W. D. 1981, *Ap. J.*, **247**, 473.

Rayo, J. F., Peimbert, M., and Torres-Peimbert, S. 1982, *Ap. J.*, **255**, 1.

Reakes, M. 1980, *M. N. R. A. S.*, **192**, 297.

Reddish, V. C. 1978, *Stellar Formation* (New York: Pergamon).

Rengarajan, T. N. 1984, *Ap. J.*, **287**, 671.

Rengarajan, T. N. and Verma, R. P. 1986, *Astr. Ap.*, **165**, 300.

Renzini, A., and Buzzoni, A. 1986, in *Spectral Evolution of Galaxies*, ed. C. Chiosi and A. Renzini, (Dordrecht: D. Reidel), p. 195.

Rice, W., Lonsdale, C. J., Soifer, B. T., Neugebauer, G. , Koplan, E. L., Lloyd, L. A., de Jong, T., and Habing, H. J. 1988, *Ap. J. Suppl.*, **68**, 91.

Rickard, L. J., Palmer, P., Turner, B. E., Morris, M., and Zuckerman, B. 1977, *Ap. J.*, **214**, 390.

Rieke, G. H. and Low, F. J. 1975, *Ap. J.*, **197**, 17.

Rieke, H., Lebofsky, M. J., Thompson, R. I., Low, F. J., and Tokunaga, A. T. 1980, *Ap.J.*, **238**, 24.

Rieke, G. H. and Lebofsky, M. J. 1985, *Ap. J.*, **288**, 618.

Rieke, G. H., Lebofsky, M. J., and Walker, C. E. 1988, *Ap. J.*, **325**, 679.

Rumstay, K. S. and Kaufman, M. 1983, *Ap. J.*, **274**, 611.

Salpeter, E. E. 1955, *Ap. J.*, **121**, 161.

Sandage, A. 1961, *The Hubble Atlas of Galaxies* (Wash., D. C.: Carnegie Inst. of Wash.).

Sandage, A. 1986, *Astr. Ap.*, **161**, 89.

Sandage, A. and Bedke, J. 1988, *Atlas of Galaxies*, (Wash., D. C.: NASA).

Sandage, A. and Tammann, G. 1974, *Ap. J.*, **172**, 593.

Sandage, A. R. and Tammann, G. A. 1981, *A Revised Shapley-Ames Catalog of Bright Galaxies* (Washington, D. C.: Carnegie Institution).

Sanders, D. B., Solomon, P. M., and Scoville, N. Z. 1984, *Ap. J.*, **276**, 182.

Sanders, D. B., Young, J. S., Scoville, N. Z., Soifer, B. T., and Danielson, G. E. 1987, *Ap. J. (Letters)*, **312**, L5.

Sanders, D. B., Soifer, B. T., Elias, J. H., Madore, B. F., Matthews, K., Neugebauer, G., and Scoville, N. Z. 1988, *Ap. J.*, **325**, 74.

Scalo, J. M. 1986, *Fundam. Cosmic Phys.*, **11**, 1.

Scalo, J. M. 1987, in *Starbursts and Galaxy Evolution*, eds. T. X. Thuan, T. Montmerle, and J. T. T. Van (Gif Sur Yvette: Editions Frontieres), p. 445.

Scalo, J. M. and Struck-Marcell, C. 1986, *Ap. J.*, **301**, 77.

Schmidt, G. D., Angel, J. R. P., and Cromwell, R. H. 1976, *Ap. J.*, **208**, 888.

Schmidt, M. 1959, *Ap. J.* , **129**, 243.

Schwarzschild, B. 1987, *Physics Today*, **40**, No. 11 (November), 17.

Schweizer, F. 1976, *Ap. J. Suppl.*, **31**, 313.

Scoville, N. Z., Soifer, B. T., Neugebauer, G., Young, J. S., Matthews, K., and Yerka, J. 1985, *Ap. J.*, **289**, 129.

Scoville, N. Z., Yun, M. J., Clemens, D. P., Sanders, D. B., and Waller, W. H. 1987, *Ap. J. Suppl.*, **63**, 821.

Scoville, N. Z., and Clemens, D. P. 1986, *Ap. J. (Letters)*, **310**, L77.

Searle, L. 1971, *Ap. J.*, **168**, 327.

Searle, L., Sargent, W. L. W., and Bagnuolo, W. G. 1973, *Ap. J.*, **179**, 427.

Sekiguchi, K. and Anderson, K. S. 1987, *A. J.*, **94**, 644.

Seaquist, E. R. and Bignell, R. C. 1976, *Astr. Ap.*, **48**, 421.

Shields, G. A. and Tinsley, B. M. 1976, *Ap. J.*, **203**, 66.

Shields, G. A. and Searle, L. 1978, *Ap. J.*, **222**, 821.

Silk, J. 1986, in *Luminous Stars and Associations in Galaxies*, IAU Symp. 116, ed. C. W. H. DeLoore, A. J. Willis, and P. Laskarides (Dordrecht: D. Reidel).

Simon, M., Simon, T., and Joyce, R. R. 1979, *Ap. J.*, **227**, 64.

Smith, H. E. 1975, *Ap. J.*, **199**, 591.

Smith, L. F., Biermann, P., and Mezger, P. G. 1978, *Astr. Ap.*, **66**, 65.

Smith, T. R. and Kennicutt, R. C. 1989, *Pub. A. S. P.*, **101**, 649.

Sofue, Y., Handa, T., Hayashi, M., and Nakai, N. 1987, in *Star Formation in Galaxies* (NASA Conf. Publ. 2466), ed. C. Persson (Wash., D. C.: NASA).

Sofue, Y. 1988, in *Galactic and Extragalactic Star Formation*, eds. R. Pudritz and M. Fich (Dordrecht: Kluwer Academic Publ.).

Soifer, B. T., Houck, J. R., and Neugebauer, G. 1987, *Ann. Rev. Astr. Ap.*, **25**, 187.

Solomon, P. M., Barrett, J., Sanders, D. B., and de Zafra, R. 1983, *Ap. J. (Letters)*, **266**, L103.

Spitzer, L. 1978, *Physical Processes in the Interstellar Medium* (New York: John Wiley and Sons).

Stark, A. A. and Blitz, L. 1978, *Ap. J. (Letters)*, **225**, L15.

Stark, A. A. and Wolff, R. S. 1979, *Ap. J.*, **229**, 118.

Stark, A. A. and Carlson, E. R. 1984, *Ap. J.*, **279**, 122.

Stasinska, G. 1980, *Astr. Ap.*, **84**, 320.

Stone, R. P. S. 1977, *Ap. J.*, **218**, 767.

Sutton, E. C., Masson, C. R., and Phillips, T. G. 1983, *Ap. J. (Letters)*, **275**, L49.

Talbot, R. J. 1980, *Ap. J.*, **235**, 821.

Tammann, G. A. and Sandage, A. R. 1968, *Ap. J.*, **151**, 825.

Telesco, C. M. 1988, *Ann. Rev. Astr. Ap.*, **26**, 343.

Telesco, C. M. and Harper, D. A. 1980, *Ap. J.*, **235**, 392.

Telesco, C. M. and Gatley, I. 1981, *Ap. J. (Letters)*, **247**, L11.

Tenorio-Tagle, G. 1982, in *Regions of Recent Star Formation* (Dordrecht: D. Reidel).

Terlevich, R. and Melnick, J. 1981, *M. N. R. A. S.*, **195**, 839.

Terlevich, R. and Melnick, J. 1985, *M. N. R. A. S.*, **213**, 841.

Thronson, H. A., Walker, C. K., and Maloney, P. 1987, *Ap. J.*, **321**, 855.

Toomre, A. and Toomre, J. 1966, *Ap. J.*, **146**, 810.

Toomre, A. 1977, in *Evolution of the Galaxies and Stellar Populations*, ed. B. M. Tinsley and R. B. Larson (Yale: University Obs.).

Torres-Peimbert, S., Peimbert, M., and Fierro, J. 1989, *Ap. J.*, in press.

Tully, R. B. and Fisher, J. R. 1987, *Nearby Galaxies Atlas* (Cambridge: Cambridge University Press).

Turner, J. L. and Ho, P. T. P. 1983, *Ap. J. (Letters)*, **268**, L79.

Tyson, A. 1987, in *Nearly Normal Galaxies from the Planck Time to the Present*, ed. S. M. Faber (Springer).

Ulrich, M. H. 1978, *Ap. J.*, **219**, 424.

Van Buren, D. 1985, *Ap. J.*, **294**, 567.

van den Bergh, S. 1976, *Ap. J.*, **206**, 883.

Viallefond, F., Goss, W. M., and Allen, R. J. 1982, *Astr. Ap.*, **115**, 373.

Viallefond, F. 1985, in *Star Forming Dwarf Galaxies*, ed. D. Kunth, T. X. Thuan, and J. Tran Thanh Van (Yvette, France: Editions Frontieres).

Vilchez, J. M. and Pagel, B. E. J. 1988, *M. N. R. A. S.*, **231**, 257.

Visvanathan, N. and Sandage, A. R. 1972, *Ap. J.*, **176**, 57.

Vogel, S. N., Kulkarni, S. R., and Scoville, N. Z. 1988, *Nature*, **334**, 402.

Waller, W. H. 1984, M.S. Thesis, University of Massachusetts.

Waller, W. H., Clemens, D. P., Sanders, D. B., and Scoville, N. Z. 1987, *Ap. J.*, **314**, 397.

Waller, W. H., Kleinmann, S. G., and Ricker, G. R. 1988, *A. J.*, **95**, 1057.

Walterbos, R. A. M. and Kennicutt, R. C. 1987, *Astr. Ap. Suppl.*, **69**, 311.

Watson, D. M., Stanger, V., and Grittiths, R. E. 1984, *Ap. J.*, **286**, 144.

Weliachew, L., Fomaloint, E. B., and Greison, E. W. 1984, *Astr. Ap.*, **137**, 335.

Williams, T. B., Caldwell, N., and Schommer, R. A. 1984, *Ap. J.*, **281**, 579.

Willner, S. P., Soifer, B. T., Russell, R. W., Joyce, R. R., and Gillett, F. C. 1977, *Ap. J. (Letters)*, **217**, L121.

Woltjer, L. 1972, *Ann. Rev. Astr. Ap.*, **10**, 129.

Wolstencraft, R. D., Tully, R. B., and Perley, R. A. 1984, *M. N. R. A. S.*, **207**, 889.

Wynn-Williams, C. G., Becklin, E. E., Matthews, K., and Neugebauer, G. 1979, *M. N. R. A. S.*, **189**, 163.

Young, J. S. and Scoville, N. Z. 1982, *Ap. J.*, **258**, 467.

Young, J. S. and Scoville, N. Z. 1982, *Ap. J. (Letters)*, **260**, L11.

Young, J. S., Gallagher, J. S., and Hunter, D. A. 1984, *Ap. J.*, **276**, 476.

Young, J. S. and Scoville, N. Z. 1984, *Ap. J.*, **287**, 153.

Young, J. S., Scoville, N. Z., and Brady, E. 1985, *Ap. J.*, **288**, 487.

Young, J. S., Kenney, J. D., Tacconi, L., Claussen, M. J., Huang, Y. L., Tacconi-Garman, L., Xie, S., and Schloerb, F. P. 1986a, *Ap. J.*, **311**, L17.

Young, J. S., Schloerb, F. P., Kenney, J., and Lord, S. D. 1986b, *Ap. J.*, **304**, 443.

Young, J. S., Kleinmann, S. G., and Allen, L. E. 1988, *Ap. J. (Letters)*, **334**, L63.

Young, J. S., Xie, S., Kenney, J. D. P., and Rice, W. L. 1989, *Ap. J. Suppl.*, in press.

Young, J. S. 1988 in *Galactic and Extragalactic Star Formation*, eds. R. Pudritz and M. Fich (Dordrecht: Kluwer Academic Publ.).

Yun, M. S., Ho, P. T. P., and Lo, K. Y. 1988, *B. A. A. S.*, **20**, 1001.

Zwicky, F. 1971, *Catalogue of Selected Compact Galaxies and Post-Eruptive Galaxies* (Zurich: Speich).